Coding Theory

Edited by Sudhakar Radhakrishnan
and Muhammad Sarfraz

Coding Theory

*Edited by Sudhakar Radhakrishnan and
Muhammad Sarfraz*

IntechOpen

Supporting open minds since 2005

Coding Theory
http://dx.doi.org/10.5772/intechopen.77427
Edited by Sudhakar Radhakrishnan and Muhammad Sarfraz

Contributors

Ashok Kumar K, P Dananjayan, Kalannagari Viswanath R.L., Vanga Karunakar Matrusri, Emtithal Ahmed Talha, Ryuji Kohno, Rajendra S. Gad, Charanarur Panem, Vinaya Gad, Satyarth Praveen, Ismail Aydogdu, Sudhan Majhi, Palash Sarkar, Sherif Elsanadily, Ali Akbari, Maria Trocan, Madhuri Suthar, Bahram Jalali, Jesús Antonio Álvarez-Cedillo, Teodoro Alvarez-Sanchez, Jacobo Sandoval-Gutierrez, Mario Aguilar-Fernandez, Mathiyalagan Palaniappan, Manikandan Annamalai, Trupti Baraskar, Vijay Mankar

Notice
Statements and opinions expressed in the chapters are these of the individual contributors and not necessarily those of the editors or publisher. No responsibility is accepted for the accuracy of information contained in the published chapters. The publisher assumes no responsibility for any damage or injury to persons or property arising out of the use of any materials, instructions, methods or ideas contained in the book.

We are IntechOpen,
the world's leading publisher of
Open Access books
Built by scientists, for scientists

4,700+
Open access books available

120,000+
International authors and editors

135M+
Downloads

151
Countries delivered to

Our authors are among the
Top 1%
most cited scientists

12.2%
Contributors from top 500 universities

Interested in publishing with us?
Contact book.department@intechopen.com

Numbers displayed above are based on latest data collected.
For more information visit www.intechopen.com

Meet the editors

Dr Sudhakar Radhakrishnan is currently the Professor and Head of the Department of Electronics and Communication Engineering, Dr Mahalingam College of Engineering and Technology, Pollachi, India. He is an editorial board member for 3 international journals namely International Journal of Computer Theory and Engineering, International Journal of Computer and Electrical Engineering, and International Arab Journal of Information Technology. He is currently an associate editor of IEEE-Access, a multidisciplinary journal published by IEEE. He is a reviewer of 16 international journals namely IEEE Transactions on Systems, Man, and Cybernetics: Systems by IEEE; International Arab Journal of Information Technology coming from Zarqa University, Jordan; International Journal of Computer and Electrical Engineering published by International Association of Computer Science and Information Technology Press (IACSIT); International Journal of Computer Theory and Engineering published by International Association of Computer Science and Information Technology Press (IACSIT); Journal of Electrical and Electronics Engineering Research; Iranian Journal of Electrical and Computer Engineering published by Iranian Research Institute for Electrical Engineering, Iran; Journal of Optical Engineering published by SPIE, USA; Journal of Electronic Imaging published by SPIE, USA; Imaging Science Journal, published by Taylor & Francis Group; International Journal of Computational Science and Engineering (IJCSE), published by Inderscience; International Journal of Image Mining(IJIM), published by Inderscience; International Journal of Biomedical Engineering and Technology (IJBET), published by Inderscience; Journal for Image Analysis & Stereology from International Society for Stereology; ETRI Journal from Korea; and the AEUE- International Journal of Electronics and Communications by Elsevier and IET Image Processing. He has written two books titled "Research Issues in Image Compression Using Wavelet Variants" published by Lambert Academic Publishing (LAP), Germany (2010) and "Practicing Signals and Systems Laboratory using MATLAB" published by LAP, Germany (2010) and two book chapters titled "Wavelet based image compression" in "Computational Intelligence Techniques in Handling Image Processing and Pattern Recognition" published by LAP, Germany (2010) and "Analysis of hand vein images using hybrid techniques" in "Hybrid Intelligence Techniques for Image Analysis and Understanding" published by Wiley. He has edited four books titled "Effective Video Coding for Multimedia Applications", "Applications of Digital Signal Processing Through Practical Approach", "Wavelet Theory and Its Applications" and "Coding Theory", all published by IntechOpen, UK (2011, 2015, 2016, and 2020). He has published 105 papers in international and national journals and conference proceedings. His areas of research include digital image processing, image analysis, wavelet transforms, and digital signal processing.

Muhammad Sarfraz is a Professor and Director of MSIT in the Department of Information Science, Kuwait University, Kuwait. His research interests include computer graphics, computer vision, image processing, machine learning, pattern recognition, soft computing, data science, intelligent systems, information technology, and information systems. Prof Sarfraz has been keynote/invited speaker at various platforms around the globe. He has advised more than 85 students for their MSc and PhD theses. He has published more than 350

publications as books and journal and conference papers. Prof Sarfraz is a member of various professional societies. He is the Chair and member of the international advisory committees and organizing committees of various international conferences. He is also editor-in-chief and editor of various international journals.

Contents

Preface

The area of coding theory consists of techniques that enable reliable delivery of digital data over unreliable communication channels. Such techniques allow coding, while decoding enables reconstruction of the original data in many cases. These techniques have various applications in a variety of fields including computer science and telecommunication. These techniques also enrich the areas of information theory and error detection with various other real-life applications.

The chapters in this comprehensive reference cover the latest developments, methods, approaches, and applications of coding theory in a wide variety of fields and endeavors. This book is compiled with a view to provide researchers, academicians, and readers with an in-depth discussion of the latest advances. It consists of twelve chapters from academicians, practitioners, and researchers from different disciplines of life.

The target audience of this book are professionals and researchers working in the field of coding theory in various disciplines, e.g. computer science, information technology, information and communication sciences, education, health, library, and others. The book is also targeted to information engineers, scientists, researchers, practitioners, academicians, and related industry professionals.

Elsanadily begins the book with a discussion on generalized low-density parity check codes used for the construction and decoding algorithms. Scientists have competed to find capacity approach codes that can be decoded with optimal and feasible decoding algorithms. Generalized LDPC (Low Density Parity Check) codes were found to compare well with such codes as they performed well. LDPC codes are well treated with both types of decoding; the Hard-Decision Decoding (HDD) and the Soft Decision Decoding (SDD). However, the authors feel that there is a need for further investigation for the iterative decoding of Generalized Low Density Parity Check (GLDPC) codes on both Additive White Gaussian Noise (AWGN) and Binary Symmetric Channel (BSC) channels. This chapter first describes the construction of the GLDPC code and discusses its iterative decoding algorithms on BSC and AWGN channels so far. The soft-input soft-output (SISO) decoders, for decoding the component codes in GLDPC codes, show very good error performance with moderate and high code rates. However, the complexities of such decoding algorithms are very high. When bit flipping (BF) algorithms by Gallager, as HDD, were presented to LDPC for its simplicity and speed, they were found to be far from the capacity of the BSC. Therefore, using LDPC codes in optical systems using such algorithms is inefficient. GLDPC codes can be introduced as a good alternative of LDPC codes as their performance under the BF algorithm can be improved and the observed error floor can be lowered or even removed. GLDPC codes would then be a competitive choice for optical communications. This chapter discusses the iterative HDD algorithms that improve decoding performance and error floor behavior of GLDPC codes. It also describes the SDD algorithms that maintain the performance but lower decoding simplicity.

This is followed by "Polynomials in Error Detection and Correction in Data Communication System" introduced by Panem et al. This chapter describes the different

types of errors encountered in a data communication system over channels and focuses on the role of polynomials in implementing various algorithms for error detection and correction codes. It discusses error detection codes such as simple parity check, two-dimensional parity check, Checksum, cyclic redundancy check; and error correction codes such as Hamming code, Bose–Chaudhuri–Hocquenghem (BCH), Golay codes, Reed-Solomon (RS) Code, LDPC, and Trellis and Turbo codes. It also gives an overview of the architecture and implementation of the codes and discusses the applications of these codes in various systems.

Sarkar and Majhi, in Chapter 3 of the book, follow with a discussion of "A Direct Construction of Intergroup Complementary Code Set for Code-division Multiple Access (CDMA)." They present a direct construction of intergroup complementary (IGC) code set by using second order generalized Boolean functions (GBFs). Their IGC code set can support interference-free code-division multiplexing. They also illustrate this construction with a graph where the zero-correlation zone (ZCZ) width depends on the number of isolated vertices present in a graph after the deletion of some vertices. The proposed construction can generate the IGC code set with more flexible parameters.

Additive codes were first introduced by Delsarte in 1973 as subgroups of the underlying abelian group in a translation association scheme. Where the association scheme is the Hamming scheme, that is, when the underlying abelian group is of order 2^n, the additive codes are of the form $\mathbb{Z}_2^\alpha \times \mathbb{Z}_4^\beta$ with $\alpha + 2\beta = n$. In 2010, Borges et al. introduced $\mathbb{Z}_2\mathbb{Z}_4$-additive codes which they defined as the subgroups of $\mathbb{Z}_2^\alpha \times \mathbb{Z}_4^\beta$. Chapter 4, "$\mathbb{Z}_2\mathbb{Z}_2[u]$-Linear and $\mathbb{Z}_2\mathbb{Z}_2[u]$-Cyclic Codes" by Aydogdu, aims to introduce $\mathbb{Z}_2\mathbb{Z}_2[u]$-linear and $\mathbb{Z}_2\mathbb{Z}_2[u]$-cyclic codes where $\mathbb{Z}_2 = \{0, 1\}$ is the binary field and $\mathbb{Z}_2[u] = \{0, 1, u, 1 + u\}$ is the ring with four elements and $u^2 = 0$. This chapter provides the standard forms of the generator and parity-check matrices of $\mathbb{Z}_2\mathbb{Z}_2[u]$-linear codes. Additionally, it also determines the generator polynomials for $\mathbb{Z}_2\mathbb{Z}_2u$-linear cyclic codes. Some examples of $\mathbb{Z}_2\mathbb{Z}_2[u]$-linear and $\mathbb{Z}_2\mathbb{Z}_2[u]$-cyclic codes are also presented in this chapter.

The current cellular networks play an important role in daily communications. They integrate a wide variety of wireless multimedia services with higher data transmission rates, capable to provide much more than basic voice calls. Chapter 5, "The Adaptive Coding Techniques for Dependable Medical Network Channel" by Talha and Kohno, is a motivation to increase the demands of reliable medical network infrastructure economically and establish reliable medical transmission via cellular networks. This chapter describes the dependable wireless medical network using an existing mobile cellular network with sophisticated channel coding technologies. It describes the novel way in which the network is adopted as a "Medical Network Channel (MNC)" system. Adding such adaptive outer coding to an existing cellular standard as inner coding makes a concatenated channel to carry out the MNC design. The adaptive design of the extra outer channel codes depends on the Quality of Services (QoS) of Wireless Body Area Networks (WBANs) and also on the remaining errors from the inner-used cellular decoders. The adaptive extra code has been optimized toward MNC for different medical data QoS priority levels. The accomplishment of QoS constraints, for different WBAN medical data, has been investigated in this chapter for MNC using the theoretical derivations. Positive acceptable results have been achieved.

Error correction codes are very important to detect and correct errors from various noise sources. When the technology is scaling down, the effect of noise sources is

high. The coupling capacitance is one of the main constraints to affect the performance of on-chip interconnects. Motivated by coupling capacitance, Chapter 6, "Combined Crosstalk Avoidance Code with Error Control Code for Detection and Correction of Random and Burst Errors" by Kummary et al., introduces the crosstalk at on-chip interconnecting wires. To control single or multiple errors, an efficient error correction code is required. By combining crosstalk avoidance with error control code, the reliable intercommunication is obtained in a network-on-chip (NoC)-based system on chip (SoC). Moreover, to reduce the power consumption of error control codes, it integrates the bus invert-based low-power code to network interface of NoC. The advanced work is designed and implemented with Xilinx 14.7; thereby the performance of improved NoC is evaluated and compared with existing works. The 8×8 mesh-based NoC is simulated at various traffic patterns to analyze the energy dissipation and average data packet latency.

Computer vision is an important part of computer science derived from digital image processing. The last three decades have witnessed a significant growth of applications in the field of remote sensing, approaching toward super resolution images, image analytics, and scalable image and video coding, biomedical imaging, and automatic surveillance due to internet use explosion. Image processing is a technique to enhance or modify the raw images received from different sources like satellites, biomedical field, and pictures taken in normal day-to-day life for various applications. Image processing systems are becoming popular due to its various applications such as: a) remote sensing, b) medical imaging, c) forensic studies, d) textiles, e) mineral science, h) film industry, and i) document processing etc. Information and processing plays a vital role in the modern era. The demand for multimedia applications has increased enormously. Like many other recent developments, the tremendous growth of image and video processing is due to the contribution from major areas such as good network access, easy availability of powerful personnel computers, devices with large memory capacities, availability of graphics software, more fast processors available in the market, and the evolution of good signal processing algorithms.

Chapter 7, by Satyarth Praveen, describes the stereo vision system. Normally a single scene is recorded from two different viewing angles, and depth is estimated from the measure of parallax error. This field has caused many researchers and mathematicians to devise novel algorithms for the accurate output of the stereo systems. This chapter gives a complete overview of the stereo system and talks about the efficient estimation of the depth of the object. It emphasizes the fact that if properly linked with other image perception techniques, stereo depth estimation can be made more efficient than the current techniques. The idea revolves around the fact that stereo depth estimation is not necessary for all the pixels of the image. This fact opens room for more complex and accurate depth estimation techniques for the fewer regions of interest in the image scene.

Everybody knows that our body is a biological machine and that the information from every biological activity is important for monitoring human activity. This biological information can be collected using physiological instruments that measure heartbeat, circulatory strain, oxygen saturation levels, blood glucose, nerve conduction, mind activity, and so on. These signals are called biological signals and the study of these signal is called bio-signal processing. This gives doctors continuous important clinical information to help them make better clinical evaluations. This leads to a field called bioinformatics where both biomedical engineers and doctors can work together for the wellbeing of humans. Chapter 8 by Mathiyalagan

Palaniappan and Manikandan Annamalai gives a comprehensive presentation on bioinformatics and will be useful researchers working in this area.

Edge detection and extraction of semantic information from medical images, electron microscopy images of semiconductor circuits, optical characters, and finger print images plays an important role in image understanding or image analysis. Chapter 9 by Madhuri Suthar and Bahram Jalali deals with an edge detection algorithm called Phase-Stretch Adaptive Gradient-Field Extractor (PAGE). This is a new engineering method that takes inspiration from the physical phenomenon of birefringence in an optical system. The introduced method controls the diffractive properties of the simulated medium as a function of spatial location and channelized frequency.

Image and video data compression refers to a process in which the amount of data used to represent image and video is reduced to meet a bit rate (coding rate) requirement (below or at most equal to the maximum available bit rate), while the quality of the reconstructed image or video satisfies a requirement for a certain application and the complexity of computation involved is affordable for the application. The required quality of the reconstructed image and video is application dependent. In still image compression, a certain amount of information loss is allowed and this is called as lossy compression. Normally a transform-based compression scheme removes interpixel correlation. The recent growth of data intensive multimedia-based web applications has not only sustained the need for more efficient ways to encode signals and images but has made compression of such signals central to storage and communication technology. The first recommended international coding standard was Joint Photographic Experts Group (JPEG) and it relies on the 8×8 block based Discrete Cosine Transform (DCT). The limitation of the JPEG standard comes from the introduction of blocking artifacts. A new standard called JPEG-2000 (using wavelets) was introduced because of the advancements in embedded quantization schemes and new transforms. The current problem is the selection of an image compression algorithm depending on criteria of compression ratio, but the quality of reconstructed images depends on the technology used. Chapter 10 is written by Jesús Antonio Alvarez-Cedillo, Teodoro Alvarez-Sanchez, Mario Aguilar-Fernandez, and Jacobo Sandoval-Gutierrez and shows the development of an novel algorithm executed in parallel using the embedded Zerotree wavelet coding scheme, in which the programs integrate parallelism techniques to be implemented and executed in the many-core system Epiphany III, which is a low-cost embedded system.

Signal modeling is a difficult task in contemporary signal and image-processing methodology. Chapter 11, written by Ali Akbari and Maria Trocan, introduces a particular signal modeling method, called synthesis sparse representation, which has been proven to be effective for many signals, such as natural images, and successfully used in a wide range of applications. In this kind of signal modeling, the signal is represented with respect to a dictionary. The authors focus is mainly on dictionary designing, which provides a simple and expressive structure for designing adaptable and efficient dictionaries. This chapter emphasizes the application of dictionary learning to image compression.

There is a huge need in our medical community to develop applications that are low cost, with high compression, as a huge amount of patient data and images need to be transmitted over the network to be reviewed by the physicians for diagnostic purpose. This leads to an area called biomedical image compression. Here image

compression without image loss is required since a small amount of loss in the data can lead to a wrong diagnosis by the physicians. Chapter 12 by Trupti N. Baraskar and Vijay R. Mankar deals with the medical image compression work through discrete wavelet-based threshold approach. Using this approach by applying N-level decomposition on 2D wavelet types, various levels of wavelet coefficients are obtained. The lossless hybrid encoding algorithm, which combines run-length encoder and Huffman encoder, has been used for compression and decompression purposes.

Structure of the book: The book contains twelve chapters grouped into three sections. Section 1 deals with Error Detection and Correction and contains six chapters. Section 2 concentrates on Signal and Processing and contains three chapters. The last section is devoted to Compression and contains three chapters.

Muhammad Sarfraz
Department of Information Science,
College of Life Sciences,
Kuwait University,
Sabah AlSalem University City,
Shadadiya, Safat, Kuwait

Dr. R. Sudhakar
Professor,
Department of Electronics and Communication Engineering,
Dr. Mahalingam College of Engineering and Technology,
NPT – MCET Campus,
Udumalai Road, Pollachi, Coimbatore – District, Tamilnadu, India

Error Detection and Correction

Chapter 1

Generalized Low-Density Parity-Check Codes: Construction and Decoding Algorithms

Sherif Elsanadily

Abstract

Scientists have competed to find codes that can be decoded with optimal decoding algorithms. Generalized LDPC codes were found to compare well with such codes. LDPC codes are well treated with both types of decoding; HDD and SDD. On the other hand GLDPC codes iterative decoding, on both AWGN and BSC channels, was not sufficiently investigated in the literature. This chapter first describes its construction then discusses its iterative decoding algorithms on both channels so far. The SISO decoders, of GLDPC component codes, show excellent error performance with moderate and high code rate. However, the complexities of such decoding algorithms are very high. When the HDD BF algorithm presented to LDPC for its simplicity and speed, it was far from the BSC capacity. Therefore involving LDPC codes in optical systems using such algorithms is a wrong choice. GLDPC codes can be introduced as a good alternative of LDPC codes as their performance under BF algorithm can be improved and they would then be a competitive choice for optical communications. This chapter will discuss the iterative HDD algorithms that improve decoding error performance of GLDPC codes. SDD algorithms that maintain the performance but lowering decoding simplicity are also described.

Keywords: channel coding, generalized LDPC codes, iterative decoding, bit-flipping, chase algorithm

1. Introduction

Generalized LDPC (GLDPC) block codes were first proposed by Tanner [1] as they internally contain block codes (which are called component codes) and not just single parity check (SPC) as the case in LDPC codes. From this definition, we know that LDPC codes can be regarded as a special class of GLDPC codes. GLDPC block codes possess many desirable features, such as large minimum distance [2], good iterative decoding performance, and low error floor [3]. At the same time, the complexity of the processed operations increases due to the inserted complicated constraints. Therefore, scientists are stirred to find a good GLDPC code with suitable subcodes achieving the desired error performance at fair complication. The methods in [4] by Fossorier and the Bahl-Cocke-Jelinek-Raviv (BCJR) algorithm

[5], APP decoding algorithm, are vastly investigated for GLDPC decoding. Both algorithms perform the task with various subcodes, such as Hamming codes [2, 6], BCH codes [6, 7], RS codes [7], and GLDPC code with hybrid subcodes [8, 9]. However, these decoders can be considered highly complicated. In [10], a kind of Hadamard-based GLDPC codes was suggested. The complicated decoding processes were avoided due to the easiness and fastness of the used subcode transform (FHT). On the other hand, this code is not convenient in many communication systems as it is described as low code rate ($R \leq 0.1$). The soft-input/soft-output (SISO) decoders for decoding the component codes in GLDPC codes were considered in [2, 6] and [11] showing very good error performance with moderate and high code rate. Two interesting approaches at GLDPC codes have been presented in [4, 12]. In [12] the proposed construction concentrates on maximizing the girth and the minimum distance of the global code. The generated codes achieved coding gain up to 11 dB over 40 GB/s optical channel. In [4] the authors propose doubly generalized LDPC codes. These codes employ local codes at both variable and check nodes. Back to LDPC codes and since their resurrection, most research efforts were directed toward the implementation of these codes over the additive white Gaussian noise (AWGN) channel. The LDPC codes were proven to perform very close to the Shannon limit of AWGN channel, and much work has been carried out to design optimal codes and improve and simplify iterative decoding of these codes over the AWGN channel. The major drawback is that it exhibits considerable computational complexity. Gallager accurately, on the other hand, analyzed the performance of LDPC codes over the binary symmetric channel (BSC) in his original paper and proposed two HDD bit-flipping (BF) algorithms, for which he provided theoretical limits under iterative decoding. However, BF algorithms did not gain much attention. Most of the work that considered BF decoding used it in conjunction with soft information obtained from AWGN channel to improve decoding performance. However, in some applications, such as optical communications, soft values are not available at the receiver. Therefore, optical channels are an excellent example of the BSC, and only hard decision decoding is possible. Currently, BCH and RS codes are exclusively used in optical communication for error control, since there are simple and efficient algorithms for decoding. With the recent introduction of wavelength division multiple access (WDMA), transmission rates in optical communications reach 40 GB/s per channel/fiber, a standard in modem optical networks, SONET/SDH. Moreover, the concept of signal regeneration was abandoned in optical communication with the advancement in lasers so that optical signal is transmitted over larger distance than before, reaching the receiver very attenuated. These developments in optical communication call for an error control code which is very powerful yet has a simple and fast decoding. Furthermore, very low error rates are needed, say BER of 10^{-15}.

The BF algorithm proposed by Gallager is a HDD algorithm and is implemented using modulo-2 logic. Therefore it satisfies the requirement for simplicity and speed. However, the performance of the decoding algorithm is far from the capacity of the BSC, and, more importantly, an error floor is generally observed, which seriously constrains implementation of LDPC codes in optical systems. GLDPC codes can be introduced as a good alternative of LDPC codes as their performance under the BF algorithm can be improved and the observed error floor can be lowered or even removed. GLDPC codes would then be a competitive choice for optical communications.

In this chapter, iterative decoding of GLDPC codes over AWGN and BSC is studied. HDD algorithms that improve decoding performance and error floor

behavior of GLDPC codes over BSC channels are discussed. They make GLDPC codes very competitive for high-rate optical communications. Soft decision decoding (SDD) algorithms that maintain the performance but lower decoding simplicity are also presented.

2. GLDPC code construction

The check node in the bipartite graph of the LDPC code, as said before, is connected to a number of variable nodes which satisfy a single parity check. The GLDPC is a more generalized form of LDPC as the bits of the VNs, connected to the same CN, constitute a valid codeword of a (n,k) linear block code (other than the simple SPC code). Therefore this (n,k) code is called a constituent code, component code, or simply subcode. The CN which associates with this generalized code is called a generalized CN (GCN). The GLDPC code is referred to as a (N, J, n) regular and "strict-sense" code, as depicted in **Figure 1**, if:

- The VN degree (denoted as q_w) is constant for all VNs ($q_w = J$).

- The GCN degree (denoted as q_c) is constant for all GCNs ($q_c = n$).

- The same constituent code (other than the simple SPC code) stands for all GCNs.
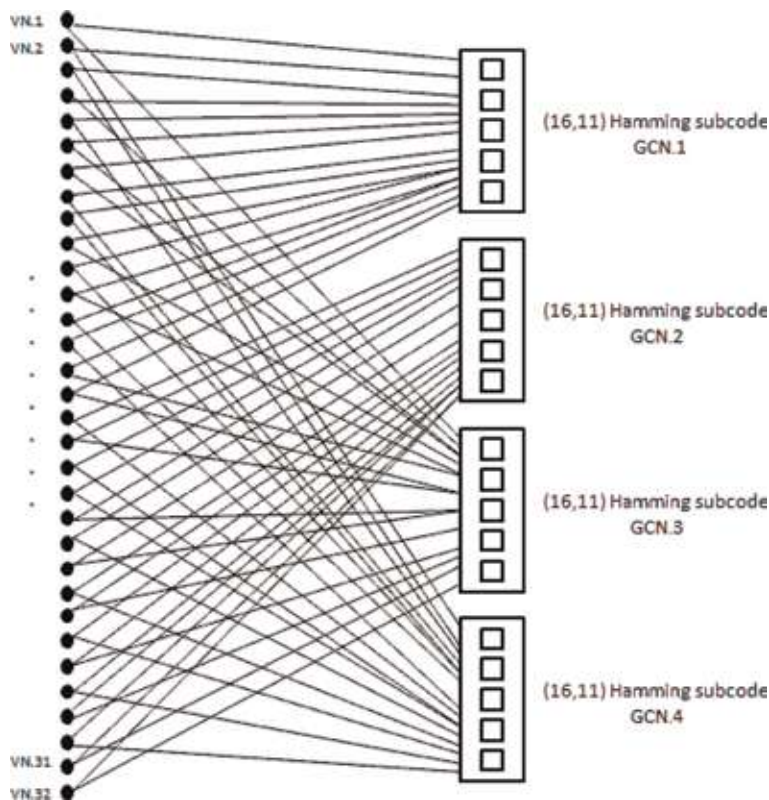
Figure 1.
The bipartite graph of the strict-sense (32,2,16) regular GLDPC code.
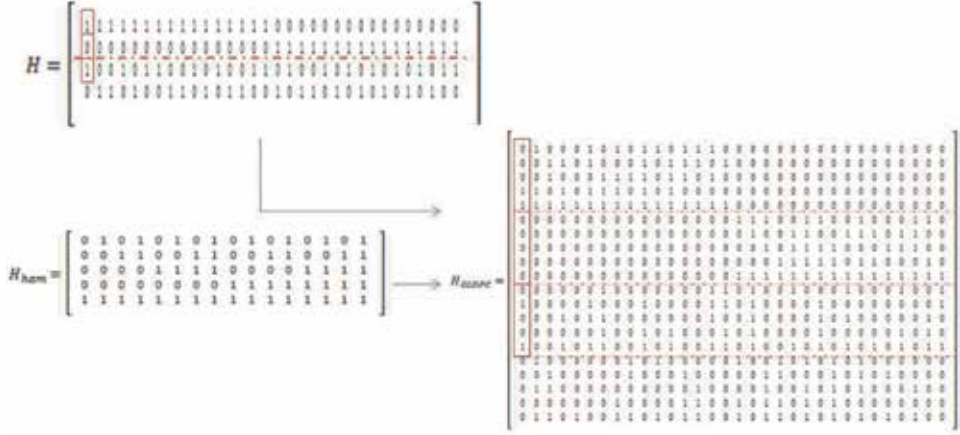
Figure 2.
The procedure of generating a (32,2,16) Hamming-based GLDPC code from its base matrix.

where J is the column weight in the parity-check matrix of the global LDPC code and N is the overall code block length. The GLDPC code is otherwise called "hybrid code" (if not all the GCNs has the same constituent code) [8, 13].

The GLDPC code rate is given by $R = K/N \geq 1 - J(1 - k/n)$, where K denotes its code dimension and N denotes its block length. The GLDPC code, according to the chosen values of its parameters, has multiple wonderful properties such as the better minimum distance (compared to LDPC code with the same code rate) [2]. The GLDPC also converges faster, and it is distinguished by the lower error floor [3]. We are interested here with GLDPC codes based on Hamming codes for simplicity and fast decoding purposes.

Figure 1 elaborates the bipartite graph of a (N, J, n) regular Hamming-based GLDPC code with (4×32) global LDPC matrix. The extended Hamming (8,4) constituent code is represented in every GCN. **Figure 2** depicts the procedures to get the overall parity-check matrix of this code from the global LDPC matrix (or referred to as the graph adjacency matrix). Every "1" in every row in the global matrix is replaced with a column from the columns of the constituent code parity-check matrix, and every "0" is replaced with a zero column. The assignments of the constituent code H columns should be randomly done to generate a code with good characteristics. There are other constructions of GLDPC which can be further discussed in [14–16].

3. SDD of GLDPC codes

SDD of Hamming-based GLDPC codes was presented in the literature and shows that GLDPC codes are asymptotically good and can achieve the capacity by iterative decoding using soft-input/soft-output subcode decoders [2, 6, 17]. The SISO decoder is typically a sub-optimal erasure decoder extended to deliver soft outputs, e.g., chase-II decoder [18], which is used in this section.

A (N, J, n) GLDPC code is constructed from a $(N.J/n)$ by N random sparse matrix H, with row weights of n and column weights of J, and the parity-check matrix H_c of a (n, k, d) subcode. The resultant GLDPC parity-check matrix is denoted as H_{GLDPC} as discussed in Section 2.

At any GCN c, the input to the chase decoder is $R_c = \{r_{c,1}, \cdots, r_{c,i}, \cdots, r_{c,n}\}$ corresponding to the transmitted word $X_c = \{x_{c,1}, \cdots, x_{c,i}, \cdots, x_{c,n}\}$ and its hard demodulated values $Y_c = \{y_{c,1}, \cdots, y_{c,i}, \cdots, y_{c,n}\}$.

A group of codewords are selected as the most likely ones that hold the transmitted words with the minimum errors. The algorithm operates on the available data (reliability) and flips all possible combinations of $p = d/2$ demodulated symbols with the least-reliable positions (LRPs). Setting the reliability information in [19] in the log-likelihood ratio (LLR) of decision $y_{c,i}$ as

$$\Lambda\left(y_{c,i}\right) = \ln\left(\frac{pr(x_{c,i} = +1/x_{c,i})}{pr(x_{c,i} = -1/x_{c,i})}\right) = \left(\frac{2}{\sigma^2}\right)r_{c,i} \qquad (1)$$

A set $Z_c = \{Z_c^q\}$ of error patterns with all possible errors confined to p LRP positions of Y_c is used to modify Y_c yielding list of test patterns T_c^q ($q \in \{1, \cdots, 2^p\}$, $T_c^q = Z_c^q + Y_c$). Then every T_c^q in the list is decoded using algebraic decoder, and the valid decoded codeword C^q is stored in a list Ω as a candidate codeword. Decision codeword $D_c = \{d_{c,1}, \cdots, d_{c,i}, \cdots, d_{c,n}\}$ should be chosen from this list as it is obtained using the rule [20]:

$$D_c = C^q \ \ if \ \ |R_c - C^q|^2 \leq |R_c - C^l|^2 \text{for every } C^l \in \Omega \qquad (2)$$

Now, every decoded symbol resulting value in the subcode (soft) is to be estimated to be passed back on the edges, linked to symbol nodes with steps as the MP algorithm iteratively to output a final estimate after performing a predefined amount of iterations or satisfying the syndrome check.

In order to calculate the reliability of each bit, $d_{c,i}$, in the decision D_c (i.e., the ith soft output of the soft-input decoder), two codewords $C^{+1(i)}$ and $C^{-1(i)}$ are to be selected from two sets of Ω with minimum Euclidean distance from R. The decision D_c is one of them, and the second one, $B_c = \{b_{c,1}, \cdots, b_{c,i}, \cdots, b_{c,n}\}$, called as competing codeword of D with $b_{c,i} \neq d_{c,i}$, should be found.

The soft outputs are generated in the LLR domain outgoing from GCN c using the following approximation formula:

$$r'_{c,i} = \left(\frac{|R_c - B_c|^2 - |R_c - D_c|^2}{4}\right)d_{c,i} \qquad (3)$$

If the competing codeword B_c is not found, the following alternative and efficient formula is used:

$$r'_{c,i} = \beta \times d_{c,i} \ \ with \ \ \beta \geq 0 \qquad (4)$$

where β is a reliability factor. Due to the variation of sample deviation in the input and in the output of the soft decoders, we put a scaling factor, α, to increase the convergence rate:

$$W_c(t+1) = R_c + \alpha(t)W_c(t) \qquad (5)$$

By subtracting the soft input $r_{c,i}$ from the soft output $r'_{c,i}$ for each $i \in \{1, 2, \cdots, n\}$ at GCN c, the extrinsic information during the tth iteration, $W(t)$, is obtained. It is then multiplied by the scaling factor, $\alpha(t)$, added to the channel observed values R_c,
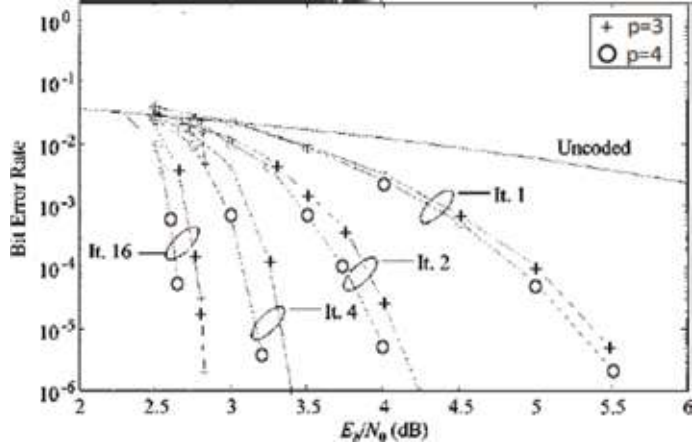
Figure 3.
Performance variation with erasures p for (65,536,2,64) GLD code.

and the result is considered as a priori information for the decoder at the next $(t + 1)$th iteration.

Figure 3 shows that a chase rather than optimal SISO decoder can be successfully employed in the decoding of high-rate extended Hamming-based GLDPC codes and the BERs are close to the capacity with the efficient fast chase decoding in [21].

4. HDD of GLDPC codes

The HDD such as BF decoding or any other algebraic decoding scheme can be generalized to GLDPC codes especially over BEC or BSC and can be applied in very high-speed applications such as the 40 GBps optical communications. The error-correcting capability of the subcodes, at the GCNs, is used to more accurately determine the position of least-reliable symbols. The iterative HDD algorithms for decoding GLDPC codes will be described in the next subsections.

4.1 WBFV algorithm

As mentioned before in BF algorithm of LDPC codes, symbols belonging to the maximum number of unsatisfied CNs, in each iteration, have the binary bits inverted before the following iteration. Subsequently, the failed CNs convey their votes of unit weight to the corresponding connected VNs, and the algorithm inverts the LR bits with the highest amount of votes.

The presented iterative weighted bit-flip voting (WBFV) in [22] employs subcode hard decision decoders (HDDs) at the GCNs that have a greater range of vote weights passed to the connected VNs. It passes the high-weight votes to a specific symbol if the HDD, at a given GCN, considers it to be in error.

As the GLDPC codes of Gallager construction, $J = 2$, and Hamming subcode are only concerned, all nonzero syndromes of these subcodes will be error-correctable. The algebraic decoders only allow for two instances:

- All-zero syndromes imply a valid codeword; in this case a vote V will be returned to all connected VNs (symbols) as in GCN 1 in **Figure 4**.

- Nonzero syndromes imply nonvalid codewords; in this case the indicated error position will be sent a vote E, and all other bits a vote e as in GCN 2 in **Figure 4**.

After votes have been cast, each symbol has received a vote pair: either VV, eV, ee, EV, Ee, or EE. In the example shown, the symbol at the two subcodes' intersection has a vote pair eV.

The strategy proceeds by passing current bit values from the VNs to the Hamming decoders at GCNs. The HDDs at these GCNs pass back n individual votes to the symbols they connect.

The magnitude of a vote marks the power of the decision for a GCN about the current symbol (reliable or not). The higher magnitudes mark the unreliable bits, and the lower ones mark the bits of more reliability.

The J arriving votes to every VN are collected such that all N variable symbols are sorted by the reliability information and the group of LRP bits inverted before the upcoming iteration.

The iterative algorithm proceeds until all symbols become of weight pair VV or the maximum number of iterations is reached. For Hamming subcodes there are only three votes V, e, and E generated by the subcode HDDs described before. The vote rules, as sets of vote weights, are defined and listed in **Table 1**.
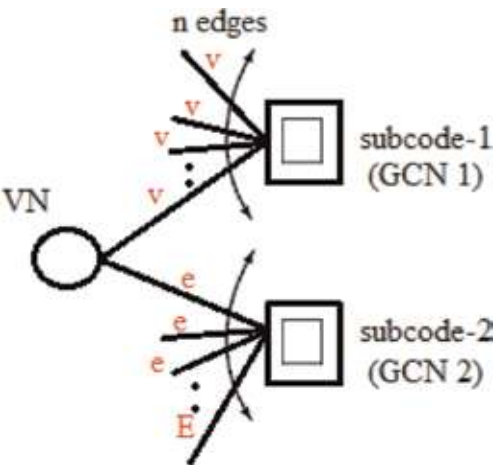
Figure 4.
Example votes from subcode decoders.

Rule A		Rule B		Rule C	
$V = 0, e = 2, E = 3$		$V = 0, e = 1, E = 2$		$V = 0, e = 1, E = 3$	
Vote pair	Total	Vote pair	Total	Vote pair	Total
EE	6	*EE*	4	*EE*	6
Ee	5	*Ee*	3	*Ee*	4
ee	4	*EV, ee*	2	*EV*	3
eV	2	*VV*	0	*eV*	1
VV	0			*VV*	0

Table 1.
Vote pair orderings for three vote rules.
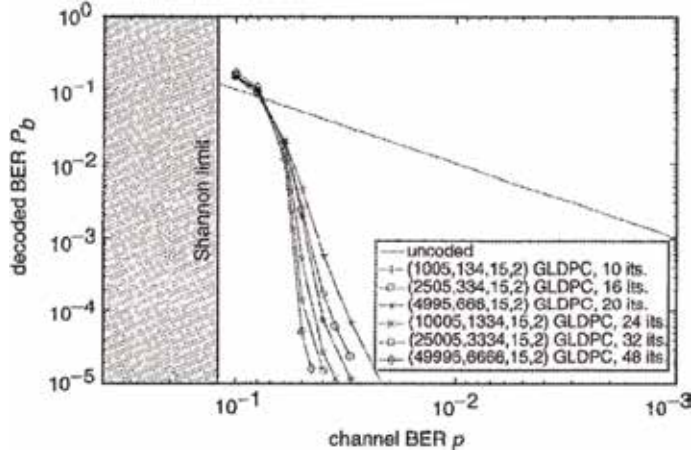
Figure 5.
Variation in performance with block length for (N,M,15,2) GLDPC codes.

Figure 5 shows that there is an obvious coding gain with increasing N. Actually, the BER curve p required to give $P_b = 10^{-5}$ versus N showing a linear relationship between $\log p$ and $\log N$.

4.2 BCH-based Fossorier decoding algorithm

In [6] GLDPC codes with BCH subcodes (instead of Hamming subcodes) were considered, but for AWGN channel and ML soft decoding due to its higher error-correcting capability. The algorithm presented here also uses the high-rate BCH and RS codes, but as HDD algorithm, and can be efficiently applied in very high-speed (40 GBps) optical systems as the soft information is not available due to optical-electrical conversions [7].

The actions of this algorithm are updated as follows: VN i is considered to be connected to the GCNs j and k. Two messages will be sent from GCN j to VN i. First, it outputs u_{ji} (the value of VN i) taken out from the sub-decoder. Second, it outputs U_{ji} (represents data about success or failure of GCN decoding). U_{ji} is then a binary signaling with estimate 1 if there is a valid word or estimate 0 if there is not. W.r.t the arriving messages from node k, the same action is applied.

The VN message v_{ij} depends on the value received from the channel y_i, and the messages received from the GCNs other than node j. Since GLDPC codes of high code rate ($J = 2$) is only concerned, there is only one other GCN k). Hence, the updating rule in the symbol node can be expressed as

$$v_{ij} = y_i \cdot \overline{U_{ki}} + u_{ki} \cdot U_{ki} \qquad (6)$$

where $\overline{U_{ki}}$ is the complement of U_{ki}. The processes of the decoder are carried out until the satisfaction of all GCNs or until reaching a certain amount of iterations. Finally, any symbol (VN) connected to a satisfied GCN will take its proposed value. If the VN connected to two unsatisfied GCNs, it will take the original received value.

RS-based GLDPC code of rate $r = 0.467$ and different lengths are examined (**Figure 6**). It shows that RS(15,11,5) product code performs better than the corresponding GLDPC of length 225, because it possesses a better minimum distance. As N increases, the BER is improved particularly in the region of error floor.
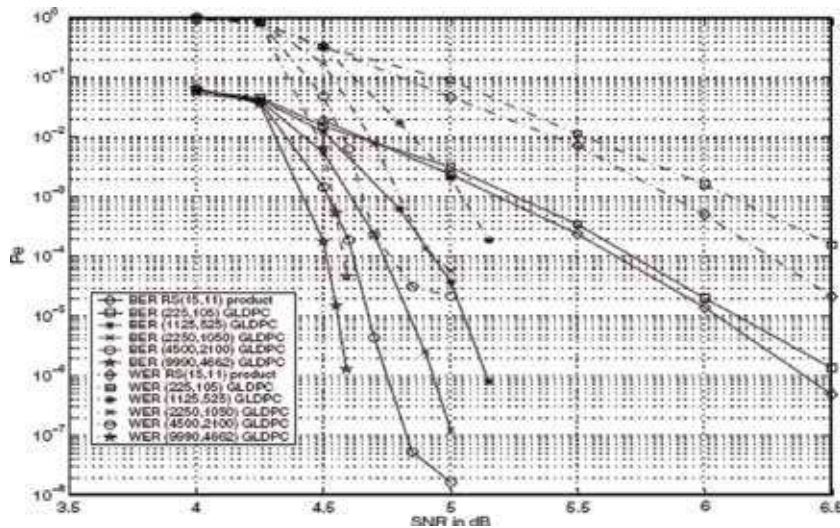
Figure 6.
Performance of GLDPC codes with RS(15,11,5) codes.

5. Modified HDD algorithms for improving the error performance

5.1 Two-side state-aided bit-flipping (TSSA-BF) algorithm

A HDD decoder founded on BF algorithm is presented in [23]. The main view depends on taking advantage of the different sub-decoder states. Therefore it adds this data representing these states as a reliability factor to be utilized for the rest of the decoding process. This additional data (in the form of additional bit) is inserted in two sides (VNs and CNs).

The goal is generally to remove all likely produced trapping sets (that generate non-editable errors) from the code construction. This approach is presently still not obtainable due to constraints in the processing speed and implementation. An alternative approach that fulfills the most of this goal is suggested (with reasonable processing speeds). That approach adds resources only operated in unusual circumstances when the previously mentioned trapping sets happen.

Taking commonness into account and due to its simplicity, the extended Hamming code is studied inside the GLDPC codes.

5.1.1 Failure analysis

In the case of using the ext-Hamming code $d_{min} = 4$, the sub-decoders of GLDPC code may output errors in both cases of decoding success or failure. At GCN failure case, it cannot clearly locate the error place. In the case of GCN decoding success, the errors may be generated from undiscovered errors (when a received word decoded to non-sent valid ones, i.e., $e \geq 4$) or faulty repair (when $e > 2$). Therefore, the errors at a given GCN can be distinguished by the following names:

1. Plain single error (element P): one error and true correction take place.

2. Unknown set (U-set): multiple errors ($e > 1$) with decoder failure (detects but can't mark errors).

3. Ambiguous set (A-set): multiple errors ($e > 2$) making the decoder flipping an assumed-correct bit (false correction).

4. Dark set (D-set): multiple errors ($e \geq 4$) not detected by the decoder which produce zero-syndrome vector.

5.1.2 Algorithm description

As GLDPC code with 1B-construction is studied in [22] as in **Figure 7**, a further bit is inserted beside the main bit moving between the VN and GCN. For VNs, it acts as the reliability of its bit value (bit 1 if suspect or bit 0 if assumed correct), and it forwards this additional data to be used by GCNs. For GCNs, this additional bit acts as the power of its decision by raising the reliability levels to 4. The GCN decodes the received word, forwards a signal (bit 1 or 0, namely, flip or keep), and appends this additional bit as the power of this signal (in ascending reliability level arrangement, $1^+(11)$, $1^-(10)$, $0^-(00)$ and $0^+(01)$, corresponding strong flip, weak flip, weak keep, and strong keep, respectively).

5.1.2.1 Horizontal processing

Specifying the ext-Hamming decoder, there are three states at a given GCN as state "0" in the case of zero syndrome, state "1" in the case of one-error repair, and state "2" in the case of decoder failure.

For any GCN c, $c = 1, 2, \cdots, M$, let $d_c^{(l)}$ be the cth GCN decoder state at the lth iteration. If $d_c^{(l)} = 0$, the decoder forwards a message (0^-) to all set elements of its connected VNs, $W(c) = \{w_1, w_2, .., w_i, .., w_n\}$. The message ($0^-$) with reliability level 3 is forwarded assuming $W(c)$ may contain a dark set (D-set). If $d_c^{(l)} = 1$, the decoder forwards (1^+) with level 1 on the assumed-error place w^* and (0^-) to the remaining set elements $W'(c)$. Elements of $W'(c)$ are given 0^- (not 0^+) assuming that they may contain A-set. Finally, If $d_c^{(l)} = 2$, it sends (1^-) with level 2 to all elements of $W(c)$ which contains a U-set.

As illustrated in **Figure 8**, let $U_{c,w_i}^{(l)} = \left[U_{c,w_i}^{(l)}(1), U_{c,w_i}^{(l)}(2) \right]$ be the two bits representing the outgoing flip message and its reliability, respectively, from GCN c to VN w_i. **Table 2** illustrates the four possible outgoing messages from GCN c to every connected VN w_i.
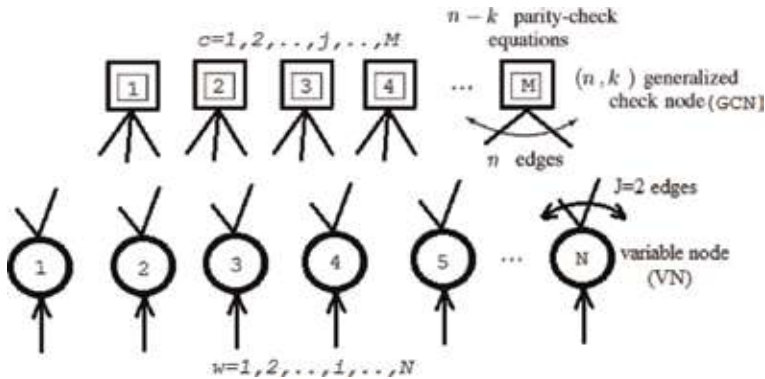
Figure 7.
GLDPC bipartite graph example.
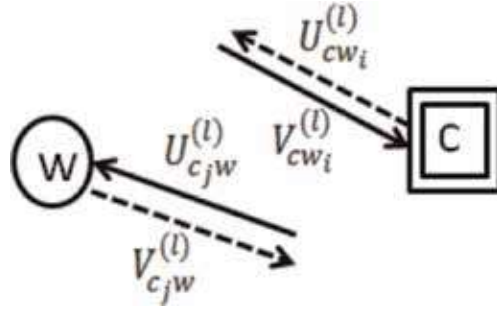
Figure 8.
Incoming and outgoing messages between GCNs and VNs.

$U_{c,w_i}^{(l)}(1)U_{c,w_i}^{(l)}(2)$	Alternative denotation	Reliability grade	Message meaning
1 1	1^+	1	Strong flip
1 0	1^-	2	Weak flip
0 0	0^-	3	Weak keep
0 1	0^+	4	Strong keep

Table 2.
Possible outgoing messages from GCN c to any connected VN.

Let $V_{c,w_i}^{(l)} = \left[V_{c,w_i}^{(l)}(1), V_{c,w_i}^{(l)}(2) \right]$ be the two bits representing arriving bit value and its reliability, respectively, at GCN c from VN w_i. For any GCN c, let initial reliability bit be $V_{c,w_i}^{(0)}(2) = 0$ for all $w_i \in W(c)$. As previously mentioned, $V_{c,w_i}^{(l)}(2) = 1$ if a suspect bit and 0 if assumed correct one.

Now a local GCN counter will be introduced to compare the present GCN state with the one of previous iteration. Let $\alpha_c^{(l)}$ be the number of consecutive previous repetitions of the state $d_c^{(l)}$, and let $\beta_c^{(l)}$ be the number of incoming suspects among the n bits connected to GCN c. According to $\alpha_c^{(l)}, \beta_c^{(l)}$ values and the additional information $V_{c,w_i}^{(l)}(2)$, the algorithm can improve its decision, and the horizontal process iteratively continues as illustrated in [23].

For $d_c^{(l)} = 0$, the counter role is to enhance the reliability from 0^- to 0^+ if the state remains for two consecutive iterations. For any GCN c and $d_c^{(l)} = 2$, if the message $V_{c,w_i}^{(l)}(2)$ from the bit w_i indicates a suspected bit and the decoder state $(d_c^{(l)} = 2)$ remains for three consecutive iterations, the decoder recalculates the syndrome after flipping this suspect. If the syndrome check is satisfied (i.e., valid codeword), the decoder estimates that bit as error and degrades its reliability from 1^- to 1^+.

5.1.2.2 Vertical processing

With four reliability levels and $J = 2$, there will be a set of 10 possible combinations of incoming messages at VN w, $w = 1, 2, \cdots, N$. This set can be divided, according to the failure analysis, into three subsets $\{s_i, i = 1, 2, 3\}$. For any VN w, its reliability state $r_w^{(l)}$ is determined based on its incoming messages (from GCNs c_j, with $j = \{1, 2\}$) to which subset it belongs:

$$s_1 = \{(1^+, 1^+), (1^+, 1^-), (1^+, 0^-)\},$$
$$s_2 = \{(1^-, 1^-), (1^-, 0^-), (0^+, 1^+)\},$$
$$s_3 = \{(0^-, 0^-), (0^+, 1^-), (0^+, 0^-), (0^+, 0^+)\}$$

$$r_w^{(l)} = \begin{cases} 0 & \text{if } \left\{ U_{c_j w}^{(l)}, j = 1, 2 \right\} \in s_1 \\ 1 & \text{if } \left\{ U_{c_j w}^{(l)}, j = 1, 2 \right\} \in s_2 \\ 2 & \text{if } \left\{ U_{c_j w}^{(l)}, j = 1, 2 \right\} \in s_3 \end{cases}$$

The VN w with least-reliable level, $r_w^{(l)} = 0$, needs to be flipped. For $r_w^{(l)} = 1$, VN state counter is appointed to make a comparison between the VN current reliability state and the one of the previous iteration. Let $\gamma_w^{(l)}$ be the number of consecutive previous repetitions of the state $r_w^{(l)}$. With $r_w^{(l)} = 1$ and according to $\gamma_w^{(l)}$ values, the VN will not be flipped but counted as a suspected bit. It sends such reliability information $\left(V_{c_j w}^{(l)}(2) = 1, j = 1, 2 \right)$ to GCNs to be taken into account. For $r_w^{(l)} = 2$, the VN is considered a reliable bit and kept with $V_{c_j w}^{(l)}(2) = 0, j = 1, 2$ (i.e., assumed correct bit).

Figures 9–11 show the block diagrams of the overall decoder, horizontal process, and vertical process, respectively. **Table 3** illustrates an example for ext-Hamming (8,4) constituent decoder employed at GCN $c(n = 8)$ at lth iteration as the shaded parts represent certain conditions satisfied.
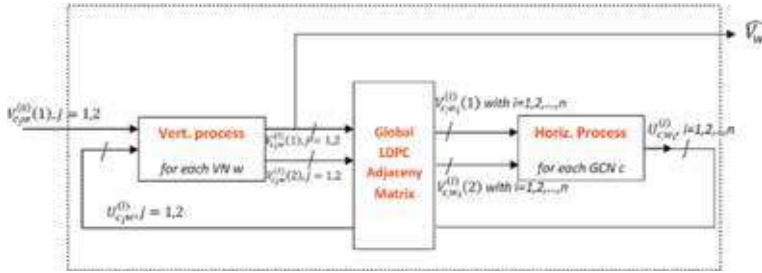

Figure 9.
Block diagram of the overall TSSA-BF decoder.
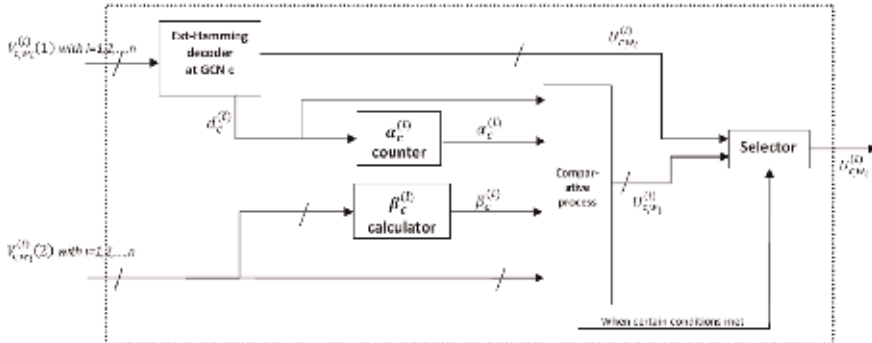
Figure 10.
Block diagram of the horizontal process of the TSSA-BF decoder.
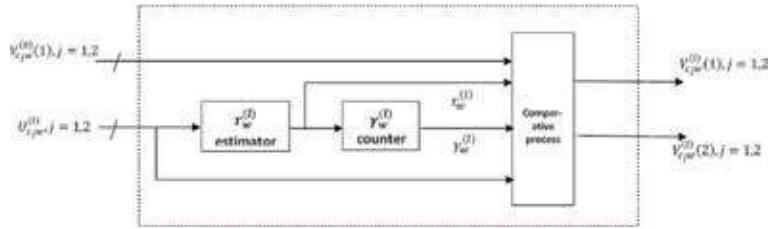
Figure 11.
Block diagram of the vertical process of the TSSA-BF decoder.

GCN State $(d_c^{(l)})$	STATE Counter $(\alpha_c^{(l)})$	# of suspects $(\beta_c^{(l)})$ if existed	$V_{cjw}^{(l)}(2), i=1,2...,n$ with ... suspect bits								o/p messages $U_{cw_i}^{(l)}, i=1,2...,n$							
			1	2	3	4	5	6	7	8	1	2	3	4	5	6	7	8
0	<2										0	0	0	0	0	0	0	0
	≥2	$\beta_c^{(l)}=0$	0	0	0	0	0	0	0	0	0^-	u^+	0^+	0^+	0^-	u^+	0^+	0^-
		$\beta_c^{(l)}>4$	1	1	0	1	0	0	0	1	0^-	u^-	0^+	0^-	0^-	u^+	0^+	0^-
1 (with w^* w_3)											0^-	0^-	1^+	0^-	0^-	0^-	0^-	0^-
>	<3										1^-	1^-	1^-	1^-	1^-	1^-	1^-	1^-
	>3	$\beta_c^{(l)}$ 1	0	1	0	0	0	0	0	0	0^-	1^+	0^-	0^-	0^-	0^-	0^-	0^-
		$\beta_c^{(l)}=2$	0	0	1	0	0	1	0	0	0^-	u^-	1^+	0^-	0^-	1^+	0^-	0^-

Table 3.
Example of ext-Hamming (8,4) constituent decoder employed at GCN c at lth iteration.

5.1.3 Important notes on the algorithm

- The output messages from VN w to its two connected GCNs $c_j, j=1, 2$ are the same (i.e., $V_{c_1w}^{(l)} = V_{c_2w}^{(l)}$).

- The initial incoming message at GCN c $V_{c_jw}^{(0)}(1) = y_w$, $V_{c_jw}^{(0)}(2) = 0, j = 1, 2$ as the overall demodulated binary sequence $Y = \{y_w, w = 1, 2, \cdots, N, y_w \in \{0, 1\}\}$.

- $U_{cw_i}^{(l)} = \left[U_{cw_i}^{(l)}(1) U_{cw_i}^{(l)}(2)\right]$ is the outgoing message from GCN c to VN w_i consisting of two bits representing the reliability level (one of four possible values 0^+, 0^-, 1^-, or 1^+).

- The GCN decoder does not output actual decoded words to its connected VNs. Instead, it sends a reliability signal (taking a value of four possible values) which is represented by two bits $U_{cw_i}^{(l)}(1)$ and $U_{cw_i}^{(l)}(2)$. On the other hand, the VN has to take a decision based on its incoming messages. The decision is (Flip), (Keep but as suspect) or (Keep as assumed correct).

- The function of GCN state counter $\left(\alpha_c^{(l)}\right)$ or VN state counter $\left(\gamma_w^{(l)}\right)$ is to count the number of consecutive iterations with the same state (at this GCN or VN) up to this present iteration (l), respectively.
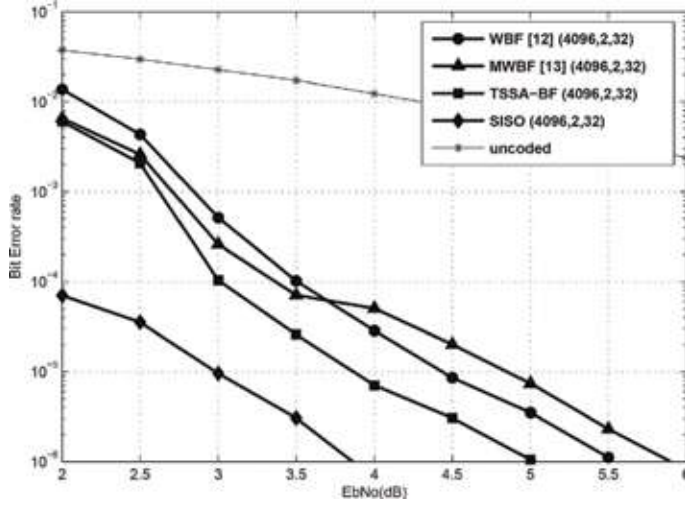
Figure 12.
Performance of GLDPC with (32,26) ext-Hamming subcodes.

Figure 12 is showing the BER performance of the ext-Hamming-based GLDPC code (with overall rate $R = 0.625$) by the TSSA-BF algorithm compared to HD decoder BF algorithms in [7, 22] and SD chase sub-decoder (number of LRPs $p = 2$). The finite-length 1B-construction-GLDPC codes of block length $N = 4096$ is used, and the maximum number of iterations (I_{max}) is set to 20. It is noted that this algorithm outperforms the other HDD ones along various values of E_b/N_o with gain not <0.5 dB at the expense of a little increase in resources used by the algorithm.

5.2 Classification-based algorithm for BF decoding with initial soft information

This algorithm is a modern bit-flipping decoding approach [24]. It is established on taking advantage of the fast BF HDD method with the help of the data extracted from the AWGN channel.

However it exploits this data at only the start phase of the decoding intentionally to make a certain classification operation. This algorithm also improves its performance by adding an additional bit in the arriving messages at VNs from CNs as a technique to enhance the decision reliability at both VNs and GCNs. The main role of this additional bit is to benefit from the subcodes states as in [23] but with a distinct fashion. This approach allows for considerable enhancement in BER at the expense of additional resources at only the side of VNs. SDD is characterized by complexity and the need to a large amount of real calculations (according to the channel soft information) all during the whole decoding procedure. However, this algorithm (accounted as HDD) needs them only in the start phase, and all processed data thereafter are hard values. Therefore this technique could reduce a significant part of the computational complexity, which was noticed in [23].

5.2.1 Algorithm description

The trapping sets, producing unrepaired errors, form the major part of the error performance letdown of the bipartite graph-based codes. The goal here is to diminish the damaging effect of most of the generated sets even by inserting supplemental resources which will be discussed below in this section.

The algorithm uses the soft channel values at the beginning of the decoding to classify the received symbols (VNs) by a predetermined threshold. Taking commonness into account and due to its simplicity, the extended Hamming code is studied inside the GLDPC codes. The extended Hamming code with increased $d_{min}(d_{min} = 4)$ is powerful and suitable for constructing standard-relevant GLDPC codes. The ext-Hamming sub-decoders may produce errors in both cases, decoding success and failure. At the GCN sub-decoder failure, it cannot locate the places of errors. At the GCN sub-decoder success, the decoder errors may emerge from two reasons: the undiscovered errors (as the received word decoded to non-transmitted valid one ($e \geq 4$), where e is the number of errors at the input of the local decoder) and the false repair ($e > 2$).

An additional bit is inserted next to the main bit in the message from the GCN to a connected VN. It acts as the decision power of GCN by raising the reliability from two to four levels. The GCN sub-decoder decodes the received word and forwards two bits (the main bit and the additional one) to every connected VN. If the main bit is seen as a decision (flip (1) or keep (0)), the additional one is seen as the decision power (strong (1) or weak (0)). The four reliability levels in descending arrangement are $0^+ (01)$, $0^- (00)$, $1^- (10)$, and $1^+ (11)$, corresponding to strong keep, weak keep, weak flip, and strong flip, respectively. This decoding contains two processes, the GCN processing and the VN processing, as will be explained below.

5.2.1.1 GCN processing

The three possible states, in which the ext-Hamming sub-decoder at a given GCN can be one of them, are defined as follows:

1. State 0: when the syndrome gives zero (i.e., the received sequence is a valid codeword).

2. State 1: is the case of one-error repair when the syndrome vector is one of the subcode parity-check matrix columns (i.e., error discovered and can be corrected). Therefore, it decodes to the right transmitted codeword or decodes to another valid codeword.

3. State 2: at the decoder failure (errors detected and cannot be corrected).

Using the same notations as in **Figure 8**, for any GCN c, $c = 1, 2, \cdots, M$, let $d_c^{(l)}$ be the decoder state of the cth GCN at the lth iteration. The procedures of the GCN sub-decoder of this algorithm are illustrated below:

- If $d_c^{(l)} = 0$, it sends 0^+ to all elements of the connected VNs set, $W(c) = \{w_1, w_2,.., w_i,.., w_n\}$. The message (0^+) is the highest reliability level.

- If $d_c^{(l)} = 1$, it sends 1^+ (level 1) on the place b^* (an assumed-error bit) and 0^- (level 3) to the rest of set elements $W'(c)$. Elements of $W'(c)$ are given 0^- (not 0^+) assuming some errors may be involved (with $e > 2$) making the decoder perform a wrong repair (an assumed-correct bit is flipped).

- If $d_c^{(l)} = 2$, it sends 1^- (level 2) to all of $W(c)$ elements as they contain a set of errors (with $e > 1$) leading to a decoder failure (errors detected with no repair capability).

Let $U_{c,w_i}^{(l)} = [U_{c,w_i}^{(l)}(1)\ U_{c,w_i}^{(l)}(2)]$ be the two bits which represent the outgoing decision message and its power, respectively, from GCN a to VN w_i. Let $V_{c,w_i}^{(l)}$ be the incoming binary bit value of the constituent codeword at c from VN w_i.

The overall set of N hard demodulated sequence bits is $Y = \{y_w, w = 1, 2, \cdots, N,$ $y_w \in \{0,1\}\}$ as $y_w = \frac{1}{2}(\text{sgn}(r_w) + 1)$ and r_w is the soft value of the wth bit in the received sequence from AWGN channel. For any VN w, the initial values $V_{cjw}^{(0)} = y_w$ for $j = 1, 2$. Therefore at any GCN c, the initial values $V_{c,w_i}^{(0)} = y_{w_i}$ for $i = 1, 2, \cdots, n$. **Table 4** illustrates an example for ext-Hamming (8,4) constituent decoder employed at GCN c (with $n = 8$) at lth iteration.

5.2.1.2 VN processing

For any VN, it is represented by two bits. The main bit is the symbol binary value. The additional bit represents the initial reliability of the symbol value, (1) if a suspect bit or (0) if an assumed-correct bit, and the VN will use this extra information as will be discussed later. The codeword symbols which are represented by VNs are classified into two categories: most-reliable bits (MR) and least-reliable bits (LR). The classification is only initiated according to the soft information received through the channel based on a predetermined threshold.

For any transmitted codeword of length N, the wth code bit $v_w \in \{0, 1\}$ are mapped to $x_w \in \{-1, 1\}$, respectively, and transmitted over AWGN channel which is characterized by the probability density function (pdf) $p(r/x)$ given by

$$p(r_w/x_w) = \frac{1}{\sqrt{2\pi\sigma^2}} \exp\left[-(r_w - x_w)^2/2\sigma^2\right] \tag{7}$$

where σ^2 is the variance of the zero-mean Gaussian noise n_w that the channel adds to the transmitted value x_w (so that $r_w = x_w + n_w$) [25].

As illustrated in **Figure 13**, let η_o be the standard threshold on which the hard demodulator decision is based. For BPSK over AWGN channel, $\eta_o = 0$ and at this value

$$p(r/x = 1) = p(r/x = -1) \tag{8}$$

Let $\delta(r)$ be the absolute difference between the two probabilities as

$$\delta(r) = |p(r/x = 1) - p(r/x = -1)| \tag{9}$$

The received symbol is assumed to be accounted as LR bit if its value r_w gets near to the zero point or η_o ($\delta = 0$). The value of r with maximum difference δ_{max} can be

GCN State $d_r^{(l)}$	o/p messages $U_{c,w_i}^{(l)}$, $i = 1, 2, \cdots, n$							
	1	2	3	4	5	6	7	8
0	$0^!$	0	$0^!$	0	0	$0^!$	0	0
1 (with $w^* = w_i$)	0^-	0^-	1^+	0^-	0^-	0^-	0^-	v
2	1^-	1^-	1^-	1^-	1^-	1^-	1^-	1^-

Table 4.
Output messages at GCN c with ext-Hamming (8,4) decoder.
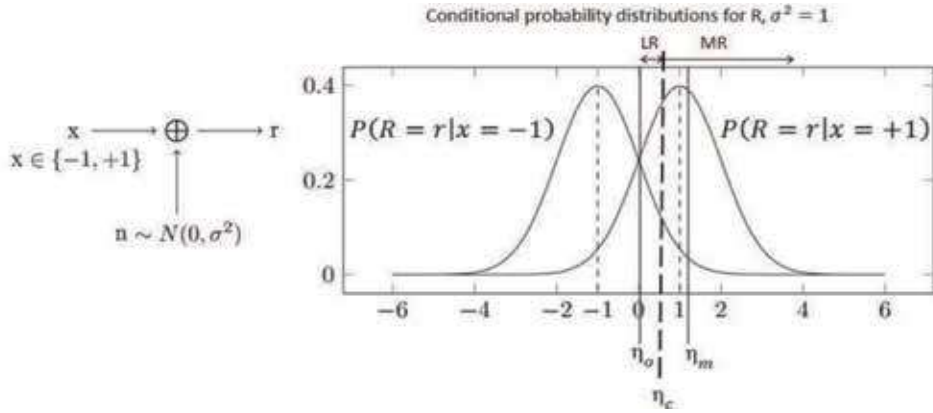
Figure 13.
The threshold η_c over AWGN channel.

taken as a second point η_m that the received symbol is accounted as MR bit if its value r_w approaches it. The absolute of the second point $|\eta_m|$ is the same for both $\pm r_w$ values as the two probability density functions are symmetric around the zero point. The equation $\delta'(r)\big|_{r=\eta_m} = 0$ should be solved to get η_m:

$$\delta = \frac{1}{\sqrt{2\pi\sigma^2}}\left[e^{-(r-1)^2/2\sigma^2} - e^{-(r+1)^2/2\sigma^2}\right] \tag{10}$$

then

$$\delta'(r)\big|_{r=\eta_m} = \frac{1}{\sqrt{2\pi\sigma^2}}\left[\frac{1-r}{\sigma^2}e^{-(r-1)^2/2\sigma^2} - \cdots \right. \tag{11}$$

$$\left. \frac{-(1+r)}{\sigma^2}e^{-(r+1)^2/2\sigma^2}\right] = 0 \tag{12}$$

therefore

$$(1-\eta_m)e^{\frac{\eta_m}{\sigma^2}} = -(1+\eta_m)e^{\frac{-\eta_m}{\sigma^2}} \tag{13}$$

This equation can be solved numerically by Newton-Raphson method and for various values of σ^2 (0.1–0.9), $\eta_m \approx 1.04$.

The classification threshold η_c for this algorithm is set to be in the middle between the two points. Therefore $\eta_c = \frac{\eta_o+\eta_m}{2} = \frac{0+1.04}{2} = 0.52$. Denote the initial reliability of the wth received bit as λ_w. According to the algorithm, this bit is classified as MR ($\lambda_w = 0$) if $|r_w| \ge \eta_c$; else it is classified as LR ($\lambda_w = 1$).

Using column weight of two and four levels of reliability, there are 10 probable combinations of these incoming messages to VN w, $w = 1, 2, \cdots, N$. These combinations are categorized into three subsets $\{s_i, i = 1, 2, 3\}$. For any VN w, its reliability state $g_w^{(l)}$ is set according to the arriving messages (belong to which subset). Motivated by TSSA-BF in [8] with inserting the new parameter λ_w

$$s_1 = \{(1^+, 1^+), (1^+, 1^-), (1^+, 0^-)\},$$

$$s_2 = \{(1^-, 1^-), (1^-, 0^-), (0^+, 1^+)\},$$

$$s_3 = \{(0^-, 0^-), (0^+, 1^-), (0^+, 0^-), (0^+, 0^+)\}$$

$$
g_w^{(l)} = \begin{cases} 0 & if \ \left\{ U_{c_jw}^{(l)}, j = 1, 2 \right\} \in s_1 \\ 1 & if \ \left\{ U_{c_jw}^{(l)}, j = 1, 2 \right\} \in s_2 \\ 2 & if \ \left\{ U_{c_jw}^{(l)}, j = 1, 2 \right\} \in s_3 \end{cases}
$$

- The VN w with least reliability, $g_w^{(l)} = 0$, needs flipping immediately.

- For $g_w^{(l)} = 1$, VN state counter is employed to compare the VN present in reliability state $g_w^{(l)}$ with one of the previous iterations $g_w^{(l-1)}$. Let $\gamma_w^{(l)}$ be the number of previous successive repetitions of this state $g_w^{(l)}$. If $g_w^{(l)} = 1$ with $\gamma_w^{(l)} = 2$ and, in the same time, $\lambda_w = 1$ (i.e., it is considered as LR bit), the VN will be flipped.

- Else, the VN is assumed a correct bit and kept without flipping.

By using the previously mentioned rules, the messages are renewed, and the algorithm proceeds until a zero overall syndrome output or it reaches a predefined number of iterations.

It is worth emphasizing that the GCN decoder does not output actual decoded word to its connected VNs. Instead, it sends a reliability signal (taking a value of four possible values) which is represented by two bits $U_{c, w_i}^{(l)}(1)$ and $U_{c, w_i}^{(l)}(2)$. On the other hand, the VN has to take a decision (flip or keep) based on its incoming messages and its initial reliability λ_w (MR or LR). The function of VN state counter $\gamma_w^{(l)}$ is to count a number of consecutive iterations with the same state $g_w^{(l)}$ (at this VN) up to this present iteration (l).

Figures 14–16 show the block diagrams of the overall decoder, horizontal process, and vertical process, respectively.

5.2.2 Important notes on the algorithm

- The output messages from VN w to its two connected GCNs $c_j, j = 1, 2$ are the same (i.e., $V_{c_1w}^{(l)} = V_{c_2w}^{(l)}$).

- The initial incoming message at GCN c $V_{c_jw}^{(0)} = y_w, j = 1, 2$ is the demodulated bit $V_w^{(0)}$ as the overall demodulated binary sequence $Y = \{y_w, w = 1, 2, \cdots, N, y_w \in \{0, 1\}\}$.
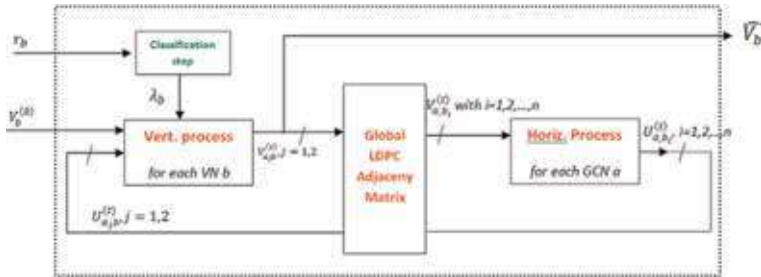

Figure 14.
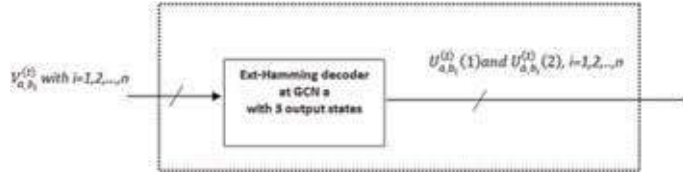*Block diagram of the overall classification-based decoder.*

Figure 15.
Block diagram of the horizontal process of the classification-based decoder.
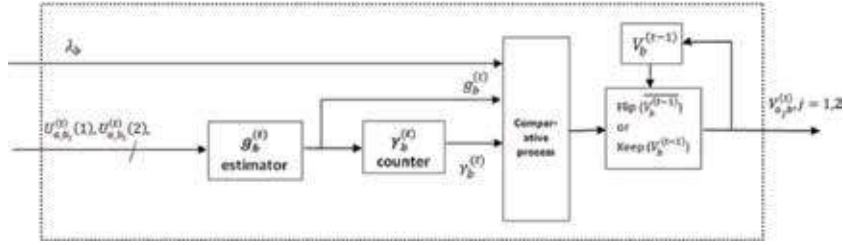
Figure 16.
Block diagram of the vertical process of the classification-based decoder.

- $U_{cw_i}^{(l)} = \left[U_{cw_i}^{(l)}(1)U_{cw_i}^{(l)}(2)\right]$ is the outgoing message from GCN c to VN w_i consisting of two bits representing the reliability level (one of four possible values 0^+, 0^-, 1^-, or 1^+). On the other hand, $V_{c_j w}^{(l)}$ is the outgoing message from VN w to GCN c_j containing just the decoded symbol bit value.

- The GCN decoder does not output actual decoded words to its connected VNs. Instead, it sends a reliability signal (taking a value of four possible values) which is represented by two bits $U_{cw_i}^{(l)}(1)$ and $U_{cw_i}^{(l)}(2)$. On the other hand, the VN has to take a decision based on its incoming messages. The decision is flip or keep.

- The function of VN state counter $\left(\gamma_w^{(l)}\right)$ is to count the number of consecutive iterations with the same state (at this VN) up to this present iteration (l).

- The algorithm manages without the greater portion of the overhead of the algorithm in [23] which was specially located in the horizontal (GCN) process.

Figure 17 shows the GLDPC BER performance using the (32,26,4) extended Hamming subcode by this decoding with respect to the bit-flipping algorithms in [7, 22] and [23]. It is noticed that this algorithm surpasses the other ones at the cost of a slight increase in computational complexity resulting from the comparison operations made at the initial classification step. It is also noticed that as N increases, a slow improvement in the performance is achieved.

The predefined number of iterations (20) is found to be very sufficient for good performance as the additional iterations beyond this limit have no considerable difference in the performance and latency in the decoding process which should be avoided for fast decoding purposes.

Not similar to the conventional GLDPC HDD BF decoding, the received sequence soft values are utilized to make appropriate classification of the received bits (variable nodes) into two classes.
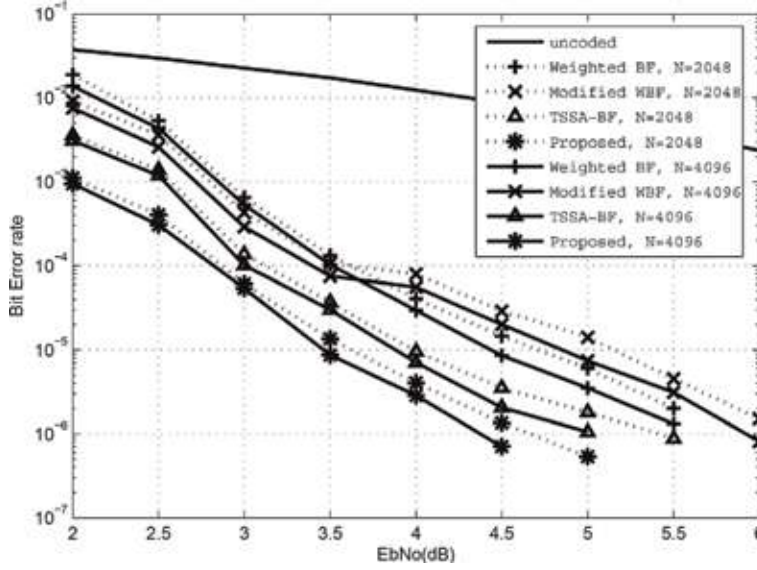
Figure 17.
Simulated BER curves of $(N, 2, 32)$ GLDPC codes.

The algorithm not only achieves a better error performance but also requires less iterations than the other competent algorithms. In terms of the impacts of the soft information (from AWGN channel) on coding gain of the GLDPC, the algorithm is revealed to exhibit considerable performance to decoder complexity trade-off. The algorithm can be adapted to handle generalized and more robust subcodes with the capability to correct more errors to improve the performance.

As discussed in [24], the computational complexity is provided in terms of the average number of executed operations for this algorithm against the rather comparable TSSA-BF algorithm. It is noticed that the complexity of this decoder is reduced by more than 60%.

6. Simplified SDD algorithm over AWGN channels

The algorithm, in [26], serves to use the chase SD decoders as minimum as possible to lower their complexity and expedites the decoding procedures. This algorithm is a variant approach from a previous one by [27] to lower the complexity of turbo product code (TPC) with multiple-error correction BCH subcodes. The chase decoder at every row or column input sequence in the product code was used as it attempts to decrease the HDD operations executed on the test patterns (TPs) produced in the chase decoder. The algorithm, explained below, will benefit from the algorithm in [27] for more reduction in the complexity.

The introduced algorithm is the MP method for decoding GLDPC with the chase-II algorithm operated as a posteriori probability decoding on GCNs. It will use extended double-error BCH (with high error-correcting capability) as a subcode to obtain a better performance. For simplicity, all GCNs are represented with the same eBCH code of parameters (n, k, d). The overall block diagram of this algorithm is depicted in **Figure 18**.

As discussed before in Section 3 and using the same notations and considerations, the soft-output value of every decoded symbol of the subcode should be calculated, by Eqs. (3) or (4), to be sent back on the connected edges to the GLDPC

VNs as followed by the MP algorithm in an iterative method to obtain a final decision after a certain number of iterations or a syndrome condition should be satisfied.

W.r.t any given GCN c, the chase-II-based SISO decoder produces 2^p TPs by making a perturbation of the p LRPs in the demodulated word with length n (subcode word). Therefore 2^p HDDs should be performed to obtain a decided codeword. Therefore algorithm will get the syndromes of Y_c.

For extended BCH2 (double-error correction), the algorithm computes two syndromes S_c^1 and S_c^3 as follows:

$$S_c^1 = y_{c2} \oplus y_{c3}x \oplus \cdots \oplus y_{cn-1}x^{n-3} \oplus y_{cn}x^{n-2}\big|_{x=\alpha},$$
$$S_c^3 = y_{c2} \oplus y_{c3}x \oplus \cdots \oplus y_{cn-1}x^{n-3} \oplus y_{cn}x^{n-2}\big|_{x=\alpha^3} \tag{14}$$

where α is the primitive element of $GF(2^m)$ that generates the BCH code polynomial.

According to the values of the syndromes as illustrated in **Table 5**, the algorithm estimates the number of errors contained in the sequence.

If there are no errors ($e = 0$), it is likely (with high percentage) that the demodulated word is the valid transmitted one and the decoder will not do its task. If $0 < e \leq 2$, the algorithm may execute the HDD (Berlekamp-Massey algorithm) and outputs the decoding decision. In these two preceding cases, the soft-output values can be estimated as the decision is highly probable to be correct as follows:
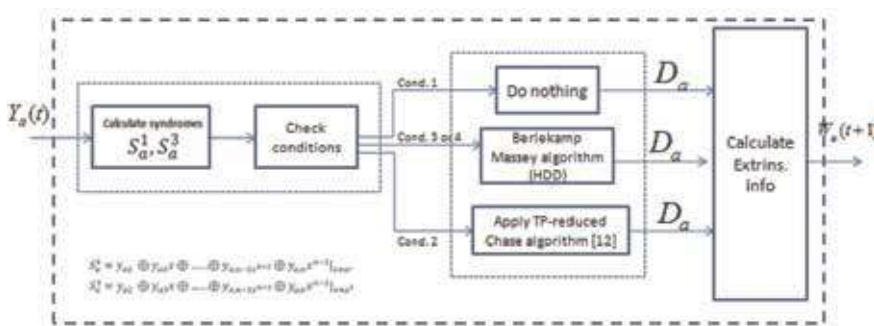
Figure 18.
The block diagram of the lowered-complexity chase-based decoding algorithm.

Syndrome of demodulated vector $S_a = Y_a.H_{bch}$	Number of contained errors (e)	Action taken (method of estimating the decision Da)	Calculation model of extrinsic information $r'_{a,i}$
$S_a^1 = S_a^3 = 0$	0	Nothing (the demodulated vector is the decision codeword)	$r'_{a,i} = \beta' x d_i$
$S_a^1 = 0, S_a^3 \neq 0$	>2	Apply TP-reduced chase algorithm [12]	Pyndiah model [15]
$(S_a^1) \oplus S_a^3 = 0$	1	Apply HDD (Berlekamp-Massey algorithm)	$r'_{a,i} = \beta' x d_i$
Else	2	Apply HDD (Berlekamp-Massey algorithm)	$r'_{a,i} = \beta' x d_i$

Table 5.
The actions of the proposed algorithm.

$$r'_{c,i} = \beta \times d_{c,i} \text{ with } \beta \geq 0$$

where β is chosen to be evolved with the decoding iterations, $\beta(l) = [0.4, 0.6, 0.8, 1, 1, 1, \cdots]$.

If $e > 2$, the chase algorithm is needed to extract a decision codeword but will not decode a complete list of 2^p test patterns (TPs). The proposed algorithm in this case will benefit from the lowered-complexity TP-reduced algorithm in [27]. The amount of reduction in HDDs of the algorithm compared to the standard one is listed in **Table 6**.

The computational complexity of this algorithm is estimated by the number of hard decision decoding processes (Berlekamp-Massey algorithm) employed at GCNs. The (64,51) eBCH subcode is chosen with double-error correction capability to exploit the multiple calculated syndroms, while keeping a moderate code rate ($R \cong 0.6$). Therefore, for keeping this rate, only GLDPC codes with column weight ($j = 2$) are considered. As shown in **Figure 19**, the number of HDDs in the decoder is calculated for two numbers of LRPs ($p = 3, p = 4$) and up to five iterations

BCH code (n,k)	N	J	Code rate	No. of LRPs (p)	Number of HDDs in standard alg. [7]	Avg. number of HDDs in proposed alg.	Percentage of complexity reduction (%)
eBCH2 (64,51)	4096	2	0.6	3	5120	3072	60
eBCH2 (64,51)	4096	2	0.6	4	10,240	5734	56
eBCH3 (64,45)	4096	2	0.41	4	10,240	5232	51.1
e8CH3 (64,45)	4096	2	0.41	5	20,480	9011	44

Table 6.
The reduction of HDDs in the lowered-complexity chase-based decoding algorithm (SNR = 2 dB at $I_{max} = 5$).
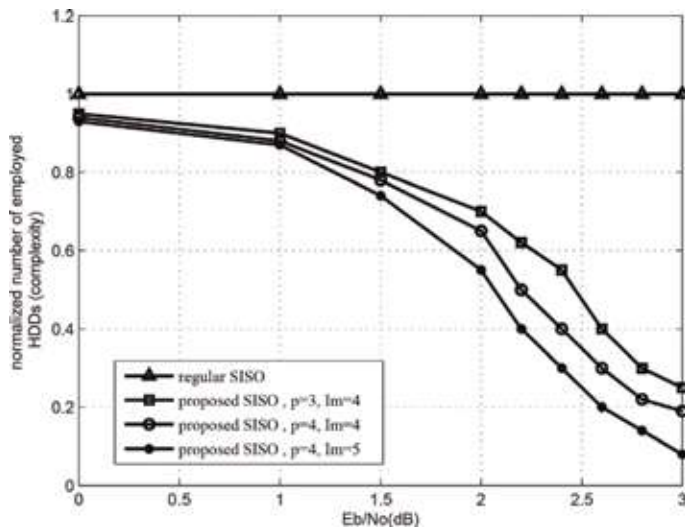
Figure 19.
Comparison of computational complexity of less-complex and conventional SISO decoding algorithms for decoding (64,51) eBCH-based GLDPC codes with length N = 4096 for various values of p and I_m.

($I_m = 5$). For clarification, the number of HDDs is normalized to the one of the conventional chase decoder. It is shown that a considerable reduction occurs especially after $E_b/N_o = 2$ dB.

The results show a significant lowering in the soft decoding operations executed at GCNs compared to conventional chase decoders with little wastage in the BER performance. This scheme is highly required in low error rate applications such as optical communication systems.

Author details

Sherif Elsanadily
EAEAT, Ministry of Military Production, Cairo, Egypt

*Address all correspondence to: sherif.elsanadily@eaeat.edu.eg

IntechOpen

References

[1] Tanner R. A recursive approach to low complexity codes. IEEE Transactions on Information Theory. 1981;**27**:533-547

[2] Lentmaier M, Zigangirov K. On generalized low-density parity check codes based on Hamming component codes. IEEE Communications Letters. 1999;**3**:248-250

[3] Liva G, Ryan W, Chiani M. Quasi-cyclic generalized LDPC codes with low error floors. IEEE Transactions on Communications. 2008;**56**:49-57

[4] Wang Y, Fossorier M. Doubly generalized LDPC codes over the AWGN channel. IEEE Transactions on Communications. 2009;**57**:1312-1319

[5] Bahl L, Cocke J, Jelinek F, Raviv J. Optimal decoding of linear codes for minimizing symbol error rate. IEEE Transactions on Information Theory. 1974;**20**:284-287

[6] Boutros J, Pothier O, Zemor G. Generalized low density (tanner) codes. In: Proc. IEEE. Int. Conf. Commun.; 1999; vol. 1, pp. 441-445

[7] Miladinovic N, Fossorier M. Generalized LDPC codes with Reed-Solomon and BCH codes as component codes for binary channels. In: Proc. IEEE Global Telecommun. Conf.; St. Louis, MO; 2005; vol. 3; p. 6

[8] Chen J, Tanner RM. A hybrid coding scheme for the Gilbert-Elliott channel. IEEE Transactions on Communications. 2006;**54**:1787-1796

[9] Abu-Surra S, Liva G, Ryan WE. Low-floor Tanner codes via Hamming-node or RSCC-node doping. In: Proc. the 16th international conf. on Applied Algebra, Algebraic Algorithms and Error-Correcting Codes; 2006; pp. 245-254

[10] Yue G, Ping L, Wang X. Generalized low-density parity-check codes based on Hadamard constraints. IEEE Transactions on Information Theory. 2007;**53**:1058-1079

[11] Hirst S, Honary B. Application of efficient chase algorithm in decoding of generalized low-density parity-check codes. IEEE Communications Letters. 2002;**6**:385-387

[12] Djordjevic I, Milenkovic O, Vasic B. Generalized low-density parity-check codes for optical communication systems. IEEE: Journal of Lightwave Technology. 2005;**23**:1939-1946

[13] Guan R, Zhang L. Hybrid Hamming GLDPC codes over the binary erasure channel. In: The 2017 11th IEEE International Conference on Anti-counterfeiting, Security, and Identification (ASID); 2017; pp. 130-133

[14] Olmos PM, Mitchell DGM, Costello DJ. Analyzing the finite-length performance of generalized ldpc codes. In: 2015 IEEE International Symposium on Information Theory (ISIT); 2015; pp. 2683-2687

[15] Yu Y, Han Y, Zhang L. Hamming-GLDPC codes in BEC and AWGN channel. In: The 6th International Conference on Wireless, Mobile and Multi-Media (ICWMMN 2015); 2015; pp. 103-106

[16] Beemer A, Habib S, Kelley CA, Kliewer J. A generalized algebraic approach to optimizing SC-LDPC codes. In: The 2017 55th Annual Allerton Conference on Communication, Control, and Computing (Allerton); 2017; pp. 672-679

[17] Pothier O, Brunel L, Boutros J. A low complexity FEC scheme based on the intersection of interleaved block codes.

In: IEEE 49th Vehicular Technology Conf. (VTC 99); Houston; 1999; vol. 1; pp. 274-278

[18] Chase D. A class of algorithms for decoding block codes with channel measurement information. IEEE Transactions on Information Theory. 1972;**18**:170-182

[19] Pyndiah RM. Near-optimum decoding of product codes: Block turbo codes. IEEE Transactions on Communications. 1998;**46**:1003-1010

[20] Pyndiah R, Glavieux A, Picart A, Jacq S. Near optimum decoding of products codes. In: Proc. IEEE GLOBECOM94 Conf., vol. 1/3; San Francisco, CA; 1994; pp. 339-343

[21] Hirst S, Honary B, Markarian G. Fast chase algorithm with application in turbo decoding. IEEE Transactions on Communications. 2001;**49**:1693-1699

[22] Hirst S, Honary B. Decoding of generalized low-density paritycheck codes using weighted bit-flip voting. IEEE Proceedings Communications. 2002;**149**:1-5

[23] Elsanadily S, Mahran A, Elghandour O. Two-side state-aided bit-flipping decoding of generalized low density parity check codes. IEEE Communications Letters. 2017;**21**: 2122-2125

[24] Elsanadily S, Mahran A, Elghandour O. Classification-based algorithm for bit-flipping decoding of GLDPC codes over AWGN channels. IEEE Communications Letters. 2018;**22**: 1520-1523

[25] Ryan WE, Lin S. Channel Codes: Classical and Modern. New York: Cambridge University Press; 2009

[26] Elsanadily S, Mahran A, Elghandour O. Lowered-complexity soft decoding of generalized LDPC codes over AWGN

channels. In: The IEEE 2017 12th International Conference on Computer Engineering and Systems (ICCES); 2017; pp. 320-324

[27] Chen GT, Cao L, Yu L, Chen CW. Test-pattern-reduced decoding for turbo product codes with multi-error-correcting EBCH codes. IEEE Transactions on Communications. 2009; **57**:307-310

Polynomials in Error Detection and Correction in Data Communication System

Charanarur Panem, Vinaya Gad and Rajendra S. Gad

Abstract

The chapter gives an overview of the various types of errors encountered in a communication system. It discusses the various error detection and error correction codes. The role of polynomials in error detection and error correction is discussed in detail with the architecture for practical implementation of the codes in a communication channel.

Keywords: error detection, error correction, burst error, channel coding, channel decoding, CRC, LDPC

1. Introduction

Different types of errors are encountered during data transmission because of physical defects in the communication medium as well as environmental interference. Environmental interference and physical defects in the communication medium can cause random bit errors during data transmission. Error coding is a method of detecting and correcting these errors to ensure that there are no errors in the information when it is sent from source to destination. Error coding is used for error-free communication in the primary and secondary memory devices such as RAM, ROM, hard disk, CD's, and DVDs, as well as in different digital data communication systems such as network communication, satellite, and cellular communication and deep space combination.

1.1 Need for error coding

Data transmission errors occur in terrestrial mobile communication due to multipath fading, diffractions or scattering in cellular wireless communications, low signal-to-noise ratio, and limited transmitted power and energy resources in satellite communication [1].

Error coding uses mathematical formulae to encode data bits at the source into longer bit words for transmission. The "code word" is then decoded at the destination to retrieve the information. The code word consists of extra bits, which provide redundancy, and at the destination, it will decode the data to find out whether the communication channel introduced any error and some schemes can even correct the errors so that there is no need to resend the data.

There are two ways to deal with errors. One way is to introduce redundant information along with the data to be transmitted, which will enable the receiver to deduce the information that has been transmitted. The second way is to include only enough redundancy to allow the receiver to detect that error has occurred, but not which error and the receiver makes a request for retransmission. The first method uses Error-Correcting Codes and the second uses Error-detecting Codes.

Consider a frame having **m** data bits (message to be sent) and **r** redundant bits (used for checking). The total number of bits in the frame will be **n(m + r)**, which is referred as n-bit code word. Consider two code-words, 11,001,100 and 11,001,111, and perform Exclusive OR and then count number of 1's in the result. The number of bits in which the codewords are different is called Hamming distance. Suppose the code words are Hamming distance d- apart, it will require d single-bit errors to connect one code word to another. The properties of error detection and error correction depend on the Hamming distance.

- A distance (d + 1) code is required to detect d errors because d-single bit errors cannot change a valid codeword into another valid code. Thus the error is detected at the receiver.

- A distance (2d + 1) code is required to correct d errors because the codewords will be so apart that the transmitted codeword will be still closer than any other valid codeword, and thus the error can be determined.

1.2 Types of errors in a communication channel

When the data travels from the sender to receiver, different types of errors are encountered in the communication channel [2].

1.2.1 Noise or electrical distortion

When the data travel through a conductor, there are different influences such as sound waves, electrical signals, noise such as electricity from motors, power switches, impulse noise, because of which data can be corrupted or destroyed. Old conductors are unable to handle these types of interference and heavy data traffic, hence the data transmission suffers.

1.2.2 Burst errors

Burst errors are large clumps of bits and occur when there are a number of inter-connected bit errors which occur at many places. These types of errors may occur because of some wrong placement in the data chain. It may contain several hundred or thousand-bit errors.

1.2.3 Random bit errors

Data sent on a communication channel consists of thousands of data bits, sent in a particular order or sequence. However, there is a probability that the bits may be rearranged by accident in the transmission process. These types of errors are known as random bit errors.

1.2.4 Cross talk and echo

Cross talk occurs when the transmission cable through which the data is transmitted, is surrounded by other transmission lines. The data and code words, which
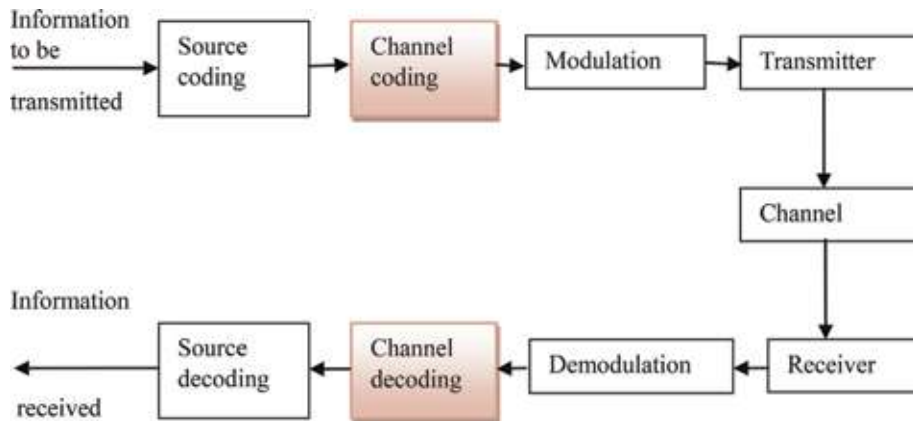
Figure 1.
Wireless communication system with channel coding.

are traveling in the neighboring line crosses over and gets superimposed on the transmission cable. Echo is similar to cross talk; how ever, it occurs in a single transmission line, through which multiple computer ports are sending data at the same time. The data from one port will echo into another, thus resulting in data corruption (**Figure 1**).

2. Error detecting codes

Error detection uses additional bits in the message to be transmitted. This adds redundancy and facilitates detection and correction of errors. Popular techniques of error detection are,

- Simple parity check.

- Two-dimensional parity check.

- Checksum.

- Cyclic redundancy check.

2.1 Simple parity checking or one-dimension parity check

This technique is most common and cheap mechanism for detection. The data unit is appended with a redundant bit known as the parity bit. A parity bit generator is used, which adds 1 to the block of data if it contains odd number of 1's, and 0 is added if there are even number of 1's. At the receiver end, the parity is computed of the block of data received and compared with the received parity bit. These scheme uses total even number of 1's; hence it is known as even parity checking. Similarly, you can use odd number of 1's, known as odd parity checking.

2.2 Two-dimension parity check

Two-dimensional parity check improves the performance. Here, the data bits are organized in the form of a table, computed for each row as well each column and are

sent along with the data. The parity is computed for the received data and compared with the received data bits.

2.2.1 Performance

Two-dimension parity checking is mainly used to detect burst errors. It detects a burst error of more than **n** bits with a high probability. However, this mechanism will not be able to detect the errors if two bits in one data unit are damaged. Example if 11000110 is changed to 01000100 and 10101010 is changed to 00101000 the error will not be detected.

2.3 Checksum

This scheme divides the data bits to be sent into **k** segments. Each segment consists of **m** bits. All the segments are added using 1's complement arithmetic. Checksum is obtained by complementing the sum, and the data segments are transmitted together. At the receiver end, again 1's complement arithmetic is used to add all received segments. The sum generated is complemented. The receiver accepts the data if the result of complementing is zero.

2.3.1 Performance

The checksum mechanism detects all errors consisting of odd number of bits. It also detects most errors having even number of bits.

2.4 Cyclic redundancy check (CRC)

Cyclic redundancy check is the most powerful and easy to implement error detection mechanism. Checksum uses addition, whereas CRC is based on binary division. In CRC, the data unit is appended at the end by a sequence of redundant bits, called cyclic redundancy check bits. The resulting data unit is exactly divisible by a second, predetermined binary number. At the receiver end, the incoming data unit is divided by the same predetermined binary number. If the remainder is zero, the data unit is assumed to be error-free and is accepted. A remainder indicates that the data unit has encountered an error in transit and therefore is rejected at the receiver. The generalized technique to generate the CRC bits is explained below:

Consider there is a **k** bit message to be transmitted. The transmitter generates an **r**-bit sequence called as FCS (frame check sequence). These **r** bits are appended to the **k** bit message, so that **(k + r)** bits are transmitted. The **r**-bit FCS is generated by dividing the **k** bit message, appended by **r** zeros, by a predetermined number. This number is **(r + 1)** bit length, and can be considered as coefficient of a polynomial, called generator polynomial. The **r**-bit FCS is generated as the remainder of binary division. Once the **(k + r)** bit frame is received, it is divided by the same predetermined number. If the remainder is zero, it means there was no error, and the frame is accepted by the receiver.

Operations at both the sender and receiver end are shown in **Figure 2**.

CRC is widely used in data communications, data storage, and data compression as a powerful method for detecting errors in the data. It is also used in testing of integrated circuits and the detection of logical faults. A cyclic redundancy code is a non-secure hash function designed to detect accidental changes to raw computer data. CRCs are popular because they are simple to implement in binary hardware, are easy to analyze mathematically, and are particularly good at detecting common
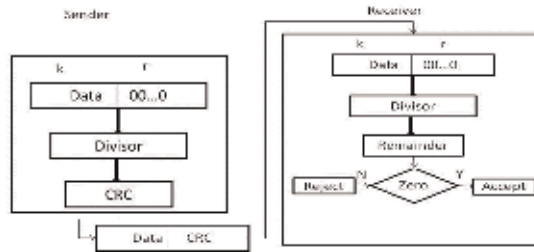
Figure 2.
Basic scheme for cyclic redundancy checking.

errors caused by noise in transmission channels. CRC-32 guarantees 99.999% probability of error detection at the receiver end; hence, this CRC is often used for Gigabit Ethernet packets [3].

Cyclic redundancy codes are a subset of cyclic [4, 5] codes that are also a subset of linear block codes. They use a binary alphabet, 0 and 1. Arithmetic is based on Galois Field GF(2), for example, modulo-2 addition (logical XOR) and modulo-2 multiplication (logical AND). The CRC method treats the data frame as a large Binary number. This number is then divided (at the generator end) by a fixed binary number (the generator polynomial) and the resulting CRC value, known as the FCS (Frame Check Sequence), is appended to the end of the data frame and transmitted. The receiver divides the message (including the calculated CRC), by the same polynomial used during transmission and compares its CRC value with the generated CRC value. If it does not match, the system requests for re-transmission of the data frame.

CRC codes are often used for error detection over frames or vectors of a certain length. The frame can be expressed as a polynomial in x, where the exponent of x is the place marker of the coefficient. The vector $a = a_{L-1}a_{L-2}....a_1a_0$ length L is represented by the degree L-1 polynomial.

$$a(x) = \sum_{i=0}^{L-1} a_i x^i = a_{L-1}x^{L-1} + a_{L-2}x^{L-2} + ... + a_1 x + a_0 \tag{1}$$

CRC coding is a generalization of the parity check bit. Parity bits are used for short vectors to detect one-bit error. However, if there are errors in two-bit positions, it will not detect the error.

2.4.1 Error detection procedure

Let the data to be transmitted consist of a length k binary vector, and represent it by the degree k-1 polynomial.

$$d(x) = d_{k-1}x^{k-1} + d_{k-2}x^{k-2} + ... + d_1 x + d_0 \tag{2}$$

Then, to add redundant bits, so the total length of the code word is n, we should add n-k bits. These redundant bits, which are the CRC bits, can be represented by the degree n-k-1 polynomial.

$$r(x) = d_{n-k-1}x^{n-k-1} + ... + r_1 x + r_0 \tag{3}$$

The polynomial for codeword is written as follows:

$$c(x) = d(x)x^{n-k} + r(x)$$
$$= d_{k-1}x^{n-1} + \ldots + d_1 x^{n-k+1} + d_0 x^{n-k} + r_{n-k-1}x^{n-k-1} + \ldots + r_1 x + r_0 \tag{4}$$

CRC polynomial is derived using a degree n-k generator polynomial.

$$g(x) = x^{n-k} + g_{n-k-1}x^{n-k-1} + \ldots + g_1 x + 1 \tag{5}$$

which is a binary polynomial, wherein the highest and lowest coefficients are non-zero (g_{n-k} = 1 and g_0 = 1).

The CRC polynomial is derived as.

$$r(x) = R_{g(x)}(d(x)x^{n-k}) \tag{6}$$

All coefficients of the polynomial are binary, and modulo-2 arithmetic is used [4].

To see how the receiver side can use this code word to detect errors, we first need to derive some properties of it. Let $z(x)$ denote the quotient in the division $d(x)x^{n-k} / g(x)$ hence, following is the data polynomial.

$$d(x)x^{n-k} = g(x)z(x) + r(x) \tag{7}$$

In modulo-2 arithmetic, addition and subtraction are alike, and the codeword polynomial can be written as.

$$c(x) = d(x)x^{n-k} + r(x) = g(x)z(x) \tag{8}$$

This gives rise to the following theorem [5].

A polynomial $c(x)$ with deg.$(c(x)) < n$ is a code word if and only if $g(x)jc(x)$. If $c(x)$ is transmitted over a channel and there occur errors, they can be represented by an addition of the polynomial $e(x)$, and the received polynomial is.

$$y(x) = c(x) + e(x) \tag{9}$$

Thus $g(x)$ is a factor of each transmitted codeword which can be used by the receiver to detect the error. The error is detected if $g(x)$ is not a factor. To check this, the remainder of the division $c(x) = g(x)$ is derived as.

$$s(x) = R_{g(x)}(y(x)) = R_{g(x)}(c(x) + e(x))$$
$$= R_{g(x)}(R_{g(x)}(c(x)) + R_{g(x)}(e(x))) = R_{g(x)}(e(x)) \tag{10}$$

This quantity is known as Syndrome. It is directly a function of the error since $R_{g(x)}(c(x))$ = 0. The syndrome plays an important role in coding theory.

2.4.2 Performance

CRC is a very effective and popular error detection technique. The error detection capabilities of CRC depend on the chosen generator polynomial.

- CRC has capacity to detect all single-bit errors.

- CRC has capacity to detect all double-bit errors (three 1's).

- CRC has capacity to detect any odd number of errors (X + 1).

- CRC has capacity to detect all burst errors of less than the degree of the polynomial.

- CRC has the capacity to detect most of the larger burst errors with a high probability.

2.4.3 Implementation

n-bit CRC can be calculated as CRC = Rem [M(x) * (xn/G(x)) J; where M(x) denotes the message polynomial, G(x) denotes the generator polynomial and n is the degree of polynomial G(x). CRC can be calculated using serial or parallel method. **Figure 3** shows the serial data input hardware implementation. The data message input is denoted as Din, clk is used to denote the clock used for the circuits. XOR gates are used before the input of each flip-flop. The output can be obtained from any input or output wire of any flip-flop.

Parallel implementation of CRC is shown in **Figure 4**. The data message input is to be XOR-ed with a calculated input. The calculated input can be obtained by using matrix method [6]. State equation for LFSRs can be written as: X(i + 1) = Fm. X (i) + H.D(i); where Xi is the ith state of register and X(i + 1) is the (i + 1)th state of
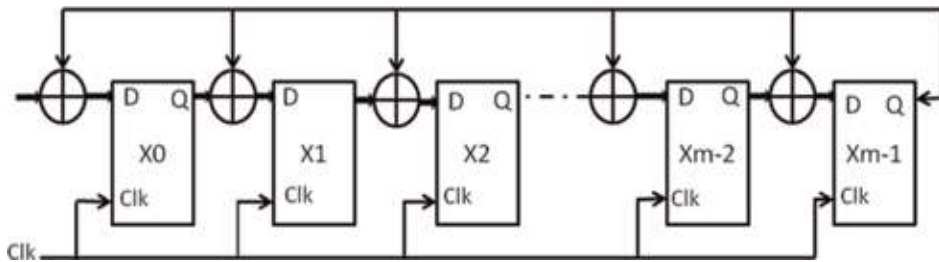
Figure 3.
Serial CRC.
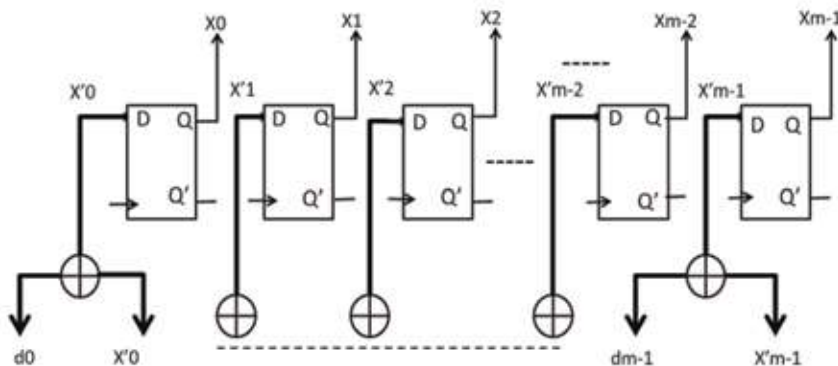
Figure 4.
Parallel CRC.

the register, D(i) is the ith serial input bit, Fm is a m x m matrix and H is a 1 x m matrix. Consider the generator polynomial G = {gm, gm-1. - - -,go}.

$$
F^{m} = \begin{bmatrix} g_{m-1} & 1 & 0 & - & - & 0 \\ g_{m-2} & 0 & 1 & - & - & 0 \\ | & - & - & - & - & - \\ | & - & - & - & - & - \\ g_1 & 0 & 0 & - & - & 1 \\ g_0 & 0 & 0 & - & - & 0 \end{bmatrix} \tag{11}
$$

$$
H = \begin{bmatrix} 0 & 0 & - & - & - & 0 & 1 & \end{bmatrix}^T \tag{12}
$$

$$
X'_{m-1} = (g_{m-1}, X_{m-1}) \oplus X_{m-2} \tag{13}
$$

$$
X'_{m-2} = (g_{m-2}, X_{m-1}) \oplus X_{m-3} \tag{14}
$$

$$
X'_1 = (g_1, X_{m-1}) \oplus X_0 \tag{15}
$$

$$
X'_0 = (g_0, X_{m-1}) \oplus d \tag{16}
$$

The above equations are used for serial computation of CRC. Following equation are used for parallel computation of CRC.

$$
X'_{m-1} = (F^m(m-1)(m-1), X_{m-1}) \oplus (F^m(m-1)(m-2), X_{m-2}) .... \oplus (F^m(m-1)(0), X_0 \oplus d_{m-1}) \tag{17}
$$

$$
X'_{m-2} = (F^m(m-2)(m-1), X_{m-1}) \oplus (F^m(m-2)(m-2), X_{m-2}) ...... \oplus (F^m(m-2)(0), X_0 \oplus d_{m-2}) \tag{18}
$$

$$
X'_0 = (F^m(0)(m-1), X_{m-1}) \oplus (F^m(0)(m-2), X_{m-2}) ...... \oplus (F^m(0)(0), X_0 \oplus d_0) \tag{19}
$$

Table 1 summaries the commonly used polynomials in different applications and **Table 2** gives a list of primitive polynomials.

Polynomial name	Polynomial	Use
CRC-1	$x+1$	Parity
CRC-4-ITU	$x^4 + x + 1$	ITU G.704
CRC-5-ITU	$x^5 + x^4 + x^2 + 1$	ITU G.704
CRC-5-USB	$x^5 + x^2 + 1$	USB
CRC-6-ITU	$x^6 + x + 1$	ITU G.704
CRC-7	$x^7 + x^3 + 1$	Telecom systems, MMC
CRC-8-ATM	$x^8 + x^2 + x + 1$	ATM HEC
CRC-8-CCITT	$x^8 + x^7 + x^3 + x^2 + 1$	1-Wire bus
CRC-8-Maxim	$x^8 + x^5 + x^4 + 1$	1-Wire bus
CRC-8	$x^8 + x^7 + x^6 + x^4 + x^2 + 1$	General

Polynomial name	Polynomial	Use
CRC-8-SAE	$x^8 + x^4 + x^3 + x^2 + 1$	SAE J1850
CRC-10	$x^{10} + x^9 + x^5 + x^4 + x + 1$	General
CRC-12	$x^{12} + x^{11} + x^3 + x^2 + x + 1$	Telecom systems
CRC-15-CAN	$x^{15} + x^{14} + x^{10} + x^8 + x^7 + x^4 + x^3 + 1$	CAN
CRC-16-CCITT	$x^{16} + x^{12} + x^5 + 1$	XMODEM,X.25, V.41, Bluetooth, PPP, IrDA, CRCCCITT
CRC-16	$x^{16} + x^{15} + x^2 + 1$	USB
CRC-24-Radix64	$x^{24} + x^{23} + x^{18} + x^{17} + x^{14} + x^{11} + x^{10} + x^7 + x^6 + x^5 + x^4 + x^3 + x + 1$	General
CRC-32-IEEE802.3	$x^{32} + x^{26} + x^{23} + x^{22} + x^{16} + x^{12} + x^{11} + x^{10} + x^8 + x^7 + x^5 + x^4 + x^2 + x + 1$	Ethernet, MPEG2
CRC-32C	$x^{32} + x^{28} + x^{27} + x^{26} + x^{25} + x^{23} + x^{22} + x^{20} + x^{19} + x^{18} + x^{14} + x^{13} + x^{11} + x^{10} + x^9 + x^8 + x^6 + 1$	General
CRC-32K	$x^{32} + x^{30} + x^{29} + x^{28} + x^{26} + x^{20} + x^{19} + x^{17} + x^{16} + x^{15} + x^{11} + x^{10} + x^7 + x^6 + x^4 + x^2 + x + 1$	General
CRC-64-ISO	$x^{64} + x^4 + x^3 + x + 1$	ISO 3309
CRC-64-ECMA	$x^{64} + x^{62} + x^{57} + x^{55} + x^{54} + x^{53} + x^{52} + x^{47} + x^{46} + x^{45} + x^{40} + x^{39} + x^{38} + x^{37} + x^{35} + x^{33} + x^{32} + x^{31} + x^{29} + x^{27} + x^{24} + x^{23} + x^{22} + x^{21} + x^{19} + x^{17} + x^{13} + x^{12} + x^{10} + x^9 + x^7 + x^4 + x + 1$	ECMA-182

Table 1.
Commonly used divisor polynomials [4, 5].

P(x)	
$x^2 + x + 1$	$x^{10} + x^3 + 1$
$x^3 + x + 1$	$x^{11} + x^2 + 1$
$x^4 + x + 1$	$x^{12} + x^6 + x^4 + x + 1$
$x^5 + x^2 + 1$	$x^{13} + x^4 + x^3 + x + 1$
$x^6 + x + 1$	$x^{14} + x^{10} + x^6 + x + 1$
$x^7 + x^3 + 1$	$x^{15} + x + 1$
$x^8 + x^4 + x^3 + x^2 + 1$	$x^{16} + x^{12} + x^9 + x^7 + 1$
$x^9 + x^4 + 1$	$x^{17} + x^3 + 1$

Table 2.
A list of some primitive polynomials [4, 5].

3. Error correcting codes

There are two ways to handle error correction. The first method is known as backward error correction wherein, and the receiver asks for retransmission of data when the error is discovered. The second method is known as backward error

connection, where the receiver uses an error correction code to correct certain errors.

The codes required for error connection are more sophisticated compared to error detection codes and require more redundant bits. Most error correction is limited to one, two or at the most three-bit errors since it requires large number of redundant bits multiple bit error or burst errors.

Different types of error detection and correction techniques are required for specific noisy channels/media, like random error or burst error or multi-path distortion or channel effects. There are two approaches for error control coding, forward error correction (FEC) and automatic repeat request (ARQ) [7].

FEC error control is used for one-way system whereas, ECC (Error Correcting Codes) with error detection and retransmission called ARQ is used for two-way communication, such as telephone and satellite communications. The classification of FEC is shown in **Figure 5**.

3.1 Single-bit error correction

A single-bit error can be easily detected using a parity bit; however, for correcting an error, the exact position of the errored bit is required to be detected.

Hamming code is a technique developed by R.W. Hamming, which is used to find out the location of the bit which is in error, Hamming code can be used for data bits of any length and uses the relationship between data bits and redundant bits where $2r \geq d + r + 1$.

Procedure for error detection using Hamming code is as follows:

- To each group of m information bits k parity bits are added to form $(m + k)$ bit code.

- Location of each of the $(m + k)$ digits is assigned a decimal value.

- The k parity bits are placed in positions 1, 2, ... , 2 k-1. k parity checks are performed on selected digits of each codeword.

- At the receiving end, the parity bits are recalculated. The decimal value of the k parity bits provide the bit-position in error if any.

Claude Elwood Shannon (1916–2001) and Richard Hamming (1915–1998), were colleagues at Bell Laboratories pioneer in coding theory. Shannon's channel coding theorem proves that if the information transmission rate is less than the channel capacity, it is possible to design an error correcting code (ECC) with almost
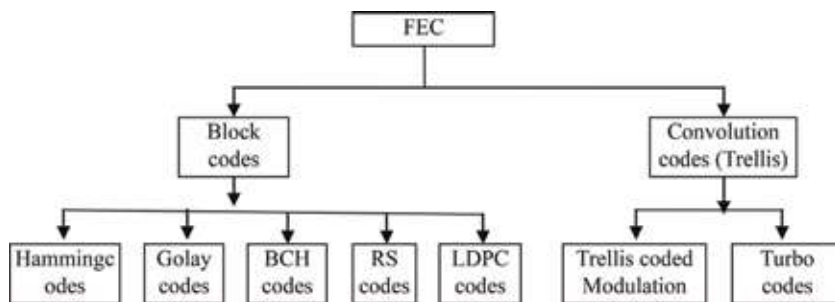

Figure 5.
Classification of FEC.

error-free information transmission. Hamming invented the first error correcting codes (ECC) in 1950. It is known as (7, 4) Hamming code.

3.2 BCH codes

The BCH code design can have a precise control over the number of symbol errors correctable by the code. Binary BCH codes can correct multiple bit errors. BCH codes are advantages since a simple algebraic method known as syndrome decoding can be used which simplifies the design of the decoder for these codes, which uses a small low-power electronic hardware.

BCH codes are used in applications such as satellite communications, compact disc players, DVDs, disk drives, solid-state drives, and two-dimensional bar codes.

BCH codes are a class of linear, cyclic codes. For a cyclic code any codeword polynomial has its generator polynomial as a factor; so the roots of the code's generator polynomial $g(x)$ are also the roots of code words. BCH codes are constructed using the roots of $g(x)$ in extended Galois field; binary primitive BCH codes, which correct multiple random errors, form an important subclass. The error correcting binary BCH code has the following parameters:

Block length $n = 2^m - 1$.

- No. of parity check bits: $n - K \leqslant mt$.

- Minimum distance: $d_{min} \; 2 \, t + 1$.

$g(x)$ generates a binary primitive BCH code ith it is the least degree polynomial over GF(2) with $\alpha, \alpha^2, \dots \dots \dots \alpha^{2t}$ as roots, α being a primitive element in GF(2^m). With this $g(x)$ must have $(x + \alpha) \, (x + \alpha^2) \dots \dots \, (x + \alpha^{\,2t})$ as a factor. This leads to g(x) of the form.

$g(x) = LCM \, [\Omega_1(x) \; \Omega_2 \, (x) \; \Omega_3 \, (x) \dots \dots \Omega_i \, (x)].$

where $\{\Omega_1(x) \; \Omega_2 \, (x) \; \Omega_3 \, (x) \dots \dots \Omega_i \, (x)\}$ is the smallest set of minimal polynomials with $(x + \alpha) \, (x + \alpha^2) \dots \dots \, (x + \alpha^{\,2t})$ as a factor.

BCH codes can be encoded using similar method.

3.2.1 Decoding of BCH codes

The decoding of BCH codes involves the following steps:

i. Form the syndrome polynomial $s(x) = s0 + s1x + s2x^2 + \cdots + s_{n-K-1x}{}^{n-K-1}$ with the set $\{s_0, s_1, s_2 \dots . s_{n-K-1}\}$ being the values of $r(x)$ at $\alpha, \alpha2, \dots . \alpha \, 2 \, t$. If $s(x)$ is zero, $r(x)$ itself is a codeword; else proceed as follows.

ii. With the syndromes obtained in step 1 above, form the error-locator polynomial $\sigma(x)$ using any of the algorithms like Berlekamp, Peterson-Gorenstein-Zierler algorithm, form the error-locator polynomial $\sigma(x)$ using the syndromes obtained in Step 1.

iii. Obtain the roots of $\sigma(x)$ and their respective inverses which indicate the error locations.

iv. Complement the bits in the positions indicated by the error locations to obtain the decoded codeword. The syndrome polynomial can be obtained alternately by dividing $r(x)$ by $g(x)$ and evaluating the remainder at $\alpha, \alpha^2, \dots . \alpha^{2t}$. This is same as the syndrome nonbinary BCH codes; nonbinary BCH codes form

another class of BCH codes where the coefficients of the code polynomial are also elements from the extended field. Encoding of non-binary BCH codes follows the same procedure as that of binary BCH codes.

3.3 The binary Golay code

The binary form of the Golay code is one of the most important types of linear binary block codes. The t-error correcting code can correct a maximum of t errors. A perfect t-error correcting code has the property that every word lies within a distance of t to exactly one code word. Equivalently, the code has $d_{min} = 2\,t + 1$, and covering radius t, where the covering radius r is the smallest number such that every word lies within a distance of r to a codeword.

The time complexity for hamming codes is $0(n2)$ since it is multiplication of two matrices. The time complexity for Golay binary code is as follows $0(n)$ for the calculating syndrome that is calculating the error.

3.4 Reed-Solomon codes

Reed-Solomon codes are block-based error correcting codes with a wide range of applications in digital communications and storage. Reed-Solomon codes are used to correct errors in many systems such as storage devices, wireless or mobile communications, satellite, DVB and high-speed modems such as ADSL, xDSL. A typical communication channel using Reed-Solomon code is shown in **Figure 6**.

The Reed-Solomon encoder takes a block of digital data and adds extra redundant bits. Errors occur during transmission or storage due to noise, interference, scratch on CD, etc. The Reed-Solomon decoder processes each block and attempts to correct errors and recover the original data. The number and type of errors that can be corrected depends on the characteristics of the Reed-Solomon code.

3.4.1 Properties of Reed-Solomon codes

Reed Solomon codes are a subset of BCH codes and are linear block codes. A Reed-Solomon code is denoted as RS (n,k) with *s*-bit symbols.

This means that the encoder takes *k* data symbols of **s** bits each and adds parity symbols to make an n symbol code word. There are *n-k* parity symbols of s bits each. A Reed-Solomon decoder can correct up to t symbols that contain errors in a code word, where *2 t = n-k*.

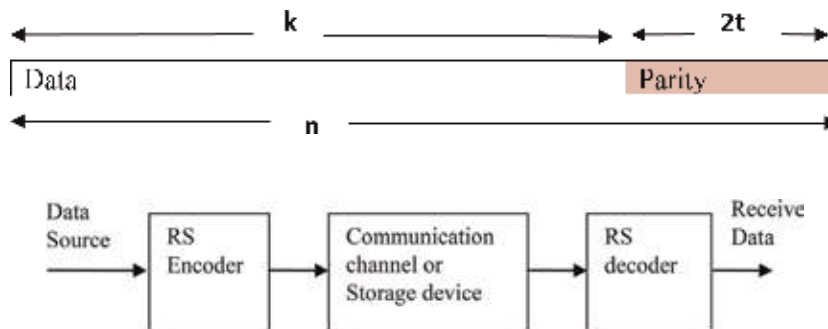The following diagram shows a typical Reed-Solomon code word.

Figure 6.
The Reed-Solomon code with communication channel.

3.4.2 Architectures for encoding and decoding Reed-Solomon codes

Reed-Solomon encoding and decoding can be carried out in software or in special-purpose hardware.

3.4.2.1 Finite (Galois) field arithmetic

Reed-Solomon codes are based on a specialist area of mathematics known as Galois fields or finite fields. A finite field has the property that arithmetic operations ($+$, $-$, $\times$, $/$ etc.) on field elements always have a result in the field. A Reed-Solomon encoder or decoder needs to carry out these arithmetic operations. These operations require special hardware or software functions to implement.

3.4.2.2 Generator polynomial

A Reed-Solomon codeword is generated using a special polynomial. All valid codewords are exactly divisible by the generator polynomial. The generator polynomial is denoted as below:

$$g(x) = (x - \alpha^i)(x - \alpha^{i+1})...(x - \alpha^{i+2t}) \tag{20}$$

and the codeword is constructed using:

$$c(x) = g(x).i(x). \tag{21}$$

where g(x) is the generator polynomial, $i(x)$ is the information block, $c(x)$ is a valid codeword and α is referred to as a primitive element of the field.

Example: Generator for RS(255,249).

$$g(x) = (x - \alpha^0)(x - \alpha^1)(x - \alpha^2)(x - \alpha^3)(x - \alpha^4)(x - \alpha^5) \tag{22}$$

$$g(x) = x^6 + g_5 x^5 + g_4 x^4 + g_3 x^3 + g_2 x^2 + g_1 x^1 + g_0 \tag{23}$$

3.4.3 Encoder architecture

The 2t parity symbols in a systematic Reed-Solomon codeword are given by:

$$p(x) = i(x)x^{n-k} \bmod g(x) \tag{24}$$

Figure 7 shows the architecture for a systematic RS(255,249) encoder:
Each of the 6 registers holds a symbol (8 bits). The arithmetic operators carry out finite field addition or multiplication on a complete symbol.

3.4.4 Decoder architecture

A general architecture for decoding Reed-Solomon codes is shown in **Figure 8**.
Key

r(x)	codeword at receiver
Si	Syndromes
L(x)	Polynomial of error locator

Xi	Locations of error
Yi	Magnitudes of error
c(x)	code word recovered
v	Errors in total
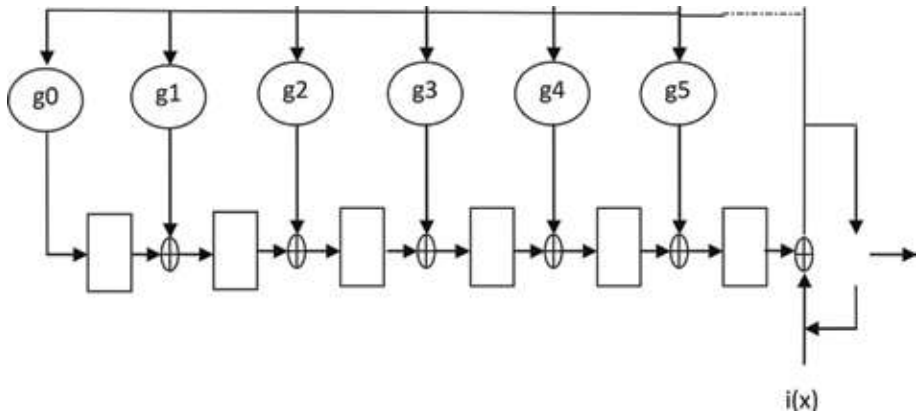
Figure 7.
Block diagram of RS encoder.
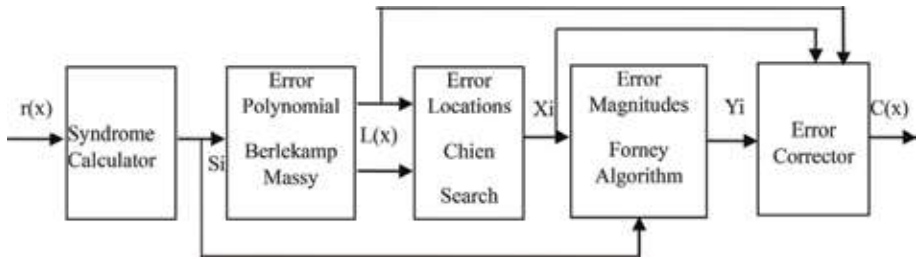
Figure 8.
Block diagram of RS decoder.

The received codeword $r(x)$ is the original (transmitted) codeword $c(x)$ plus errors:

$r(x) = c(x) + e(x).$

A Reed-Solomon decoder attempts to identify the position and magnitude of up to t errors (or $2t$ erasures) and to correct the errors or erasures.

Syndrome calculation: This is a similar to parity calculation. A Reed-Solomon codeword has $2t$ syndromes that depend only on errors (not on the transmitted codeword). The syndromes can be calculated by substituting the 2 t roots of the generator polynomial g(x) into r(x).

Finding the symbol error locations: Error locations are found by solving simultaneous equations with t unknowns. It uses several fast algorithms, which take the advantage of the special matrix structure of these codes and reduce the computational effort. In general two steps are involved.

Find an error locator polynomial: This can be done using the Berlekamp-Massey algorithm or Euclid's algorithm. Euclid's algorithm is more popular because it is easier to implement: however, the Berlekamp-Massey algorithm has efficient hardware and software implementations.

Find the roots of this polynomial: This is done using the Chien search algorithm.

Finding the symbol error values: Again, this involves solving simultaneous equations with t unknowns. A widely-used fast algorithm is the Forney algorithm.

3.5 Low-density parity check codes

Low-density parity check (LDPC) codes are a class of linear block code. The term "Low Density" refers to the parity check matrix which contains only few '1's in comparison to '0's. LDPC codes are arguably the best error correction codes in existence at present. LDPC codes were first introduced by R. Gallager in his Ph.D. thesis in 1960. However, they were forgotten due to introduction of Reed-Solomon codes and since there were problems with implementation of LDPC codes due to limited technological know-how. The LDPC codes were rediscovered in mid-90s by R. Neal and D. Mackay at the Cambridge University.

N bit long LDPC code is defined code in terms of M number of parity check equations, and these equations can be described as an M × N parity check matrix H.

where, M is the number of parity check equations and N is the number of bits in the code word.

Consider the 6-bit long codeword in the form $c = \left[c_1, c_2, c_3, c_4, c_5, c_6 \right]$ which satisfies 3 parity check equations as shown below.

$$c_1 \oplus c_2 \oplus c_5 = 0 \tag{25}$$

$$c_1 \oplus c_4 \oplus c_6 = 0 \tag{26}$$

$$c_1 \oplus c_2 \oplus c_3 \oplus c_6 = 0 \tag{27}$$

We can now define 3 × 6 parity check matrix as,

$$c_1 \oplus c_2 \oplus c_5 \tag{28}$$

$$H = \begin{bmatrix} 1 & 1 & 0 & 0 & 1 & 0 \\ 1 & 0 & 0 & 1 & 0 & 1 \\ 1 & 1 & 1 & 0 & 0 & 1 \end{bmatrix} \tag{29}$$

w_r and w_c changes, therefore this is an irregular parity check matrix.

The density of '1's in LDPC code parity check matrix is very low, row weight $\left(w_c \right)$ is the number of '1's in a row, number of symbols taking part in a parity check, column weight is the number of '1's in a column, number of times a symbol takes part in parity checks.

$$H = \begin{bmatrix} 1 & 1 & 0 & 0 & 1 & 0 \\ 1 & 0 & 0 & 1 & 0 & 1 \\ 1 & 1 & 1 & 0 & 0 & 1 \end{bmatrix} \tag{30}$$

The $H_{M \times N}$ parity check matrix defines a rate $R = K/N$, $R = K/N$ code where $K = N - M$ Codeword is said to be valid if it satisfies the syndrome calculation $z = c.H^T = 0$.

We can generate the codeword c by multiplying message m with generator matrix G.

$$c = m.G \tag{31}$$

We can obtain the generator matrix G from parity check matrix H by

1. arranging the parity check matrix in systematic form using row and column operations and

$$H_{sys} = \left[I_M | P_{M \times K} \right] H_{sys} = \begin{bmatrix} 1 & 0 & 0 & 1 & 0 & 1 \\ 0 & 1 & 0 & 1 & 1 & 1 \\ 0 & 0 & 1 & 0 & 1 & 1 \end{bmatrix} \tag{32}$$

2. rearranging the systematic parity check matrix.

$$G = \left[P_{K \times M}^T | I_K \right] \tag{33}$$

$$G = \begin{bmatrix} 1 & 1 & 0 & 1 & 0 & 0 \\ 0 & 1 & 1 & 0 & 1 & 0 \\ 1 & 1 & 1 & 0 & 0 & 1 \end{bmatrix} \tag{34}$$

3. we can verify our results as

$$G.H^T = 0 \tag{35}$$

$$H = \begin{bmatrix} 1 & 1 & 0 & 0 & 1 & 0 \\ 1 & 0 & 0 & 1 & 0 & 1 \\ 1 & 1 & 1 & 0 & 0 & 1 \end{bmatrix} \tag{36}$$

Tanner graph is a graphical representation of parity check matrix specifying parity check equations. Tanner graph for LDPC codes, as shown in **Figure 9**, consists of N number of variable nodes and M number of check nodes. In Tanner graph, m^{th} check node is connected to n^{th} variable node if and only if n^{th} element in m^{th} row in parity check matrix H, h_{mn} is a '1'.

The marked path $z_2 \rightarrow c_1 \rightarrow z_3 \rightarrow c_6 \rightarrow z_2$ is an example for short cycle of 4. The number of steps needed to return to the original position is known as the girth of the code.

3.6 Convolution codes

Convolutional codes differ from block codes in that the encoder contains memory. The n encoder outputs at any time unit depend not only on the k inputs but also on m previous input blocks. An (n, k, m) convolutional code can be implemented with a k-input, n-output linear sequential circuit with input memory m. Typically, n and k are small integers. Wozencraft proposed sequential decoding as an efficient decoding scheme for convolution codes, and many experimental studies were
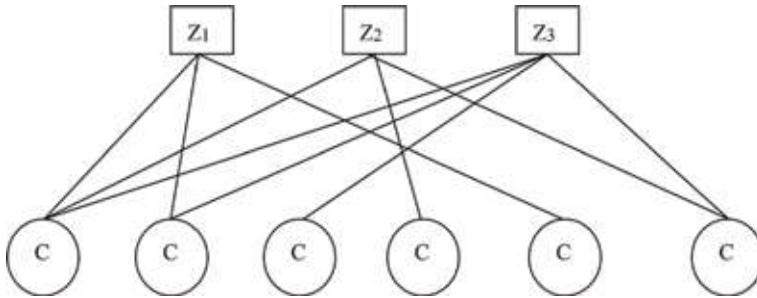

Figure 9.
LDPC codes tanner graph representation.

performed on the same. In 1963, Massey proposed a method which was simpler to implement called threshold decoding. Then in 1967, Viterbi proposed a maximum likelihood decoding scheme that was relatively easy to implement for codes with small memory orders. Viterbi decoding was combined with improved versions of sequential decoding and convolutional codes were used in deep-space and satellite communication in early 1970s. A convolutional code is generated by passing the information sequence to be transmitted through a linear finite-state shift register. In general, the shift register consists of K (k-bit) stages and n linear algebraic function generators.

Convolution codes have simple encoding and decoding methods and are quite a simple generalization of linear codes and have encodings as cyclic codes.

An (n,k) convolution code (CC) is defined by a $k \times n$ generator matrix, entries of which are polynomials over F_2.

$$G_1 = [x^2 + 1, x^2 + x + 1] \tag{37}$$

is the generator matrix for a (2,1) convolution code CC_1 and

$$G_2 = \begin{pmatrix} 1+x & 0 & x+1 \\ 0 & 1 & x \end{pmatrix} \tag{38}$$

is the generator matrix for a (3,2) convolution code CC_2.

3.6.1 Encoding of finite polynomials

An (n,k) convolution code with a $k \times n$ generator matrix G can be used to encode a k-tuple of plain-polynomials.

$$I = (I_0(x), I_1(X), \dots, I_{k-1}(x)). \tag{39}$$

to get an n-tuple of crypto-polynomials.

$$C = (C_0(x), C_1(x), \dots, C_{n-1}(x)). \tag{40}$$

As follows

$$C = I.G. \tag{41}$$

3.6.2 Turbo codes

Turbo codes were proposed by Berrou and Glavieux in the 1993 International Conference in Communications. Turbo codes demonstrated a performance within 0.5 dB of the channel capacity limit for BPSK. Turbo codes use parallel concatenated coding, recursive convolutional encoders, and Pseudo-random interleaving.

Turbo codes have a remarkable power efficiency in Additive White Gaussian Noise (AWGN) and flat-fading channels for moderately low BER, mostly used in delivery of multimedia services. However turbo codes have a long latency and poor performance at very low BER since turbo codes operate at very low SNR, channel estimation and tracking is a critical issue. The principle of iterative or "turbo" processing can be applied to other problems; Turbo-multiuser detection can improve performance of coded multiple-access systems. Performance close to the Shannon Limit can be achieved ($E_b/N_0 = -1.6$ dB if $R_b \rightarrow 0$) at modest complexity. Turbo codes have been proposed for low-power applications such as deep-space and

satellite communications, as well as for limited interference applications such as third generation cellular, personal communication services, ad hoc, and sensor networks.

The information capacity (or channel capacity) C of a continuous channel with bandwidth B Hertz can be perturbed by additive Gaussian white noise of power spectral density $N_0/2$, provided bandwidth B satisfies.

$$C = B \log_2 \left(1 + \frac{P}{N_0 B} \right) \quad bits/second \tag{42}$$

where P is the average transmitted power $P = E_b R_b$ (for an ideal system, $R_b = C$), E_b is the transmitted energy per bit, R_b is transmission rate.

3.6.2.1 Turbo code encoder

The fundamental of turbo encoder is using two identical recursive systematic convolutional (RSC) code arranged in parallel form separated by an interleaver. The nature of the interleaver in turbo code is pseudo-random in order to minimize the correlation between the outputs of encoders that make the best results, and its matrix forms with rows and columns, depending on the block size of the code [8]. The structure of turbo encoder is shown in **Figure 10**.

Interleaver/deinterleaver are used and play an important role in the performance of turbo codes. The interleaver helps to increase the minimum distance and break the low weight of the input sequence by spreading out the burst errors. This is done by mapping the sequence of bits to another sequence of bits. When the length of the interleaver is very large, Turbo codes achieve excellent performance [9]. According to the structure of turbo encoder, puncturing technique will be used to obtain high rate. Puncturing is operating on the parity bits only, but the systematic bits are not punctured [10].

3.6.2.2 Turbo decoder

Turbo decoders consist of a pair of convolutional decoders which cooperatively and iteratively exchange soft-decision information. The information can be passed from one decoder to the other, where each decoder takes the information corresponding to the systematic, parity bits from the encoder and a priori information from the other decoder and the resulting output generated by the decoder should be soft decisions or estimates. The passing of information between the first and second decoder continues until a given number of iterations is reached. With

X: Information

Yi: Redundancy Information
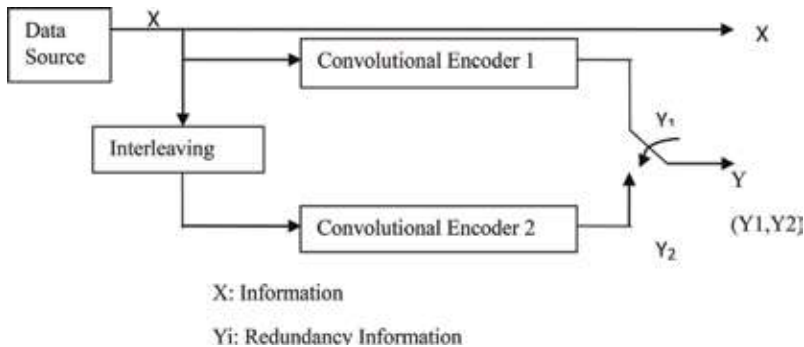
Figure 10.
Turbo code encoder.
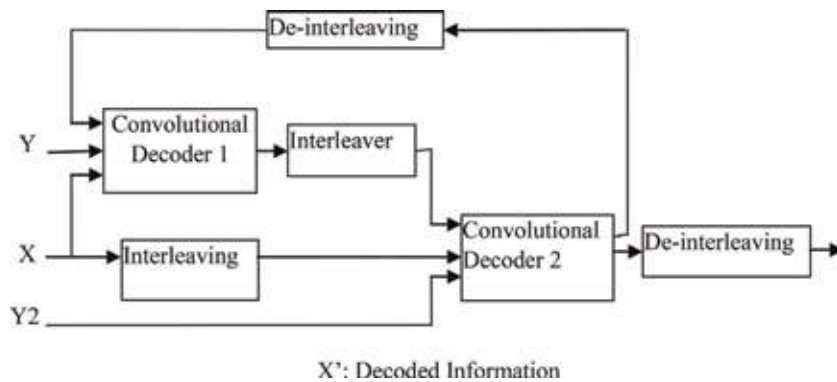
Figure 11.
Turbo code decoder.

each iteration, the estimates of the information bits improve. A correct estimate of the message is achieved by increasing the number of iterations. However, this improvement does not increase linearly. Practically, it is enough to utilize a small number of iterations to achieve acceptable performance [11, 12]. **Figure 11** illustrates the structure of turbo decoder.

The decoder produces a soft-decision to each message bits in logarithmic form known as a log likelihood ratio (LLR) [11, 12]. At the end of this process, a hard decision is carried out at the second decoder to convert the final signal to 1's and 0's and compare it with the original message" [13, 14].

3.6.3 Trellis coded modulation (TCM)

Error probability can be decreased by adding more code bits - the code rate is increased. Combine both encoding and modulation (using Euclidean distance only). Allow parallel transition in the trellis, and it has significant coding gain (3∼4 dB) without bandwidth compromise. It has the same complexity (same amount of computation, same decoding time and same amount of memory needed). Trellis
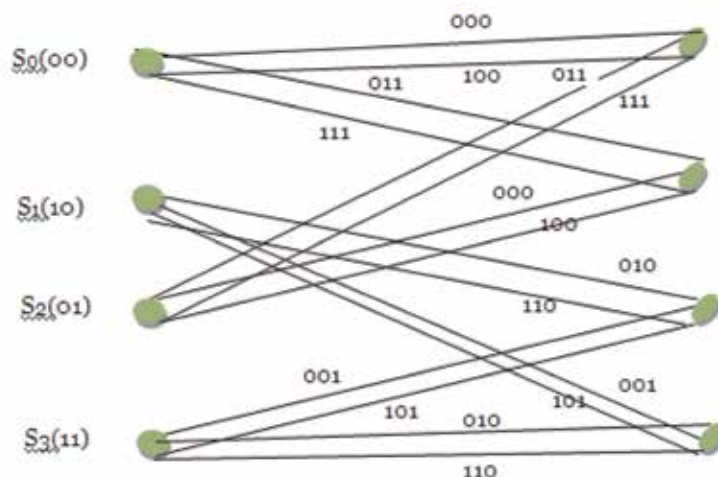
Figure 12.
Encoder for four state Trellis TCM.
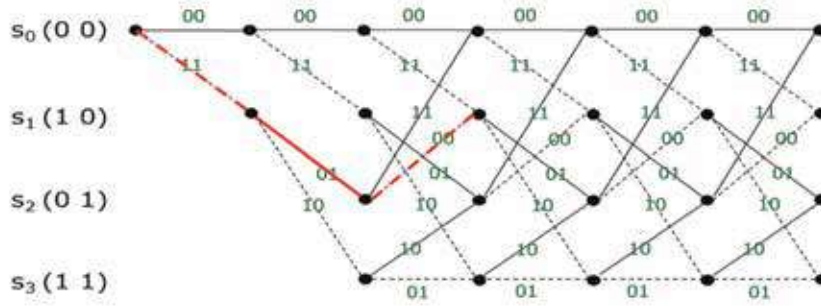
Figure 13.
Trellis representation QPSK.

code has great potential for fading channel and widely used in Modem. **Figure 12** shows encoder for four state Trellis TCM.

There is increase in constellation size compared to uncoded communication, increase in throughput (b/s/Hz), and decline in BER performance due to decrease of $d_{min.}$ Trellis coded modulation (TCM) is used to offset loss resulting from constellation size increase. TCM achieves this higher gain by jointly using the distance properties of the code and the distance properties of the constellation, by carefully mapping coded and uncoded bits to the constellation points. TCM uses "set partitioning" to map the bits to the constellation points. **Figure 13** shows Trellis representation for QPSK.

Input: 101 → Output: 001011.

### 3.7 Application areas for error correcting codes (ECCs)

Deep Space communication. used a concatenation of Reed-Solomon code and convolutional code.

Storage media. BCH codes and Reed-Solomon codes are used in applications like compact disk players, DVDs, disk drives, NAND flash drives, and 2D bar codes. LDPC codes are used for SSDs and fountain codes are erasure codes used in data-storage applications.

Mobile communication. ARQ is sometimes used with Global System for Mobile (GSM) communication to guarantee data integrity. Traffic channels in 2G standard use convolution code. Convolution and turbo codes are used in 3G (UMTS) networks; convolution coding can be used for low data rates and turbo coding for higher rates.

WiMAX (IEEE 802.16e standard for microwave communications) and high-speed wireless LAN (IEEE 802.11n) use LDPC as a coding scheme.

Satellite communication. For reliable communication in WiMax, optical communication, and power line communication, or in multi-layer flash memories, turbo and LDPC codes are desirable.

Hybrid ARQ is another technique for spectrum efficiency and reliable link. Network coding is one of the most important breakthroughs in information theory in recent years.

4. Conclusion

The chapter describes the different types of errors encountered in a data communication system over channels and focuses on the role of polynomials in implementing various algorithms for error detection and correction codes. It

discusses error detection codes such as Simple Parity check, Two-dimensional Parity check, Checksum, Cyclic redundancy check; and error corrections codes such as Hamming code, BCH, Golay codes, RS Code, LDPC, Trellis and Turbo codes. It also gives an overview of the architecture and implementation of the codes and discusses the applications of these codes in various systems.

Author details

Charanarur Panem[1], Vinaya Gad[2] and Rajendra S. Gad[1]*

1 Altera SoC Laboratory, Department of Electronics, Goa University, Goa, India

2 Department of Computer Science, G.V.M.'s College, Ponda, Goa, India

*Address all correspondence to: rsgad@unigoa.ac.in

IntechOpen

References

[1] Available at: https://nptel.ac.in/courses/106105080/pdf/M3L2.pdf

[2] Available at: https://www.techwalla.com/articles/types-of-errors-in-data-communication

[3] Bertsekas D, Gallager R. Data Networks. 2nd ed. Prentice Hall; 1992. Available at: web.mit.edu/dimitrib/www/datanets.html

[4] Forouzan B. Data Communications and Networking. 5th ed. McGraw Hill; 2013

[5] Lin S, Costello DJ. Error Control Coding. 2nd ed. Prentice Hall; 2004

[6] McEliece R. Finite Fields for Computer Scientists and Engineers. Springer; 1986

[7] Available at: https://electronicsforu.com/technology-trends/error-correcting-codes-comm-storage

[8] Benkeser C, Burg A, Cupaiuolo T, Huang Q. Design and optimization of an HSDPA Turbo Decoder ASIC. Journal of Solid-State Circuits. 2009

[9] Sadjadpour HR, Sloane NJA, Salehi M, Nebe G. Interleaver design for turbo codes. IEEE Journal on Selected Area In Communications. 2001;**19**(5):831-837

[10] Raad IS, Yakan M. Implementation of a turbo codes test bed in the Simulink environment. In: International Symposium on Signal Processing and Its Applications. Piscataway: IEEE; 2005. pp. 847-850

[11] Kaza J, Chakrabarti C. Design and implementation of low energy turbo decoders. IEEE Transactions on Very Large Scale Integration (VLSI) Systems. 2004;**12**(9):968-977

[12] Moreira JC, Farrell PG. Essential of Error Control Coding. Wiley; 2006

[13] Moon TK. Error Correction Coding: Mathematical Methods and Algorithms. Wiley; 2005

[14] Yi B-N. Turbo code design and implementation of high-speed parallel decoder. Telkomnika. 2013;**11**(4):2116-2123

Chapter 3

A Direct Construction of Intergroup Complementary Code Set for CDMA

Palash Sarkar and Sudhan Majhi

Abstract

A collection of mutually orthogonal complementary codes (CCs) is said to be complete complementary codes (CCCs) where the number of CCs are equal to the number of constituent sequences in each CC. Intergroup complementary (IGC) code set is a collection of multiple disjoint code groups with the following correlation properties: (1) inside the zero-correlation zone (ZCZ), the aperiodic autocorrelation function (AACF) of any IGC code is zero for all nonzero time shifts; (2) the aperiodic cross-correlation function (ACCF), of two distinct IGC codes, is zero for all time shifts inside the ZCZ when they are taken from the same code groups; and (3) the ACCF, for two IGC codes from two different code groups, is zero everywhere. IGC code set has a larger set size than CCC, and both can be applicable in multicarrier code-division multiple access (CDMA). In this chapter, we present a direct construction of IGC code set by using second-order generalized Boolean functions (GBFs), and our IGC code set can support interference-free code-division multiplexing. We also relate our construction with a graph where the ZCZ width depends on the number of isolated vertices present in a graph after the deletion of some vertices. Here, the construction that we propose can generate IGC code set with more flexible parameters.

Keywords: complementary code (CC), code-division multiple access (CDMA), generalized, Boolean function (GBF), intergroup complementary (IGC) code set, zero-correlation zone, (ZCZ) sequences

1. Introduction

Code-division multiple access (CDMA) [1] is an important communication technology where sequence signatures with good correlation properties are used to separate multiple users. In CDMA systems, multipath interference (MPI) and multiple access interference (MAI) degrade the performance where MPI and MAI occur due to the multipath propagation, non-ideal synchronization, and non-ideal correlation properties of spreading codes. Spreading code plays a significant role on the overall performance of a CDMA system. The interference-resist capability and system capacity are determined by the correlation properties and available number of spreading codes. Due to ideal auto- and cross-correlation properties, complete complementary codes (CCCs) have been applied to asynchronous multicarrier CDMA (MC-CDMA) [2] communications in order to provide zero interference performance.

Golay proposed a pair of sequences in Golay [3] known as Golay complementary pair (GCP) which is a set of two equal length sequences with the property that the sum of their aperiodic autocorrelation function (AACF) is zero everywhere except at the zero shift. Tseng and Liu [4] extended the idea of GCP to complementary set or complementary code (CC) which contains two or more than two sequences. Davis and Jedwab [5] proposed a direct construction of GCP called Golay-Davis-Jedwab (GDJ) pair by using second-order generalized Boolean functions (GBFs) to reduce peak-to-mean envelope power ratio (PMEPR) for OFDM system. As a generalization of GDJ pair, Paterson introduced a construction of CC Paterson [6] by associating each CC with a graph. Recently, a construction of CC has been reported in Sarkar et al. [7] which is a generalization of Paterson's CC construction. Later, Rathinakumar and Chaturvedi extended Paterson's construction to CCC Rathinakumar and Chaturvedi [8] which is a collection of mutually orthogonal CCs. Although CCs have ideal AACF and aperiodic cross-correlation function (ACCF), they are unable to support a maximum number of users as the set size cannot be larger than the flock size [9–11], where the flock size denotes the number of constituent sequences in each CC. The application of CCC has been extended for the enabling of interference-free MC-CDMA communication by designing a fractional-delay-resilient receiver in Liu et al. [12].

The binary Z-complementary sequences were first introduced by Fan et al. [13] and later extended to quadriphase Z-complementary sequences by Li et al. [14].

Recently, a construction of binary Z-complementary pairs has been reported in Adhikary et al. [15]. A direct construction of polyphase Z-complementary codes has been reported in Sarkar et al. [16], which is an extension of Rathinakumar's CCC construction. Due to favorable correlation properties of Z-complementary codes, it can be easily utilized for MC-CDMA system as spreading sequences to mitigate MPI and MAI efficiently [17]. The theoretical bound given in Liu et al. [18] shows that the Z-complementary codes have a much larger set size than CCCs.

IGC code set was first proposed by Li et al. [19] based on CCCs. Their code assignment algorithm shows that the CDMA systems employing the IGC codes (IGC-CDMA) outperform traditional CDMA with respect to bit error rate (BER). However, the ZCZ width of IGC codes [19] is fixed to the length of the elementary codes of the original CCCs, which limits the number of IGC codes. Another improved construction method of IGC codes is proposed in Feng et al. [20] based on the CCCs, interleaving operation, and orthogonal matrix which provides a flexible choice of the ZCZ width. However, there is no such construction which can directly produce IGC code set without having operation on CCCs; it motivates us to give a direct construction of IGC code set.

This chapter contains a direct method to construct IGC code set by applying second-order GBFs. This construction is capable of generating IGC code set with more flexible parameters such as ZCZ width and set size. We also relate our construction with a graph, and it has been shown that ZCZ width and set size of the IGC code set obtained by using our method depend on the number of isolated vertices present in a graph which is achieved by deleting some vertices from a graph.

2. Preliminary

2.1 Correlations of sequences

The ACCF between two sequences $\mathbf{a} = (a_0, a_1, ..., a_{L-1})$ and $\mathbf{b} = (b_0, b_1, ..., b_{L-1})$ is defined as follows:

$$C(\mathbf{a}, \mathbf{b})(\tau) = \begin{cases} \sum_{i=0}^{L-1-\tau} a_{i+\tau} b_i^*, & 0 \leq \tau < L, \\ \sum_{i=0}^{L+\tau-1} a_j b_{i-\tau^j}^*, & -L < \tau < 0, \\ 0, & \text{otherwise}, \end{cases} \tag{1}$$

where τ is an integer. The above defined function in Eq. (1) is said to be AACF of $\mathbf{a}$ (or, $\mathbf{b}$) if $\mathbf{a} = \mathbf{b}$. The AACF of $\mathbf{a}$ at τ is denoted by $A(\mathbf{a})(\tau)$.

Definition 1 *An ordered set $\{\mathbf{a}^0, \mathbf{a}^1, ..., \mathbf{a}^{P-1}\}$ containing P sequences of equal length L is called CC lf*

$$\sum_{i=0}^{P-1} A(\mathbf{a}^j)(\tau) = \begin{cases} LP, & \tau = 0, \\ 0, & \text{otherwise}. \end{cases} \tag{2}$$

Definition 2 *Let $\{\mathbf{C}^0, \mathbf{C}^1, ..., \mathbf{C}^{K-1}\}$ be a set of K CCs where each of the CC contains $P(K \leq P)$ constituent sequences of length L. The αth constituent sequence of $\mathbf{C}^i$ is $\mathbf{C}_{i,\alpha} = (C_{i,\alpha,0}, C_{i,\alpha,1}\ C_{i,\alpha,L-1})$ where $\alpha = 0, 1, ..., P-1, i = 0, 1, ..., K-1$. The ACCF of the CCs is given by*

$$C(\mathbf{C}^i, \mathbf{C}^j)(\tau) = \sum_{\alpha=0}^{P-1} C(\mathbf{C}_{i,\alpha} \mathbf{C}_{j,\alpha})(\tau) = 0, \quad \forall \tau, \ i \neq j. \tag{3}$$

The code set is said to be CCC when $K = P$.

Definition 3 *Given an IGC code set I (K,P,L,Z) (Li et al. [19]), K denotes a number of codes, P denotes the number of constituent sequences in each code, L denotes the length of each constituent sequence, and Z denotes ZCZ width, where $K = PL/Z$. The K codes can be divided into P code groups denoted by $I^g (g = 0, 1, ..., P-1)$, each group contains $K/P = L/Z$ codes. The code set $I(K, P, L, Z)$ has the following properties:*

$$C(\mathbf{C}^i, \mathbf{C}^j)(\tau) = \begin{cases} PL, & i = j, \tau = 0, \\ 0, & i = j, 0 < |\tau| < Z, \\ 0, & i \neq j, \mathbf{C}^i, \mathbf{C}^j \in I^g, |\tau| < Z, \\ 0, & \mathbf{C}^i \in I^{g_1}, \mathbf{C}^j \in I^{g_2}, g_1 \neq g_2, |\tau| < L, \\ \text{others}, & \text{otherwise}. \end{cases} \tag{4}$$

2.2 Generalized Boolean functions

Let $f : \{0,1\}^m \to \mathbb{Z}_q$ (q is average number, not less than 2) be a function of m variables $x_0, x_1, ..., x_{m-1}$. The product of k distinct variables $\chi_{i_0} \chi_{i_1} ... \chi_{i_{k-1}} (0 \leq i_0 < i_1 < \cdots < i_{k-1} \leq m-1)$ is called a monomial of degree k. The monomials $1, x_0, ..., x_{m-1}, x_0 x_1, ..., x_{m-2} x_{m-1}, ..., x_0 x_1 ... x_{m-1}$ are the list of 2^m monomials over the variables $x_0, x_1, ..., x_{m-1}$. A GBF f can uniquely be presented as a linear combination of these 2^m monomials, where the coefficient of each monomial belongs to $\mathbb{Z}_q$. We denote the complex valued sequence corresponding to the GBF f by $\psi(f)$ and define it as

$$\psi(f) = (\omega^{f_0}, \omega^{f_1}, ..., \omega^{f_{2^{m-1}}}), \tag{5}$$

where $f_i = f(i_0, i_1, ..., i_{m-1})$, $\omega = \exp(2\pi\sqrt{-1}/q)$, and $(i_0, i_1, ..., i_{m-1})$ are the binary representation of the integer $i (i = \sum_{i=0}^{m-1} i_j 2^j)$. Let $\mathbf{C}$ be an order set of P Boolean functions given by $\mathbf{C} = \{f_0, f_1, ..., f_{P-1}\}$. Then the complex valued code

corresponding to the set of Boolean function $\mathbf{C}$ is denoted by $\psi(\mathbf{C})$, given by $\psi(\mathbf{C}) = \{\psi(f_0), \psi(f_1), ..., \psi(f_{P-1})\}$. The code can also be viewed as a matrix where $\psi(f_{i-1})$ is the ith row of the matrix.

For any given GBF f of m variables, the function $f(1 - x_0, 1 - x_1, ..., 1 - x_{m-1})$ is denoted by $\tilde{f}$. For a $\mathbb{Z}_q$ valued vector $\mathbf{e} = (e_0, e_1, ..., e_{L-1})$, we denote the vector $\overline{\mathbf{e}}$ by $(\overline{e}_0, \overline{e}_1, ..., \overline{e}_{L-1})$ where $\overline{e}_i = \frac{q}{2} - e_i (i = 0, 1, ..., L - 1)$. Now, we define the following notations $\overline{\mathbf{a}}$ and $\mathbf{a}^*$, where $\overline{\mathbf{a}}$ is derived from $\mathbf{a}$ by reversing it and $\mathbf{a}^*$ is the complex conjugate of $\mathbf{a}$.

2.3 Quadratic forms and graphs

In this context, we introduce some lemmas and new notations which will be used for our proposed construction.

Definition 4 Let f be a GBF of variables $x_0, x_1, ..., x_{m-1}$ over $\mathbb{Z}_q$. Consider a list of $k(0 \leq k < m)$ indices $0 \leq j_0 < j_1 < \cdots j_k < m$, and write $\mathbf{x} = (x_{j_0}, x_{j_1}, ..., x_{j_{k-1}})$. Consider $\mathbf{c} = (c_0, c_1, ..., c_{k-1})$ to be a fixed binary vector. Then we define $\psi(f|_{\mathbf{x}=\mathbf{c}})$ as a complex valued vector with $\omega^{f(i_0, i_1, ..., i_{m-1})}$ as a ith component if $i_{j_\alpha} = c_\alpha$ for each $0 \leq \alpha < k$ and equal to zero otherwise. For $k = 0$, the complex valued vector $\psi(f|_{\mathbf{x}=\mathbf{c}})$ is nothing, but the vector $\psi(f)$ is defined before.

Let $Q : \{0,1\}^m \to \mathbb{Z}_q$ be a quadratic form of m variables $x_0, x_1, ..., x_{m-1}$. A quadratic GBF is of the form Rathinakumar and Chaturvedi [8]

$$f = Q + \sum_{i=0}^{m-1} g_i x_i + g', \tag{6}$$

where $g', g_i \in \mathbb{Z}_q$ are arbitrary.

For a quadratic GBF, f, $G(f)$ denotes the graph of f. The $G(f)$ is obtained by joining the vertices x_i and x_j by an edge if there is a term $q_{i,j} x_i x_j (0 \leq i < j \leq m - 1)$ in the GBF f with $q_{i,j} \neq 0 \left(q_{i,j} \in \mathbb{Z}_q\right)$. Consider a function $f|_{x_j=c}$, derived by fixing x_j at c in f. The graph of $f|_{x_j=c}$ is denoted by $G\left(f|_{x_j=c}\right)$ which is obtained by deleting the vertex x_j and all the edges which are connected to x_j from $G(f)$. Then $G(f|_{\mathbf{x}=\mathbf{c}})$ is obtained from $G(f)$ by deleting $x_{j_0}, x_{j_1}, ..., x_{j_{k-1}}$. $G(f|_{\mathbf{x}=\mathbf{c}})$ represent the same graph for all $\mathbf{c} \in \{0,1\}^k$. Therefore, for all $\mathbf{c}$ in $\{0,1\}^k$, $f\big|_{\mathbf{x}=\mathbf{c}}$ have the same quadratic form. Note that the quadratic forms of f and $\tilde{f}$ are the same; thus, they have associated with the same graph.

Lemma 1 Construction of CCC [8].

Let $f: \{0, 1\}^m \to \mathbb{Z}_q$ be a GBF and f its reversal. Assume that $G(f|_{\mathbf{x}=\mathbf{c}})$ is a path for each $\mathbf{c} \in \{0, 1\}^k$ and the edges in the path have the same weight $q/2$. Let $(b_0, b_1, ..., b_{k-1})$ be the binary representation of the integer t. Define the order sets of GBFs $\mathbf{C}^t$ to be

$$\left\{ f + \frac{q}{2} \left(\sum_{\alpha=0}^{k-1} d_\alpha x_{j_\alpha} + \sum_{\alpha=0}^{k-1} b_\alpha x_{j_\alpha} + d x_\gamma \right) : d, d_\alpha \in \{0,1\} \right\}, \tag{7}$$

and the order set of GBFs $\tilde{\mathbf{C}}t$ *to be*

$$\left\{ \tilde{f} + \frac{q}{2} \left(\sum_{\alpha=0}^{k-1} d_\alpha \overline{x}_{j_\alpha} + \sum_{\alpha=0}^{k-1} b_\alpha \overline{x}_{j_\alpha} + \overline{d} x_\gamma \right) : \overline{d}, d_\alpha \in \{0,1\} \right\}, \tag{8}$$

where x_γ is one of the end vertices in the path. Then

$$\{\psi(\mathbf{C}^t) : 0 \le t < 2^k\} \cup \left\{\psi^* \left(\tilde{\mathbf{C}}^t\right) : 0 \le t < 2^k\right\} \tag{9}$$

generates a set of CCC, where $\psi^*(\cdot)$ denotes the complex conjugate of $\psi(\cdot)$.

3. Construction of IGC code set from GBFs

In this section, we propose a direct construction of IGC code set by using Boolean algebra and graph theory. Before proposing the main theorem of the construction, we define some sets and vectors and present some lemmas. First we define some notations which will be used throughout in our construction:

- $\mathbf{x} = \left(x_{j_0}, x_{j_1}, ... x_{j_{k-1}}\right) \in \mathbb{Z}_2^k$, $\mathbf{x}' = \left(x_{m-p'}x_{m-p+1}, ..., x_{m-1}\right) \in \mathbb{Z}_2^p$.

- $\mathbf{b} = (b_0, b_1, ..., b_{k-1})$, $\mathbf{b}_i = (b_{i,0}, b_{i,1}, ..., b_{i,k-1}) \in \mathbb{Z}_2^k (i = 1, 2, ..., 2^k)$.

- $\mathbf{d} = (d_0, d_1, ..., d_{k-1}) \in \mathbb{Z}_2^k$, $\mathbf{d}' = \left(d_1', d_2', ..., d_p'\right)$ and
  $\mathbf{d}_j' = \left(d_{j,1}', d_{j,2}', ..., d_{j,p}'\right) \in \mathbb{Z}_2^p (j = 1, 2, ..., 2^p)$.

- $\Gamma = \left(g_{m-p'}g_{m-p+1'}...g_{m-1}\right) \in \mathbb{Z}_q^p$.

- $\mathbf{a} \cdot \mathbf{b}$ denotes the dot products of any two vectors $\mathbf{a}$ and $\mathbf{b}$ which are of the same length.

- $\mathbf{A} \otimes \mathbf{B}$ denotes the Kronecker product of any two matrices of arbitrary size.

- $\left[(\cdot)_{i,j}\right]$, $i = 0, 1, ..., M - 1$ and $j = 1, 2, ..., N$ denotes a matrix of order $M \times N$.

Let f be a GBF of m variables $x_0, x_1, ..., x_{m-1}$ over $\mathbb{Z}_q$. For $\mathbf{b} \in \mathbb{Z}_2^k$, $\mathbf{d}' \in \mathbb{Z}_2^p$, we define order sets $S_{\mathbf{bd}'}$ and $\tilde{S}_{\mathbf{bd}'}$ corresponding to the GBF f as follows:

$$S_{\mathbf{bd}'} \left\{f + \frac{q}{2}\left(\sum_{\alpha=0}^{k} d_\alpha x_{j_\alpha} + \sum_{\alpha=0}^{-1} b_\alpha x_{j_\alpha} + \sum_{\alpha=1}^{p} d_\alpha' x_{m-p+\alpha-1} + dx_\gamma\right) : d, d_\alpha \in \{0,1\}\right\}, \tag{10}$$

or

$$S_{\mathbf{bd}'} = \left\{f + \frac{q}{2}\left((d + \mathbf{b}) \cdot \mathbf{x} + \mathbf{d}' \cdot \mathbf{x}' + dx_\gamma\right) : d \in \mathbb{Z}_2, \mathbf{d} \in \mathbb{Z}_2^k\right\}, \tag{11}$$

and

$$\tilde{S}_{\mathbf{bd}'} = \left\{\tilde{f} + \frac{q}{2}\left((d + b) \cdot \overline{\mathbf{x}} + \mathbf{d}' \cdot \overline{\mathbf{x}}' + \overline{d}x_\gamma\right) : d \in \mathbb{Z}_2, \mathbf{d} \in \mathbb{Z}_2^k\right\} \tag{12}$$

From the above expression, it is clear that each of the order sets $S_{\mathbf{bd}'}$ and $\tilde{S}_{\mathbf{bd}'}$ contains 2^{k+1} GBFs.

Lemma 2 *Let f be a GBF of m variables with the property that each $\mathbf{c} \in \{0,1\}^k$, $G(f|_{\mathbf{x}=\mathbf{c}})$ contains a path over $m - k - p(0 \leq k < m, \ p \geq 0)$ vertices and p isolated vertices labeled $m - p, \ m - p + 1, \ ..., \ m - 1$ such that $0 \leq k + p \leq m - 2(m \geq 2)$. Further, assume that there was no edges between deleted vertices (as defined before, the restricted variables in a GBF are considered as the vertices to be deleted in the graph of the Boolean function) and isolated vertices before the deletion. Let x_γ be one of the end vertices of the path in $G(f|_{\mathbf{x}=\mathbf{c}})$ and the weight of each edge in the path be $q/2$. Let $\mathbf{a}'_1, \mathbf{a}'_2, ..., \mathbf{a}'_{2^{m-p}}$ be binary vector representations of $0, 1, 2^{m-p} - 1$ of length $m - p$ and $\mathbf{r}_1, \mathbf{r}_2, ..., \mathbf{r}_{2^p}$ be binary vector representations of $0, 1, 2^p - 1$ of length p. Also let l be a positive integer such that $l = \Sigma_{i=0}^{k-1} d_i 2^j + d 2^k$. Then for any choice of $g', g_j \in \mathbb{Z}_q$, the codes $\psi(S_{\mathbf{bd}'})$ and $\psi(\tilde{S}_{\mathbf{bd}'})$ can be expressed as*

$$\psi(S_{\mathbf{bd}'}) = \left[\psi(F_{\mathbf{b}l}) \omega^{\left(\Gamma + \frac{q}{2} \mathbf{d}' \right) \cdot \mathbf{r}_{j'}} \right], \quad l = 0, 1, ..., 2^{k+1} - 1, j' = 1, 2, ..., 2^p,$$

$$\psi\left(\tilde{S}_{\mathbf{bd}'}\right) = \left[\psi(F'_{\mathbf{b}l}) \omega^{\left(\Gamma + \frac{q}{2} \mathbf{d}' \right) \cdot \bar{\mathbf{r}}_{j'}} \right], \quad l = 0, 1, ..., 2^{k+1} - 1, j' = 1, 2, ..., 2^p,$$

$$\tag{13}$$

where

$$\psi(F_{\mathbf{b}l}) = \left(\omega^{F_{\mathbf{b}l}\left(\mathbf{a}'_1\right)}, , \omega^{F_{\mathbf{b}l}\left(\mathbf{a}'_2\right)}, ..., , \omega^{F_{\mathbf{b}l}\left(\mathbf{a}'_{2^{m-p}}\right)} \right),$$

$$\psi(F_{\mathbf{b}l}') = \left(\omega^{F'_{\mathbf{b}l}\left(\mathbf{a}'_1\right)}, , \omega^{F'_{\mathbf{b}l}\left(\mathbf{a}'_2\right)}, ..., , \omega^{F'_{\mathbf{b}l}\left(\mathbf{a}'_{2^{m-p}}\right)} \right),$$

$$F_{\mathbf{b}l} = f' + \frac{q}{2}\left((\mathbf{d} + \mathbf{b}) \cdot \mathbf{x} + d x_\gamma \right),$$

$$\tag{14}$$

$$F'_{\mathbf{b}l} = \tilde{f}' + \frac{q}{2}\left((\mathbf{d} + \mathbf{b}) \cdot \bar{\mathbf{x}} + \bar{d} x_\gamma \right),$$

$$f' = Q + \sum_{i=0}^{m-p-1} g_i x_i + g'.$$

Proof 1 *Since there are no edges between the deleted and isolated vertices before the deletion of k vertices $x_{j_0}, x_{j_1}, ..., x_{j_{k-1}}$, the quadratic form Q presented in $G(f)$ can be expressed as*

$$Q = \frac{q}{2} \sum_{\alpha=0}^{m-k-p-1} x_{\pi(\alpha)} x_{\pi(\alpha+1)} + \sum_{0 \leq \mu < v \leq k-1} b'_{j_\mu, j_v} x_{j_\mu} x_{j_v} + \sum_{\alpha=0}^{m-k-p-1} \sum_{\sigma=0}^{k-1} c'_{\pi(\alpha)j_\sigma} x_{\pi(\alpha)} x_{j_\sigma},$$

$$\tag{15}$$

where π is a permutation over the set $\{0, \ 1, \ ..., m - 1\} \backslash \{j_0, j_1, \ ..., j_{k-1}\} \cup \{m - p, \ m - p + 1, \ ..., \ m - 1\}$, $b'_{j_\mu, j_v} \ (\in \mathbb{Z}_q)$ which denotes the weight between the vertices x_{j_μ} and x_{j_v} and $c'_{\pi(\alpha), j_\sigma} \ (\in \mathbb{Z}_q)$ denotes the weight between the vertices $x_{\pi(\alpha)}$ and $x_{j\sigma}$. Therefore, f' is a GBF of $m - p$ variables $x_0, x_1, ..., x_{m-p-1}$, and the GBF f of m variables can be expressed as.

$$f = f' + \sum_{i=m-p}^{m-1} g_i x_i \tag{16}$$

or

$$f = f' + \Gamma \cdot \mathbf{x}'. \tag{17}$$

Now we define a GBF $F_l^{\mathbf{b}}$ over m variables by

$$
\begin{aligned}
F_l^{\mathbf{b}} &= f + \frac{q}{2} \left((\mathbf{d} + \mathbf{b}) \cdot \mathbf{x} + \mathbf{d}' \cdot \mathbf{x}' + d x_\gamma \right) \\
&= F_{\mathbf{b}l} + \left(\Gamma + \frac{q}{2} \mathbf{d}' \right) \cdot \mathbf{x}'.
\end{aligned}
\tag{18}
$$

Let $\mathbf{a}_1, \mathbf{a}_2, ..., \mathbf{a}_{2^m}$ be binary vector representations of $0, 1, 2^m - 1$ of length m, given in **Table 1**. The truth table given in Table 1 can also be expressed as the truth table given in **Table 2**. **Table 3** contains a truth table over $m - p$ variables.

From **Tables 1–3**, it is observed that the code $\psi(S_{\mathbf{bd}'})$ can be expressed as

$$
\psi(S_{\mathbf{bd}'}) = \left[\omega^{F_l^{\mathbf{b}}(\mathbf{a}_j)} \right], \quad l = 0, 1, \ 2^{k+1} - 1, j = 1, 2, ..., 2^m
\tag{19}
$$

$\mathbf{a}_1$
$\mathbf{a}_2$
$\vdots$
$\mathbf{a}_{2^m}$

Table 1.
Truth table over m variables.

$\mathbf{a}_1'\mathbf{r}_1$
$\mathbf{a}_{2'}\mathbf{r}_1$
$\vdots$
$\mathbf{a}_{2^{m-p}}'\mathbf{r}_1$
$\mathbf{a}_1'\mathbf{r}_2$
$\mathbf{a}_{2'}\mathbf{r}_2$
$\vdots$
$\mathbf{a}_{2^{m-p}}'\mathbf{r}_2$
$\vdots$
$\mathbf{a}_1'\mathbf{r}_{2p}$
$\mathbf{a}_2'\mathbf{r}_{2p}$
$\vdots$
$\mathbf{a}_{2^{m-p}}'\mathbf{r}_{2p}$

Table 2.
Truth table over m variables.

$\mathbf{a}_1'$
$\mathbf{a}_2'$
$\vdots$
$\mathbf{a}_{2^{m-p}}'$

Table 3.
Truth table over $m - p$ variables.

or

$$\psi(S_{\mathbf{bd'}}) = \left[\psi(F_{\mathbf{b}l})\omega^{\left(\Gamma + \frac{q}{2}\mathbf{d'}\right)\cdot\mathbf{r}_{j'}} \right], \quad l = 0, 1, ..., 2^{k+1} - 1, j' = 1, 2, ..., 2^p, \qquad (20)$$

where

$$\psi(F_{\mathbf{b}l}) = \left(\omega^{F_{\mathbf{b}l}(\mathbf{a}'_1)}, \omega^{F_{\mathbf{b}l}(\mathbf{a}'_2)}, ..., \omega^{F_{\mathbf{b}l}\left(\mathbf{a}'_{2^{m-0}}\right)} \right), \quad l = 0, 1, \ 2^{k+1} - 1. \qquad (21)$$

Similarly, we can show that

$$\psi\left(\tilde{S}_{\mathbf{bd'}}\right) = \left[\psi(F'_{\mathbf{b}l})\omega^{\left(\Gamma + \frac{q}{2}\mathbf{d'}\right)\cdot\overline{\mathbf{r}}_{j'}} \right], \qquad l = 0, 1, \ 2^{k+1} - 1, j' = 1, 2, ..., 2^p. \qquad (22)$$

Example 1 *Let f be a GBF of four variables over $\mathbb{Z}_4$, given by*

$$f(x_0, x_1, x_2, x_3) = 2x_1x_2 + 3x_0(x_1 + x_2) + x_0 + x_2 + x_3 + 1. \qquad (23)$$

*From the $G(f)$, given in **Figure 1**, it is clear that after the deletion of the vertex x_0, the resultant graph contains a path over the vertices x_1, x_2 and an isolated vertex x_3. For this example $k = 1$ and $p = 1$. Therefore, the vectors $\mathbf{b}$, $\mathbf{d}$, $\mathbf{d'}$, $\mathbf{x}$, Γ and $\mathbf{x'}$ are of length one and belong to $\mathbb{Z}_2$.*

Hence, $\mathbf{b} = (b_{j_0}) = (b_0) = b_0$, $\mathbf{d} = (d_0) = d_0$, $\mathbf{d'} = (d'_1) = d'_1$, $\mathbf{x} = (x_{j_0}) = (x_0) = x_0$, $\Gamma = (g_{m-p}) = (g_0) = 1$, and $\mathbf{x'} = (x_{m-p}) = (x_3) = x_3$. The set of Boolean functions $S_{b_0d'_1}$ and $\tilde{S}_{b_0d'_1}$ are given below:

$$S_{b_0d'_1} = \left\{ f + \frac{q}{2}\left(d_0x_0 + b_0x_0 + d'_1x_3 + dx_2\right) \ : \ d, \ d_0 \in \{0, 1\} \right\}, \qquad (24)$$

and

$$\tilde{s}_{b_0d'_1} = \left\{ \tilde{f} + \frac{q}{2}\left(d_0\overline{x}_0 + b_0\overline{x}_0 + d'_1\overline{x}_3 + \overline{d}x_2\right) : d, \ d_0 \in \{0, 1\} \right\}. \qquad (25)$$

The GBFs F_{b_0l} and F'_{b_0l} are given by

$$F_{b_0l} = 2x_1x_2 + 3x_0(x_1 + x_2) + x_0 + x_2 + 1 + \frac{q}{2}(d_0x_0 + b_0x_0 + dx_2) \qquad (26)$$
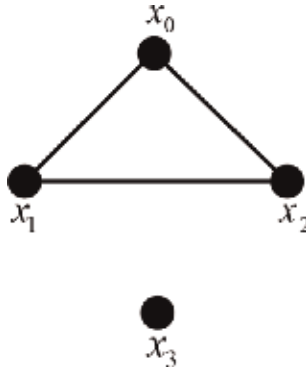

Figure 1.
The graph of the GBF $2x_1x_2 + 3x_0(x_1 + x_2) + x_0 + x_2 + x_3 + 1$.

and

$$F'_{b_0 l} = 2\overline{x}_1\overline{x}_2 + 3\overline{x}_0(\overline{x}_1 + \overline{x}_2) + \overline{x}_0 + \overline{x}_2 + 1 + \frac{q}{2}\left(d_0\overline{x}_0 + b_0\overline{x}_0 + \overline{d}x_2\right), \qquad (27)$$

where $l = 0, 1, 2, 3$.
The codes corresponding to the sets of Boolean functions are listed below:

$$1) \quad \psi(S_{00}) = \begin{bmatrix} \omega^1\omega^2\omega^1\omega^1\omega^2\omega^2\omega^0\omega^3\omega^2\omega^3\omega^2\omega^2\omega^3\omega^3\omega^1\omega^0 \\ \omega^1\omega^0\omega^1\omega^3\omega^2\omega^0\omega^0\omega^1\omega^2\omega^1\omega^2\omega^0\omega^3\omega^1\omega^1\omega^2 \\ \omega^1\omega^2\omega^1\omega^1\omega^0\omega^0\omega^2\omega^1\omega^2\omega^3\omega^2\omega^2\omega^1\omega^1\omega^3\omega^2 \\ \omega^1\omega^0\omega^1\omega^3\omega^0\omega^2\omega^2\omega^3\omega^2\omega^1\omega^2\omega^0\omega^1\omega^3\omega^3\omega^0 \end{bmatrix}$$
$$= \begin{bmatrix} \omega^0\psi(\mathbf{C}^0) & \omega^1\psi(\mathbf{C}^0) \end{bmatrix} \qquad (28)$$

where

$$\psi(\mathbf{C}^0) = \begin{bmatrix} \omega^1\omega^2\omega^1\omega^1\omega^2\omega^2\omega^0\omega^3 \\ \omega^1\omega^0\omega^1\omega^3\omega^2\omega^0\omega^0\omega^1 \\ \omega^1\omega^2\omega^1\omega^1\omega^0\omega^0\omega^2\omega^1 \\ \omega^1\omega^0\omega^1\omega^3\omega^0\omega^2\omega^2\omega^3 \end{bmatrix}.$$

$$2) \quad \psi(\tilde{S}_{00}) = \begin{bmatrix} \omega^0\omega^1\omega^3\omega^3\omega^0\omega^0\omega^1\omega^0\omega^3\omega^0\omega^2\omega^2\omega^3\omega^3\omega^0\omega^3 \\ \omega^2\omega^1\omega^1\omega^3\omega^2\omega^0\omega^3\omega^0\omega^1\omega^0\omega^0\omega^2\omega^1\omega^3\omega^2\omega^3 \\ \omega^0\omega^1\omega^3\omega^3\omega^2\omega^2\omega^3\omega^2\omega^3\omega^0\omega^2\omega^2\omega^1\omega^1\omega^2\omega^1 \\ \omega^2\omega^1\omega^1\omega^3\omega^0\omega^2\omega^1\omega^2\omega^1\omega^0\omega^0\omega^2\omega^3\omega^1\omega^0\omega^1 \end{bmatrix}$$
$$= \begin{bmatrix} \omega^1\psi(\tilde{\mathbf{C}}^0) & \omega^0\psi(\tilde{\mathbf{C}}^0) \end{bmatrix} \qquad (29)$$

where

$$\psi(\tilde{\mathbf{C}}^0) = \begin{bmatrix} \omega^3\omega^0\omega^2\omega^2\omega^3\omega^3\omega^0\omega^3 \\ \omega^1\omega^0\omega^0\omega^2\omega^1\omega^3\omega^2\omega^3 \\ \omega^3\omega^0\omega^2\omega^2\omega^1\omega^1\omega^2\omega^1 \\ \omega^1\omega^0\omega^0\omega^2\omega^3\omega^1\omega^0\omega^1 \end{bmatrix}.$$

$$3) \quad \psi(S_{01}) = \begin{bmatrix} \omega^1\omega^2\omega^1\omega^1\omega^2\omega^2\omega^0\omega^3\omega^0\omega^1\omega^0\omega^0\omega^1\omega^1\omega^3\omega^2 \\ \omega^1\omega^0\omega^1\omega^3\omega^2\omega^0\omega^0\omega^1\omega^0\omega^3\omega^0\omega^2\omega^1\omega^3\omega^3\omega^0 \\ \omega^1\omega^2\omega^1\omega^1\omega^0\omega^0\omega^2\omega^1\omega^0\omega^1\omega^0\omega^0\omega^3\omega^3\omega^1\omega^0 \\ \omega^1\omega^0\omega^1\omega^3\omega^0\omega^2\omega^2\omega^3\omega^0\omega^0\omega^3\omega^0\omega^2\omega^3\omega^1\omega^1\omega^2 \end{bmatrix}.$$
$$= \begin{bmatrix} \omega^0\psi(\mathbf{C}^0) & \omega^3\psi(\mathbf{C}^0) \end{bmatrix} \qquad (30)$$

$$4) \quad \psi(\tilde{S}_{01}) = \begin{bmatrix} \omega^2\omega^3\omega^1\omega^1\omega^2\omega^2\omega^3\omega^2\omega^3\omega^0\omega^2\omega^2\omega^3\omega^3\omega^0\omega^3 \\ \omega^0\omega^3\omega^3\omega^1\omega^0\omega^2\omega^1\omega^2\omega^1\omega^0\omega^0\omega^2\omega^1\omega^3\omega^2\omega^3 \\ \omega^2\omega^3\omega^1\omega^1\omega^0\omega^0\omega^1\omega^0\omega^3\omega^0\omega^2\omega^2\omega^1\omega^1\omega^2\omega^1 \\ \omega^0\omega^3\omega^3\omega^1\omega^2\omega^0\omega^3\omega^0\omega^1\omega^0\omega^0\omega^2\omega^3\omega^1\omega^0\omega^1 \end{bmatrix}.$$
$$= \begin{bmatrix} \omega^3\psi(\tilde{\mathbf{C}}^0) & \omega^0\psi(\tilde{\mathbf{C}}^0) \end{bmatrix} \qquad (31)$$

5) $\quad \psi(S_{10}) = \begin{bmatrix} \omega^1\omega^0\omega^1\omega^3\omega^2\omega^0\omega^0\omega^1\omega^2\omega^1\omega^2\omega^0\omega^3\omega^1\omega^1\omega^2 \\ \omega^1\omega^2\omega^1\omega^1\omega^2\omega^2\omega^0\omega^3\omega^2\omega^3\omega^2\omega^2\omega^3\omega^3\omega^1\omega^0 \\ \omega^1\omega^0\omega^1\omega^3\omega^0\omega^2\omega^2\omega^3\omega^2\omega^1\omega^2\omega^0\omega^1\omega^3\omega^3\omega^0 \\ \omega^1\omega^2\omega^1\omega^1\omega^0\omega^0\omega^2\omega^1\omega^2\omega^3\omega^2\omega^2\omega^1\omega^1\omega^3\omega^2 \end{bmatrix}$

$$= \begin{bmatrix} \omega^0\psi(\mathbf{C}^1) & \omega^1\psi(\mathbf{C}^1) \end{bmatrix}$$

(32)

where

$$\psi(\mathbf{C}^1) = \begin{bmatrix} \omega^1\omega^0\omega^1\omega^3\omega^2\omega^0\omega^0\omega^1 \\ \omega^1\omega^2\omega^1\omega^1\omega^2\omega^2\omega^0\omega^3 \\ \omega^1\omega^0\omega^1\omega^3\omega^0\omega^2\omega^2\omega^3 \\ \omega^1\omega^2\omega^1\omega^1\omega^0\omega^0\omega^2\omega^1 \end{bmatrix}.$$

6) $\quad \psi(\tilde{S}_{10}) = \begin{bmatrix} \omega^2\omega^1\omega^1\omega^3\omega^2\omega^0\omega^3\omega^0\omega^1\omega^0\omega^0\omega^2\omega^1\omega^3\omega^2\omega^3 \\ \omega^0\omega^1\omega^3\omega^3\omega^0\omega^0\omega^1\omega^0\omega^3\omega^0\omega^2\omega^2\omega^3\omega^3\omega^0\omega^3 \\ \omega^2\omega^1\omega^1\omega^3\omega^0\omega^2\omega^1\omega^2\omega^1\omega^0\omega^0\omega^2\omega^3\omega^1\omega^0\omega^1 \\ \omega^0\omega^1\omega^3\omega^3\omega^2\omega^2\omega^3\omega^2\omega^3\omega^0\omega^2\omega^2\omega^1\omega^1\omega^2\omega^1 \end{bmatrix}$

$$= \begin{bmatrix} \omega^1\psi(\tilde{\mathbf{C}}^1) & \omega^0\psi(\tilde{\mathbf{C}}^1) \end{bmatrix}$$

(33)

where

$$\psi(\tilde{\mathbf{C}}^1) = \begin{bmatrix} \omega^1\omega^0\omega^0\omega^2\omega^1\omega^3\omega^2\omega^3 \\ \omega^3\omega^0\omega^2\omega^2\omega^3\omega^3\omega^0\omega^3 \\ \omega^1\omega^0\omega^0\omega^2\omega^3\omega^1\omega^0\omega^1 \\ \omega^3\omega^0\omega^2\omega^2\omega^1\omega^1\omega^2\omega^1 \end{bmatrix}.$$

7) $\quad \psi(S_{11}) = \begin{bmatrix} \omega^1\omega^0\omega^1\omega^3\omega^2\omega^0\omega^0\omega^1\omega^0\omega^3\omega^0\omega^2\omega^1\omega^3\omega^3\omega^0 \\ \omega^1\omega^2\omega^1\omega^1\omega^2\omega^2\omega^0\omega^3\omega^0\omega^1\omega^0\omega^0\omega^1\omega^1\omega^3\omega^2 \\ \omega^1\omega^0\omega^1\omega^3\omega^0\omega^2\omega^2\omega^3\omega^0\omega^3\omega^0\omega^2\omega^3\omega^1\omega^1\omega^2 \\ \omega^1\omega^2\omega^1\omega^1\omega^0\omega^0\omega^2\omega^1\omega^0\omega^1\omega^0\omega^0\omega^3\omega^3\omega^1\omega^0 \end{bmatrix}.$$

$$= \begin{bmatrix} \omega^0\psi(\mathbf{C}^1) & \omega^3\psi(\mathbf{C}^1) \end{bmatrix}$$

(34)

8) $\quad \psi(\tilde{S}_{11}) = \begin{bmatrix} \omega^0\omega^3\omega^3\omega^1\omega^0\omega^2\omega^1\omega^2\omega^1\omega^0\omega^0\omega^2\omega^1\omega^3\omega^2\omega^3 \\ \omega^2\omega^3\omega^1\omega^1\omega^2\omega^2\omega^3\omega^2\omega^3\omega^0\omega^2\omega^2\omega^3\omega^3\omega^0\omega^3 \\ \omega^0\omega^3\omega^3\omega^1\omega^2\omega^0\omega^3\omega^0\omega^1\omega^0\omega^0\omega^2\omega^3\omega^1\omega^0\omega^1 \\ \omega^2\omega^3\omega^1\omega^1\omega^0\omega^0\omega^1\omega^0\omega^3\omega^0\omega^2\omega^2\omega^1\omega^1\omega^2\omega^1 \end{bmatrix}.$$

$$= \begin{bmatrix} \omega^3\psi(\tilde{\mathbf{C}}^1) & \omega^0\psi(\tilde{\mathbf{C}}^1) \end{bmatrix}$$

(35)

Theorem 1 *Let f be a GBF over m variables as defined in Lemma 1 and Lemma 2. Suppose $I^0, I^1, ..., I^{2^{k+1}-1}$ are a list of $2^k + 1$ code groups defined by*

$$I^t = \left\{I^t_\mathbf{s} : 0 \leq s < 2^p\right\} = \left\{\psi(S_{\mathbf{bd'}}) : \mathbf{d'} \in \{0, 1\}^p\right\} \tag{36}$$

and

$$I^{2^k+t} = \left\{I^{2^k+t}_\mathbf{s} : 0 \leq s < 2^p\right\} = \left\{\psi^*\left(\tilde{S}_{\mathbf{bd'}}\right) : \mathbf{d'} \in \{0, 1\}^p\right\}, \tag{37}$$

which forms an IGC code set $I\left(2^{k+p+1}, 2^{k+1}, 2^m, 2^{m-p}\right)$.

Proof 2 *Let $\psi\left(S_{\mathbf{bd'_1}}\right)$ and $\psi\left(S_{\mathbf{bd'_2}}\right)$ be any two codes from a code group I^t. Then the ACCF of $\psi\left(S_{\mathbf{bd'_1}}\right)$ and $\psi\left(S_{\mathbf{bd'_2}}\right)$ at the time shift $\eta 2^{m-p} + \tau$ (where $0 \leq \eta < 2^p$, $\eta \in \mathbb{Z}$, $0 \leq \tau < 2^{m-p}$, $\tau \in \mathbb{Z}$) is*

$$
\begin{aligned}
&C\left(\psi\left(S_{\mathbf{bd'_1}}\right), \psi\left(S_{\mathbf{bd'_2}}\right)\right)(\eta 2^{m-p} + \tau) \\
&= \sum_{l=0}^{2^{k+1}-1} C(\psi(F_{\mathbf{b}l}), \psi(F_{\mathbf{b}l})(\tau) \sum_{i=1}^{2^p-\eta} \omega^{\left(\Gamma+\frac{q}{2}\mathbf{d'_1}\right)\cdot\mathbf{r}_{i+\eta} - \left(\Gamma+\frac{q}{2}\mathbf{d'_2}\right)\cdot\mathbf{r}_i} \\
&\quad + \sum_{l=0}^{2^{k+1}-1} C(\psi(F_{\mathbf{b}l}), \psi(F_{\mathbf{b}l})(\tau - 2^{m-p}) \sum_{i=1}^{2^p-\eta-1} \omega^{\left(\Gamma+\frac{q}{2}\mathbf{d'_1}\right)\cdot\mathbf{r}_{i+\eta+1} - \left(\Gamma+\frac{q}{2}\mathbf{d'_2}\right)\cdot\mathbf{r}_i} \\
&= C(\psi(\mathbf{C}^t), \psi(\mathbf{C}^t))(\tau) \sum_{i=1}^{2^p-\eta} \omega^{\left(\Gamma+\frac{q}{2}\mathbf{d'_1}\right)\cdot\mathbf{r}_{i+\eta} - \left(\Gamma+\frac{q}{2}\mathbf{d'_2}\right)\cdot\mathbf{r}_i} \\
&\quad + C(\psi(\mathbf{C}^t), \psi(\mathbf{C}^t))(\tau - 2^{m-p}) \sum_{i=1}^{2^p-\eta-1} \omega^{\left(\Gamma+\frac{q}{2}\mathbf{d'_1}\right)\cdot\mathbf{r}_{i+\eta+1} - \left(\Gamma+\frac{q}{2}\mathbf{d'_2}\right)\cdot\mathbf{r}_i} \\
&= A(\psi(\mathbf{C}^t))(\tau) \sum_{i=1}^{2^p-\eta} \omega^{\left(\Gamma+\frac{q}{2}\mathbf{d'_1}\right)\cdot\mathbf{r}_{i+\eta} - \left(\Gamma+\frac{q}{2}\mathbf{d'_2}\right)\cdot\mathbf{r}_i} \\
&\quad + A(\psi(\mathbf{C}^t))(\tau - 2^{m-p}) \sum_{i=1}^{2^p-\eta-1} \omega^{\left(\Gamma+\frac{q}{2}\mathbf{d'_1}\right)\cdot\mathbf{r}_{i+\eta+1} - \left(\Gamma+\frac{q}{2}\mathbf{d'_2}\right)\cdot\mathbf{r}_i}.
\end{aligned} \tag{38}
$$

For $\mathbf{d'_1} = \mathbf{d'_2} = \mathbf{d'}$, the ACCF given in Eq. (38) *reduced to AACF as follows:*

$$
A(\psi(S_{\mathbf{bd'}}))(\eta 2^{m-p} + \tau) = \begin{cases} 2^{m+k-p+1} \\ \times \Sigma_{i=1}^{2^p-\eta} \omega^{\left(\Gamma+\frac{q}{2}\mathbf{d'_1}\right)\cdot\mathbf{r}_{i+\eta} - \left(\Gamma+\frac{q}{2}\mathbf{d'_2}\right)\cdot\mathbf{r}_i}, & \tau = 0, 0 \leq \eta < 2^p, \\ 0, & 0 < |\tau| < 2^{m-p}, \\ & 0 \leq \eta < 2^p. \end{cases} \tag{39}
$$

For $\mathbf{d'_1} \neq \mathbf{d'_2}$, the ACCF given in Eq. (38) *can be expressed as*

$$
C\left(\psi\left(S_{\mathbf{bd'_1}}\right), \psi\left(S_{\mathbf{bd'_2}}\right)\right)(\eta 2^{m-p} + \tau) = \begin{cases} 2^{m+k-p+1} \\ \times \Sigma_{i=1}^{2^p-\eta} \omega^{\left(\Gamma+\frac{q}{2}\mathbf{d'_1}\right)\cdot\mathbf{r}_{i+\eta} - \left(\Gamma+\frac{q}{2}\mathbf{d'_2}\right)\mathbf{r}_i}, & \tau = 0, 0 < \eta < 2^p, \\ 0, & \tau = 0, \eta = 0, \\ 0, & 0 < |\tau| < 2^{m-p}, \\ & 0 \leq \eta < 2^p. \end{cases} \tag{40}
$$

The terms in Eqs. (39) and (40) *are derived from the autocorrelation properties of the $CC\psi(\mathbf{C}^t)$. It is also observed that the codes from the same code group I^t have ideal auto- and cross-correlation properties inside the ZCZ width 2^{m-p}. Similarly, we can show that*

$$
A\left(\psi^*\left(\tilde{S}_{\mathbf{bd}'}\right)\right)(\eta 2^{m-p}+\tau)=\begin{cases}2^{m+k-p+1}\\\times\Sigma_{i=1}^{2^p-\eta}\omega^{\left(\Gamma+\frac{q}{2}\mathbf{d}_2'\right)\cdot\bar{\mathbf{r}}_i-\left(\Gamma+\frac{q}{2}\mathbf{d}_1'\right)\cdot\bar{\mathbf{r}}_{i+\eta}},&\tau=0,\ 0\le\eta<2^p,\\0,&0<|\tau|<2^{m-p},\\&0\le\eta<2^p,\end{cases}\tag{41}
$$

and for $\mathbf{d}_1'\ne\mathbf{d}_2'$,

$$
C\left(\psi^*\left(\tilde{S}_{\mathbf{bd}_1'}\right),\psi^*\left(\tilde{S}_{\mathbf{bd}_2'}\right)\right)(\eta 2^{m-p}+\tau)=\begin{cases}2^{m+k-p+1}\\\times\Sigma_{i=1}^{2^p-\eta}\omega^{\left(\Gamma+\frac{q}{2}\mathbf{d}_2'\right)\cdot\bar{\mathbf{r}}_i-\left(\Gamma+\frac{q}{2}\mathbf{d}_1'\right)\cdot\bar{\mathbf{r}}_{i+\eta}},&\tau=0,\ 0<\eta<2^p,\\0,&\tau=0,\ \eta=0,\\0,&0<|\tau|<2^{m-p},\\&0\le\eta<2^p.\end{cases}
$$
$$\tag{42}$$

From Eqs. (41) and (42), *we get that the codes from the same code group I^{2^k+t} have ideal auto- and cross-correlation properties inside the ZCZ width 2^{m-p}.*

Now we show that the ACCFs between any two codes of any two different code groups I^{t_1} and I^{t_2} $\left(0\le t_1,t_2<2^k\right)$ are zeros everywhere. Let $\psi\left(S_{\mathbf{b}_1\mathbf{d}_1'}\right)\in I^{t_1}$, $\psi\left(S_{\mathbf{b}_2\mathbf{d}_2'}\right)\in I^{t_2}$ where $\mathbf{b}_1$, $\mathbf{b}_2$ are binary vector representations of t_1,t_2, and $\mathbf{d}_1'$, $\mathbf{d}_2'$ are any two binary vectors in $\mathbb{Z}_2^p$. Then

$$
\begin{aligned}
&C\left(\psi\left(S_{\mathbf{b}_1\mathbf{d}_1'}\right),\psi\left(S_{\mathbf{b}_2\mathbf{d}_2'}\right)\right)(\eta 2^{m-p}+\tau)\\
&=\sum_{l=0}^{2^{k+1}-1}C(\psi(F_{\mathbf{b}_1l}),\psi(F_{\mathbf{b}_2l})(\tau)\sum_{i=1}^{2^p-\eta}\omega^{\left(\Gamma+\frac{q}{2}\mathbf{d}_1'\right)\cdot\mathbf{r}_{i+\eta}-\left(\Gamma+\frac{q}{2}\mathbf{d}_2'\right)\cdot\mathbf{r}_i}\\
&\quad+\sum_{l=0}^{2^{k+1}-1}C(\psi(F_{\mathbf{b}_1l}),\psi(F_{\mathbf{b}_2l})(\tau-2^{m-p})\sum_{i=1}^{2^p-\eta-1}\omega^{\left(\Gamma+\frac{q}{2}\mathbf{d}_1'\right)\cdot\mathbf{r}_{i+\eta+1}-\left(\Gamma+\frac{q}{2}\mathbf{d}_2'\right)\cdot\mathbf{r}_i}\\
&=C(\psi(\mathbf{C}^t),\psi(\mathbf{C}^t))(\tau)\sum_{i=1}^{2^p-\eta}\omega^{\left(\Gamma+\frac{q}{2}\mathbf{d}_1'\right)\cdot\mathbf{r}_{i+\eta}-\left(\Gamma+\frac{q}{2}\mathbf{d}_2'\right)\cdot\mathbf{r}_i}\\
&\quad+C(\psi(\mathbf{C}^t),\psi(\mathbf{C}^t))(\tau-2^{m-p})\sum_{i=1}^{2^p-\eta-1}\omega^{\left(\Gamma+\frac{q}{2}\mathbf{d}_1'\right)\cdot\mathbf{r}_{i+\eta+1}-\left(\Gamma+\frac{q}{2}\mathbf{d}_2'\right)\cdot\mathbf{r}_i}\\
&=0\quad\forall\tau,\eta.
\end{aligned}\tag{43}
$$

Similarly, we can also show that the ACCFs between any two codes of any two different code groups $I^{2^k+t_1}$ and $I^{2^k+t_2}$ $\left(0\le t_1,t_2<2^k\right)$ are zeros everywhere, i.e.,

$$
\begin{aligned}
&C\left(\psi*\left(\tilde{S}_{\mathbf{b}_1\mathbf{d}_1'}\right),\psi*\left(\tilde{S}_{\mathbf{b}_2\mathbf{d}_2'}\right)\right)(\eta 2^{m-p}+\tau)\\
&=\sum_{l=0}^{2^{k+1}-1}C(\psi*\left(F_{\mathbf{b}_1l}'\right),\psi*\left(F_{\mathbf{b}_2l}'\right)(\tau)\sum_{i=1}^{2^p-\eta}\omega^{\left(\Gamma+\frac{q}{2}\mathbf{d}_2'\right)\cdot\mathbf{r}_i-\left(\Gamma+\frac{q}{2}\mathbf{d}_1'\right)\cdot\mathbf{r}_{i+\eta}}\\
&\quad+\sum_{l=0}^{2^{k+1}-1}C(\psi*\left(F_{\mathbf{b}_1l}'\right),\psi*\left(F_{\mathbf{b}_2l}'\right)(\tau-2^{m-p})\sum_{i=1}^{2^p-\eta-1}\omega^{\left(\Gamma+\frac{q}{2}\mathbf{d}_2'\right)\cdot\mathbf{r}_i-\left(\Gamma+\frac{q}{2}\mathbf{d}_1'\right)\cdot\mathbf{r}_{i+\eta+1}}\\
&=C\left(\psi*\left(\tilde{\mathbf{C}}^{t_1}\right),\psi*\left(\tilde{\mathbf{C}}^{t_2}\right)\right)(\tau-2^{m-p})\sum_{i=1}^{2^p-\eta-1}\omega^{\left(\Gamma+\frac{q}{2}\mathbf{d}_2'\right)\cdot\mathbf{r}_i-\left(\Gamma+\frac{q}{2}\mathbf{d}_1'\right)\cdot\mathbf{r}_{i+\eta}}\\
&\quad+C\left(\psi*\left(\tilde{\mathbf{C}}^{t_1}\right),\psi*\left(\tilde{\mathbf{C}}^{t_2}\right)\right)(\tau-2^{m-p})\sum_{i=1}^{2^p-\eta-1}\omega^{\left(\Gamma+\frac{q}{2}\mathbf{d}_2'\right)\cdot\mathbf{r}_i-\left(\Gamma+\frac{q}{2}\mathbf{d}_1'\right)\cdot\mathbf{r}_{i+\eta+1}}\\
&=0\quad\forall\tau,\eta.
\end{aligned}\tag{44}
$$

The results in Eqs. (43) *and* (44) *are obtained by using the ideal cross-correlation properties of CCCs. To complete the proof, now we only need to show that the ACCFs of any code from* I^{t_u} *and* $I^{2^k+t_v}\left(u,\ v\in Z,\ 1\le u,\ v\le 2^k\right)$ *are zeros everywhere. In this case,* t_u *and* t_v *are any two integers in* $\left[0,2^k\right)$ *and may or may not be equal. Let* $\psi(S_{b_u d_{1'}}\in I^{t_u},\ \psi^*\left(\tilde{S}_{b_v d_{2'}}\right)\in I^{2^k+t_v}$ *where* $b_u,\ b_v$ *are binary vector representations of* $t_u, t_v,$ *respectively. Then*

$$
\begin{aligned}
&C\left(\psi\left(S_{\mathbf{b}_u \mathbf{d}_1'}\right), \psi*\left(\tilde{S}_{\mathbf{b}_v \mathbf{d}_2'}\right)\right)(\eta 2^{m-p}+\tau) \\
&= \sum_{l=0}^{2^{k+1}-1} C(\psi*\left(F_{\mathbf{b}_u l}'\right), \psi*\left(F_{\mathbf{b}_v l}'\right))(\tau)\sum_{i=1}^{2^p-\eta}\omega^{\left(\Gamma+\frac{q}{2}\mathbf{d}_1'\right)\cdot\mathbf{r}_{i+\eta}-\left(\Gamma+\frac{q}{2}\mathbf{d}_2'\right)\cdot\mathbf{r}_i} \\
&\quad + \sum_{l=0}^{2^{k+1}-1} C(\psi*\left(F_{\mathbf{b}_u l}'\right), \psi*(F_{\mathbf{b} v l}))(\tau)\sum_{i=1}^{2^p-\eta}\omega^{\left(\Gamma+\frac{q}{2}\mathbf{d}_1'\right)\cdot\mathbf{r}_{i+\eta}-\left(\Gamma+\frac{q}{2}\mathbf{d}_2'\right)\cdot\mathbf{r}_i} \\
&= C(\psi*(\mathbf{C}^{t_u}), \psi*(\mathbf{C}^{t_v}))(\tau-2^{m-p})\sum_{i=1}^{2^p-\eta-1}\omega^{\left(\Gamma+\frac{q}{2}\mathbf{d}_1'\right)\cdot\mathbf{r}_{i+\eta}-\left(\Gamma+\frac{q}{2}\mathbf{d}_2'\right)\cdot\mathbf{r}_i} \\
&\quad + C\left(\psi*(\mathbf{C}^{t_u}), \psi*\left(\tilde{\mathbf{C}}^{t_v}\right)\right)(\tau-2^{m-p})\sum_{i=1}^{2^p-\eta-1}\omega^{\left(\Gamma+\frac{q}{2}\mathbf{d}_1'\right)\cdot\mathbf{r}_{i+\eta+1}-\left(\Gamma+\frac{q}{2}\mathbf{d}_2'\right)\cdot\mathbf{r}_i} \\
&= 0 \quad \forall\tau, \eta.
\end{aligned}
\tag{45}
$$

The above result is also obtained by using the ideal cross-correlation properties of CCCs. From Eqs. (39)-(45), *we observed that the AACFs and ACCFs of the codes of the same group are zeros inside the ZCZ width* 2^{m-p} *and the ACCFs of the codes from different code groups are zeros everywhere. Hence, we can conclude that* $I^0, I^1, ..., I^{2^{k+1}-1}$ *form an IGC code set* $I\left(2^{k+p+1}, 2^{k+1}, 2^m, 2^{m-p}\right).$

***Example** 2 Let f be a GBF of* four *variables as given in Example* 1. *Then the obtained IGC code set* $I(8, 4, 16, 8)$ *corresponding to the* GBF *f is given below:*

Code group 1:

$$I_0^0 = \psi(S_{00})$$

$$
= \begin{bmatrix}
\omega^1\omega^2\omega^1\omega^1\omega^2\omega^2\omega^0\omega^3\omega^2\omega^3\omega^2\omega^2\omega^3\omega^3\omega^1\omega^0 \\
\omega^1\omega^0\omega^1\omega^3\omega^2\omega^0\omega^0\omega^1\omega^2\omega^1\omega^2\omega^0\omega^3\omega^1\omega^1\omega^2 \\
\omega^1\omega^2\omega^1\omega^1\omega^0\omega^0\omega^2\omega^1\omega^2\omega^3\omega^2\omega^2\omega^1\omega^1\omega^3\omega^2 \\
\omega^1\omega^0\omega^1\omega^3\omega^0\omega^2\omega^2\omega^3\omega^2\omega^1\omega^2\omega^0\omega^1\omega^3\omega^3\omega^0
\end{bmatrix}
$$

$$I_1^0 = \psi(S_{01})$$

$$
= \begin{bmatrix}
\omega^1\omega^2\omega^1\omega^1\omega^2\omega^2\omega^0\omega^3\omega^0\omega^1\omega^0\omega^0\omega^1\omega^1\omega^3\omega^2 \\
\omega^1\omega^0\omega^1\omega^3\omega^2\omega^0\omega^0\omega^1\omega^0\omega^3\omega^0\omega^2\omega^1\omega^3\omega^3\omega^0 \\
\omega^1\omega^2\omega^1\omega^1\omega^0\omega^0\omega^2\omega^1\omega^0\omega^1\omega^0\omega^0\omega^3\omega^3\omega^1\omega^0 \\
\omega^1\omega^0\omega^1\omega^3\omega^0\omega^2\omega^2\omega^3\omega^0\omega^3\omega^0\omega^2\omega^3\omega^1\omega^1\omega^2
\end{bmatrix}.
$$

$$\tag{46}$$

Code group 2:

$$I_0^1 = \psi(S_{10})$$

$$= \begin{bmatrix} \omega^1\omega^0\omega^1\omega^3\omega^2\omega^0\omega^0\omega^1\omega^2\omega^1\omega^2\omega^0\omega^3\omega^1\omega^1\omega^2 \\ \omega^1\omega^2\omega^1\omega^1\omega^2\omega^2\omega^0\omega^0\omega^3\omega^2\omega^3\omega^2\omega^2\omega^3\omega^3\omega^1\omega^0 \\ \omega^1\omega^0\omega^1\omega^3\omega^0\omega^2\omega^2\omega^3\omega^2\omega^1\omega^2\omega^0\omega^1\omega^3\omega^3\omega^0 \\ \omega^1\omega^2\omega^1\omega^1\omega^0\omega^0\omega^2\omega^1\omega^2\omega^3\omega^2\omega^2\omega^1\omega^1\omega^3\omega^2 \end{bmatrix}$$

$$I_1^1 = \psi(S_{11})$$

$$= \begin{bmatrix} \omega^1\omega^0\omega^1\omega^3\omega^2\omega^0\omega^0\omega^1\omega^0\omega^3\omega^0\omega^2\omega^1\omega^3\omega^3\omega^0 \\ \omega^1\omega^2\omega^1\omega^1\omega^2\omega^2\omega^0\omega^3\omega^0\omega^1\omega^0\omega^0\omega^1\omega^1\omega^3\omega^2 \\ \omega^1\omega^0\omega^1\omega^3\omega^0\omega^2\omega^2\omega^3\omega^0\omega^3\omega^0\omega^2\omega^3\omega^1\omega^1\omega^2 \\ \omega^1\omega^2\omega^1\omega^1\omega^0\omega^0\omega^2\omega^1\omega^0\omega^1\omega^0\omega^0\omega^3\omega^3\omega^1\omega^0 \end{bmatrix}.$$

(47)

Code group 3:

$$I_0^2 = \psi^*\left(\tilde{S}_{00}\right)$$

$$= \begin{bmatrix} \omega^0\omega^3\omega^1\omega^1\omega^0\omega^0\omega^3\omega^0\omega^1\omega^0\omega^2\omega^2\omega^1\omega^1\omega^0\omega^1 \\ \omega^2\omega^3\omega^3\omega^1\omega^2\omega^0\omega^1\omega^0\omega^3\omega^0\omega^0\omega^2\omega^3\omega^1\omega^2\omega^1 \\ \omega^0\omega^3\omega^1\omega^1\omega^2\omega^2\omega^1\omega^2\omega^1\omega^0\omega^2\omega^2\omega^3\omega^3\omega^2\omega^3 \\ \omega^2\omega^3\omega^3\omega^1\omega^0\omega^0\omega^2\omega^3\omega^2\omega^3\omega^0\omega^0\omega^2\omega^1\omega^3\omega^0\omega^0\omega^3 \end{bmatrix}$$

$$I_1^2 = \psi^*\left(\tilde{S}_{01}\right)$$

$$= \begin{bmatrix} \omega^2\omega^1\omega^3\omega^3\omega^2\omega^2\omega^1\omega^2\omega^1\omega^0\omega^2\omega^2\omega^1\omega^1\omega^0\omega^1 \\ \omega^0\omega^1\omega^1\omega^3\omega^0\omega^2\omega^3\omega^2\omega^3\omega^0\omega^0\omega^2\omega^3\omega^1\omega^2\omega^1 \\ \omega^2\omega^1\omega^3\omega^3\omega^0\omega^0\omega^0\omega^3\omega^0\omega^1\omega^0\omega^2\omega^2\omega^3\omega^3\omega^2\omega^3 \\ \omega^0\omega^1\omega^1\omega^3\omega^2\omega^0\omega^1\omega^0\omega^3\omega^0\omega^0\omega^2\omega^1\omega^3\omega^0\omega^3 \end{bmatrix}.$$

(48)

Code group 4:

$$I_0^3 = \psi^*\left(\tilde{S}_{10}\right)$$

$$= \begin{bmatrix} \omega^2\omega^3\omega^3\omega^1\omega^2\omega^0\omega^1\omega^0\omega^3\omega^0\omega^0\omega^2\omega^3\omega^1\omega^2\omega^1 \\ \omega^0\omega^3\omega^1\omega^1\omega^0\omega^0\omega^3\omega^0\omega^1\omega^0\omega^2\omega^2\omega^1\omega^1\omega^0\omega^1 \\ \omega^2\omega^3\omega^3\omega^1\omega^0\omega^2\omega^3\omega^2\omega^3\omega^0\omega^0\omega^2\omega^1\omega^3\omega^0\omega^3 \\ \omega^0\omega^3\omega^1\omega^1\omega^2\omega^2\omega^1\omega^2\omega^1\omega^0\omega^2\omega^2\omega^3\omega^3\omega^2\omega^3 \end{bmatrix}$$

$$I_1^3 = \psi^*\left(\tilde{S}_{11}\right)$$

$$= \begin{bmatrix} \omega^0\omega^1\omega^1\omega^3\omega^0\omega^2\omega^3\omega^2\omega^3\omega^0\omega^0\omega^2\omega^3\omega^1\omega^2\omega^1 \\ \omega^2\omega^1\omega^3\omega^3\omega^2\omega^2\omega^1\omega^2\omega^1\omega^0\omega^2\omega^2\omega^1\omega^1\omega^0\omega^1 \\ \omega^0\omega^1\omega^1\omega^3\omega^2\omega^0\omega^1\omega^0\omega^3\omega^0\omega^0\omega^2\omega^1\omega^3\omega^0\omega^3 \\ \omega^2\omega^1\omega^3\omega^3\omega^0\omega^0\omega^3\omega^0\omega^1\omega^0\omega^2\omega^2\omega^3\omega^3\omega^2\omega^3 \end{bmatrix}.$$
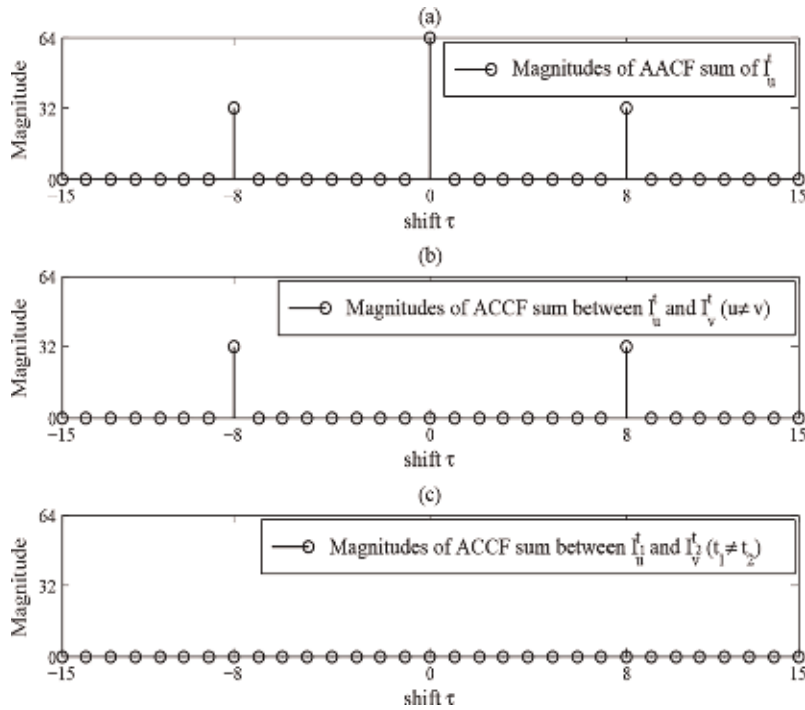
(49)

Figure 2.
Correlation plots of $I(8, 4, 16, 8)$.

The correlation properties of I (8, 4, 16, 8) are described in **Figure 2** where **Figure 2a** presents the absolute value of AACF sum of each code in $I(8, 4, 16, 8)$, **Figure 2b** shows absolute value of ACCF sum between any two distinct codes from the same code group, and **Figure 2c** presents the absolute value of ACCF sum between any two distinct codes from different code groups.

4. Summary

In this chapter, we have presented a direct construction of IGC code set by using second-order GBFs. The AACF sidelobes of the codes of constructed IGC code set are zeros within ZCZ width, and the ACCFs of any two different codes of the same code group are zeros inside the ZCZ width, whereas the ACCFs of any two different codes from two different code groups are zeros everywhere. We have shown that there is a relation between our proposed construction and graph. The ZCZ width of the proposed IGC code set depends on the number of isolated vertices present in a graph after the deletion of some vertices. We also have shown that the ZCZ width of the proposed IGC code set by our construction is flexible and it can extend their applications. It is observed that most of the constructions given in literature are based on CCCs, whereas our construction can produce IGC code set directly.

Author details

Palash Sarkar and Sudhan Majhi*
IIT Patna, India

*Address all correspondence to: smajhi@iitp.ac.in

IntechOpen

References

[1] Hanzo LL, Yang L-L, Kuan E-L, Yen K. CDMA Overview. United States: IEEE; 2004. Available from: https://ieee xplore.ieee.org/document/5732958

[2] Fazel K, Kaiser S. MC-CDMA and MC-DS-CDMA. United States: Wiley; 2008. Available from: https://ieeexplore. ieee.org/document/8043168

[3] Golay M. Complementary series. IRE Transactions on Information Theory. 1961;7(2):82-87

[4] Tseng C-C, Liu C. Complementary sets of sequences. IEEE Transactions on Information Theory. 1972;**18**(5):644-652

[5] Davis JA, Jedwab J. Peak-to-mean power control in OFDM, Golay complementary sequences, and Reed-Muller codes. IEEE Transactions on Information Theory. 1999;**45**(7): 2397-2417

[6] Paterson KG. Generalized Reed-Muller codes and power control in OFDM modulation. IEEE Transactions on Information Theory. 2000;**46**(1): 104-120

[7] Sarkar P, Majhi S, Liu Z. A direct and generalized construction of polyphase complementary set with low PMEPR and high code-rate for OFDM system. n. d. Available from: http://arxiv.org/abs/ 1901.05545

[8] Rathinakumar A, Chaturvedi AK. Complete mutually orthogonal Golay complementary sets from Reed-Muller codes. IEEE Transactions on Information Theory. 2008;**54**(3): 1339-1346

[9] Ke P, Zhou Z. A generic construction of Z-periodic complementary sequence sets with flexible flock size and zero correlation zone length. IEEE Signal Processing Letters. 2015;**22**(9): 1462-1466

[10] Liu Z, Guan YL, Parampalli U. New complete complementary codes for peak-to-mean power control in multi-carrier CDMA. IEEE Transactions on Communications. 2014;**62**(3):1105-1113

[11] Das S, Budišin S, Majhi S, Liu Z, Guan YL. A multiplier-free generator for polyphase complete complementary codes. IEEE Transactions on Signal Processing. 2018;**66**(5):1184-1196

[12] Liu Z, Guan YL, Chen HH. Fractional-delay-resilient receiver design for interference-free MC-CDMA communications based on complete complementary codes. IEEE Transactions on Wireless Communications. 2015;**14**(3):1226-1236

[13] Fan P, Yuan W, Tu Y. Z-complementary binary sequences. IEEE Signal Processing Letters. 2007; **14**(8):509-512

[14] Li X, Fan P, Tang X, Hao L. Constructions of quadriphase Z-complementary sequences. In: Fourth International Workshop on Signal Design and its Applications in Communications; 2009. pp. 36-39

[15] Adhikary AR, Majhi S, Liu Z, Guan YL. New sets of even-length binary Z-complementary pairs with asymptotic ZCZ ratio of 3/4. IEEE Signal Processing Letters. 2018;**25**(7):970-973

[16] Sarkar P, Majhi S, Liu Z. Optimal Z-complementary code set from generalized Reed-Muller codes. IEEE Transactions on Communications. 2019; **67**(3):1783-1796

[17] Zhang C, Tao X, Yamada S, Hatori M. Sequence set with three zero correlation zones and its application in MC-CDMA system. IEICE Transactions on Fundamentals of Electronics, Communications and Computer Sciences. 2006;**E89-A**(9):2275-2282

[18] Liu Z, Guan YL, Ng BC, Chen HH. Correlation and set size bounds of complementary sequences with low correlation zone. IEEE Transactions on Communications. 2011;**59**(12): 3285-3289

[19] Li J, Huang A, Guizani M, Chen HH. Inter group complementary codes for interference resistant CDMA wireless communications. IEEE Transactions on Wireless Communications. 2008;**7**(1): 166-174

[20] Feng L, Zhou X, Fan P. A construction of inter-group complementary codes with flexible ZCZ length. Journal of Zhejiang University SCIENCE-C. 2011;**12**(10):846-854

Chapter 4

$Z_2Z_2[u]$-Linear and $Z_2Z_2[u]$-Cyclic Codes

Ismail Aydogdu

Abstract

Additive codes were first introduced by Delsarte in 1973 as subgroups of the underlying abelian group in a translation association scheme. In the case where the association scheme is the Hamming scheme, that is, when the underlying abelian group is of order 2^n, the additive codes are of the form $\mathbb{Z}_2^\alpha \times \mathbb{Z}_4^\beta$ with $\alpha + 2\beta = n$. In 2010, Borges et al. introduced $\mathbb{Z}_2\mathbb{Z}_4$-additive codes which they defined them as the subgroups of $\mathbb{Z}_2^\alpha \times \mathbb{Z}_4^\beta$. In this chapter we introduce $\mathbb{Z}_2\mathbb{Z}_2[u]$-linear and $\mathbb{Z}_2\mathbb{Z}_2[u]$-cyclic codes where $\mathbb{Z}_2 = \{0, 1\}$ is the binary field and $\mathbb{Z}_2[u] = \{0, 1, u, 1+u\}$ is the ring with four elements and $u^2 = 0$. We give the standard forms of the generator and parity-check matrices of $\mathbb{Z}_2\mathbb{Z}_2[u]$-linear codes. Further, we determine the generator polynomials for $\mathbb{Z}_2\mathbb{Z}_2[u]$-linear cyclic codes. We also present some examples of $\mathbb{Z}_2\mathbb{Z}_2[u]$-linear and $\mathbb{Z}_2\mathbb{Z}_2[u]$-cyclic codes.

Keywords: $\mathbb{Z}_2\mathbb{Z}_2[u]$-linear codes, cyclic codes, generator matrix, duality, parity-check matrix, minimal spanning set

1. Introduction

In coding theory, the most important class of error-correcting codes is the family of linear codes, because the encoding and decoding procedures for a linear code are faster and simpler than those for arbitrary nonlinear codes. Many practically important linear codes have also an efficient decoding. Specifically, a linear code $\mathcal{C}$ of length n is a vector subspace of $\mathbb{F}_q^n$, where $\mathbb{F}_q$ is a finite field with q elements. Among all the codes over finite fields, binary linear codes (linear codes over $\mathbb{F}_2$) have a very special and important place because of their easy implementations and applications. In the beginning, researchers were mainly studying on linear codes over fields, especially binary fields. However, in 1994, a remarkable paper written by Hammons et al. [1] brought a new direction to studies on coding theory. In this paper, they showed that some well-known nonlinear codes, the Nordstrom-Robinson code, Kerdock codes, and Delsarte-Goethals code, are actually binary images of some linear codes over the ring of integers modulo, 4, i.e., $\mathbb{Z}_4$. Such connections motivate the researchers to study on codes over different rings even over other structural algebras such as groups or modules. Even though the structure of binary linear codes and quaternary linear codes (codes over $\mathbb{F}_4$ or $\mathbb{Z}_4$) have been studied in details for the last 50 years, recently, in 2010, a new class of error-correcting codes over the ring $\mathbb{Z}_2^\alpha \times \mathbb{Z}_4^\beta$ called additive codes that generalizes the class of binary linear codes and the class of quaternary linear codes have been introduced by Borges et al. in [2]. A $\mathbb{Z}_2\mathbb{Z}_4$-additive code $\mathcal{C}$ is defined as a subgroup of

$\mathbb{Z}_2^\alpha \times \mathbb{Z}_4^\beta$, where α and β are positive integers and $\alpha + 2\beta = n$. Despite the fact that $\mathbb{Z}_2\mathbb{Z}_4$-additive codes are a new type of codes, they have shown to have some applications in fields such as the field of steganography. Another important ring of four elements which is not isomorphic to $\mathbb{Z}_4$ is the ring $\mathbb{Z}_2 + u\mathbb{Z}_2 = \{0, 1, u, 1 + u\}$ $= \mathcal{R} = \mathbb{Z}_2[u]$ where $u^2 = 0$. Working with the ring $\mathcal{R}$ has some advantages compared to the ring $\mathbb{Z}_4$. For example, the Gray images of linear codes over $\mathcal{R}$ are always binary linear codes which is not always the case for $\mathbb{Z}_4$. Further, since the finite field $\mathbb{F}_2$ is a subring of the ring $\mathcal{R}$, the factorization of polynomials over $\mathcal{R}$ is the same with the factorization of polynomials over $\mathbb{F}_2$, so we do not need Hensel's lift for factorization. Moreover, decoding algorithm of cyclic codes over $\mathcal{R}$ is easier than that over $\mathbb{Z}_4$. In this chapter of the book, we introduce $\mathbb{Z}_2\mathbb{Z}_2[u]$-linear and $\mathbb{Z}_2\mathbb{Z}_2[u]$-cyclic codes. The original study about linear and cyclic codes over $\mathbb{Z}_2\mathbb{Z}_2[u]$ was done by Aydogdu et al. in [3, 4]. So, this chapter is a survey on $\mathbb{Z}_2\mathbb{Z}_2[u]$-linear and $\mathbb{Z}_2\mathbb{Z}_2[u]$-cyclic codes which were introduced in [3, 4].

2. $\mathbb{Z}_2\mathbb{Z}_2[u]$-linear codes

Let $\mathbb{Z}_2 = \{0, 1\}$ be the finite field and $\mathcal{R} = \mathbb{Z}_2 + u\mathbb{Z}_2 = \{0, 1, u, 1 + u\}$, $u^2 = 0$ be the finite ring of four elements. Since $\mathbb{Z}_2$ is a subring of $\mathcal{R}$, we define the following set:

$$\mathbb{Z}_2\mathcal{R} = \{(c_1, c_2) | c_1 \in \mathbb{Z}_2 \text{ and } c_2 \in \mathcal{R}\}$$

This set is not well defined with respect to the usual multiplication by $u \in \mathcal{R}$. So it is not an $\mathcal{R}$-module. Hence the set $\mathbb{Z}_2\mathcal{R}$ cannot be endowed with an algebraic structure directly. Therefore we introduce a new multiplication to make it well defined and enriched with an algebraic structure.

Let $d \in \mathcal{R}$; then d can be expressed in the form $d = r + uq$ with $r, q \in \mathbb{Z}_2$. We define the following map:

$$\eta : \mathcal{R} \to \mathbb{Z}_2$$
$$\eta(d) = r = \overline{d}$$

as $\eta(0) = 0$, $\eta(1) = 1$, $\eta(u) = 0$ and $\eta(1 + u) = 1$. It is easy to see that the mapping η is a ring homomorphism. Now, using this map we define the following $\mathcal{R}$-scalar multiplication on $\mathbb{Z}_2\mathcal{R}$. For any element $d \in \mathcal{R}$:

$$d(c_1, c_2) = (\eta(d)c_1, dc_2) = (\overline{d}c_1, dc_2)$$

This new multiplication is well defined and also can be extended over $\mathbb{Z}_2^\alpha \times \mathcal{R}^\beta$ as follows. Let $d \in \mathcal{R}$ and $v = (a_0, a_1, ..., a_{\alpha-1}, b_0, b_1, ..., b_{\beta-1}) \in \mathbb{Z}_2^\alpha \times \mathcal{R}^\beta$; then define

$$dv = (\eta(d)a_0, \eta(d)a_1, ..., \eta(d)a_{\alpha-1}, db_0, db_1, ..., db_{\beta-1})$$
$$= (\overline{d}a_0, \overline{d}a_1, ..., \overline{d}a_{\alpha-1}, db_0, db_1, ..., db_{\beta-1}).$$

Lemma 2.1. $\mathbb{Z}_2^\alpha \times \mathcal{R}^\beta$ is an $\mathcal{R}$-module with respect to the multiplication defined above.

Definition 2.2. Let $\mathcal{C}$ be a non-empty subset of $\mathbb{Z}_2^\alpha \times \mathcal{R}^\beta$. $\mathcal{C}$ is called a $\mathbb{Z}_2\mathbb{Z}_2[u]$-linear code if it is an $\mathcal{R}$-submodule of $\mathbb{Z}_2^\alpha \times \mathcal{R}^\beta$.

Note that the ring $\mathcal{R}$ is isomorphic to $\mathbb{Z}_2^2$ as an additive group. Therefore, any $\mathbb{Z}_2\mathbb{Z}_2[u]$-linear code $\mathcal{C}$ is isomorphic to a group of the form $\mathbb{Z}_2^{k_0+k_2} \times \mathbb{Z}_2^{2k_1}$, for some $k_0, k_1, k_2 \in \mathbb{Z}^+$. Now let us consider the following sets:

$$\mathcal{C}_\beta^F = \left\langle \left\{ (a,b) \in \mathbb{Z}_2^\alpha \times \mathcal{R}^\beta | b \text{ is free over } \mathcal{R}^\beta \right\} \right\rangle$$

where if $\langle b \rangle = \mathcal{R}^\beta$, then b is called free over $\mathcal{R}^\beta$:

$$\mathcal{C}_0 = \left\langle \left\{ (a,ub) \in \mathbb{Z}_2^\alpha \times \mathcal{R}^\beta | a \neq 0 \right\} \right\rangle \subseteq \mathcal{C} \backslash \mathcal{C}_\beta^F$$

$$\mathcal{C}_1 = \left\langle \left\{ (a,ub) \in \mathbb{Z}_2^\alpha \times \mathcal{R}^\beta | a = 0 \right\} \right\rangle \subseteq \mathcal{C} \backslash \mathcal{C}_\beta^F$$

Now, denote the dimension of $\mathcal{C}_0$, $\mathcal{C}_1$, and $\mathcal{C}_\beta^F$ as k_0, k_2, and k_1, respectively. Hence, if $\mathcal{C} \subseteq \mathbb{Z}_2^\alpha \times \mathcal{R}^\beta$ is a $\mathbb{Z}_2\mathbb{Z}_2[u]$-linear code group isomorphic to $\mathbb{Z}_2^{k_0+k_2} \times \mathbb{Z}_2^{2k_1}$, then we say $\mathcal{C}$ is of type $(\alpha, \beta; k_0, k_1, k_2)$. We can consider any $\mathbb{Z}_2\mathbb{Z}_2[u]$-linear code $\mathcal{C}$ as a binary code under the special Gray map.

Definition 2.3. Let $\left(a_0, a_1, ..., a_{\alpha-1}, b_0, b_1, ..., b_{\beta-1}\right) \in \mathbb{Z}_2^\alpha \times \mathcal{R}^\beta$ with $b_i = p_i + uq_i$. We define the Gray map as follows:

$$\Psi : \mathbb{Z}_2^\alpha \times \mathcal{R}^\beta \to \mathbb{Z}_2^n$$

$$\Psi\left(a_0, a_1, ..., a_{\alpha-1}, p_0 + uq_0, p_1 + uq_1, ..., p_{\beta-1} + uq_{\beta-1}\right)$$

$$= \left(a_0, a_1, ..., a_{\alpha-1}, q_0, q_1, ..., q_{\beta-1}, p_0 + q_0, p_1 + q_1, ..., p_{\beta-1} + q_{\beta-1}\right)$$

where $n = \alpha + 2\beta$. The Gray map Ψ is an isometry which transforms the Lee distance in $\mathbb{Z}_2^\alpha \times \mathcal{R}^\beta$ to the Hamming distance in $\mathbb{Z}_2^n$. The Hamming and the Lee distance between two codewords is the Hamming weight and the Lee weight of their differences, respectively. The Hamming weight of a codeword is defined as the number of its non-zero entries, and the Lee weights of the elements of $\mathcal{R}$ are defined as $wt_L(0) = 0, wt_L(1) = 1, wt_L(u) = 2, wt_L(1+u) = 1$. It is worth mentioning that the Gray map Ψ is linear, i.e., for a $\mathbb{Z}_2\mathbb{Z}_2[u]$-linear code $\mathcal{C}$, we have $\Psi(\mathcal{C})$ as a binary linear code which is not the case for $\mathbb{Z}_2\mathbb{Z}_4$-additive codes in general. We can extend the definition of the Lee weight of a codeword in $\mathcal{R}$ to the Lee weight of a codeword $v = (v_1, v_2) \in \mathbb{Z}_2^\alpha \times \mathcal{R}^\beta$ as follows:

$$wt(v) = wt_H(v_1) + wt_L(v_2)$$

where $wt_H(v_1)$ is the Hamming weight of v_1 and $wt_L(v_2)$ is the Lee weight of v_2. Further, the minimum distance of the $\mathbb{Z}_2\mathbb{Z}_2[u]$-linear code $\mathcal{C}$, denoted by $d(\mathcal{C})$, is naturally defined as

$$d(\mathcal{C}) = \min\{d(c_1, c_2) | c_1, c_2 \in \mathcal{C} \text{ such that } c_1 \neq c_2\}$$

where $d(c_1, c_2) = wt(c_1 - c_2)$. If $\mathcal{C}$ is a $\mathbb{Z}_2\mathbb{Z}_2[u]$-linear code of type $(\alpha, \beta; k_0, k_1, k_2)$, then Gray image $\Psi(\mathcal{C})$ is a binary linear code of length $n = \alpha + 2\beta$ and size 2^n. It is also called a $\mathbb{Z}_2\mathbb{Z}_2[u]$-linear code.

2.1 Generator matrices of $\mathbb{Z}_2\mathbb{Z}_2[u]$-linear codes

A generator matrix for a linear code $\mathcal{C}$ is the matrix G with rows that are formed by a minimal spanning set of $\mathcal{C}$. All linear combinations of the rows of the generator

matrix G constitute the linear code $\mathcal{C}$. We can produce an equivalent code to the $\mathcal{C}$ by applying elementary row and column operations on the generator matrix G. For given two linear codes, if one can be obtained from the other by permutation of their coordinates or (if necessary) changing the coordinates by their unit multiples, then these codes are said to be permutation equivalent code or only equivalent code. Furthermore, the standard form of the matrix G is a special form which is obtained by applying elementary row operations to G. Having the standard form of the generator matrix is very useful that we can easily determine the type of the code and then calculate its size directly. Note that the generator matrices in the standard form of linear codes over a ring contain the minimum number of rows. The theorem below determines the standard form of the generator matrix of a $\mathbb{Z}_2\mathbb{Z}_2[u]$-linear code $\mathcal{C}$.

Theorem 2.1.1. [3] Let $\mathcal{C}$ be a $\mathbb{Z}_2\mathbb{Z}_2[u]$-linear code of type $(\alpha, \beta; k_0, k_1, k_2)$. Then $\mathcal{C}$ is a permutation equivalent to a $\mathbb{Z}_2\mathbb{Z}_2[u]$-linear code with the following generator matrix of the standard form:

$$
G_s = \begin{bmatrix} I_{k_0} & A_1 & 0 & 0 & uT \\ 0 & S & I_{k_1} & A & B_1 + uB_2 \\ 0 & 0 & 0 & uI_{k_2} & uD \end{bmatrix}
\tag{1}
$$

where $A, A_1, B_1, B_2, T,$ and D are matrices with all entries from $\mathbb{Z}_2$ and I_{k_0}, I_{k_1}, and I_{k_2} are identity matrices with given sizes. Further $\mathcal{C}$ has $2^{k_0+2k_1+k_2}$ codewords.

Proof. It is well known that any linear code of length β over the ring $\mathcal{R} = \mathbb{Z}_2 + u\mathbb{Z}_2$ has the generator matrix of the form $\begin{bmatrix} I_{k_1} & A' & B_1' + uB_2' \\ 0 & uI_{k_2}' & uD' \end{bmatrix}$. Moreover, any binary linear code of length α can be generated by the matrix $\begin{bmatrix} I_{k_0}' & A_1' \end{bmatrix}$. Since $\mathcal{C}$ is a $\mathbb{Z}_2\mathbb{Z}_2[u]$-linear code of length $\alpha + \beta$, then $\mathcal{C}$ can be generated by the following matrix:

$$
\left[\underbrace{\begin{matrix} I_{k_0}' & A_1' \\ S_{01} & S_{02} \\ S_{11} & S_{12} \end{matrix}}_{\alpha} \middle| \underbrace{\begin{matrix} T_{01} & T_{02} & T_{03} \\ I_{k_1} & A' & B_1' + uB_2' \\ 0 & uI_{k_2}' & uD' \end{matrix}}_{\beta} \right]
$$

with all binary entries. By applying the necessary row operations to the above matrix, we have the desired form.

Example 2.1.2. Let $\mathcal{C}$ be a $\mathbb{Z}_2\mathbb{Z}_2[u]$-linear code with the generator matrix $\begin{bmatrix} 1 & 1 & 0 & 1+u & 1+u \\ 0 & 1 & 1 & 1 & 1+u \end{bmatrix}$. First, adding the second row to the first row, we have

$$
\begin{bmatrix} 1 & 0 & 1 & u & 0 \\ 0 & 1 & 1 & 1 & 1+u \end{bmatrix}.
$$

Then multiplying the second row by u and adding it to first row, we have the following standard form of the generator matrix:

$$\left[\begin{array}{cc|cc} \boxed{1} & \boxed{0 \quad 1} & \boxed{0} & \boxed{u} \\ \boxed{0} & \boxed{1 \quad 1} & \boxed{1} & \boxed{1+u} \end{array}\right] = \left[\begin{array}{cc|cc} I_{k_0} & A_1 & 0 & uT \\ 0 & S & I_{k_1} & B_1 + uB_2 \end{array}\right] \quad (2)$$

Therefore,

- $\mathcal{C}$ is of type $(3, 2; 1, 1, 0)$.

- $\mathcal{C}$ has $2^{1+2\cdot1} = 8$ codewords:

$$\mathcal{C} = \{(0, 0, 0, | 0, 0), (1, 0, 1, | 0, u), (0, 1, 1, | 1, 1+u), (1, 1, 0, | 1, 1), (0, 1, 1, | 1+u, 1),$$

$$(1, 1, 0, | 1+u, 1+u), (0, 0, 0, | u, u), (1, 0, 1, | u, 0)\}.$$

Moreover, the Gray image $\Psi(\mathcal{C})$ of $\mathcal{C}$ is a simplex code of length 7 with parameters [7, 3, 4] which is the dual of the well-known [7, 4, 3] Hamming code.

2.2 Duality on $\mathbb{Z}_2\mathbb{Z}_2[u]$-linear codes and parity-check matrices

In the literature, there is a very well-known concept for the duals of the codes over finite fields and rings. If $\mathcal{C}$ is a linear code over $\mathbb{F}_q^n$, the dual code $\mathcal{C}^\perp$ of $\mathcal{C}$ in $\mathbb{F}_q^n$ is the set of all codewords that are orthogonal to every codeword of $\mathcal{C}$. A generator matrix for $\mathcal{C}^\perp$ is called a parity-check matrix of $\mathcal{C}$. In this part, we determine the standard form of the parity-check matrix of a $\mathbb{Z}_2\mathbb{Z}_2[u]$-linear code $\mathcal{C}$. Let us begin with the definition of an inner product over $\mathbb{Z}_2^\alpha \times \mathcal{R}^\beta$.

Definition 2.2.1 Let v and w be the two elements in $\mathbb{Z}_2^\alpha \times \mathcal{R}^\beta$. The inner product of v and w is defined by

$$\langle v, w \rangle = u\left(\sum_{i=1}^{\alpha} v_i w_i\right) + \sum_{j=\alpha+1}^{\alpha+\beta} v_j w_j \in \mathcal{R}.$$

Further, the dual code $\mathcal{C}^\perp$ of a $\mathbb{Z}_2\mathbb{Z}_2[u]$-linear code $\mathcal{C}$ is defined in the usual way with respect to this inner product as

$$\mathcal{C}^\perp = \left\{w \in \mathbb{Z}_2^\alpha \times \mathcal{R}^\beta | \langle v, w \rangle = 0 \text{ for all } v \in \mathcal{C}\right\}.$$

Hence, if $\mathcal{C}$ is a $\mathbb{Z}_2\mathbb{Z}_2[u]$-linear code, then $\mathcal{C}^\perp$ is also a $\mathbb{Z}_2\mathbb{Z}_2[u]$-linear code. It is worth mentioning that any two codewords of a $\mathbb{Z}_2\mathbb{Z}_2[u]$-linear code may be orthogonal to each other, but the binary parts of the codewords may not be orthogonal. For example, $(1, 1| 1+u, u), (0, 1| u, u) \in \mathbb{Z}_2^2 \times \mathcal{R}^2$ are orthogonal to each other, whereas the binary or $\mathcal{R}$-components are not orthogonal. Moreover, the Gray map Ψ preserves the orthogonality.

We give the standard form of the parity-check matrices of $\mathbb{Z}_2\mathbb{Z}_2[u]$-linear codes with the following theorem.

Theorem 2.2.2. [3] Let $\mathcal{C}$ be a $\mathbb{Z}_2\mathbb{Z}_2[u]$-linear code of type $(\alpha, \beta; k_0, k_1, k_2)$ with the standard form generator matrix (1). Then the parity-check matrix of $\mathcal{C}$ (the generator matrix of the dual code $\mathcal{C}^\perp$) is given by

$$H_s = \begin{bmatrix} -A_1^t & I_{\alpha-k_0} & -uS^t & 0 & 0 \\ -T^t & 0 & -(B_1 + uB_2)^t + D^t A^t & -D^t & I_{\beta-k_1-k_2} \\ 0 & 0 & -uA^t & uI_{k_2} & 0 \end{bmatrix}.$$

Furthermore, $|\mathcal{C}^\perp| = 2^{\alpha-k_0}2^{2(\beta-k_1-k_2)}2^{k_2}$.

Proof. It can be easily checked that $G_s \cdot H_s^t = 0$. Therefore every row of H_s is orthogonal to the rows of G_s. Further, since the generator matrices in the standard form of linear codes contain the minimum number of rows, $\mathcal{C}^\perp$ has $2^{\alpha-k_0}2^{2(\beta-k_1-k_2)}2^{k_2}$ codewords. Hence, $|\mathcal{C}|\,|\mathcal{C}^\perp| = 2^{k_0}2^{2k_1}2^{k_2}2^{\alpha-k_0}2^{2(\beta-k_1-k_2)}2^{k_2} = 2^{\alpha+2\beta}$. So, the rows of the matrix H_s are not only orthogonal to $\mathcal{C}$, but also they generate all dual space.

Example 2.2.3. Let $\mathcal{C}$ be a $\mathbb{Z}_2\mathbb{Z}_2[u]$-linear code of type $(3, 2; 1, 1, 0)$ with the standard form of the generator matrix in (2). Then the parity-check matrix of $\mathcal{C}$ is

$$
\begin{bmatrix}
-A_1^t & I_{3-1} & & -uS^t & & 0 \\
-T^t & 0 & & -(B_1+uB_2)^t + D^tA^t & I_{2-1-0}
\end{bmatrix}
=
\left[
\begin{array}{cc|cc|c|c}
\boxed{0} & \boxed{\begin{matrix}1 & 0\end{matrix}} & & \boxed{u} & & \boxed{0} \\
\boxed{1} & \boxed{\begin{matrix}0 & 1\end{matrix}} & & \boxed{u} & & \boxed{0} \\
\boxed{1} & \boxed{\begin{matrix}0 & 0\end{matrix}} & & \boxed{1+u} & & \boxed{1}
\end{array}
\right].
$$

Therefore, $\mathcal{C}^\perp$ is of type $(3, 2; 2, 1, 0)$ and has $2^2 2^{2\cdot1} 2^0 = 16$ codewords. The Gray image $\Psi(\mathcal{C}^\perp)$ is a well-known Hamming code with parameters $[7, 4, 3]$.

Corollary 2.2.4. If $\mathcal{C}$ is a $\mathbb{Z}_2\mathbb{Z}_2[u]$-linear code of type $(\alpha, \beta; k_0, k_1, k_2)$, then $\mathcal{C}^\perp$ is of type $(\alpha, \beta; \alpha - k_0, \beta - k_1 - k_2, k_2)$.

3. $\mathbb{Z}_2\mathbb{Z}_2[u]$-linear cyclic codes

Cyclic codes form a very small but highly structured and important subset of the set of linear codes. In general, these codes are much easier to implement, and hence they have a very rich algebraic structure that allows them to be encoded and decoded in a relatively easier way. Since cyclic codes can be identified as ideals in a certain ring, they are also of considerable interest from an algebraic point of view. Cyclic codes over finite fields were first introduced by E. Prange in 1957 and 1959 with two Air Force Cambridge Research Laboratory reports. In this section we study the structure of $\mathbb{Z}_2\mathbb{Z}_2[u]$-linear cyclic codes for a positive odd integer β. We give the generator polynomials and the spanning sets for a $\mathbb{Z}_2\mathbb{Z}_2[u]$-linear cyclic code $\mathcal{C}$.

Definition 3.1. An $\mathcal{R}$-submodule $\mathcal{C}$ of $\mathbb{Z}_2^\alpha \times \mathcal{R}^\beta$ is called a $\mathbb{Z}_2\mathbb{Z}_2[u]$-linear cyclic code if for any codeword $v = (a_0, a_1, ..., a_{\alpha-1}, b_0, b_1, ..., b_{\beta-1}) \in \mathcal{C}$, its cyclic shift $T(v) = (a_{\alpha-1}, a_0, ..., a_{\alpha-2}, b_{\beta-1}, b_0, ..., b_{\beta-2})$ is also in $\mathcal{C}$.

Lemma 3.2. If $\mathcal{C}$ is a $\mathbb{Z}_2\mathbb{Z}_2[u]$-linear cyclic code, then the dual code $\mathcal{C}^\perp$ is also a $\mathbb{Z}_2\mathbb{Z}_2[u]$-linear cyclic code.

Proof. Let $\mathcal{C}$ be a $\mathbb{Z}_2\mathbb{Z}_2[u]$-linear cyclic code and $w = (d_0, d_1, ..., d_{\alpha-1}, e_0, e_1, ..., e_{\beta-1}) \in \mathcal{C}^\perp$. We will show that $T(w) \in \mathcal{C}^\perp$. Since $w \in \mathcal{C}^\perp$, for $v = (a_0, a_1, ..., a_{\alpha-1}, b_0, b_1, ..., b_{\beta-1}) \in \mathcal{C}$, we have

$$
\langle v, w \rangle = u(a_0d_0 + a_1d_1 + \cdots + a_{\alpha-1}d_{\alpha-1}) + (b_0e_0 + b_1e_1 + \cdots + b_{\beta-1}e_{\beta-1}) = 0.
$$

Now, let $\theta = \mathrm{lcm}(\alpha, \beta)$. Since $\mathcal{C}$ is cyclic, then $T^\theta(v) = v$, and $T^{\theta-1}(v) = (a_1, a_2, ..., a_0, b_1, b_2, ..., b_0) = z \in \mathcal{C}$. Therefore,

$$
\begin{aligned}
0 = \langle z, w \rangle \ &= u(a_1 d_0 + a_2 d_1 + \cdots + a_0 d_{\alpha-1}) + (b_1 e_0 + b_2 e_1 + \cdots + b_0 e_{\beta-1}) \\
&= u(a_0 d_{\alpha-1} + a_1 d_0 + \cdots + a_{\alpha-1} d_{\alpha-2}) + (b_0 e_{\beta-1} + b_1 e_0 + \cdots + b_{\beta-1} e_{\beta-2}) \\
&= \langle v, T(w) \rangle.
\end{aligned}
$$

Hence, $T(w) \in \mathcal{C}^\perp$ and so $\mathcal{C}^\perp$ is also cyclic.

Let $\mathcal{C} \subseteq \mathbb{Z}_2^\alpha \times \mathcal{R}^\beta$ and $v = (a_0, a_1, ..., a_{\alpha-1}, b_0, b_1, ..., b_{\beta-1}) \in \mathcal{C}$. $v \in \mathcal{C}$ can be identified with a module element consisting of two polynomials each from different rings in $\mathcal{R}_{\alpha,\beta} = \mathbb{Z}_2[x]/\langle x^\alpha - 1 \rangle \times \mathcal{R}[x]/\langle x^\beta - 1 \rangle$ such that

$$
\begin{aligned}
v(x) &= (a_0 + a_1 x + \cdots + a_{\alpha-1} x^{\alpha-1}, b_0 + b_1 x + \cdots + b_{\beta-1} x^{\beta-1}) \\
&= (a(x), b(x)).
\end{aligned}
$$

This identification gives a one-to-one correspondence between elements in $\mathbb{Z}_2^\alpha \times \mathcal{R}^\beta$ and elements in $\mathcal{R}_{\alpha,\beta}$.

Definition 3.3. Let $d(x) \in \mathcal{R}[x]$ and $(v(x), w(x)) \in \mathcal{R}_{a,\beta}$. We define the following scalar multiplication:

$$
d(x) * (v(x), w(x)) = (d(x)v(x) \bmod u, d(x)w(x))
$$

This multiplication is well defined, and moreover, $\mathcal{R}_{\alpha,\beta}$ is a $\mathcal{R}[x]$-module with respect to this multiplication.

The codewords of $\mathcal{C}$ may be represented as polynomials in $\mathcal{R}_{\alpha,\beta}$ by using the above identification. Thus, if $\mathcal{C} \subseteq \mathbb{Z}_2^\alpha \times \mathcal{R}^\beta$ is a cyclic code, then the element $v = (a_0, a_1, ..., a_{\alpha-1}, b_0, b_1, ..., b_{\beta-1}) \in \mathcal{C}$ can be viewed as

$$
v(x) = (a_0 + a_1 x + \cdots + a_{\alpha-1} x^{\alpha-1}, b_0 + b_1 x + \cdots + b_{\beta-1} x^{\beta-1}) \in \mathcal{R}_{\alpha,\beta}.
$$

Further, the property $T(v) = (a_{\alpha-1}, a_0, ..., a_{\alpha-2}, b_{\beta-1}, b_0, ..., b_{\beta-2}) \in \mathcal{C}$ translates to

$$
x * v(x) = (a_{\alpha-1} + a_0 x + \cdots + a_{\alpha-2} x^{\alpha-1}, b_{\beta-1} + b_0 x + \cdots + b_{\beta-2} x^{\beta-1}) \in \mathcal{R}_{\alpha,\beta}.
$$

Hence we give the following theorem.

Theorem 3.4. A code $\mathcal{C}$ is a $\mathbb{Z}_2\mathbb{Z}_2[u]$-linear cyclic code if and only if $\mathcal{C}$ is an $\mathcal{R}[x]$-submodule of $\mathcal{R}_{\alpha,\beta}$.

3.1 The generators and the spanning sets of $\mathbb{Z}_2\mathbb{Z}_2[u]$-linear cyclic codes

Let $\mathcal{C}$ be a $\mathbb{Z}_2\mathbb{Z}_2[u]$-linear code. We know that both $\mathcal{C}$ and $\mathcal{R}[x]/\langle x^\beta - 1 \rangle$ are $\mathcal{R}[x]$-modules. Then we define the following map:

$$
\Phi : \mathcal{C} \to \mathcal{R}[x]/\langle x^\beta - 1 \rangle
$$

$$
\Phi(f_1(x), f_2(x)) = f_2(x).
$$

It is clear that Φ is a module homomorphism where the $\mathrm{Im}(\Phi)$ is an $\mathcal{R}[x]$-submodule of $\mathcal{R}[x]/\langle x^\beta - 1 \rangle$ and $\ker(\Phi)$ is a submodule of $\mathcal{C}$. Since $\Phi(\mathcal{C})$ is an ideal of the ring $\mathcal{R}[x]/\langle x^\beta - 1 \rangle$, we have

$\Phi(\mathcal{C}) = \langle g(x) + ua(x) \rangle$ with $a(x)|g(x)|x^\beta - 1 \bmod 2$.

Further the kernel of Φ is

$$\ker(\Phi) = \left\{ (f(x), 0) \in \mathcal{C} \mid f(x) \in \mathbb{Z}_2^{\alpha} \times \mathcal{R}^{\beta} \right\}.$$

Now, define the set

$$I = \{ f(x) \in \mathbb{Z}_2[x]/\langle x^{\alpha} - 1 \rangle \mid (f(x), 0) \in \ker(\Phi) \}.$$

It is clear that I is an ideal and hence a cyclic code in the ring $\mathbb{Z}_2[x]/\langle x^{\alpha} - 1 \rangle$. So, by the well-known results about the generators of binary cyclic codes, I is generated by $f(x)$, i.e., $I = \langle f(x) \rangle$.

Now, let $(m(x), 0) \in \ker\Phi$. So, we have $m(x) \in I = \langle f(x) \rangle$, and hence $m(x) = k(x)f(x)$ for some polynomial $k(x) \in \mathbb{Z}_2[x]/\langle x^{\alpha} - 1 \rangle$. Therefore $(m(x), 0) = k(x) * (f(x), 0)$, and this implies that $\ker\Phi$ is a submodule of $\mathcal{C}$ generated by one element of the form $(f(x), 0)$ with $f(x) \mid (x^{\alpha} - 1) \bmod 2$. Then by the First Isomorphism Theorem, we have

$$\mathcal{C}/\ker\Phi \cong \langle g(x) + ua(x) \rangle.$$

Let $(l(x), g(x) + ua(x)) \in \mathcal{C}$ such that $\Phi(l(x), g(x) + ua(x)) = \langle g(x) + ua(x) \rangle$. This discussion shows that any $\mathbb{Z}_2\mathbb{Z}_2[u]$-linear cyclic code $\mathcal{C}$ can be generated as a $\mathcal{R}[x]$-submodule of $\mathcal{R}_{\alpha,\beta}$ by two elements of the form $(f(x), 0)$ and $(l(x), g(x) + ua(x))$ such that

$$d_1(x) * (f(x), 0) + d_2(x)(l(x), g(x) + ua(x))$$

where $d_1(x), d_2(x) \in \mathcal{R}[x]$. Since the polynomial $d_1(x)$ can be restricted to a polynomial in $\mathbb{Z}_2[x]$, we can write

$$\mathcal{C} = \langle (f(x), 0), (l(x), g(x) + ua(x)) \rangle$$

with binary polynomials $f(x)$ and $l(x)$ where $f(x) \mid (x^{\alpha} - 1) \bmod 2$ and $a(x) \mid g(x) \mid (x^{\beta} - 1) \bmod 2$.

Theorem 3.1.1. [4] Let $\mathcal{C}$ be a $\mathbb{Z}_2\mathbb{Z}_2[u]$-linear cyclic code in $\mathcal{R}_{\alpha,\beta}$. Then $\mathcal{C}$ can be identified uniquely as $\mathcal{C} = \langle (f(x), 0), (l(x), g(x) + ua(x)) \rangle$ where $f(x) \mid (x^{\alpha} - 1) \bmod 2$, $a(x) \mid g(x) \mid (x^{\beta} - 1) \bmod 2$, and $l(x)$ is a binary polynomial satisfying $\deg(l(x)) < \deg(f(x))$ and $f(x) \mid \left(\frac{x^{\beta} - 1}{a(x)} \right) l(x) \bmod u$.

Proof. We can easily see from the above discussion and Theorem 11 in [5] that $\mathcal{C} = \langle (f(x), 0), (l(x), g(x) + ua(x)) \rangle$ with the polynomials $f(x), l(x), g(x)$ and $a(x)$ are as stated in the theorem. So, we need to only show the uniqueness of the generator polynomials. Since $\langle f(x) \rangle$ and $\langle g(x) + ua(x) \rangle$ are cyclic codes over $\mathbb{Z}_2$ and over $\mathcal{R}$, respectively, this implies the uniqueness of the polynomials $f(x), g(x)$ and $a(x)$. Now suppose that $\deg(l(x)) > \deg(f(x))$ with $\deg(l(x)) - \deg(f(x)) = t$. Let

$$\mathcal{D} = \langle (f(x), 0), (l(x) + x^t f(x), g(x) + ua(x)) \rangle = \langle (f(x), 0), (l(x), g(x) + ua(x)) \rangle + x^t * \langle (f(x), 0) \rangle.$$

Therefore $\mathcal{D} \subseteq \mathcal{C}$. On the other hand,

$$\langle l(x), g(x) + ua(x) \rangle = \langle l(x) + x^t f(x), g(x) + ua(x) \rangle - x^t * \langle (f(x), 0) \rangle.$$

So, $\mathcal{C} \subseteq \mathcal{D}$ and hence $\mathcal{D} = \mathcal{C}$.

Definition 3.1.2. Let $\mathcal{N}$ be an $\mathcal{R}$-module. A linearly independent subset $\mathcal{P}$ of $\mathcal{N}$ that spans $\mathcal{N}$ is called a basis of $\mathcal{N}$. If an $\mathcal{R}$-module has a basis, then it is called a free $\mathcal{R}$-module.

Note that for a $\mathbb{Z}_2\mathbb{Z}_2[u]$-linear cyclic code $\mathcal{C} = \langle (f(x), 0), (l(x), g(x) + ua(x)) \rangle$, if $g(x) \neq 0$, then $\mathcal{C}$ is a free $\mathcal{R}$-module. However, if $g(x) = 0$ and $a(x) \neq 0$, then it is not a free $\mathcal{R}$-module. But we can still present $\mathcal{C}$ with the minimal spanning sets. The following theorem determines the minimal spanning sets for a $\mathbb{Z}_2\mathbb{Z}_2[u]$-linear cyclic code $\mathcal{C}$.

Theorem 3.1.3. [4] Let $\mathcal{C} = \langle (f(x), 0), (l(x), g(x) + ua(x)) \rangle$ be a $\mathbb{Z}_2\mathbb{Z}_2[u]$-linear cyclic code in $\mathcal{R}_{\alpha, \beta}$ with $f(x), l(x), g(x),$ and $a(x)$ in Theorem 3.1.1. Let

$$S_1 = \bigcup_{i=0}^{\deg(h_f(x))-1} \{x^i(f(x), 0)\},$$

$$S_2 = \bigcup_{i=0}^{\deg(h_g(x))-1} \{x^i(l(x), g(x) + ua(x))\},$$

$$S_3 = \bigcup_{i=0}^{\deg(b(x))-1} \{x^i(h_g(x)l(x), uh_g(x)a(x))\}$$

where $f(x)h_f(x) = x^\alpha - 1, g(x)h_g(x) = x^\beta - 1$ and $g(x) = a(x)b(x)$. Then $S = S_1 \cup S_2 \cup S_3$ forms a minimal spanning set for $\mathcal{C}$ as an $\mathcal{R}$-module. Furthermore, $\mathcal{C}$ has $2^{\deg(h_f(x))} 4^{\deg(h_g(x))} 2^{\deg(b(x))}$ codewords.

Proof. Please see the proof of the Theorem 4 in [4].

Example 3.1.4. Let $\mathcal{C} = \langle (f(x), 0), (l(x), g(x) + ua(x)) \rangle$ be a $\mathbb{Z}_2\mathbb{Z}_2[u]$-linear cyclic code in $\mathbb{Z}_2[x]/\langle x^7 - 1 \rangle \times \mathcal{R}[x]/\langle x^7 - 1 \rangle$ with the following generator polynomials:

$$f(x) = x^7 - 1, l(x) = 1 + x^2 + x^3$$
$$g(x) = 1 + x + x^2 + x^3 + x^4 + x^5 + x^6, a(x) = 1 + x^2 + x^3.$$

Therefore, we have $g(x) = a(x)b(x) \Rightarrow b(x) = 1 + x + x^3$ and $g(x)h_g(x) = x^7 - 1 \Rightarrow h_g(x) = 1 + x$. Hence by using the minimal spanning sets in Theorem 3.1.3, we can write the generator matrix for the $\mathbb{Z}_2\mathbb{Z}_2[u]$-linear cyclic code $\mathcal{C}$ as follows:

$$G = \begin{bmatrix} 1 & 0 & 1 & 1 & 0 & 0 & 0 & 1+u & 1 & 1+u & 1+u & 1 & 1 & 1 \\ 1 & 1 & 1 & 0 & 1 & 0 & 0 & u & u & u & 0 & u & 0 & 0 \\ 0 & 1 & 1 & 1 & 0 & 1 & 0 & 0 & u & u & u & 0 & u & 0 \\ 0 & 0 & 1 & 1 & 1 & 0 & 1 & 0 & 0 & u & u & u & 0 & u \end{bmatrix}.$$

It is worth mentioning that the Gray image $\Phi(\mathcal{C})$ of $\mathcal{C}$ is a linear binary code with the parameters [21, 5, 10], which are optimal. If the code $\mathcal{C}$ has the best minimum distance compared to the existing bounds for fixed length and the size, then $\mathcal{C}$ is called optimal or good parameter code.

Example 3.1.5. Let us consider the cyclic code $\mathcal{C} = \langle (f(x), 0), (l(x), g(x) + ua(x)) \rangle$ in $\mathbb{Z}_2[x]/\langle x^7 - 1 \rangle \times \mathcal{R}[x]/\langle x^9 - 1 \rangle$ with generators:

$$f(x) = 1 + x^2 + x^3 + x^4, l(x) = 1 + x + x^3,$$
$$g(x) = 1 + x + x^2 + x^3 + x^4 + x^5 + x^6 + x^7 + x^8, a(x) = 1 + x + x^2.$$

Again by using the minimal spanning sets in the above theorem, we have the following generator matrix for $\mathcal{C}$:

$$G = \begin{bmatrix}
1 & 0 & 1 & 1 & 1 & 0 & 0 & 0 & 0 & 0 & 0 & 0 & 0 & 0 & 0 & 0 \\
0 & 1 & 0 & 1 & 1 & 1 & 0 & 0 & 0 & 0 & 0 & 0 & 0 & 0 & 0 & 0 \\
0 & 0 & 1 & 0 & 1 & 1 & 1 & 0 & 0 & 0 & 0 & 0 & 0 & 0 & 0 & 0 \\
1 & 1 & 0 & 1 & 0 & 0 & 0 & 1+u & 1+u & 1+u & 1 & 1 & 1 & 1 & 1 & 1 \\
1 & 0 & 1 & 1 & 1 & 0 & 0 & u & 0 & 0 & u & 0 & 0 & 0 & 0 & 0 \\
0 & 1 & 0 & 1 & 1 & 1 & 0 & 0 & u & 0 & 0 & u & 0 & 0 & 0 & 0 \\
0 & 0 & 1 & 0 & 1 & 1 & 1 & 0 & 0 & u & 0 & 0 & u & 0 & 0 & 0 \\
1 & 0 & 0 & 1 & 0 & 1 & 1 & 0 & 0 & 0 & u & 0 & 0 & u & 0 & 0 \\
1 & 1 & 0 & 0 & 1 & 0 & 1 & 0 & 0 & 0 & 0 & u & 0 & 0 & u & 0 \\
1 & 1 & 1 & 0 & 0 & 1 & 0 & 0 & 0 & 0 & 0 & 0 & u & 0 & 0 & u
\end{bmatrix}.$$

The Gray image $\Phi(\mathcal{C})$ of $\mathcal{C}$ is a $[25, 11, 4]$ linear binary code. Moreover we can write the standard form of this generator matrix as

Hence $\mathcal{C}$ is of type $(7, 9; 3, 1, 6)$ and has $2^{11} = 2048$ codewords.

4. Conclusion

In this chapter we introduced $\mathbb{Z}_2\mathbb{Z}_2[u]$-linear and $\mathbb{Z}_2\mathbb{Z}_2[u]$-cyclic codes. We determined the standard forms of the generator and parity-check matrices of $\mathbb{Z}_2\mathbb{Z}_2[u]$-linear codes. We further gave the generator polynomials and minimal

spanning sets for $\mathbb{Z}_2\mathbb{Z}_2[u]$-linear cyclic codes. We also presented some illustrative examples of both $\mathbb{Z}_2\mathbb{Z}_2[u]$-linear codes and $\mathbb{Z}_2\mathbb{Z}_2[u]$-cyclic codes.

Acknowledgements

Author details

Ismail Aydogdu
Yildiz Technical University, Istanbul, Turkey

*Address all correspondence to: iaydogdu@yildiz.edu.tr

IntechOpen

References

[1] Hammons AR, Kumar V, Calderbank AR, Sloane NJA, Solé P. The Z4-linearity of Kerdock, Preparata, Goethals, and related codes. IEEE Transactions on Information Theory. 1994;**40**:301-319

[2] Borges J, Fernández-Córdoba C, Pujol J, Rifà J, Villanueva M. Z2Z4-linear codes: Generator matrices and duality. Designs, Codes and Cryptography. 2010;**54**(2):167-179

[3] Aydogdu I, Abualrub T, Siap I. On Z2Z2[u]−additive codes. International Journal of Computer Mathematics. 2015;**92**(9):1806-1814

[4] Aydogdu I, Abualrub T, Siap I. Z2Z2[u]-cyclic and constacyclic codes. IEEE Transactions on Information Theory. 2017;**63**(8):4883-4893

[5] Abualrub T, Siap I, Aydin N. Z2Z4-additive cyclic codes. IEEE Transactions on Information Theory. 2014;**60**(3): 1508-1514

The Adaptive Coding Techniques for Dependable Medical Network Channel

Emtithal Ahmed Talha and Ryuji Kohno

Abstract

The readily existing cellular networks play an important role in the daily life communications by integrating a wide variety of wireless multimedia services with higher data transmission rates, capable to provide much more than basic voice calls. In order to increase the demands of reliable medical network infrastructure economically and establish reliable medical transmission via cellular networks, this chapter has been designed as a dependable wireless medical network using an existing mobile cellular network with sophisticated channel coding technologies, providing a new novel way of the network that is adopted as a "Medical Network Channel (MNC)" system. Adding such adaptive outer coding with an existing cellular standard as inner coding makes a concatenated channel to carry out the MNC design. The adaptive design of extra outer channel codes depends on the Quality of Services (QoS) of Wireless Body Area Networks WBANs and also on the remaining errors from the inner-used cellular decoders. The adaptive extra code has been optimized toward "Medical Network Channel (MNC)" for different medical data QoS priority levels. The accomplishment of QoS constraints for different WBAN medical data has been investigated in this chapter for "Medical Network Channel (MNC)" by using the theoretical derivations, where positive acceptable results were achieved.

Keywords: UMTS, LTE, WBANs, QoS, concatenated codes

1. Introduction

A medical telemonitoring system is one of the telecommunication techniques that access delivery to healthcare services and one of the main applications for Medical Information Communication Technology (MICT). Recently, Information and Communication Technology (ICT) for medical and healthcare application has drawn substantial attention, which plays an important role to support dependable and effective medical technologies to solve significant problems in any society. The WBAN technology has proved out newly in the latest standardization as IEEE 802.15.6 [1]. WBAN standard aims to provide an international standard for short range, low power, and extremely reliable wireless communication within the surrounding area of the human body, supporting an enormous range of data rates from 75.9 Kbps narrow band (NB) up to 15.6 Mbps ultra-wide band (UWB) for various sets of applications [2]. WBAN technology is growing as a key technology for MICT

to transfigure the future of healthcare; therefore, WBANs have been attracting a great treaty of attentions from researchers both in academia and industry in the last few years [3]. A QoS is a major concern for WBAN medical application. Therefore, the researcher concerning QoS issues in WBANs should handle all of that very seriously in an effective way [4]. The cellular standards have been adopted by the European Union (EU) as a mandatory standard for member states and are spreading throughout much of the world. The cellular standards have been developed by considering enhancement in all aspects such as transmission speed, transmission way, data rate, error correction capabilities, channel capacity and QoS as general. UMTS is the main standard of the third generation (3G) with Wide Code Division Multiply Access (WCDMA) air interface, and LTE is the main standard of the fourth generation (4G). The bandwidth of a WCDMA is 5 MHz, and it is enough to provide data rates of 144 and 384 Kbps and even 2 Mbps in good conditions. On the other hand, LTE provides UL peak rates of 75 Mb/s, and QoS facilities permitting a transfer latency of less than 5 ms in the radio access network and supports accessible carrier bandwidth from 1.4 to 20 MHz. UMTS and LTE are used to cover both Frequency Division Duplex (FDD) and Time Division Duplex (TDD) operations and integrate a wide variety of wireless multimedia services with high data transmission rates, capable of providing much more than basic voice calls [5–7].

The way to connect WBAN technology network with other networks such as cellular networks UMTS and LTE is a key point for this chapter to serve the WBAN medical data transmission through the readily existing cellular networks. Therefore, the concept is to use the error controlling coding and decoding based on the concatenated channel codes with the cellular readily existing codes to design the "Medical Network Channel (MNC)" system. Reliable transmission of medical data is critical and essential since it is related to diagnosis and treatments of human body diseases. In ICT field, the reliable transmission procedures must guarantee detection and correction of erroneous transmissions. However, the transmission channel is often subject to various disturbances and interferences from the external environment conditions (noise).

The chapter focuses on the dependability of medical telemonitoring system from WBANs through UMTS and LTE via "Medical Network Channel (MNC)" system. Dependability of medical data transmission via MNC is defined as the probability of the "Medical Network Channel (MNC)" system to operate successfully, which means transmitted medical data reach their destination completely uncorrupted and guarantee minimum performances with lower error rate as much as possible under different environmental conditions. There are different methods that can be employed to overcome the channel impairments, such as increasing transmission power or the use of error control coding schemes in information theory field. A high level of reliability can be obtained by introducing redundancy bits in the signal transmission (encoding).

Medical Network Channel (MNC) system has been introduced to solve the reliability issues for medical data transmission when considering different QoS levels. The WBAN medical data are sensitive and any type of noise can corrupt them during transmission. Although the cellular standards include significant amounts of error detection and correction techniques, which are designed for daily life conversation mainly, some errors may still be present in the received data, and these transmission errors are not serious for the daily communication, but when considered for medical uses, they can have fatal outcomes. For that reason, the UMTS and LTE codes are designed for certain levels of channel condition, and if the error becomes more than the estimated condition, then the error becomes more serious and the cellular network standards perform worse using the preexisting error detection and correction capability. The Medical QoS levels have different

reliability required based on the BER for different medical data and other constraints [8].

The error control coding plays an important role in modifying the reliability issues. The concatenated codes are one of the error control coding techniques that have been widely adopted due to their simplicity and effectiveness [10]. Therefore, the chapter proposes a novel way of conducting error control encoding and decoding with QoS constraints by using the concatenated code techniques to build the MNC system. Consequently, the MNC intends to add extra channel code in order to combine the WBANs and the cellular networks and optimize the technical parameters for this extra channel depending on the reliability required for the medical data QoS levels and channel conditions as well. Therefore, the adaptive external channel code choice has six pairs of encoding and decoding, three for QoS levels (high, medium, and low) and then two for the channel condition (normal and worse). The restriction of UMTS or LTE channel codes is a standard, which is fixed by the European Telecommunication Standard Institute (ETSI) [5–7]. The technical parameters cannot be changed in order to provide good system performance. The only way is to design and optimize good adaptive extra outer channel codes with strong decoding capabilities resulting in better performance for MNC to transmit the WBAN medical data robustly.

The objective of the chapter is to design a reliable and dependable MNC system through the cellular networks to provide reliable transmission for all QoS medical data coming from WBANs. The structural design of MNC is based on channel coding of those using concatenated channel code techniques in the serial manner which adds extra channel codes to the cellular UMTS or LTE codes. The inner channel codes in MNC are cellular network standard UMTS or LTE error correction codes that cannot be changed in order to enhance the error performances, with regard to the international standards. On the other hand, the extra outer channel code in MNC is a changeable parameter for achieving different QoS constraints of medical data, which used the convolution code as the main error correction technique. Then, it will add end-to-end connection of WBANs to this MNC system using WBAN standard error correction techniques itself. According to QoS of WBANs O/P, MNC can be with or without extra code.

This chapter reflects about categorizing the eighth level QoS of WBANs to three different QoS (lower, medium, and higher) set levels. To achieve the chosen QoS, there is a need for adaptive external code with limited or strong error correcting capability with high, medium, or low coding rate and redundancy. Through those techniques, the MNC system is adaptive to varying propagation conditions and also adaptive to various QoS constraints. Therefore, the work here focuses to overcome different PHY errors that may occur during the transmission in an unpredictable way, making the channel situation time-to-time change, such as Gaussian noise AWGN, Rayleigh fading, or burst noise.

2. The dependable medical network channel configurations

The "Medical Network Channel (MNC)" system is a new system adopted in this chapter, which works to serve transmission of medical data robustly from WBANs through the cellular standard networks. It is mainly based on the error control coding techniques to ensure the dependability required for such medical data. The idea of the concatenated codes was used for connecting the WBANs with the cellular networks. The purpose is to have reliable and dependable medical data transmissions through the readily existing cellular network.

Figure 1 shows the whole "Medical Network Channel (MNC)" system that is the core base of this chapter. The different medical data QoS levels from the WBANs have been considered in designing the phase as well as the different assumed channel conditions. The structural design of the proposal is described in **Figure 2** by using the concatenated code techniques for different QoS of WBANs. The inner code for the MNC structure is introduced in **Table 1**. The UMTS and LTE provide both error detection and error correction as channel coding scheme. Here, it is assumed that the inner channel of the "Medical Network Channel (MNC)" system uses uplink UMTS channel as Common Packet Channel (CPCH) working by the convolution code rate 1/2. Similarly, the downlink UMTS channel was assumed
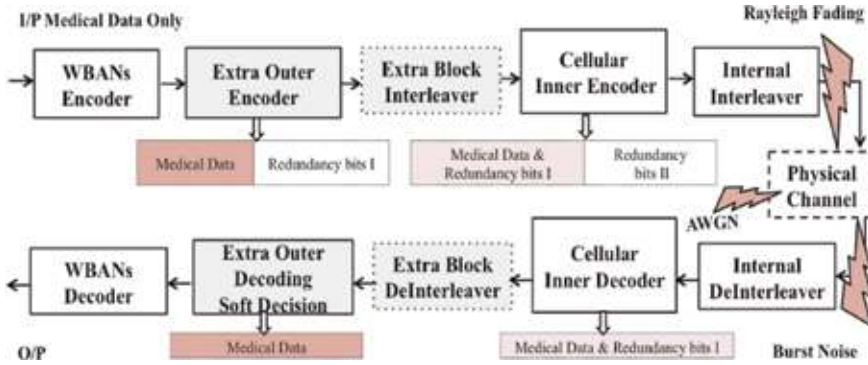
Figure 1.
Medical network channel codes via cellular networks.
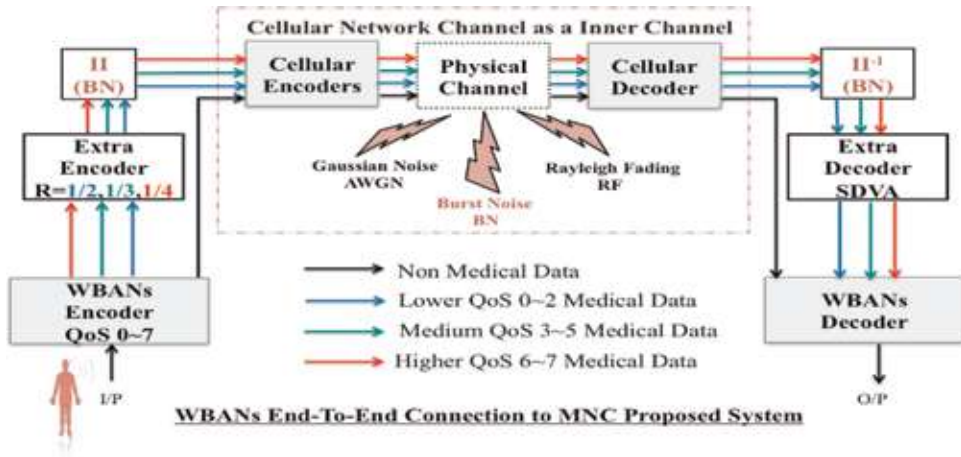
Figure 2.
The medical network channel system for QoS of WBAN medical data.

	TRCH type	Coding type	Coding rate R and constraint length K	Number of encoded bits
UMTS UL	CPCH	Convolution	R = 1/2 & K = 9	Di = 2*Ki + 16
UMTS DL	FACH	Convolution	R = 1/3 & K = 9	Di = 3*Ki + 24
LTE	BCH	Convolution	R = 1/3 & K = 7	Di = 3*Ki + 18

Table 1.
The inner cellular network code techniques.

using Forward Access Channel (FACH) working by the convolution code rate 1/3. Furthermore, LTE was assumed using Broadcast Channel (BCH) working by the convolution code rate 1/3.

The technical parameters for the extra channel detailed here by using extra outer encoder as convolution encoder are concatenated to the inner cellular standard channel codes. Among all the FEC codes, the convolution codes have great advantages using continuous data streams and can manage the performance with only two parameters: the code rate R and the constraint length K. Also, convolution codes have high error correction in comparison to block codes and less complexity in comparison to turbo codes. The soft decoding algorithm and the hard decoding algorithm, can make easily changes in the performances. Since the extra channel is a key point to have high performance for "Medical Network Channel (MNC)"-proposed system, the choice here of the extra code is driven by convolution codes. The outer channel is the existing WBAN channel that uses BCH code as a main code to correct the error. The system "Medical Network Channel (MNC)" has been considering the performance with and without end-to-end connection of the WBAN codes. The assumption is that the medical data coming from the WBANs with transmission rate 75.9Kb/s are entering the extra outer channel that will be the only optimized channel in "Medical Network Channel (MNC)" system, and then are entering the inner cellular channels within data rate less than the channel capacities.

3. Adaptive dependable system for WBAN medical data

The "Medical Network Channel (MNC)"-proposed system is dependable, which ensures to give the different QoS level of medical data transmission within acceptable performance capability such as 10^{-3}, 10^{-5} and 10^{-7} BER for low, medium, and high QoS levels within higher required bit energy to interference (E_b/N_o) values as possible under different assumed noise conditions. The WBAN has eight QoS levels. The QoS levels for the medical data have divided to three parts as lower priority QoS level, medium priority QoS level, and higher priority QoS level. Depending on these priority levels, the proposed system MNC has been designed as shown in **Figure 2**.

Table 2 shows all the error-correcting capabilities related to the UL and DL inner channels' technical capabilities for the UMTS and LTE with regard to the international standards of error correction code.

The criteria of the extra code selections in "Medical Network Channel (MNC)" system have two main parts in the structure: the fixed parts, which are related to the cellular standard networks or WBAN technology, and the changeable parts, which are external that are added to receive the medical data only.

	Data rate	R	K	G	D_{free}	Error (t)	Guard space (g)	Trellis paths (E)	Sum W_d
3G-UL	144Kb/s	1/2	9	[561 753]	12	6	17λ	256*L	122,694
3G-DL	144Kb/s	1/3	9	[557 663 711]	18	9	26λ	256*L	2275
4G	75 Mb/s	1/3	7	[133 171 165]	15	7	20λ	64*L	416

Table 2.
The inner cellular network code capabilities.

QoS data sets	Code	R & K	G	d_{free}	t	Sum W_d	II Size
Lowest QoS level		1/2 & 8	[247 371]	10	5	10,970	126 bits/block
Medium QoS level	Outer	1/3 & 8	[225 331 367]	16	8	425	189 bits/block
Highest QoS level		1/4 & 8	[235 275 313 357]	22	11	169	252 bits/block

Table 3.
Designing parameters of MNC adaptive codes related to QoS priority levels.

The assumption in this chapter is a WBAN chip installed in the mobile device to carry-on the medical data via the cellular systems through the "Medical Network Channel (MNC)" system to ensure the reliability required for the different sets of medical data. The extra code is adaptive by carrying parameters that are selectable with regard to the two main requirements: first, with regard to various kinds of the QoS of medical data entering the extra code from the WBAN code and second, with regard to the kind of the channel conditions that affected the transmission in PHY channels.

The goal of "Medical Network Channel (MNC)" is figured out by designing the extra code with regard to the QoS by analyzing the WBAN medical data QoS needed. **Table 3** categorizes the QoS of the WBAN medical data into three sets, with regard to the priority level, in order to design the MNC system. The first set is the highest priority level such as a biological signal (ECG, EMG, and EEG), the second set is a medium priority level such as medical data (temperature, blood pressure, and blood sugar), and the third set is the lowest priority level such as data management, audio, and video.

"Medical Network Channel (MNC)" used the three sets later to design and optimize the MNC system depending on that. The first set highest priority level will carry on through strong design MNC achieving 10^{-7} BER, then the second set medium priority design system achieves 10^{-5} BER, and then the third set lowest priority design system achieves 10^{-3} BER within higher E_b/N_o as possible.

In the "Medical Network Channel (MNC)" super PHY channel, the remaining error from the inner cellular decoder optimized the technical parameters of the extra outer code as shown in **Table 3**.

I/P	100 Kb/s [51 bits/s length]		
Outer WBAN encoder	63 bits/s		
Adaptive extra channel encoders	**Lowest QoS level**	**Medium QoS level**	**Highest QoS level**
	(2,1,8) D_{free} 10 T = 5 I/P 63b/s O/P 126 b/s	(3,1,8) D_{free} 16 T = 8 I/P 63b/s O/P 189 b/s	(4,1,8) D_{free} 22 T = 11 I/P 63b/s O/P 252 b/s
UMTS UL inner encoder	(2,1,9) D_{free} 12 T = 6 I/P 126 b/s O/P 252 b/s	(2,1,9) D_{free} 12 T = 6 I/P 189 b/s O/P 378 b/s	(2,1,9) D_{free} 12 T = 6 I/P 252 b/s O/P 504 b/s
UMTS DL inner encoder	(3,1,9) D_{free} 18 T = 9 I/P 126 b/s O/P 378 b/s	(3,1,9) D_{free} 18 T = 9 I/P 189 b/s O/P 567 b/s	(3,1,9) D_{free} 18 T = 9 I/P 252 b/s O/P 756 b/s
LTE UL inner encoder	(3,1,7) D_{free} 15 T = 7 I/P 126 b/s O/P 378 b/s	(3,1,7) D_{free} 15 T = 7 I/P 189 b/s O/P 567 b/s	(3,1,7) D_{free} 15 T = 7 I/P 252 b/s O/P 756 b/s

Table 4.
All error-correcting capabilities for MNC-proposed system codes.

The system design that is detailed above has been adjusted for the different QoS levels of medical data. The technical parameters of the extra channel codes have been fixed for the "Medical Network Channel (MNC)." The capabilities have been determined for the AWGN channel and for the Rayleigh fading with a parameter distribution function equal to 0.55. However, for seeking the reality, these channel conditions may be good or worse than those determined. **Table 4** details all the "Medical Network Channel (MNC)" adaptive design parameters with regard to the capability of correcting the channel errors.

4. Theoretical error-bound performance calculation key points

The error-bound probabilities are calculated depending on the inner, outer, and extra outer decoders separately. Continuously, the code performance is analyzed in terms of decoded BER. BER is normally calculated as a function of E_b/N_o. Here E_b represents the average energy transmitted per information bit and N_o represents the single-sided power spectral density of the assumed AWGN channel.

The performance bounds theoretically are driven under AWGN with and without adding WBANs end to end to "Medical Network Channel (MNC)"-proposed system. Then, the performance bounds theoretically are driven under Rayleigh fading channel without adding WBANs end to end; this step is only to demonstrate the feasibility of the "Medical Network Channel (MNC)" system and to find out the numbers of errors in the output of inner cellular decoders and to test the optimized extra channel code theoretically in "Medical Network Channel (MNC)" for different QoS medical data levels under AWGN and Rayleigh fading channels.

Table 5 explains all the technical parameters used in the theoretical evaluations. The theoretical bound follows number of steps to calculate the error probabilities for the adaptive "Medical Network Channel (MNC)" concatenated channel codes: the first step in the O/P of the inner cellular decoders, then second in the O/P of the extra channels decoders (the three sets for different QoS levels), and at last, in the O/P of the WBAN outer decoders. These numerical evaluations have been done in the two assumed inner cellular channel codes: UMTS and LTE.

The theoretical calculations for the error bound of the "Medical Network Channel (MNC)"-proposed system via AWGN could be done as many steps in the decoding side as in (Eq. (1)–(11)). The inner and extra channel used convolutional

QoS data	Code	R & K	G	d_f	$C_{2dfree-1}^{dfree}$	Sum of W_d
LTE		1/3&7	[133 171 165]	15	29!/15! × 14! 77558760	$W_d = \sum$[7 8 22 44 22 94 219] = 416
UMTS-UL	Inner	1/2&9	[561 753]	12	23!/12! × 11! 1352078	$W_d = \sum$ [33 281 2179 15035 105166] = 122694
UMTS-DL		1/3&9	[557 663 711]	18	35!/18! × 17! 4.5376e+009	$W_d = \sum$[11 32 195 564 1473] = 2275
Lowest QoS level		1/2&8	[247 371]	10	19!/10! × 9! 92378	$W_d = \sum$[2 22 60 148 340 1008 2642 6748] = 10970
Medium QoS level	Outer	1/3&8	[225 331 367]	16	32!/16! × 15! 300540195	$W_d = \sum$[1 24 113 287] = 425
Highest QoS level		1/4&8	[235 275 313 357]	22	43!/22! × 21! 1.0520e+012	$W_d = \sum$[2 10 108 10 11 54 64] = 169

Table 5.
Error correcting code capabilities for MNC system.

decoder that works using Viterbi algorithm and the outer WBAN channel used the block code decoder. First of all, the UMTS inner decoder calculates the first inner probability bit errors P_{bi} bound as in Eq.(1)–(4).

$$P_{bi} \leq \frac{1}{bi} \sum_{di=0}^{\infty} W_{di} P_{ei}(di) \tag{1}$$

where $P_{ei}(di)$ is the probability of confusing two sequences differing in distance di and positions of inner cellular code, and can be calculated as in Eq. (2). W_{di} is the weight spectrum that is the average number of bit errors associated with sequences of weigh di, and it is calculated for all codes that work in this "Medical Network Channel (MNC)" system as in **Table 5**; w(d), d $\geq$ df. W_{di} term can be evaluated using the transfer function of the convolution code. Generally, for codes whose constraint length is greater than a few units (typically, $\nu \geq 5$), the calculation of the transfer function can prove to be complex; then it is preferred to determine the spectrum of the code, or at least the first terms of this spectrum, using an algorithm that explores the various paths of the lattice diagram [9, 10].

$$P_{ei}(di) = Q\left(\sqrt{2\,diRi\ {}^{E_b}\!/_{N_0}}\right) \tag{2}$$

where di is an inner cellular code free distance and Ri is an inner cellular code rate, both showed in **Table 5**. Q function is clear in information theory and can be calculated using infinity integration as in Eq. (3).

$$Q(x) \cong \int_{x}^{\infty} \frac{1}{\sqrt{2\pi}} e^{-t^2/2} dt \tag{3}$$

$$P_{bi} \leq \frac{1}{bi} \sum_{di=0}^{\infty} W_{di} \cdot Q\left(\sqrt{2\,diRi\ {}^{E_b}\!/_{N_0}}\right) \tag{4}$$

Generally speaking, the data stream coming from the cellular inner codes feed to the extra outer codes. The code performance of the extra outer code is a function of the cellular inner code. Second, the extra outer decoder calculates the second outer probability bit errors P_{bo} bound separately as in Eq. (5)–Eq. (6) by the outer code parameter introduced in **Table 5** for the three different QoS levels of WBAN medical data.

$$P_{bo} \leq \frac{1}{bo} \sum_{do=0}^{\infty} W_{do} \cdot Q\left(\sqrt{2\,doRo\ {}^{E_b}\!/_{N_0}}\right) \tag{5}$$

$$P_b \ withno\ WBAN \leq P_{bi} \cdot P_{bo} \tag{6}$$

The outer code performances of the MNC system can be calculated by Eq. (6) for lower, medium, and higher QoS classes of medical data depending on the parameters applied to the extra channel. The last step is introduced by calculating the final outer code performance of the system. The WBAN decoder (63, 51, 2) calculates the last probability bit error P bound using Eq. (7)–Eq. (10), which is a function of the extra outer code.

$$P_b \leq \sum_{i=t+1}^{n} \binom{n}{i} P_x^i (1 - P_x)^{n-i} \ where\ \binom{n}{i} = \frac{n!}{(n-i)! \cdot i!} \tag{7}$$

$$P_b \leq \sum_{i=2+1}^{63} \binom{63}{i} P_x^i (1 - P_x)^{63-i} \tag{8}$$

$$P_x = Q\left(\sqrt{2R\,E_b/N_0}\right) = Q\left(\sqrt{2 \times 51/63 \cdot E_b/N_0}\right) \tag{9}$$

By using Eq. (9) as a function of Eq. (6) to calculate the final bound, we can have Eq. (10).

$$P_x \; with \; WBAN = P_b \; withno \; WBAN \cdot P_x \tag{10}$$

Then, by applying Eq. (10) in Eq. (7), we will have the final MNC system by adding WBAN code end to end for all QoS assumed and via AWGN channel in Eq. (11).

$$P_b \; with \; WBAN \leq \sum_{i=2+1}^{63} \binom{63}{i} P_x^i \; withno \; WBAN \, (1 - P_x \; withno \; WBAN)^{63-i} \tag{11}$$

The theoretical calculations for the error bound of the MNC system via Rayleigh fading channel could be done by the same steps of calculating it via AWGN channel without end-to-end connection of the WBANs. For this part, the $P_{j,I}$ attenuations are random independent Rayleigh variables of probability density as in Eq. (12).

$$P\left(\rho_{j,i}\right) \cong \frac{1}{\sigma_\rho^2}\rho_{j,i}e^{\left(-\frac{\rho_{j,i}^2}{2\sigma_\rho^2}\right)} \prod_{\rho_{j,i}} \geq 0 \tag{12}$$

where $e^{\Lambda}\left(-\frac{\rho_{j,i}^2}{2\sigma_\rho^2}\right)$ and $\prod_{\rho_{j,i}} \geq 0$ are the indicators of the set $\{\rho_{j,i} \geq 0\}$, which equals 1 if $\rho_{j,i} \geq 0$, and 0 if not. In all theoretical work of MNC system, this Rayleigh variable has been estimated as 0.55, which is greater than 0, to evaluate the super PHY channel of MNC system. First of all, the cellular decoder calculates the first inner probability bit errors P_{bi} bound as a function of the performance of the BFSK modulation as in Eq. (13).

$$P_{bfsk} \cong \frac{1}{2}\left[1 - \sqrt{\frac{\overline{E_b/N_o}}{1 + \overline{E_b/N_o}}}\right] \tag{13}$$

$$P_b \leq \frac{w(df)}{b}C_{2df-1}^{df}\left(\frac{1}{4R\,\overline{E_b/N_o}}\right)^{df} \tag{14}$$

where C can be calculated using the free distance d_{freei} of the inner cellular code by Eq. (15) and appeared in **Table 5**. E_b represents the average energy received per symbol of transmitted information, and it is calculated as in Eq. (16). Then, the inner cellular code performance can be calculated by Eq. (17).

$$C_{2df-1}^{df} = \frac{(2d-1)!}{d! \cdot (d-1)!} \tag{15}$$

$$\overline{E_b} = E\left(\rho_{j,i}^2\right)E_b = 2\sigma_\rho^2 E_b = 0.55E_b \; assumed \tag{16}$$

$$P_{bi} \leq P_{bfsk} \cdot \frac{w(dfreei)}{bi}C_{2dfreei-1}^{dfreei}\left(\frac{1}{4Ri\,\overline{E_b/N_o}}\right)^{dfreei} \tag{17}$$

Generally speaking, the data stream coming from the cellular inner code feeds the extra channel code. The code performance of the extra outer code is a function of the inner cellular code. Second, the outer decoder calculates the second outer

probability bit errors P_{bo} bound separately as in Eq. (18) by the outer code parameters introduced in **Table 5**.

$$P_{bo} \leq P_{bfsk} \cdot \frac{w(dfreeo)}{bo} C_{2dfreeo-1}^{dfreeo} \left(\frac{1}{4Ro\ \overline{E_b}/N_o} \right)^{dfreeo} \qquad (18)$$

Then, the extra outer code performances of super PHY channel MNC system under Rayleigh fading can be calculated by Eq. (19).

$$P_b \leq P_{bi} \cdot P_{bo} \qquad (19)$$

The theoretical performances have been calculated for the MNC system with different QoS levels by using the cellular standards as an inner code via AWGN and Rayleigh fading noisy channels.

The first case is via WBANs. In this case, where the inner codes work as a UMTS channel, there are two kinds of codes, when using the cellular parameters in **Table 2**. One is the error probability as in Eq. (20) for UL and other is the error probability as in Eq. (21) for DL.

$$P_{bi}UL \leq 122694\ Q\left(\sqrt{12\ E_b/N_0} \right) \qquad (20)$$

$$P_{bi}DL \leq 2275\ Q\left(\sqrt{12\ E_b/N_0} \right) \qquad (21)$$

In the second step in the O/P of the extra channel code, there are three targeting QoS levels. Therefore, the probability of the error can be calculated from Eq. (5) as in Eq. (22)–Eq. (24) for the different code sets.

$$P_{bo}\ LQoS \leq 10970\ Q\left(\sqrt{10\ E_b/N_0} \right) \qquad (22)$$

$$P_{bo}\ MQoS \leq 425\ Q\left(\sqrt{32/3\ E_b/N_0} \right) \qquad (23)$$

$$P_{bo}\ HQoS \leq 169\ Q\left(\sqrt{11\ E_b/N_0} \right) \qquad (24)$$

From here, the error probability for the "Medical Network Channel (MNC)"-proposed system without end-to-end connection of WBANs can be calculated from Eq. (6) as six levels of error probability as in Eq. (25).

$$P_b\ withno\ WBAN \leq P_{bi}\ UL, DL \cdot P_{bo}\ LQoS, MQoS, HQoS \qquad (25)$$

The final steps here can be done when the WBANs are connected end to end through the system. Therefore, using Eq. (25) in Eq. (11), we can have the final error probability of the system.

$$P_b\ with\ WBAN \leq \sum_{i=2+1}^{63} \binom{63}{i} P_x^i\ withno\ WBAN\ (1 - P_x\ withno\ WBAN)^{63-i} \qquad (26)$$

The second case is via WBANs. In this case where the inner codes work as an LTE channel, when using the LTE cellular parameters in **Table 2**, we will have the probability of errors as in Eq. (27).

$$P_{bi}\ LTE \leq 416\ Q\left(\sqrt{10E_b/N_0} \right) \qquad (27)$$

In the second step in the O/P of the extra channel code, there are three targeting QoS levels. Therefore, the probability of the error can be calculated from Eq. (5) as in Eq. (22)–(24) for the different code sets. From here, the error probability for the MNC system without end-to-end connection of WBANs through the LTE can be calculated from Eq. (6) as six levels of error probability as in Eq. (28).

$$P_b \ withno \ WBAN \le P_{bi} \ LTE \cdot P_{bo} \ LQoS, MQoS, HQoS \qquad (28)$$

The final step here can be done when the WBANs are connected end to end through the proposed system. Therefore, using Eq. (28) in Eq. (11), we can have the final error probability of the "Medical Network Channel (MNC)" system.

$$P_b with \ WBAN - LTE \le \sum_{i=2+1}^{63} \binom{63}{i} P_b^i withno \ WBAN \ (1 - P_b \ withno \ WBAN)^{63-i}$$

$$(29)$$

The third case is via Rayleigh fading. In this case where the inner codes work as a UMTS channel, there are two kinds of codes: UL and DL. By using the cellular parameters, we will have the probability of errors as in Eq. (30) in the case of UL and Eq. (31) in the case of DL.

$$P_{bi} \ UL \le P_{bfsk} \cdot \frac{w(dfreei)}{b} C_{2dfreei-1}^{dfreei} \left(\frac{1}{4Ri \ \overline{E_b}/N_o} \right)^{dfreei} \qquad (30)$$

$$P_{bi} \ DL \le P_{bfsk} \cdot \frac{w(dfreei)}{bi} C_{2dfreei-1}^{dfreei} \left(\frac{1}{4Ri \ \overline{E_b}/N_o} \right)^{dfreei} \qquad (31)$$

In the second step in the O/P of the extra channel code, there are three targeting QoS levels. Therefore, the probability of the error can be calculated from Eq. (18) as in Eq. (32)–(34).

$$P_{bo} \ LQoS \le P_{bfsk} \cdot \frac{w(dfreeo)}{bo} C_{2dfreeo-1}^{dfreeo} \left(\frac{1}{4Ro \ \overline{E_b}/N_o} \right)^{dfreeo} \qquad (32)$$

$$P_{bo} \ MQoS \le P_{bfsk} \cdot \frac{w(dfreeo)}{bo} C_{2dfreeo-1}^{dfreeo} \left(\frac{1}{4Ro \ \overline{E_b}/N_o} \right)^{dfreeo} \qquad (33)$$

$$P_{bo} \ HQoS \le P_{bfsk} \cdot \frac{w(dfreeo)}{bo} C_{2dfreeo-1}^{dfreeo} \left(\frac{1}{4Ro \ \overline{E_b}/N_o} \right)^{dfreeo} \qquad (34)$$

From here, the error probability for the "Medical Network Channel (MNC)"-proposed system without end-to-end connection of WBANs could be calculated from Eq. (19) as three levels of error probability as in Eq. (35).

$$P_b \ withno \ WBAN \le P_{bi} \ UL, DL \cdot P_{bo} \ LQoS, MQoS, HQoS \qquad (35)$$

The fourth case is via Rayleigh fading. In the case where the inner codes work as an LTE channel, when using the cellular parameters in Eq. (17), we will have the probability of errors as Eq. (36).

$$P_{bi} \ LTE \le P_{bfsk} \cdot \frac{w(dfreei)}{b} C_{2dfreei-1}^{dfreei} \left(\frac{1}{4Ri \ \overline{E_b}/N_o} \right)^{dfreei} \qquad (36)$$

Then, from here, the error probability for the "Medical Network Channel (MNC)" system without end-to-end connection of WBANs can be calculated from Eq. (19) as three levels of error probability as in Eq. (37).

$$P_b \; withno \; WBAN \leq P_{bi} \; LTE \cdot P_{bo} \; LQoS, MQoS, HQoS \qquad (37)$$

Finally, **Table 6** shows the numerical evaluation of the "Medical Network Channel (MNC)" system with different categories, with the inner channel as UMTS UL, DL, and LTE as well. Regarding to the figures results, **Figure 3** shows the theoretical performance when the channel is affected by AWGN for MNC via

The results via AWGN						
E_b/N_o	0 dB	1 dB	2 dB	3 dB	4 dB	5 dB
WBANs	0.1763	0.1379	0.0933	0.0515	0.0215	0.0062
LTE	0.3256	0.0807	0.0143	0.0017	0.0001	0.0000
Low-QoS	2.7957	0.1717	0.0054	0.0001	0.0000	0.0000
Medium-QoS	0.0755	0.0042	0.0001	0.0000	0.0000	0.0000
High-QoS	0.0251	0.0014	0.0000	0.0000	0.0000	0.0000
Low-QoS-WBANs	1.0000	0.0506	0.0000	0.0000	0.0000	0.0000
Medium-QoS-WBANs	0.0127	0.0000	0.0000	0.0000	0.0000	0.0000
High-QoS-WBANs	0.5854	0.0000	0.0000	0.0000	0.0000	0.0000
The results via Rayleigh fading of PDF 0.55						
E_b/N_o	0 dB	1 dB	2 dB	3 dB	4 dB	5 dB
UMTS-UL	4.9532	0.0001	0.0000	0.0000	0.0000	0.0000
Low-QoS	1.9352	0.0000	0.0000	0.0000	0.0000	0.0000
Medium-QoS	9.0438	0.0000	0.0000	0.0000	0.0000	0.0000
High-QoS	4.5376	0.0000	0.0000	0.0000	0.0000	0.0000

Table 6.
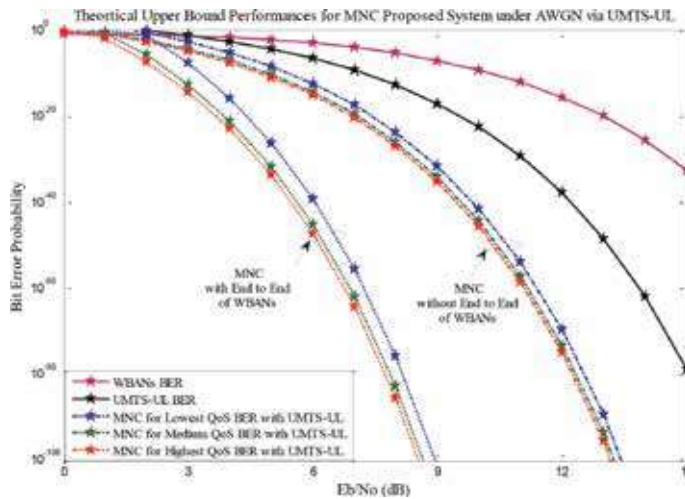*Theoretical error bit performances for MNC system.*

Figure 3.
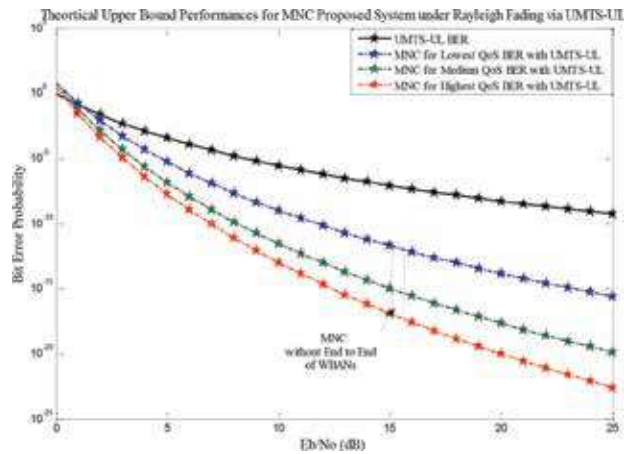*All priority results via UMTS under AWGN theoretically.*

Figure 4.
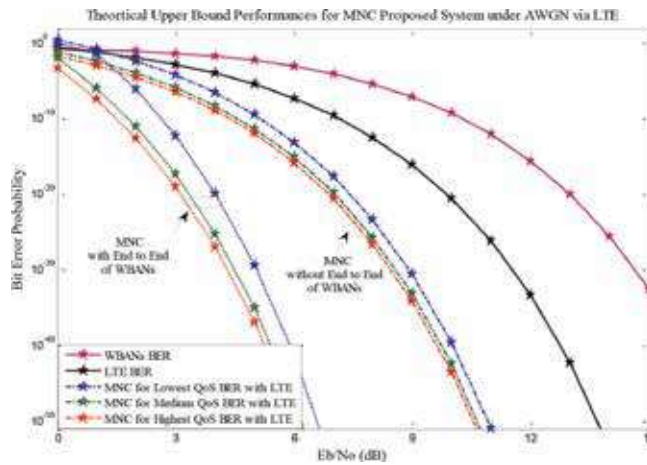*All priority results via UMTS under Rayleigh fading theoretically.*

Figure 5.
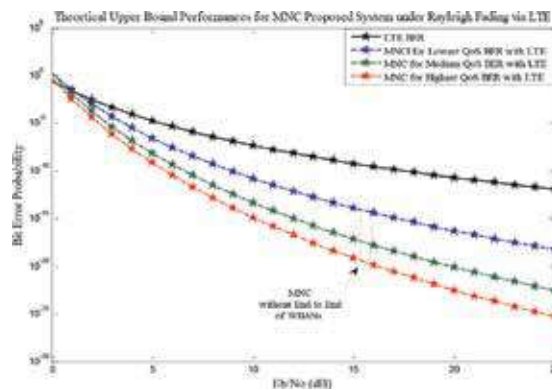*All priority results via LTE under AWGN theoretically.*

Figure 6.
All priority results via LTE under Rayleigh fading theoretically.

UMTS networks. **Figure 4** shows the theoretical performance when the channel is affected by Rayleigh fading for MNC via UMTS networks. **Figure 5** shows the theoretical performance when the channel is affected by AWGN for MNC via LTE networks. Finally, **Figure 6** shows the theoretical performance when the channel is affected by Rayleigh fading for MNC via LTE networks.

5. Conclusions

The main purpose of "Medical Network Channel (MNC)" systems is to have a reliable medical network channel via the cellular infrastructure networks by end-to-end WBAN connection. Therefore, the stanchions establishment of "Medical Network Channel (MNC)" with error controlling coding and decoding through existing infrastructure networks such as UMTS and LTE is introduced in this chapter with an end-to-end connection of WBANs and without the connection of WBANs considering the medical data coming from different sources. The understanding of the eight levels of the QoS medical data has been done well; however, the optimizations here have been classified into three classes (lower, medium, and higher) for all medical QoS data. Therefore, the MNC system is a novel way considering the dependability issues by this way for the first time with regard to the QoS constraint for the different medical applications of WBANs. Although the adaptive extra outer code for "Medical Network Channel (MNC)" is based on the convolution code, the choice of the technical parameters is different from one to another depending on the QoS targeted and on the capability of cellular standard itself, which is a remaining error in the O/P of the inner cellular code.

Although the current cellular standard has strong error detection and correction capability, it is designed well for the daily life communication without considering medical data transmission, and in some hard noisy channel situations that exceed the design capabilities, the cellular network cannot perform well. Therefore, the Medical Networks channel MNC system has been introduced new novel approach to connect WBANs end-to-end via the cellular networks by providing very large BER for the different assumed QoS levels of medical data to be transmit robustly and achieving the enhancement E_b/N_o gap under all the environments condition that assumed in compare to conventional cellular system alone. Then the adaptive "Medical Network Channel (MNC)" system overcomes the weakness of cellular networks with regard to the dependability issues and provides even better performance than the cellular network for the purpose of medical data transmission. These performances allow MNC equivalence for transmitting medical data by the highest possible level of the dependability required. In regard to achieving different QoS of WBAN requirements, the results in **Table 6** and BER **Figures 3–6** cleared all the study cases carefully for adaptive "Medical Network Channel (MNC)" system. Generally, the adaptive medical network channel introduced in this chapter is through the cellular networks. However, all communication network standards can be applied using error correcting techniques to be adaptive for medical data transmission.

Conflict of interest

There is no conflict of interest for this work from anyone.

Author details

Emtithal Ahmed Talha[1*] and Ryuji Kohno[2]

1 Sudan International University, Khartoum, Sudan

2 Yokohama National University, Yokohama, Japan

*Address all correspondence to: Emtithal-talha-xb@ynu.jp

IntechOpen

References

[1] IEEE. IEEE standard for local and metropolitan area networks–Part 15.6: Wireless Body Area Networks. IEEE Std 802.15.6-2012; 2012

[2] Yuce MR, Khan J. Wireless Body Area Networks: Technology, Implementation, and Applications. Pan Stanford: CRC Press; 2011

[3] Movassaghi S, Abolhasan M, Lipman J, Smith D, Jamalipour A. Wireless body area networks: A survey. IEEE Communications Surveys & Tutorials. 2014;**16**(3):1658-1686. Third

[4] Murtaza S. QoS Taxonomy towards wireless body area network solutions. International Journal of Application or Innovation in Engineering & Management (IJAIEM). 2013;**2**(4)

[5] ETSI. Universal Mobile Telecommunications System (UMTS); Multiplexing and Channel Coding (FDD). European Telecommunications Standards Institute, Technical Specification TS 125 212; 2011

[6] ETSI. Universal Mobile Telecommunications System (UMTS); Multiplexing and Channel Coding (TDD). European Telecommunications Standards Institute, Technical Specification TS 125 222; 2010

[7] ETSI. LTE; Evolved Universal Terrestrial Radio Access (E-UTRA); Multiplexing and Channel Coding. European Telecommunications Standards Institute, Technical Specification TS 136 212; 2013

[8] Xing J, Zhu Y. A Survey on body area network. In: 5th International Conference on Wireless Communications, Networking and Mobile Computing, 2009. WiCom '09. pp. 1-4; 2009

[9] Alain Glavieux, Channel Coding in Communication Networks: From Theory to Turbocodes. ISTE Ltd, Wiley; 2007

[10] Semenov S, Krouk E. Modulation and Coding Techniques in Wireless Communications. John Wiley & Sons; 2011

Chapter 6

Combined Crosstalk Avoidance Code with Error Control Code for Detection and Correction of Random and Burst Errors

Ashok Kumar Kummary, Perumal Dananjayan,
Kalannagari Viswanath and Vanga Karunakar Reddy

Abstract

Error correction codes are majorly important to detect and correct occurred errors because of various noise sources. When the technology is scaling down, the effect of noise sources is high. The coupling capacitance is one of the main constraints to affect the performance of on-chip interconnects. Because of coupling capacitance, the crosstalk is introduced at on-chip interconnecting wires. To control the single or multiple errors, an efficient error correction code is required. By combining crosstalk avoidance with error control code, the reliable intercommunication is obtained in network-on-chip (NoC)-based system on chip (SoC). To reduce the power consumption of error control codes, the bus invert-based low-power code is integrated to network interface of NoC. The advanced work is designed and implemented with Xilinx 14.7; thereby the performance of improved NoC is evaluated and compared with existing work. The 8×8 mesh-based NoC is simulated at various traffic patterns to analyze the energy dissipation and average data packet latency.

Keywords: NoC, CAC, ECC LPC, SoC, FPGA

1. Introduction

As technology is scaling up, a number of circuits are integrated in on-chip. The intercommunication among the on-chip devices is majorly important because of millions of integrated devices in the system on chip (SoC). The communication architectures of SoC are not efficient to provide high performance; thereby network-on-chip (NoC) is the new paradigm introduced [1]. Because of parallelism, the NoC is providing high performance in terms of scalability and flexibility even in the case of millions of on-chip devices. Still, NoC suffers with design parameters that affect the performance of NoC. As technology is scaling up, the performance of NoC is mainly affected with coupling capacitance. The effect of crosstalk capacitance is more in horizontal than in vertical; thereby the crosstalk errors frequently occur in on-chip interconnecting wires [2]. An efficient error correction code is required to control the crosstalk error that may occur once or multiple times. The crosstalk avoidance codes (CAC) are popularized to control the error in on-chip interconnects; thereby a reliable communication is obtained.
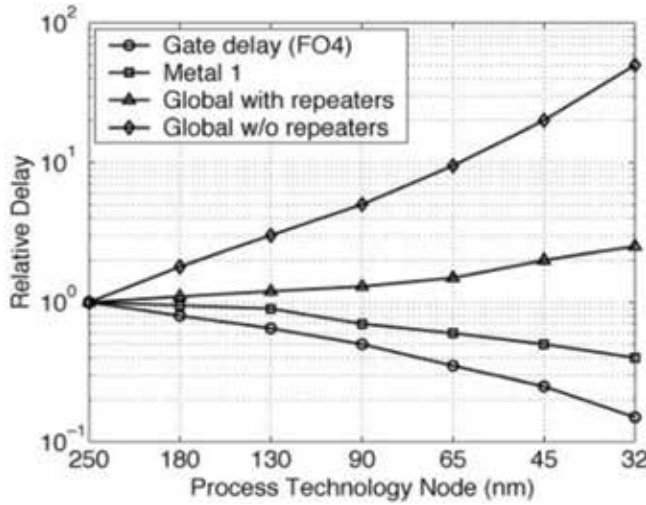
Figure 1.
Trend of relative delay with scaling of technology [3].

The CAC reduced the worst-case switching capacitance in on-chip interconnects by avoiding the switching transitions of data that is 010-101. This condition reduced the worst-case capacitance from $(1 + 4\lambda) C_L$ to $(1 + 2\lambda) C_L$; hence, the energy dissipation is reduced from $(1 + 4\lambda) C_L \alpha V^2_{dd}$ to $(1 + 2\lambda) C_L \alpha V^2_{dd}$ where λ is the ratio of coupling capacitance to total capacitance, C_L is the self-capacitance of interconnection wire, α is the transition factor, and V_{dd} is the supply voltage for the system. The energy dissipation is reduced by reducing the transition activity of interconnection wires for the data packet. The behavior of relative delay with scaling of technology is shown in **Figure 1**.

International Technology Roadmap for Semiconductor (ITRS-2011) predicted that when the delay from the gates is reduced, the delay from wires is increased with scaling of technology because the interconnecting wires are affected more when scaling of technology is less than 45 nm [3]. Hence, the interconnecting wires affected the performance of NoC-based SoC in terms of delay as well as energy consumption, and it is huge in case of the errors.

The errors mainly occur in interconnecting wires because of coupling capacitance; thereby strong error correction code (ECC) is required to detect and correct errors [4]. The error may occur once or multiple times, and also multiple errors occurred in interconnection wires; hence, the ECCs are not enough to detect and correct errors. In literature, different techniques are proposed for detection and correction of multiple errors. The parity check, dual rail (DR), modified dual rail (MDR), boundary shift code (BSC), and CAC are popularized among various techniques for control of multiple errors in interconnection wires.

The remaining chapter is as follows: Section 2 includes the related work of error control methods and also discussed the merits and demerits. Section 3 presented the proposed encoder and decoder of combined CAC-ECC method. Section 4 gives the advanced encoding and decoding of NoC router with combined LPC-CAC-ECC scheme. Section 5 discussed the implementation of proposed work in NoC architecture, and finally, Section 6 concludes the chapter.

2. Related work

The detection and correction of errors present in the on-chip interconnects are majorly important because it leads to drop or block data packet; hence the performance

of NoC architecture is reduced. Huge research is going on for the error detection and correction of on-chip interconnects. Parity code is used to detect 1-bit error in data packet. It is simple but errors are not corrected. Hamming code is proposed for detection of 2-bit errors and also correction of 1-bit error [5]. Various error control codes are introduced with the help of hamming code because it is easy to implement.

To reduce delay in on-chip interconnects, forbidden overlap condition (FOC), forbidden transition condition (FTC), and forbidden pattern condition (FPC) of crosstalk avoidance code are used [6]. The crosstalk avoidance codes are reduced delay from $(1 + 4\lambda) C_L$ to $(1 + 2\lambda) C_L$ and also energy dissipation. Still, the area utilization has increased because the extra bits are added to the original data packet. To control multiple errors, duplicate parity (DAP) is proposed by duplicating data packets, and then hamming code is used for transmission of duplicated data [7]. The average data packet latency is reduced by DAP-based method, although the power consumption has increased because the number of interconnecting wires is increased. To reduce the power consumption in the case of crosstalk avoidance codes, Sridhara and Shanbhag [8] proposed and combined a low-power code (LPC) with crosstalk avoidance codes.

The FOC, FTC, and FPC are used for detection and correction of errors due to crosstalk; thereby the data packet latency is reduced. To reduce power consumption, bus invert-based technique is used and combined with error control codes. The joint LPC-CAC code improved the performance of NoC, but still, area utilization has increased. To obtain reliable on-chip communication, Single Error Correcting-Burst Error Detecting (SEC-BED) with Hybrid Automatic Repeat reQuest (HARQ) is proposed. The single random error is detected and corrected, whereas the retransmission is requested when double random and burst errors are detected. The SEC-BED scheme detected errors efficiently, although the delay, area, and power consumption have increased because of Ex-Or-based tree structure used in calculating parity check bits and go-back-N-based retransmission used in HARQ.

To reduce worst-case bus delay, joint crosstalk avoidance with triple error correction (JTEC) code is proposed. In encoding operation, the code word is used with hamming code and then duplicated. Because hamming code is duplicated, the decoder detected 4-bit errors and corrected 3-bit errors. Because JTEC required large area, JTEC is advanced as JTEC-simultaneous quadruple error detection (JTEC-SQED). The JTEC-SQED replaced hamming codes into Hsiao codes; thereby the performance is improved when compared with JTEC. To increase error control capability, triplicate add parity (TAP) is used for encoding data and compared with sent parity bit in decoder to detect and correct the errors in interconnecting wires [9]. The TAP-based error control scheme efficiently detected and corrected 1-bit, 2-bit, and some 3-bit errors. Still, the power consumption has increased because the required number of interconnecting wires increases.

To reduce the power consumption with TAP-based scheme, this chapter proposes joint LPC-CAC-ECC scheme to detect and correct 1-bit, 2-bit, and some 3-bit burst errors efficiently, and also the power consumption of codec module is reduced with the help of BI technique. The proposed work is mainly concentrated on controlling of multiple errors and also improving of NoC communication architecture.

3. Joint CAC-ECC

The ability of error control method is determined by the reliable communication which is provided in the presence of errors. By embedding the error control schemes, the performance of the system is reduced when compared with error control scheme-less system. The data packet latency and power consumption

affect more in the presence of error control schemes. To detect and correct multiple errors efficiently, the CAC-ECC methods are combined. In this chapter, the 1-bit and 2-bit errors due to crosstalk are detected and corrected and also some of the 3-bit errors.

Triplicate add parity (TAP)-based encoder is used to transfer the data from source to destination through the interconnection wires. **Figure 2** depicts TAP-based encoder of joint CAC-ECC scheme. The 32-bit data triplicates to encode to the destination through interconnection wires. In the advanced encoder, each data bit triplicates and also calculates overall parity of 32-bit data; hence, a total of 97-bits of data are encoded to the decoder section. By triplication, the errors are efficiently controlled in the interconnecting wires.

The parity bit is also measured with Ex-Or operation and encoded to the decoder section to check the parity of received data. By the comparison of parity, the errors are detected and corrected efficiently. The decoder structure of joint CAC-ECC scheme is shown in **Figure 3**.

The decoder divides encoded data into three groups, and parity of each group is calculated and compared with sent parity bit. The encoded data are divided into three groups of 32-bit data with the help of group separator, and sent parity bit (p0) is used to compare with the parity of each group (p1, p2, p3). The 1-bit and 2-bit errors are detected when parity of group changed from sent parity. **Table 1** depicts the different possibilities of errors at data bits in interconnection wires. The 1-bit errors are detected with its parity. The 2- and 3-bit errors are identified by considering the following instances:

Instance I: p1 = p2 and p2 ≠ p3.

To find out error-less group, the parity of group 1 is compared with sent parity (p0). If p0 is equal to p1, then group 1 is considered as error-less, otherwise group 3 is considered as error-less.

Instance II: p1 ≠ p2 and p2 = p3.

To find out error-less group, the parity of group 1 is compared with sent parity. If p0 is equal to p1, then group 1 is considered as error-free, otherwise group 2 is error-free.
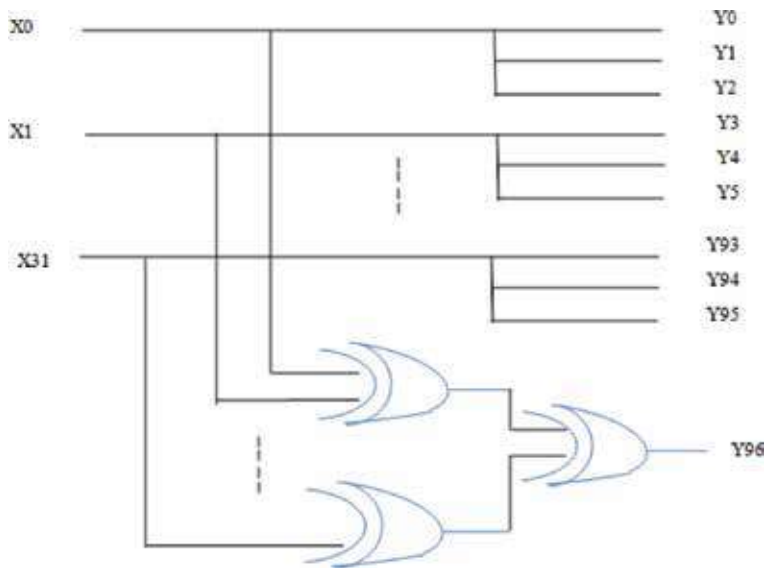

Figure 2.
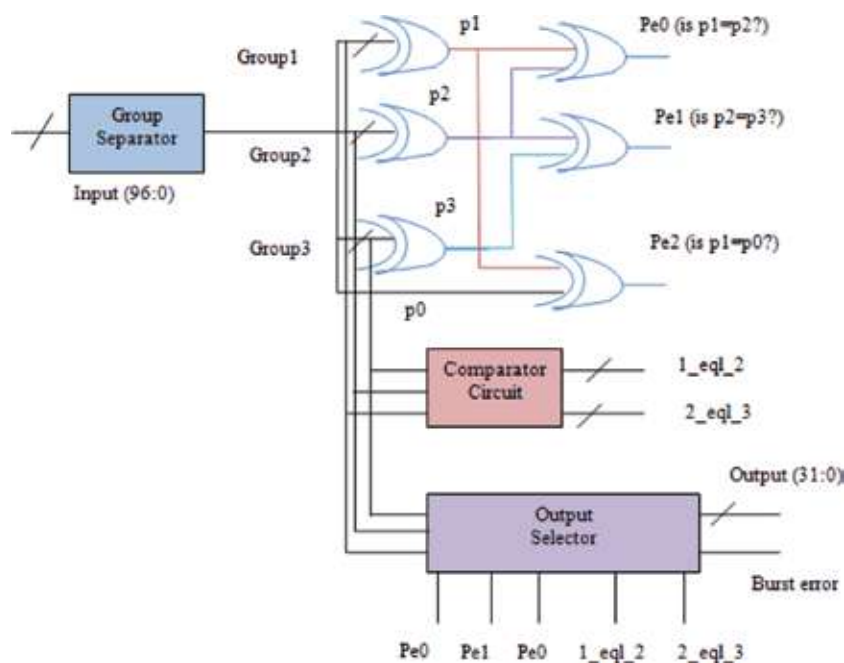*TAP-based encoder of proposed scheme.*

Figure 3.
Decoder structure of joint CAC-ECC scheme.

Instance III: $p1 \neq p2$ and $p2 \neq p3$.

To find out error-less group, the parity of group 1 is compared with sent parity. If $p0 = p1$, then the group is considered as error-free, otherwise group 2 is error-free.

Instance IV: $p1 = p2$ and $p2 = p3$.

The error bits highlighted in **Table 1** are considered for this instance. Because of not detecting the even parities, the error bits having even parities are divided into two categories. (i) 1-bit error in three groups is called burst error. When $p0 = p1$ and $p1 = p2$, then burst error is detectable or else consider another category. (ii) The original data of group 1, group 2, and group 3 are compared to select error-free group. When group 1 is equal to group 2, then group 2 is selected as error-free or else group 2 and group 3 are compared again. When group 2 is equal to group 3, then group is considered as error-free or else group-1 is considered as error-free.

The number of detection and correction bits of ECC depended on the hamming distance of technique. The hamming distance of TAP-based scheme is four; that is, the triplication of data is presented, the hamming distance is three, and also one is from added parity bit. If the hamming distance of original data packets is k, then

	1-bit error				2-bit errors						3-bit errors								
Group 1 (p1)	1	0	0	1	0	1	**2**	**0**	**0**	**1**	0	1	0	3	0	0	1	2	2
Group 2 (p2)	0	1	0	1	1	0	**0**	**2**	**0**	**1**	1	0	2	0	3	0	2	1	0
Group 3 (p3)	0	0	1	0	1	1	**0**	**0**	**2**	**1**	2	2	1	0	0	3	0	0	1
	Correct				Correct						Correct					Incorrect			

Table 1.
Different possible error bits in interconnecting wires.

the number of detection error bits is k – 1 and the number of correction bits is $\frac{k-1}{2}$; hence, CAC-ECC scheme detected three error bits and corrected two error bits.

Though the CAC-ECC scheme has detected and corrected crosstalk errors efficiently, the power consumption and data packet latency have huge increase because more number of interconnecting wires are used in the advanced error control scheme. Because of triplication of original data, the combined CAC-ECC scheme used more number of wires; thereby the power consumption of advanced method has increased.

4. Advanced NoC router

The errors affect more on the performance of NoC-based SoC because of more number of interconnection links involved for parallel processing. The combined CAC-ECC scheme is embedded in the network interface (NI) of router; thereby the errors are controlled and also avoided to propagate to remaining network. The encoder of error control scheme is embedded to transmit NI (TX-NI), and decoder of error control scheme is added to the receive NI (RX-NI); thereby the original data are transferred efficiently. Because of embedded combined CAC-ECC in the NI, the router of NoC presented huge power consumption; hence, there is a need of reducing the power consumption in NoC. By analyzing various error control schemes in NI, flexible unequal error control (FUEC) methodology is introduced and generalized to any kind of error control codes [10].

4.1 Combined LPC-CA-ECC scheme

To reduce power consumption in NoC architecture in the case of error control schemes, the low-power code is added to the error control codes; thereby the power consumption is reduced and also errors are corrected efficiently. Bus invert (BI) method is used to reduce the transition activity of interconnecting wires; thereby the power consumption is reduced. The power consumption is given in eq. (1).

$$P_d = \alpha C_L f_c V_{dd}^2 \tag{1}$$

where α is the transition activity, C_L is the load capacitance, f_c is the maximum clock frequency, and v_{dd} is the supply voltage. From Eq. (1), it is known that the dynamic power consumption is directly proportional to the transition activity.

The bus invert-based low-power code (LPC) is shown in **Figure 4**. The BI technique reduced the number of transitions by using the hamming distance of original data packet; thereby the original data are inverted before encoding. The original data are inverted when the hamming distance is more than half, otherwise it is sent to encoder without inverting. The majority of voter circuit with combination of Ex-Or gates inverted the data when it is required. The majority of voter circuit is composed of a number of full-adders, which increases the size of circuit.

4.2 HARQ

The combined LPC-CAC-ECC scheme detected and corrected multiple crosstalk errors and also reduced the power consumption of on-chip interconnects. The error control scheme does not correct some of the 3-bit errors; hence, the hybrid automatic retransmission request (HARQ) is enabled to retransfer the data from source to destination. The HARQ resend the data packets when the receiver asserted continuous three negative acknowledgments (NACK).
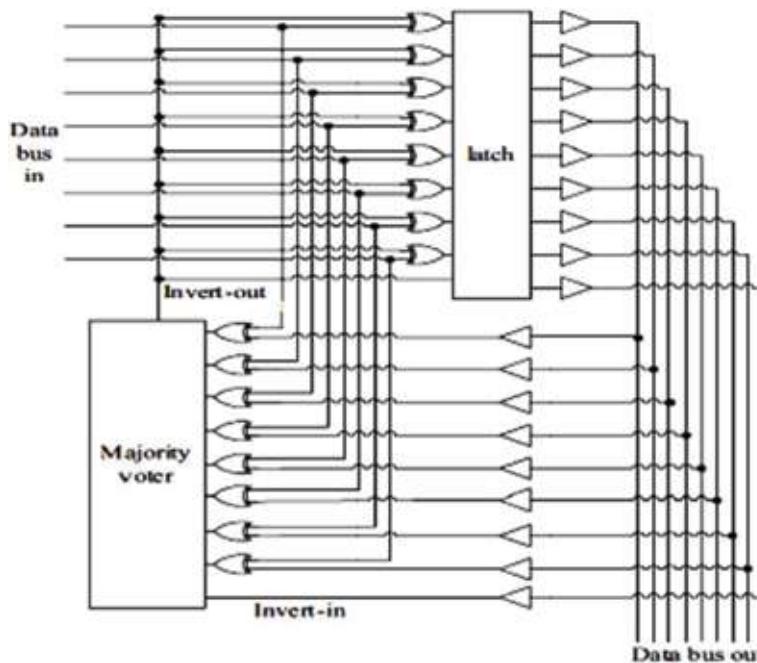
Figure 4.
Bus invert method of low-power code.

The advanced work of error control scheme is embedded in the NI of the NoC, and also codec module is responsible for encoding and decoding of the data without errors. To improve the data transfer speed of NoC, each router is added with an extra PE; thereby the number of router required to complete data transfer is reduced. To control arbitration among ports of router, the advanced scheduling algorithms are used in arbiter. The selected port transferred the data to the output through crossbar switch. To avoid deadlock error, each port of router is composed of buffer memory and its controller. A store and forward packet switching (SF) and minimal routing algorithm are used to improve the performance of mesh-based NoC architecture [11].

5. Implementation

The advanced error control scheme is designed in Xilinx 14.7 and implemented on Virtex-6 Field Programmable Gate Array (FPGA) target device. The simulation and synthesis are demonstrated for each module of NoC. The performance of NoC is evaluated in terms of area utilization (occupied slices, LUT-FF pairs, and bonded IOBs), latency (delay), and power consumption. **Table 2** shows the performance of encoder and decoder of joint CAC-ECC scheme. The area utilization and delay of codec module are increased linearly with the increase of data width because of the number of interconnection wires in encoder and also the number of cycles required to detect and correct error in decoder.

The data transfer of the encoder is more than the decoder because of the number of rounds required to detect and correct. The required cycles increase more in the case of more number of error bits and also higher data width. **Tables 3** and **4** show the performance of NoC router with CAC-ECC scheme and joint CAC-ECC-LPC scheme. From **Table 3**, it is inferred that the data transfer speed of NoC in the presence of soft errors decreased with the increase of data width because more number of interconnecting

Family	Number of occupied slices		Number of slice LUTs		Number of bonded IOBs		Delay (ns)	
	Encoder	Decoder	Encoder	Decoder	Encoder	Decoder	Encoder	Decoder
8-bit	1	15	2	39	35	36	1.01	2.82
16-bit	3	24	2	42	67	68	1.37	3.15
32-bit	7	49	7	79	131	132	1.53	3.20

Table 2.
Area utilization and delay of codec module of CAC-ECC scheme.

Family	Number of slice registers	Number of slice LUTs	Number of fully used LUT-FF pairs	Latency (ns)	Power consumption (mW)
8-bit	814	566	375	3.70	9.56
16-bit	952	636	453	5.52	47.42
32-bit	1858	1485	676	6.06	89.55

Table 3.
Performance of NoC router with CAC-ECC scheme.

wires are required for encoder of CAC-ECC scheme and also more number of cycles are required in decoder to detect and correct the soft errors in on-chip interconnecting wires. Hence, the power consumption is huge when data width is large.

From **Table 4**, it is clear that the low-power code is reducing the total power consumption even in the case of error control schemes. It is observed that the data transfer speed of NoC maintained the same and the power consumption is reduced from little to huge when data width is increased. Still, the area utilization is increased in joint LPC-CAC-ECC scheme because of a number of combinational circuits required in BI method to reduce the power consumption.

As BI code worked based on hamming distance of original data, the area utilization is increased. Still, it is reduced when hamming distance of original data is less than half; hence, the performance of NoC is improved.

Table 5 shows the comparison of proposed error control scheme with recent schemes for 32-bit of data width. From **Table 5**, it is observed that the proposed method shows better results than the existing error control methods. The comparison is shown with various parameters such as number of wires used, number of error detection and correction, swing voltage of interconnect, delay for detection and correction, and also power consumption. Among all methods, CADEC provided better results than the proposed work. Still, detection and correction of CADEC are limited to 2-bit errors. The power consumption of proposed work has improved to 11% than JTEC.

Family	Number of slice registers	Number of slice LUTs	Number of fully used LUT-FF pairs	Latency (ns)	Power consumption (mW)
8-bit	823	635	440	3.70	9.40
16-bit	996	764	518	5.52	46.90
32-bit	1926	1599	1014	6.06	81.64

Table 4.
Performance of NoC router with joint LPC-CAC-ECC method.

S. no.	Coding scheme	Data width	Number of wires used	Error detection	Error correction	Link swing voltage (V)	Delay	Power consumption (µW)
1	Hamming	32	38	Double	Single	1.02	1 + 4λ	49.30
2	Hsiao SEC-DED [12]	32	39	Double	Single	1.02	1 + 4λ	51.60
3	DAP [13]	32	65	Double	Single	1.02	1 + 2λ	16.22
4	CADEC [7]	32	77	Random and burst error of two	1-bit and 2-bit errors	0.89	1 + 2λ	26.77
5	JTEC [14]	32	77	Random and burst error of three	1-bit and 2-bit errors	0.81	1 + 2λ	39.49
6	Joint LPC-CAC-ECC	32	97	Random and burst error of three	1-bit, 2-bit errors, and some of 3	0.61	1 + 2λ	34.86

Table 5.
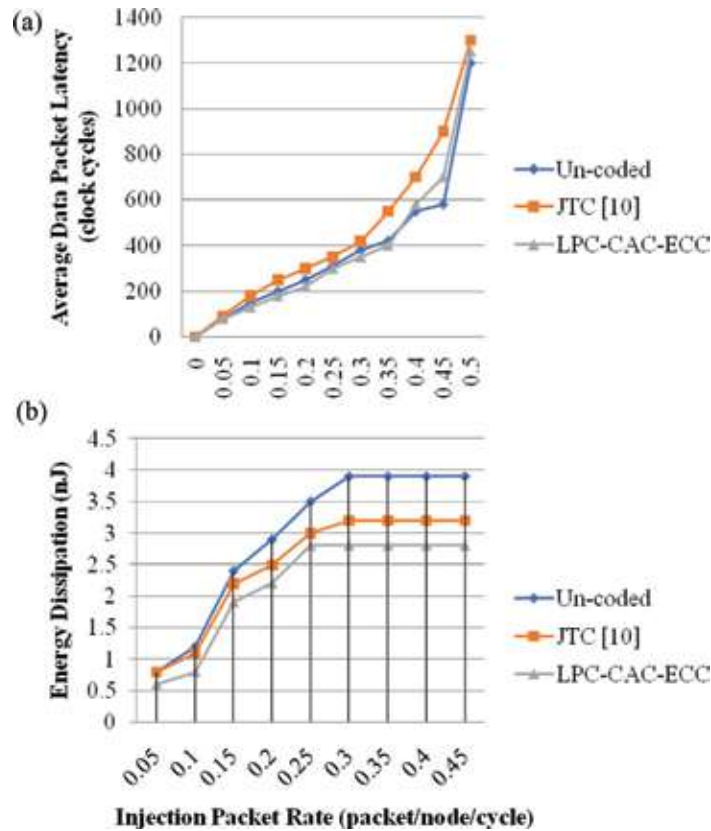*Comparison of advanced error control scheme with recent work.*

Figure 5.
Simulation results of data packet latency (a) and energy dissipation (b) of advanced NoC with others.

To analyze the data packet latency and energy dissipation, the advanced NoC architecture is simulated 32 times at uniform-random traffic in Riviera-pro windows version. Each experiment of simulation showed less latency and less energy dissipation. The 8×8 mesh-based NoC is simulated and compared with recent NoC, that is, JTC [14], and also uncoded NoC. From **Figure 5**, it is clear that the advanced NoC has lesser data packet latency and has greater than uncoded because the advanced router transfers the data with joint CAC-ECC scheme in case of occurred errors; otherwise it transfers without error control scheme. The energy dissipation of advanced NoC is lesser than both existing works because the BI-based LPC is utilized in router in case of error control code being embedded in the NI.

6. Conclusion

The scaling of technology introduces number of errors in on-chip interconnects. The crosstalk errors majorly affected the performance of NoC communication architecture due to the coupling capacitance between the interconnecting wires. This chapter discussed number of errors and their control schemes. To control multiple errors, joint CAC-ECC scheme is embedded in NI; hence the errors are controlled and avoided to propagate remaining network. As error control scheme presented more power consumption, the BI-based method of low-power code used to reduce the case of error control scheme is used. The performance of advanced NoC is simulated and compared with recent work; thereby 11% improvement is shown when compared with JTC. To analyze the data packet latency and energy dissipation, the 8×8 mesh-based NoC architecture is simulated and compared with recent work; thereby the advanced NoC architecture shows better results than the recent NoC.

Conflict of interest

It is declared that this article has no "conflict of interest."

Author details

Ashok Kumar Kummary[1*], Perumal Dananjayan[2], Kalannagari Viswanath[3] and Vanga Karunakar Reddy[1]

1 Matrusri Engineering College, Hyderabad, Telangana, India

2 Pondicherry Engineering College, Puducherry, India

3 R.L. Jalappa Institute of Technology, Bangalore, India

*Address all correspondence to: kashok483@gmail.com

IntechOpen

References

[1] Benini L, De Micheli G. Networks on chips: A new SoC paradigm. Computer-IEEE Computer Society. 2002;**35**:70-78. DOI: 10.1109/2.976921

[2] Patel KN, Markov IL. Error-correction and crosstalk avoidance in DSM busses. In: Proceedings of the 2003 International Workshop on System-Level Interconnect Prediction 2003 Apr 5; ACM. pp. 9-14. DOI: 10.1145/639929.639933

[3] The International Technology Roadmap for Semiconductors [Internet]. 2011. Available from: http://www.itrs2.net/2013-itrs.html

[4] Fu B, Ampadu P. Error Control for Network-on-Chip Links. New York; Springer Science & Business Media, Verlag; 2011. DOI: 10.1007/978-1-4419-9313-7

[5] Hamming RW. Error detecting and error correcting codes. Bell System Technical Journal. 1950;**29**(2):147-160. DOI: 10.1002/j.1538-7305.1950.tb00463.x

[6] Pande PP, Zhu H, Ganguly A, Grecu C. Energy reduction through crosstalk avoidance coding in NoC paradigm. In: Digital System Design: Architectures, Methods and Tools, 2006. DSD 2006. 9th EUROMICRO Conference on 2006 Sep; IEEE. pp. 689-695. DOI: 10.1109/DSD.2006.49

[7] Ganguly A, Pande PP, Belzer B, Grecu C. Design of low power & reliable networks on chip through joint crosstalk avoidance and multiple error correction coding. Journal of Electronic Testing. 2008;**24**(1-3):67-81. DOI: 10.1007/s10836-007-5035-1

[8] Sridhara SR, Shanbhag NR. Coding for system-on-chip networks: A unified framework. IEEE Transactions on Very Large Scale Integration (VLSI) Systems. 2005;**13**(6):655-667. DOI: 10.1109/TVLSI.2005.848816

[9] Maheswari M, Seetharaman G. Design of a novel error correction coding with crosstalk avoidance for reliable on-chip interconnection link. International Journal of Computer Applications in Technology. 2014;**49**(1):80-88. DOI: 10.1504/IJCAT.2014.059097

[10] Gracia-Morán J, Saiz-Adalid LJ, Gil-Tomás D, Gil-Vicente PJ. Improving error correction codes for multiple-cell upsets in space applications. IEEE Transactions on Very Large Scale Integration (VLSI) Systems. 2018;**26**:2132-2142. DOI: 10.1109/TVLSI.2018.2837220

[11] Kumar K A, Dananjayan P. Reduction of power consumption using joint low power code with crosstalk avoidance code in case of crosstalk and random burst errors. International Journal of Engineering & Technology. 2018;**7**(3.12):62-68. DOI: 10.14419/ijet.v7i3.12.15864

[12] Fu B, Ampadu P. Burst error detection hybrid ARQ with crosstalk-delay reduction for reliable on-chip interconnects. In: Defect and Fault Tolerance in VLSI Systems, 2009. DFT'09. 24th IEEE International Symposium on 2009; IEEE. pp. 440-448. DOI: 10.1109/DFT.2009.45

[13] Pande PP, Ganguly A, Feero B, Belzer B, Grecu C. Design of low power & reliable networks on Chip through joint crosstalk avoidance and forward error correction coding. In: Null 2006 Oct 4; IEEE. pp. 466-476. DOI:10.1109/DFT.2006.22

[14] Ganguly A, Pande PP, Belzer B. Crosstalk-aware channel coding schemes for energy efficient and reliable NOC interconnects. IEEE Transactions on Very Large Scale Integration (VLSI) Systems. 2009;**17**(11):1626-1639. DOI: 10.1109/TVLSI.2008.2005722

Section 2

Signal and Imaging Processing

Efficient Depth Estimation Using Sparse Stereo-Vision with Other Perception Techniques

Satyarth Praveen

Abstract

The stereo vision system is one of the popular computer vision techniques. The idea here is to use the parallax error to our advantage. A single scene is recorded from two different viewing angles, and depth is estimated from the measure of parallax error. This technique is more than a century old and has proven useful in many applications. This field has made a lot of researchers and mathematicians to devise novel algorithms for the accurate output of the stereo systems. This system is particularly useful in the field of robotics. It provides them with the 3D understanding of the scene by giving them estimated object depths. This chapter, along with a complete overview of the stereo system, talks about the efficient estimation of the depth of the object. It stresses on the fact that if coupled with other perception techniques, stereo depth estimation can be made a lot more efficient than the current techniques. The idea revolves around the fact that stereo depth estimation is not necessary for all the pixels of the image. This fact opens room for more complex and accurate depth estimation techniques for the fewer regions of interest in the image scene. Further details about this idea are discussed in the subtopics that follow.

Keywords: stereo vision, computer vision, disparity, depth estimation, camera, feature extraction

1. Introduction

As researchers and innovators, we have often tried to take hints and ideas from nature and convert them into beautiful versions of technology that can be used for the betterment and advancement of the human race. The human eyes inspire yet another artificial visual system, the stereo vision. The idea is to use the parallax error from two different viewing angles of the same object to estimate the distance of the object from the camera. The parallax error is inversely proportional to the depth and brings it down to a single trivial equation, whereas the estimation of the parallax error, known as the disparity between the pixels in the image frames, is a much engaging nontrivial task to handle. Depth estimation is possible only for the overlapping fields of view between the two views as shown in **Figure 1**. The multi-view system is a much better, reliable, and robust setup for depth estimation of the objects in the image compared to a monocular view. Details regarding this are discussed in the following subsections of the chapter.
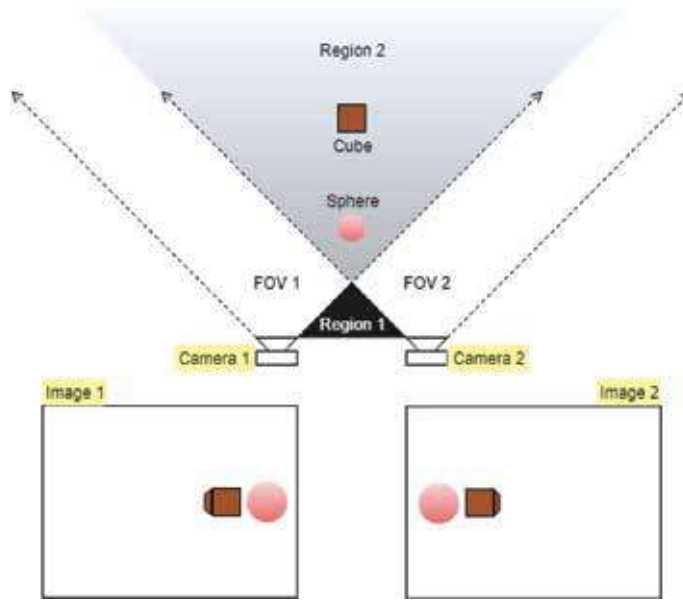
Figure 1.
The stereo setup.

This instrument was first described to us in 1838 by Charles Whitestone to view relief pictures. He called it the stereoscope. A lot of other inventors and visionaries later used this concept to develop their versions of stereoscopes. It even led to the establishment of the London Stereoscopic Company in 1854. The concept of depth estimation using multiple views was used even for the estimation of the distance of the far away astronomical objects in the early times. The depth is also directly proportional to the distance between the two cameras of the stereo vision system, also called the baseline. Hence the estimation of such vast distances demanded us to use the longest possible baseline length that we could use. So the data was recorded from Earth being on either side of the sun, making the baseline length to be the same as the diameter of the Earth's orbit around the sun, and then the depth of the astronomical objects is measured. This method was called the stellar parallax or trigonometric parallax [1].

Considering other applications, robotic applications demand plenty of stereo vision systems for close object depth estimations. Be it humanoids, robots for folding clothes or picking objects, or even autonomous vehicles, stereo vision systems solve many complexities. On top of that, if the use case is for unidirectional short-range applications, good stereo systems can even eradicate the need for lidars or radars and hence aid toward much cost-cutting.

This chapter presents a new idea while using the existing techniques for depth estimation. The motivation is to make the depth estimation procedure a lot lighter and faster. In simple words, the intension is to avoid the calculation of depth for the pixels that are not required. It is most usable when coupled with other perception techniques like object-detection and semantic-segmentation. These perception steps help us rule out the unrequired pixels for which depth estimation can be avoided. The implications and findings of this are discussed later.

Future sections of the chapter are primarily segregated as the Background and the Proposed Approach. The Background is arranged as follows: the overview of the architecture; camera calibration; stereo matching problem, i.e., disparity; and depth estimation. Further, the proposed approach contains the algorithm, the results, and possible future works.

2. Background

2.1 The overview of the stereo architecture

This architecture presents a simple overview of how the stereo system works. As shown in **Figure 2**, cameras with similar properties are calibrated individually for their intrinsic calibration parameters (Subtopic 2.2.1). The two cameras are then mounted on a rigid stereo rig and calibrated together as a single system to get the extrinsic calibration parameters (Subtopic 2.2.2). The images collected from the two cameras are then undistorted to remove the camera distortion effects. From the extrinsic calibration parameters, we know the rotation and translation of one camera w.r.t. the other (right camera w.r.t. the left camera); we use this information to align the two images from the stereo system along the epipolar line (Subtopic 2.2.2). The image pair is then used for disparity estimation (Topic 2.3), the most nontrivial part of the process. The concept proposed in this chapter targets this substep of the process. Perfect pixel matching is a hard problem in itself. So, achieving a real-time performance on images makes the problem nothing but more complex. Once we have a pixel-to-pixel correspondence between the two images, i.e., the disparity for each pixel, we can directly compute the depth for each of them using a single formula. The following topics discuss the steps as mentioned above in greater detail.

2.2 Camera calibration

Camera calibration is a fundamental step in computer vision applications. There are two aspects of camera calibration, namely, intrinsic calibration and extrinsic calibration. Some of the experts whose algorithms are used for camera calibration are Zhang [2], Scaramuzza [3], Jean-Yves Bouguet [4], and Tsai [5].

2.2.1 Intrinsic camera calibration

Intrinsic calibration, Step 2 in **Figure 2**, provides us with the internal properties of the camera, such as focal length in pixels, optical center in pixels, shear constant, aspect ratio, and distortion coefficients.

- The *optical center* is the position in the image that coincides with the principal axis of the camera setup.
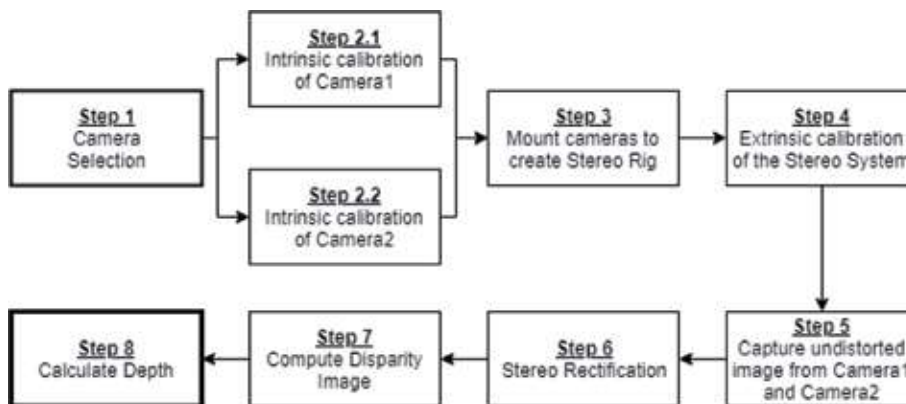

Figure 2.
The architecture overview.

- *Shear* is the slant orientation of the image recorded. This disorientation may occur during the digitized process of grabbing the image frame from the sensors. Based on today's technical advancements and complex systems, it is safe to assume that the recorded image has zero or very close to zero shears.

- *Aspect ratio* defines the shape of the pixels of the image sensor. For example, the National Television System Committee (NTSC) TV system defines non-square image pixels with an aspect ratio of 10:11. However, in most of the general cases, it is safe to assume that pixels are square and hence the aspect ratio is 1.

- *Distortion coefficients* are used to undistort the recorded image from the camera. The camera image is prone to pick up some distortions based on the built of the lenses and the camera system or based on the position of the object and the camera. The former is called optical distortion, and the latter is called perspective distortion. Distortion coefficients are used to undistort the optical distortions only. Undistorting the images ensures that the output image is not affected by any of the manufacturing defects in the camera, at least in the ideal case. There are three kinds of optical distortions:

  - *Barrel distortion*: the lines seem to be curving inward as they move away from the camera center.

  - *Pincushion distortion*: the lines seem to be curving outward as they move away from the camera center.

  - *Mustache distortion*: this is a mix of the two distortions and the toughest one to handle.

2.2.2 Extrinsic camera calibration

While intrinsic calibration provides us with intrinsic camera properties, extrinsic calibration provides us with external details like the effective movement w.r.t., a reference point in the three-dimensional world coordinate system. These constants incorporate the movement of the camera frame in six degrees of freedom. Considering the axes shown in **Figure 3**, if the image plane lies in the X-Y plane and the camera is oriented along the Z-axis, the six degrees of freedom are translation along the X-axis, translation along the Y-axis, translation along the Z-axis, rotation along the X-axis (pitch), rotation along the Y-axis (yaw), and rotation along the Z-axis (roll).

Extrinsic calibration, Step 4 in **Figure 2**, is particularly crucial in the stereo camera setup because it gives the exact baseline distance between the two camera centers. The approximate baseline is decided initially before setting up the camera units. This decision is necessary and different depending on the application of the stereo system. As the baseline length is directly proportional to the detected object depth, a more extended baseline would increase the range of the system to measure more considerable distances, while a shorter baseline would allow only short-range depth estimation. The downside to a larger baseline is the smaller overlap between the views of the two cameras. So although the system would have a greater range, it will only be for a smaller section of the view, whereas a stereo system with a smaller baseline would have a much larger overlapping view and hence would provide short-range distance estimation for a more extensive section of the view. Neither of the two systems can replace one another. Hence, keeping this significant difference in mind while choosing the correct baseline is essential.
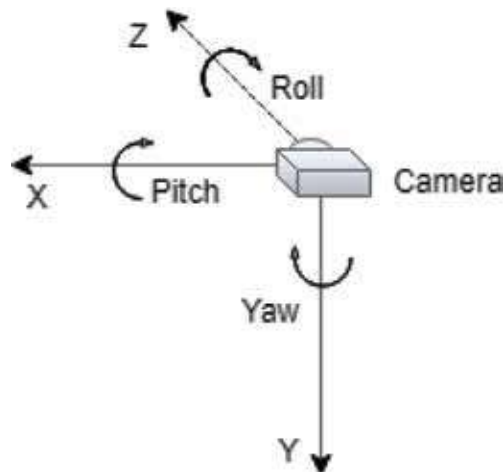
Figure 3.
Camera axes.

In the stereo camera system, one camera is the reference frame, and the other camera is calibrated w.r.t. the first camera. Hence, after the extrinsic calibration, if the two cameras are arranged along the X-axis, the baseline length information is returned as the translation along the same axis. Along with the rotation and translation, stereo calibration also updates the focal length of the overall stereo camera system. This focal length is common to both the cameras in the stereo system and is different from that of the individual focal lengths of the two cameras. The reason is that the two cameras now need to look at the joint portion of the scene; hence, choosing similar cameras, Step 1 in **Figure 2**, if not identical, can be an essential factor for a good stereo system. Dissimilar cameras significantly affect the image quality when using a common focal length. The camera with a more considerable difference between the old focal length and the new focal length gives a highly pixelated image. This difference in the image quality of the two cameras reflects in the later stage of disparity estimation. It makes the process of finding the corresponding pixels in the two images much harder; hence, it might lead to wrong disparity estimation or unnecessary noise.

Another use of the extrinsic parameters is image rectification, Step 6 in **Figure 2**. Computing disparity is not impossible without this step, but the problem statement becomes a lot easier if we rectify the output images of the stereo pair. Also, unrectified images are more prone to incorrect disparity estimation. In this step, we warp the output image of the second camera using the extrinsic parameters w.r.t. the reference camera. This warping ensures that the pixels belonging to the same objects in the two cameras lie along the same scan line in both images. So instead of the larger search space, i.e., the complete image, the search for disparity estimation can be restricted to a single row of the image. This scan line is called the epipolar line, and the plane that intersects with this epipolar line and the object point in 3D world coordinate is called the epipolar plane (see **Figure 4**). This process dramatically reduces the computations required by the disparity algorithm.

2.3 Disparity/stereo matching

This section talks about the most nontrivial aspect of the entire process of depth estimation using stereo, i.e., computing the disparity map from the stereo image pair. If considering the raw image pair from the stereo, the entire image is the search space to find the corresponding matching pixel. Although we might be able
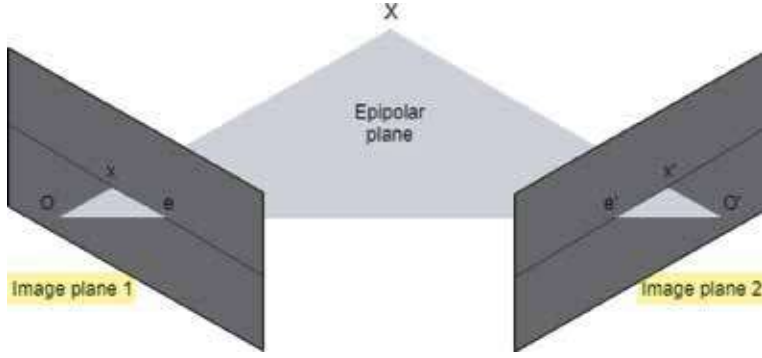
Figure 4.
The epipolar plane. X is the object point in the world coordinates, x and x′ are the corresponding pixels in the two image planes, e and e′ are the epipoles of the two image planes, and O and O′ are the corresponding camera centers.

to streamline the search space a little bit based on common sense, that will still not be comparable to searching a single row of the image. In an ideal case, the most robust system would be the one that can overlook all the image distortions, artifacts, and occlusion cases and give us a pixel-to-pixel disparity estimation by finding its perfect match in the corresponding image. [6–8] are some of the datasets that provide us with the ground truth disparity images along with the stereo image pair (see **Figure 5**). Researchers came up with different novel ideas and techniques involving custom calibration methods, high-end camera units, sensors, and better disparity estimation techniques to estimate sub-pixel disparities for highly accurate ground truth [9, 10]. While these methods are suitable to generate ground truths, real-time systems demand inexpensive solutions. Hence, in most of the cases, the applications do not require extremely accurate calibration but rely on fairly good camera calibration, inexpensive image rectification, and simple matching algorithms to get good enough disparity maps.

One of the significant elements of the stereo matching algorithms is the cost function that is used to evaluate the similarity. Some of the significant cost functions are:

The sum of squared difference (SSD)

$$C_{SSD}(d) = \sum_{(u,v) \in W_m(x,y)} [I_L(u,v) - I_R(u-d,v)]^2 \qquad (1)$$

Figure 5.
Middlebury stereo dataset. Scene (left), ground truth disparity (right).

The sum of absolute difference (SAD)

$$C_{SAD}(d) = \sum_{(u,v) \in W_m(x,y)} |I_L(u,v) - I_R(u-d,v)| \qquad (2)$$

Normalized cross-correlation (NCC)

$$\text{Normalized pixel} : \hat{I}(x,y) = \frac{I(x,y) - \bar{I}}{||I - \bar{I}||_{W_m(x,y)}} \qquad (3)$$

$$C_{NC}(d) = \sum_{(u,v) \in W_m(x,y)} \hat{I}_L(u,v)\hat{I}_R(u-d,v) \qquad (4)$$

In Eqs. (1)–(4), below is the legend for the symbols used:

I_L − *Left image or first camera image*

I_R − *Right image or second camera image*

W_m − *Matching window*

d − *Pixel disparity*

$I(u,v)$ − *Image pixel intensity at location u, v*

Although these cost functions are decent choices for similarity measure, they are considerably affected by factors such as illumination differences and viewing angles. To minimize the effect these factors have on the output, the pixel patches used for similarity check can be normalized before using SSD or SAD similarity values. Some other approaches that help make the algorithm independent of such factors are rank transform and census transform. These transformations eliminate the sensitivity toward absolute intensity and outliers.

Despite handling these sensitive cases, it takes a lot to estimate a dense disparity output. Obtaining a "dense" disparity map with restricted computations is the major challenge when designing algorithms. The dominant factors affecting the similarity measure of the corresponding pixels are as follows:

• Photometric constraints (Lambertian/non-Lambertian surfaces)

Lambertian surfaces follow the property of Lambertian reflectance, i.e., they look the same to the observer irrespective of the viewing angle. An ideal "matte" surface is an excellent example of a Lambertian surface. If the surface in the scene does not follow this property, it might appear to be different regarding illuminance and brightness in the two camera views. This characteristic can lead to incorrect stereo matching and hence wrong disparity values.

• Noise in the two images

Noise can be present in the images as a result of low-quality electronic devices or shooting the images at higher ISO settings. Higher ISO settings make the sensor more sensitive to the light entering the camera. This setting can magnify the effect of unwanted light entering the camera sensor and is nothing but noise. This noise is most certainly different for the two cameras and hence again making disparity estimation harder.

• Pixels containing multiple surfaces

This issue occurs mainly for an object lying far away in the scene. Since the baseline is directly proportional to the distance of objects, stereo systems with smaller

baseline face this issue even at average distances, whereas systems with larger baseline face it at a greater distance. It's something similar along the lines of Johnson's criteria [11] that we are a little helpless for this kind of problem. Hence it is crucial to choose the stereo baseline suitable to one's use case.

- Occluded pixels

These are those pixels of the 3D scene that are visible in one frame and not visible in the other (see **Figure 6**). It is practically impossible to find the disparity of these pixels as no match exists for that pixel in the corresponding image. The disparities for these pixels are only estimated with the help of smart interpolation techniques or reasonable approximations.

- The surface texture of the 3D object

This property of the object is another factor leading to confused or false disparity estimation. Surfaces such as a blank wall, road, or sky have no useful texture, and hence it is impossible to compute their disparity based on simple block matching techniques. These kinds of use cases require the intelligence of global methods that consider the information presented in the entire image instead of just a single scan line (discussed later in the chapter).

- The uniqueness of the object in the scene

If the object in the scene is not unique, there is a good chance that the disparity computed is incorrect because the algorithm is vulnerable to matching with the wrong corresponding pixel. A broader view of the matching patch can help here up to a certain extent, but that comes with the additional cost of required computations.

- Synchronized image capture from the two cameras

The images captured from the two cameras must be taken at the same time, especially in the moving environment scenarios. In the case of continuous scene recording, the output from the two cameras can be synchronized at the software level, or the two cameras can be hardware-triggered for the synchronized output image. While hardware trigger gives perfectly synchronized output, software level synchronization is a lot more easily achieved with decently accurate synchronization.
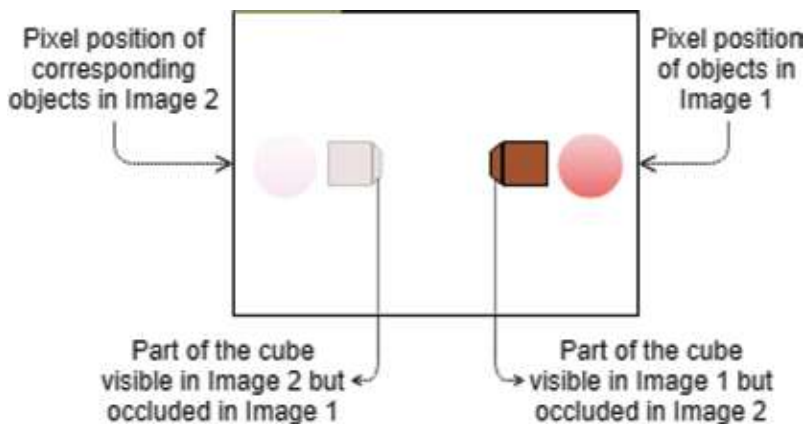

Figure 6.
Occlusion.

A few of these unfavorable aftereffects can be handled with post-processing of the disparity maps, but they can aid us only to a certain extent. A dense disparity map at real time is still a nontrivial task. Some of the cases to be kept in mind when working on a post-processing algorithm are as follows:

- Removal of spurious stereo matches

The median filter is an easy way to tackle this problem. However, it might fail in the case of a little larger spurious disparity speckles. Speckle filtering can be done using other approaches, such as the removal of tiny blobs that are inconsistent with the background. This approach gives decent results. Though this removes most of the incorrect disparity values, it leaves the disparity maps with a lot of holes or blank values.

- Filling of holes in the disparity map

Many factors lead to blank values in the disparity map. These holes are caused mainly due to occlusion or the removal of false disparity values. Occlusion can be detected using the left–right disparity consistency check, i.e., two disparity maps, each w.r.t. the first and second camera image can be obtained, and the disparity values of the corresponding pixels must be the same; the pixels that are left out are ideally the occluded pixels. These holes can be filled by surface fitting or distributing neighboring disparity estimates.

- Sub-pixel estimation

Most of the algorithms give integer disparity values. However, such discrete values give discontinuous disparity maps and lead to a lot of information loss, particularly at more considerable distances. Some of the common ways to handle this are gradient descent and curve fitting.

Having seen the cost functions and the challenges in computing the disparity, we can now go on to the algorithms used for its computation. Starting from a broader classification of the approaches, they are talked about in the following subtopics for the most common techniques of disparity estimation.

2.3.1 Local stereo matching methods

Local methods tend to look at only a small patch of the image, i.e., only a small group of pixels around the selected pixel is considered. This local approach lacks the overall understanding of the scene but is very efficient and less computationally expensive compared to global methods. The issue with not having the complete understanding of the whole image leads to more erroneous disparity maps as it is susceptible to the local ambiguities of the region such as occluded pixels or uniform-textured surfaces. This noise is taken care of up to a certain extent by some post-processing methods. The post-processing steps have also received significant attention from the experts as it helps keep the process inexpensive. Area-based methods, feature-based methods, as well as methods based on a gradient optimization lie in this category.

2.3.2 Global stereo matching methods

Global methods have almost always beaten the local methods concerning output quality but incur large computations. These algorithms are immune to local

peculiarities and can sometimes handle difficult regions that would be hard to handle using local methods. Dynamic programming and nearest neighbor methods lie in this category. Global methods are rarely used because of their high computational demands. Researchers mostly incline toward the local stereo matching methods because of its vast range of possible applications with a real-time stereo output.

Block matching is among the simplest and most popular disparity estimation algorithms. It involves the comparison of a block of pixels surrounding the pixel under study. This comparison between the two patches is made using one or a group of cost functions that are not restricted to the ones mentioned above. SSD and SAD perform pretty well and hence are the first choices in many algorithms (see **Figure 7** for the disparity output of the stereo block matching algorithm).

Some modifications to this basic approach that exists in the current literature are variations in the shape, size, and count of the pixel blocks used for each pixel of interest. Other areas of modification include the cost function and preprocessing and post-processing of the disparity map. [12–14] are some examples of the approaches mentioned above. Although most of these modifications show improvement in the accuracy and quality of the obtained disparity map, they all come with an added computational expense. Hence, like most of the algorithmic choices, even the stereo matching algorithms boil down to the direct trade-off between computation and accuracy. So it is particularly important to choose the algorithms based on the specific applications and the use case that governs their usability. With these limitations in place, the time has presented us with excellent technical advances, and hence many researchers are now devising solutions with the power of GPUs in mind. Parallelizing the above algorithms makes them compatible to run on GPUs and overcome most of the speed limitations. Though the number of computations being done is almost the same, their parallel execution takes a lot less time compared to their serial execution. This advancement opens doors for the execution of more complex algorithms much faster and hence allows better quality outputs in real time.

2.4 Depth estimation

2.4.1 Conventional method

Once we already have the disparity map for a pair of stereo images, getting the pixel-wise distance from it is the easy part. This information can be obtained using a linear formula (see Eq. (5)):
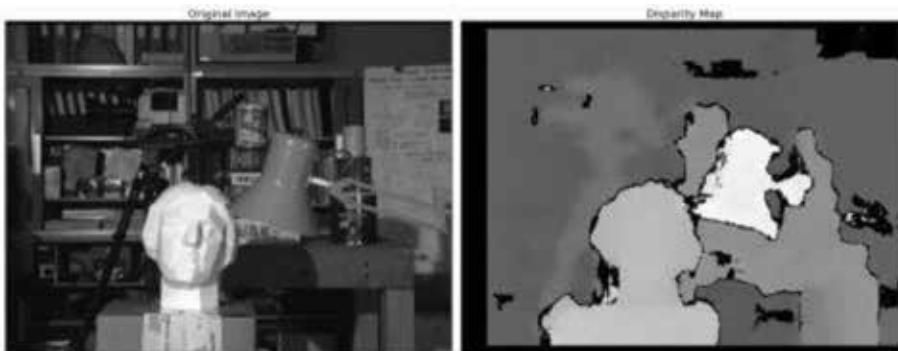

Figure 7.
Disparity output using stereo block matching algorithm.

$$z = \frac{f \times B}{d} \tag{5}$$

As discussed earlier, the formula for depth incorporates its inversely proportional relation to the disparity as well as the directly proportional relation to the baseline. Focal length and baseline are stereo camera constants that are obtained from the stereo calibration.

In Eq. (5) and **Figure 8**, below is the legend for the symbols used:

z – *Depth of the object point from the stereo unit in meters*

f – *Effective focal length of the stereo unit in pixels*

B – *Baseline distance between the two camera units in meters*

d – *Pixel disparity*

O – *Object point in the world frame*

C_1, C_2 – *Camera 1 and Camera 2*

I_1, I_2 – *Corresponding image from Camera 1 and Camera 2*

Eq. (5) can be better understood using the following simple depth proof:

As we can see from the diagram in **Figure 8**, the camera plane is parallel to the image plane:

$$\therefore \Delta OPC_1 \sim \Delta C_1 MI_1 \tag{6}$$

$$and \ \Delta OPC_2 \sim \Delta C_2 NI_2 \tag{7}$$

from Eq. (6), we know that

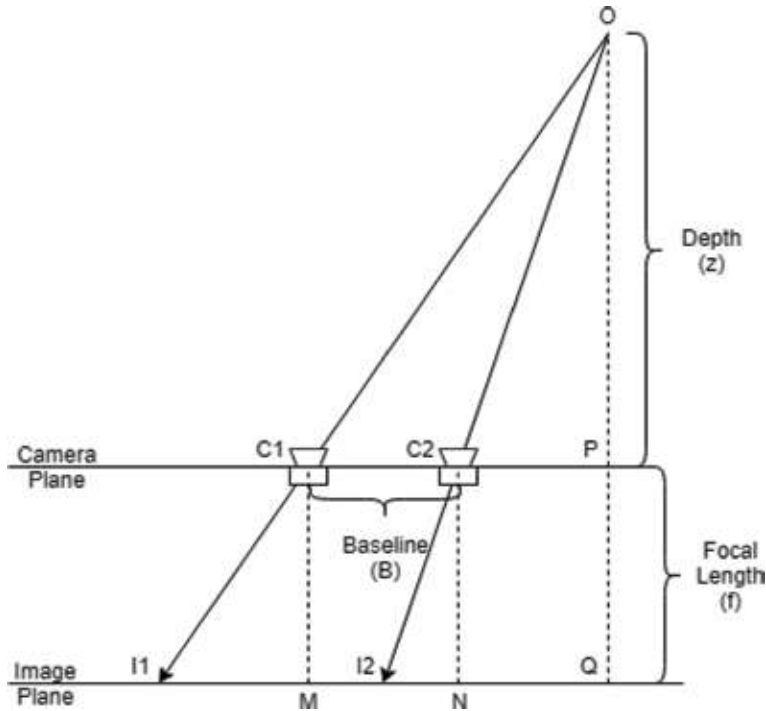**Figure 8.**
The stereo vision geometry.

$$\frac{z}{f} = \frac{C_1P}{I_1M} \tag{8}$$

and from Eq. (7),

$$\frac{z}{f} = \frac{C_2P}{I_2N} \tag{9}$$

Since baseline is the distance between the two cameras in a stereo unit,

$$\therefore B = C_1P - C_2P \tag{10}$$

from Eqs. (8) and (9), we can rewrite Eq. (10) as

$$B = \frac{z}{f} \times (I_1M - I_2N) \tag{11}$$

From the definition, it is evident that $(I_1M - I_2N)$ is nothing but disparity. Therefore, from Eq. (11) we arrive at the original equation of depth, i.e.,

$$z = \frac{f \times B}{d} \tag{12}$$

The proof for the above equation implies that the depth from the stereo unit is only dependent on the stereo focal length, the baseline length, and the disparity between the corresponding pixels in the image pair. For this exact reason, depth estimation using stereo is more robust and better suited. It is independent of any orientation or poses of the stereo unit w.r.t. the scene in the 3D world coordinates. The depth of an object shown by the stereo unit is not affected by any movement of the unit at the same distance from the object. This characteristic does not hold when the depth is being estimated using the monocular camera using methods other than deep learning. Calculating depth using a monocular camera is highly dependent on the exact pose of the unit w.r.t. the scene in the 3D world coordinates. The pose constants that work for depth estimation in one pose of the camera are most certainly guaranteed not to work when the camera is repositioned to some other pose at the same depth from the object.

2.4.2 Deep learning method

All the methods discussed above are ultimately static methods that work on the base ground of traditional computer vision. Deep learning, gaining popularity in the recent years, has shown promising results in almost all fields that it has been applied to. Sticking to the trend, the researchers and experts used it to estimate depths and disparity as well, and as expected, the results are encouraging enough for all enthusiasts for further motivated research.

Exploiting the limits of deep learning, it has also shown motivating results for depth on monocular images as well. This idea is particularly interesting because in this approach the learning model can be trained without the need for disparity map or depth information [15–17]. The output from one camera is treated as the ground truth for the other camera's input image. The logic is, to give as output, a disparity map which when used to shift the pixels of the first camera image gives us an image that is equivalent to the second camera image. This disparity output is then used to compute depth using the simple depth formula (**Figures 9–11**).

Figure 9.
Disparity output using deep learning methods [15].

3. Proposed approach

Many researchers have been working and brainstorming on the issue of sparse disparity maps. A lot of the real-time non-deep learning disparity methods fail to generate dense disparity maps. And deep learning methods have been lagging behind in this case because they are slower and lack accuracy. The performance comparison mainly assumes embedded hardware and not high-end compute machines. However, this approach aims to eradicate their need for certain use cases. The focus of this approach is to quest on the fact if sparse disparity map is really an issue. Sticking to the motivation of this chapter, sparse disparity maps are more than enough to give meaningful information if combined with other smart perception techniques. For example, if methods like object-detection [18, 19] or semantic-segmentation [20–23] give an output of identified object pixels in the image, sparse stereo output can be used to estimate the depth of the entire identified pixel group with the help of only a few major feature pixels. As a researcher, it is essential to acknowledge the fact that "one solution fits all" is not always the best approach for performance-centric problems. Moreover, because the dense disparity maps take up much computational power, we drop the aim of doing so.

If the obtained output is a sparse disparity, high credibility is a nonnegotiable requirement. While many hacks are used to filter the nonsensical disparity values, they are ultimately heuristics and not smart techniques that have any understanding of the scene. There is always the possibility that sometimes the good disparity values are filtered out. Since the current approach works on mostly the most critical feature points, the credibility for their disparity is the maximum in the selected region of pixels. More so, multiple distance functions reaffirm the calculated disparity. Higher confidence in the output disparity can be obtained by making use of higher level structural information of the objects in the scene. The structural buildup of the scene is lost information that is mostly neglected in the non-deep learning approaches. The approach proposed in this chapter intends to use this information to our advantage.

3.1 Algorithm

The conventional techniques start with a window scan of the entire image and look for the best disparity values. Mostly a post-processing step follows which

deletes the spurious disparity values from the final output. In this proposed approach, a post-processing step is not required, and the correspondence algorithm runs for a much smaller number of pixels compared to the entire image. Following the above statement, this approach starts with finding the most prominent features in the two input images. It is critical because it ensures three things—the selection of discrete pixels that ensure high disparity confidence, the removal of any post-processing step, and a drastic reduction in the input size for disparity estimation. The first point takes care of high credibility, whereas the other two points ensure a significant performance boost.

Once we have the features of the two input images, we use a combination of multiple techniques. Since it is a conventional image processing technique with the requirement of not being computationally heavy, there is only so much information that each method can carry. A combination of the same has the potential to overcome this flaw.

The first technique, i.e., the **feature matching technique**, is the most dynamic part of the algorithm. It requires modification for every different type of feature selection. As the feature of interest for this chapter is line segments, the discussion restricts to the same. Here the features not only are matched by pixel values but depend on the feature properties as well. For example, the slope is an essential property for a line. It helps to identify the similarity in the structure of the compared scene. However, this has the naïve loophole that it can match with any similar-looking line. Hence, it is not possible to entirely rely on this distance estimation technique.

The second technique is the typical **window matching technique** (see **Figure 12**). However, the difference is the size and shape of the window decided for each individual feature. The line segment detected in that area governs the shape and size of each window. The window must cover entirely the smaller of the two lines (detected lines in the two input images). For a little context, a few pixels pad the feature line within the window (see **Figure 12**). This one difference from the typical window matching makes much difference because each feature has a unique size which indicates that each window captures a significant image feature in its entirety and not just clueless parts of it. Irrespective of the added advantage, this method still has all the flaws of the box matching technique, the significant difference being the difference in the illumination of the two camera views. This difference can lead to erroneous disparity values. The next distance estimation technique handles this flaw.

Figure 10.
Left image overlapped with the detected feature lines [7].

Figure 11.
Right image overlapped with the detected feature lines [7].
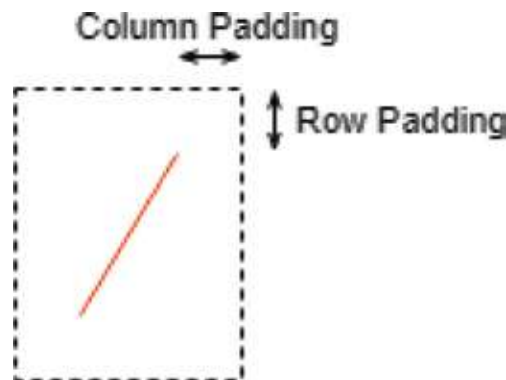

Figure 12.
Window matching technique: the window covers the entire feature segment along with some pixel padding.

The third technique is the **census feature matching technique** (see **Figure 13**) which makes the pixel matching intensity independent. It captures the relationship between the intensity values in a selected neighborhood and does not rely on exact intensity values. Although this step makes the previous distance estimation seem redundant, it helps in the cases where the relation between pixels intensities is the same for multiple positions of the search space. On top of that, unlike the window matching technique, the census features require a single point of interest for each window and hence cannot have a non-square window size for the image features. **Figure 13** shows the use of census features for this approach.

While the above metrics help find an accurate match of the corresponding pixels, it is necessary to identify the pixels that do not have a corresponding matching pixel. It is mainly the case with occluded pixels and is a significant factor to take care of to ensure high accuracy. The steps that ensure this necessity are feature matching and disparity aggregation (discussed later) steps. In the feature matching step, a corresponding match is searched only for features that are fundamentally and structurally the same. Failure to find such candidates leads to dropping the particular feature. After this initial screening, disparity aggregation does the final screening. Here if the disparity values obtained from the different metrics go out of a range, they are rejected. This thresholding can be relied upon because the estimated ranges are in the depth space.
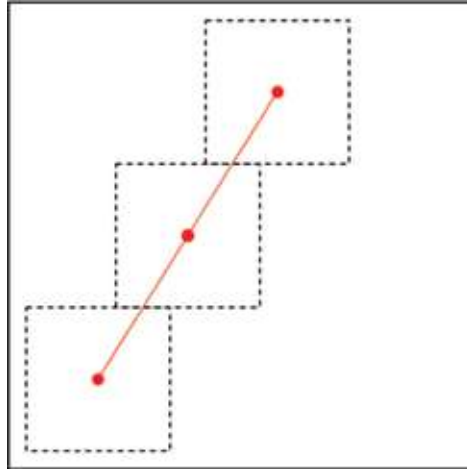
Figure 13.
Census feature matching technique—redline is the feature segment, the red dots are the pixels of interest on the feature segment, the dashed squares are the census feature kernels for the pixels of interest.

Next is the **disparity aggregation** step that combines the disparity values obtained from all of the above metrics. The main characteristic encapsulated here is the fact that this aggregation step can reject outlier disparity values as well. The upper and lower bound of the disparity values can be obtained from Eq. (12). Extending the same we can get the disparity error range in the pixel space (Eq. (13)).

$$Disparity\ Error\ Range = -fB\frac{(x+y)}{(z-x)(z+y)} \qquad (13)$$

In Eq. (13), below is the legend for the symbols used:

z − *Depth of the object point from the stereo unit in meters*

f − *Effective focal length of the stereo unit in pixels*

B − *Baseline distance between the two camera units in meters*

x − *Arbitrary margin distance in meters taken infront of the object*

y − *Arbitrary margin distance in meters taken behind the object*

3.2 Results

Figure 14 shows the final result of the above approach. The disparity values of the image features are color-coded based on the disparity values. Visually the output looks much inferior to the standard disparity estimation techniques, but the motivation of this chapter has been different since the beginning. This approach is capable of performing better than the typical approaches because in a combined pipeline, i.e., its combination with other smart perception techniques, it's capable of performing much better because it mostly avoids the false disparity values.

3.3 Future work

Although the proposed method is promising in some instances, it will not always perform better for obvious reasons. In case there is a requirement to estimate the disparity of some pixel that does not lie in the feature pool, this algorithm is bound

Figure 14.
Final feature disparity map—red denotes closer pixels, blue denotes farther pixels.

to fail. In such cases, custom image descriptors, where closest feature points can define the pixel of interest, can be used to overcome the above flaw. Getting this right is a challenge because the disparity between the two stereo images makes it a nontrivial problem to select the correct features to describe the pixel of interest. Since the introduced disparity can lead to some difference in the background of the two input images, hence not all features can be used to describe the pixel of interest.

Another critical factor that can help in improving the performance of the output is better identification of the edges of the detected objects. Something that I would like to call "dislocated kernels" might help improve the accuracies. The idea is – not to be restricted by the fact that the pixel of interest needs to lie at the center of the kernel.

All of the above ideas and approaches work behind a single motivation of attaining the maximum credibility of the computed output. Along the same lines, if the current approach can be optimized enough, we might have enough room for the conventional yet effective stereo consistency check. Since even this check is to be performed on the feature elements of the image, the number of input pixels is meager and can lead to very high confidence overall.

4. Conclusion

Throughout this chapter, we talked about the fundamental details with a slight background of the stereo vision system and about how sparse disparity maps can be highly credible. We discussed the primary use cases and applications along with the conceptual working of this system. As discussed earlier, there are a lot of complex challenges to be taken care of when using stereos for any application. The solutions to these challenges are no magic bullet and require some digging in to figure out the solution that works best for the chosen application. Many experts have launched ready-made stereo vision systems with a reasonable amount of accuracy to save researchers from the efforts of setting up a good stereo system themselves. These are fit to be used for almost all personal projects, and some of them are even suitable for extensive projects. Examples of some of these products are ZED Stereo, Microsoft Kinect, Bumblebee, and many more. Multiple solutions have come into existence, to speed up the process of depth estimation. While some of these devices use custom-built hardware for faster computation, others use a variety of cameras, e.g., infrared cameras, to make the process of stereo matching much more comfortable. The approach proposed in this chapter guides toward making use of even the sparse disparity maps with greater confidence.

This chapter was an attempt to cover most of the fundamental concepts that govern the working of the stereo vision systems and give an alternative for fast depth estimation techniques. The intention was to give enthusiastic readers enough information about the topic by the end of the chapter, to make them capable of digging deeper into advances sections of the module.

Acknowledgements

Author details

Satyarth Praveen
Master of Engineering in Robotics, University of Maryland, College Park, Maryland, United States of America

*Address all correspondence to: satyarth@terpmail.umd.edu

IntechOpen

References

[1] The ABC's of Distances [Internet]. 2018. Available from: http://www.astro. ucla.edu/~wright/distance.html [Accessed: 07-09-2018]

[2] Zhang Z. A flexible new technique for camera calibration. IEEE Transactions on Pattern Analysis and Machine Intelligence. 2000;**22**: 1330-1334

[3] Scaramuzza D, Martinelli A, Siegwart R. A toolbox for easily calibrating omnidirectional cameras. In: Intelligent Robots and Systems, 2006 IEEE/RSJ International Conference on 9 October 2006; IEEE; pp. 5695-5701

[4] Camera Calibration Toolbox for Matlab [Internet]. 2015. Available from: http://www.vision.caltech.edu/bougue tj/calib_doc/ [Accessed: 14-10-2015]

[5] Tsai Camera Calibration [Internet]. 2003. Available from: http://homepages. inf.ed.ac.uk/rbf/CVonline/LOCAL_ COPIES/DIAS1/ [Accessed: 05-11-2003]

[6] Scharstein D, Szeliski R. A taxonomy and evaluation of dense two-frame stereo correspondence algorithms. International Journal of Computer Vision. 2002;**47**(1–3):7-42

[7] Geiger A, Lenz P, Urtasun R. Are we ready for autonomous driving? The kitti vision benchmark suite. Computer Vision and Pattern Recognition (CVPR). In: 2012 IEEE Conference on 16 June 2012; IEEE; pp. 3354-3361

[8] Silberman N, Hoiem D, Kohli P, Fergus R. Indoor segmentation and support inference from rgbd images. In: European Conference on Computer Vision. Berlin, Heidelberg: Springer; 2012. pp. 746-760

[9] Scharstein D, Szeliski R. High-accuracy stereo depth maps using structured light. In: Computer Vision and Pattern Recognition, 2003; Proceedings 2003 IEEE Computer Society Conference on 18 June 2003; IEEE; Vol. 1. pp. I-I

[10] Scharstein D, Hirschmüller H, Kitajima Y, Krathwohl G, Nešić N, Wang X, et al. High-resolution stereo datasets with subpixel-accurate ground truth. In: German Conference on Pattern Recognition. Cham: Springer; 2014. pp. 31-42

[11] Sjaardema TA, Smith CS, Birch GC. History and evolution of the Johnson criteria. SANDIA Report, SAND2015-6368. 2015

[12] Hirschmuller H. Accurate and efficient stereo processing by semi-global matching and mutual information. In: Computer Vision and Pattern Recognition CVPR 2005; IEEE Computer Society Conference on 20 June 2005; IEEE; 2005. Vol. 2. pp. 807-814

[13] Hirschmuller H. Stereo processing by semiglobal matching and mutual information. IEEE Transactions on Pattern Analysis and Machine Intelligence. 2008;**30**(2):328-341

[14] Spangenberg R, Langner T, Adfeldt S, Rojas R. Large scale semi-global matching on the CPU. In: Intelligent Vehicles Symposium Proceedings, 2014 IEEE. 2014. pp. 195-201

[15] Godard C, Mac Aodha O, Brostow GJ. Unsupervised monocular depth estimation with left-right consistency. CVPR. 2017;**2**(6):7

[16] Zbontar J, LeCun Y. Stereo matching by training a convolutional neural network to compare image patches. Journal of Machine Learning Research. 2016;**17**(1–32):2

[17] Mayer N, Ilg E, Hausser P, Fischer P, Cremers D, Dosovitskiy A, et al. A large dataset to train convolutional networks for disparity, optical flow, and scene flow estimation. In: Proceedings of the IEEE Conference on Computer Vision and Pattern Recognition. 2016. pp. 4040-4048

[18] Redmon J, Divvala S, Girshick R, Farhadi A. You only look once: Unified, real-time object detection. In: Proceedings of the IEEE Conference on Computer Vision and Pattern Recognition. 2016. pp. 779-788

[19] Liu W, Anguelov D, Erhan D, Szegedy C, Reed S, Fu CY, et al. Ssd: Single Shot Multibox Detector. In: European Conference on Computer Vision. Cham: Springer; 2016. pp. 21-37

[20] Paszke A, Chaurasia A, Kim S, Culurciello E. Enet: A deep neural network architecture for real-time semantic segmentation. arXiv preprint arXiv:1606.02147. 2016

[21] Dissecting the Camera Matrix, Part 3: The Intrinsic Matrix [Internet]. 2013. Available from: http://ksimek.github.io/2013/08/13/intrinsic/ [Accessed: 13-08-2013]

[22] Bhatti A. Current Advancements in Stereo Vision. Rijeka: InTech; 2012. https://scholar.google.com/scholar?oi=gsb95&q=current%20advances%20in%20stereo%20vision%20rijeka&lookup=0&hl=en

[23] Hartley R, Zisserman A. Multiple View Geometry in Computer Vision. Cambridge University Press; 2003. https://scholar.google.com/scholar?hl=en&as_sdt=0%2C5&q=multiple+view+geometry+in+computer+vision&btnG=&oq=multiple+view+

Chapter 8

Advances in Signal and Image Processing in Biomedical Applications

Mathiyalagan Palaniappan and Manikandan Annamalai

Abstract

Our bodies are continually passing on information about our prosperity. This information can be collected using physiological instruments that measure beat, circulatory strain, oxygen drenching levels, blood glucose, nerve conduction, mind activity, and so on. For the most part, such estimations are taken at unequivocal spotlights in time and noted on a patient's outline. Working with conventional bio-estimation apparatuses, the sign can be figured by programming to give doctors continuous information and more noteworthy bits of knowledge to help in clinical evaluations. By utilizing progressively modern intends to break down what our bodies are stating, we can conceivably decide the condition of a patient's wellbeing through increasingly noninvasive measures.

Keywords: patient, bio signals, Medical image, processing, decision

1. Introduction

The signals are measured and analyzed from the organs of human body using various instruments. These types of signal processing called bio signal processing. The major challenges are to remove the noise from the signals and the resulting information is more useful for the clinicians [1–10].

The MRI, PET, CT, etc., generates more images and these images are processed using Artificial Intelligence and machine learning algorithms. The bio signal processing and machine learning [12] based medical image analysis accurately diagnosis the diseases by doctors.

2. Advancement of biomedical applications

This section aims to collect a diverse and complementary set of emerging techniques that demonstrate new developments and applications of advanced signal and image processing in medical imaging. It will help both physicians and radiologists in the image interpretation, and help technicians to exchange the latest technical progresses.

2.1 Signal processing in networked cyber-physical systems

A noteworthy test for execution of sign handling arrangements in cyber-physical systems (CPS) is the trouble of gaining information from topographically circulated

perception hubs and putting away/preparing the amassed information at the combination focus (FC) [1, 2]. All things considered, there has been an ongoing flood of enthusiasm for improvement of conveyed and shared sign preparing advancements where adjustment, estimation, as well as control are performed locally and correspondence is constrained to nearby neighborhoods.

Cyber-physical systems provides major facilities and it has more potential digital and physical assaults by enemies on sign handling modules could prompt an assortment of extreme outcomes including client data spillage, devastation of foundations, and jeopardizing human lives [3]. Then again, the requirement for participation between neighboring hubs makes it basic to anticipate the revelation of delicate nearby data during conveyed data combination step.

2.2 Cyber-physical systems in signal processing

Cyber-physical systems give strategies and help to tackle prognostic issues in an assortment of medicinal areas [4]. Machine leaning algorithms (ML) are used to examine the significance of clinical parameters, e.g. expectation of ailment movement, therapeutic learning, patient administration, etc.., [5]. ML is being utilized for information examination in medical field [6]. It contend that the fruitful execution of ML strategies can help the combination of PC based frameworks in the medicinal services condition giving chances to encourage and upgrade crafted by medicinal specialists.

2.3 Multimodal multimedia signal processing

Analysts in various fields use multimodal information. One of its most regular usages is in the field of human computer interaction (HCI). Here, a methodology is a characteristic method for collaboration: discourse, vision, confront articulations, penmanship, motions, head, and body developments [7, 8]. Multimodal interfaces encourages human computer interface [9] supplant the conventional console and mouse. Multimodal speaker recognition, distinguishes the dynamic speaker in a sound video grouping, which contains a few speakers, in light of the connection between the sound and the development in the video [10].

2.4 Statistical signal processing

Statistical signal processing is an approach to signal processing which treats signals as stochastic processes, utilizing their statistical properties to perform signal processing tasks. Statistical techniques are widely used in signal processing applications [13, 14].

2.5 Signal processing techniques for data hiding and audio watermarking

In signal processing techniques for data hiding a novel system for embeddings and recuperating "shrouded" information in sound documents. In this procedure, the period of picked segments of the host sound flag is controlled in a way that might be identified by a collector with the best possible "key" [15]. Without the key, the shrouded information is imperceptible; both aurally and through visually impaired computerized flag handling assaults. The technique portrayed is both aurally straightforward and vigorous and can be connected to both simple and computerized sound flags, the last including uncompressed and additionally packed sound record designs. Information stowing away present by relative stage encoding and quantization record adjustment stage encoding technique [16].

2.6 Optical signal processing

Optical signal processing unites different fields of optics and signal processing to be specific, nonlinear gadgets and procedures, simple and computerized signal, and propelled information tweak arrangements to accomplish fast signal processing capacities that can conceivably work at the line rate of fiber optic interchanges [17, 18]. Data can be encoded in abundancy, stage, wavelength, polarization and spatial highlights of an optical wave to accomplish high-limit transmission. Different optical nonlinearities and chromatic scattering have been appeared to empower key sub-framework applications, for example, wavelength transformation, multicasting, multiplexing, demultiplexing, and tunable optical postponements. Optical flag preparing utilizing cognizant optical recurrence looks over could have different potential applications for optical correspondences. At first a way to deal with accomplish a tunable optical high-arrange QAM [19] age in light of multichannel total and an all-optical pilot-tone based self-homodyne-recognition is utilized by two situations: (i) numerous WDM channels with adequate intensity of pilot tones, and (ii) a solitary channel with a low-control pilot tone. At long last, a divided data transmission assignment empowered by reconfigurable channel cutting and sewing.

2.7 Virtual physiological human initiative

The virtual physiological human is synonymous with a program in computational biomedicine that plans to build up a system of strategies and advancements to examine the human body in general [20, 21]. It is predicated on the transformational character of data innovation, offered as a powerful influence for that most essential of human concerns, our own wellbeing and prosperity. The VPH is a composed gathering of computational structures and ICT-based instruments for the multilevel displaying and recreation of the human life structures and physiology. Once adequately built up, the VPH [22] will give a fundamental innovative foundation to the Physiome Project, to pathology-particular activities in translational research, and to vertical answers for the biomedical business.

2.8 Brain-computer interfaces

Research in electroencephalogram (EEG) based brain-computer interfaces (BCIs) has been extensively extending during the most recent couple of years. To Such extent owes an enormous degree to the multidisciplinary and testing nature of BCI inquire about. Sign preparing and example acknowledgment without a doubt comprise fundamental segments of a BCI framework. Sign handling calculations are connected to the EEG sign to interpret mental states which are pertinent for BCI activity. In this instructional exercise, the fundamental BCI ideas, for example, mind movement checking, BCI task, and the important mental states for BCI, are presented. The fundamental kinds of significant mental states for BCI, to be specific engine symbolism (ERD/ERS), enduring state visual evoked possibilities (SSVEP) [23], and occasion related possibilities are introduced alongside commonsense application precedents.

The EEG preparing for mental state disentangling is depicted inside and out. The multivariate idea of the EEG joined with the neuroscience learning on hemispheric cerebrum specialization is beneficially considered to infer ideal mixes of the individual sign creating the EEG [24]. BCIs are named by the kind of mind action utilized for control. Among a few classifications of EEG-based BCIs, including P300, unfaltering state visual evoked potential (SSVEP), occasion related desynchronization (ERD), and moderate cortical potential based sign preparing.

3. Neural networks and computing

In humans, interactions between neuron circuits, systems and signals among micro-, meso- and macro-scales of brain dynamics underpin the functional organization of the brain that supports our daily life activity. Mathematical, computational and experimental neuroscientists apply a variety of methods, techniques and algorithms, both in animals and humans, ranging from single cell recordings to whole brain imaging, in order to identify the core mechanisms that govern the interactions among these scales. Although our knowledge of neural mechanisms, circuits and networks underlying brain dynamics and functions constantly grows, the integration of this knowledge to provide a conceptual framework of emergent behavior [25] and pattern formation occurring on different levels of spatial organization remains challenging.

4. Big data in bioinformatics

In biomedical calculation, the nonstop difficulties are: the board, investigation, and capacity of the biomedical information. The Spark engineering enables us to create suitable and productive strategies to use an enormous number of pictures for characterization, which can be redone as for one another [27]. In prescription, the information experienced are for the most part acquired from patients. This information comprise of physiological sign, pictures, and recordings. They can be put away or transmitted utilizing proper equipment and systems. One of the administrations utilized in prescription for the capacity and transmission of picture information is the picture archiving and communication system (PACS).

The enormous information innovations are ordered into four classes [28, 29]: (1) information stockpiling and recovery, (2) mistake ID, (3) information examination, and (4) stage mix arrangement. These classifications are related and may cover; for example, most information input applications may bolster basic information examination, or the other way around.

5. Image reconstruction and analysis

The examination model has been recently abused as an option in contrast to the traditional scanty amalgamation model for planning picture recreation techniques. Applying an appropriate examination administrator on the picture of intrigue yields a cosparse result [30] which empowers us to remake the picture from under sampled information. Moreover earlier in the investigation setting and hypothetically ponder the uniqueness issues as far as examination administrators when all is said in done position and the particular 2D limited distinction administrator. In light of the possibility of iterative co-bolster discovery (ICD) a novel picture remaking model and a successful calculation, accomplishing essentially better recreation execution.

5.1 Biomedical imaging

Utilization of computer-aided technologies in tissue engineering research and development has evolved a development of a new field of computer-aided tissue engineering (CATE). Three dimensional (3D) printing is an added substance producing process. This innovation furnishes us with the chance to make 3D structures by including material a layer-by-layer premise, utilizing various types of materials, for example, earthenware production, metals, plastics, and polymers. These days,
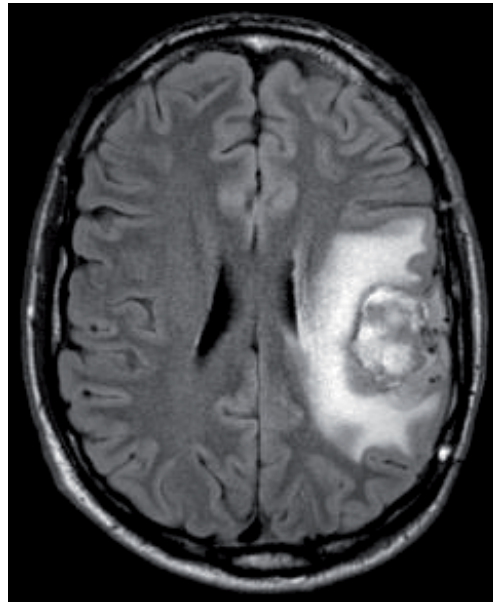
Figure 1.
Tumor MR image taken after 15 days.

tissue building examinations are occurring on an across the board premise in the fields of recovery, reclamation, or substitution of blemished or harmed useful living organs and tissues. 3D bio-printing [31] is a flexible developing innovation that is discovering its way through all parts of human life. The capability of 3D printers can be abused in territories of biomedical designing, for example, key research, tranquilize conveyance, testing, and additionally in clinical practice. About all present therapeutic nonorganic inserts, for example, ear prostheses, are made in foreordained sizes and designs that are generally utilized for patients. This method permits more precise customized assembling of gadgets made to the patient's own particulars. Bio-printing is being utilized to make more exact nonbiologic and organic research. Describe a method for hiding data in audio files that employs the manipulation of the phase of selected spectral components of the host audio file we describe a method for hiding data in audio files that employs the manipulation of the phase of selected spectral components of the host audio file.

For an example, in **Figure 1** automated quantification of tumors remains to quantify signal intensity changes in MR images, and this is a difficult problem because of the artifacts affecting images such as partial volume effects and intensity in homogeneities. Low level segmentation methods such as intensity thresholding, edge detection, region growing, region merging and morphological operation are not well suited for automated quantification of the signal abnormalities as these techniques rely on image operators that analyze intensity, texture or shape locally in each voxel, and therefore too easily mislead by ambiguities in the image or require user interaction.

5.2 Intelligent imaging

Data driven systems have gotten expanding consideration as of late to solve different issues in biomedical imaging. Information driven models and methodologies so forth., give promising execution in picture remaking issues in attractive reverberation imaging, processed tomography, and different modalities in respect
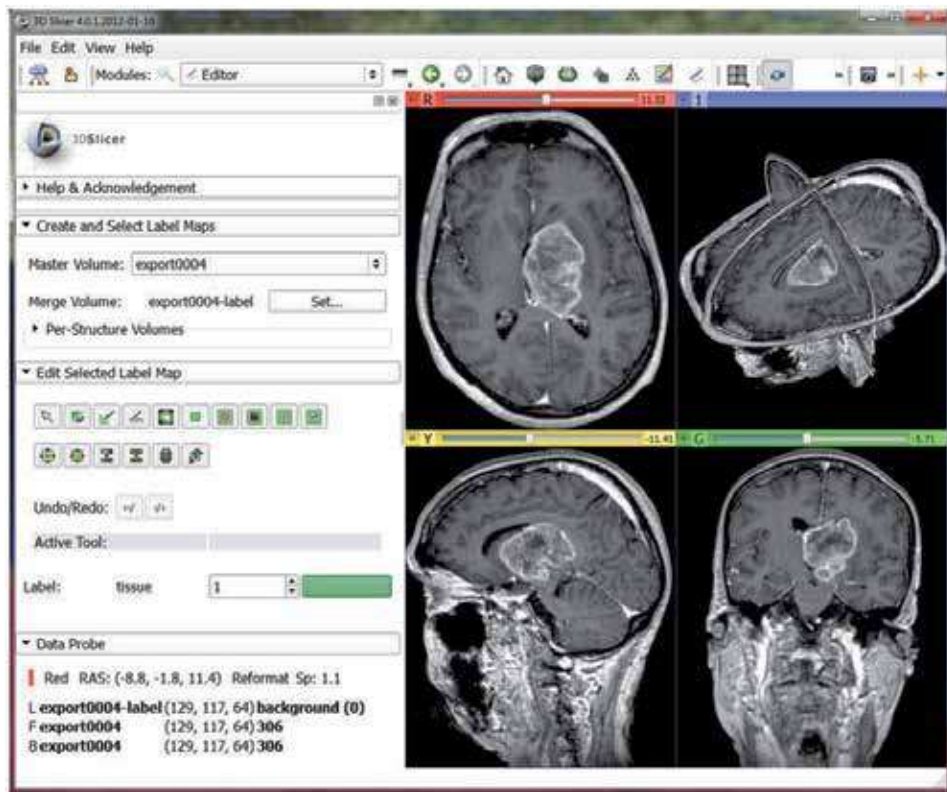
Figure 2.
3D MRI image visualization using 3D slicer. Image courtesy of the 3D slicer.

to conventional methodologies utilizing hand-created models, for example, the discrete cosine change, wavelets. In this term envelops the most recent methodologies for making all parts of imaging framework information driven, including information procurement and examining, picture recreation, and handling/examination. Intelligent imaging frameworks would ceaselessly gain from huge datasets and on-the-fly and adjust for speed, productivity, and picture execution or quality.

A best example of intelligent imaging is the identification of affected and healthy images based on the discrimination capabilities in fundus image textures. For this purpose, as a texture descriptor for retinal eye images has been done and the area and time consumption has been reduced by the means of extended binary patterns (EBP). The main aim is to reduce the size and time consumption and also differentiate between age-related macular degeneration (AMD) and diabetic retinopathy (DR), and normal fundus images with the retina background texture by leaving lesions previous segmentation stage with the proposed procedure and obtaining promising results. The best results of each experiment on the model set are highlighted in tables. This work makes use of the EBP operator. In particular, the performance of EBP was compared with LPB as shown in **Figure 2**.

5.3 PDE based image analysis

The real issue with the exact mode disintegration (EMD) calculation is its absence of a hypothetical system. In this way, it is hard to portray and assess 2-D case, the utilization of an elective usage to the algorithmic meaning of the alleged "filtering process" utilized as a part of the first EMD strategy. This approach,

particularly in light of fractional differential conditions (PDEs) and depends on a nonlinear dissemination based sifting procedure to tackle the mean envelope estimation issue. In the 1-D case, the productivity of the PDE-based technique, contrasted with the first EMD algorithmic rendition, was additionally delineated in an ongoing paper. As of late, a few 2-D expansions of the EMD strategy have been proposed. Regardless of some exertion, 2-D adaptations for EMD show up inadequately performing and are extremely tedious. So an expansion to the 2-D space of the PDE-based approach is widely depicted. This approach has been connected in instances of both flag and picture decay. The acquired outcomes affirm the value of the new PDE-based filtering process for the disintegration of different sorts of information. The adequacy of the approach empowers its utilization in various signal and image applications such as denoising, detrending or texture analysis.

5.4 Visualization of 3D MRI brain tumor image

Figure 2 demonstrates the visualization of 3D MRI image using 3D slicer used to perform various analysis on brain tumor in early stages.

5.5 Hyperspectral imaging

In recent years, hyperspectral imaging (HSI) [32] has risen as a promising optical innovation for biomedical applications, principally forever sciences look into, yet in addition went for nonintrusive conclusion and picture guided medical procedure. Hyperspectral imaging (HSI) innovations have been utilized broadly in medicinal research, focusing on different organic wonders and various tissue writes. Their high ghostly determination over an extensive variety of wavelengths empowers procurement of spatial data comparing to various light interacting natural mixes. It is fit for giving constant quantitative data to a few organic procedures in both solid and ailing tissues. Hyperspectral inspecting and determination are for the most part considered the key factors that recognize HSI and MSI, while MSI centers around discrete and generally separated wavelength groups, HSI basically uses extremely tight and neighboring otherworldly groups over a nonstop phantom range, as to recreate the range of every pixel in the image.

5.6 Artificial neural networks in image processing

Medicinal imaging procedures have generally been being used in the finding and identification of disease. Microcalcifications and masses are the soonest indications of tumor which must be identified utilizing current procedures. The trouble in characterization of generous and harmful microcalcifications [33] likewise causes a critical issue in restorative picture handling. Computerized classifiers might be valuable for radiologists in recognizing benevolent and dangerous examples. Consequently, an artificial neural system (ANN) [11, 26] which can be filled in as a computerized classifier is examined. In medicinal picture preparing, ANNs have been connected to an assortment of information order and example acknowledgment errands and turn into a promising characterization instrument in bosom malignancy. In this way, extraordinary determinations of picture highlights will bring about various arrangement choices. These requests can be parceled into three sorts: in any case, the method in light of estimations, for instance, support vector machine; second, the methodology in perspective on oversee, for instance, decision tree and unforgiving sets; and third, fake neural framework. Diverse ANNs made rely upon extending the veritable positive (TP) revelation rate and decreasing the bogus positive (FP) and false negative (FN) acknowledgment

rate for the perfect result. Use of wavelet in ANNs, for instance, particle swarm optimized wavelet neural network (PSOWNN), biorthogonal spline wavelet ANN, second-orchestrate dim dimension ANN, and Gabor wavelets ANN can improve the affectability and explicitness which are acquired in masses and microcalcification acknowledgment.

6. Discussion

Biomedical sign and picture handling comprises particular interests in the informative and research field in biomedical structure. With the redesigned physiological data, a wide course of action of innovative works in clinical techniques makes usage of this thought in the restorative applications. With headway in biomedical imaging, the proportion of data created by multimodality picture strategies, e.g., stretching out from computed tomography (CT), magnetic resonance imaging (MRI), ultrasound, single photon emission computed tomography (SPECT), and positron emission tomography (PET), magnetic particle imaging, EE/MEG, optical microscopy and tomography, photoacoustic tomography, electron tomography, and atomic force microscopy, has grown exponentially and the possibility of such data has logically ended up being more amazing. This represents an awesome test on the best way to grow new propelled imaging strategies and computational models for productive information handling, investigation and displaying in clinical applications and in understanding the basic natural process. Signal and image processing is pervasive in present day biomedical imaging, as it gives fundamental procedures to picture development, upgrade, coding, stockpiling, transmission, examination, comprehension, and representation from any of an expanding number of various multidimensional detecting modalities. To address this difficulty, usually natural image preprocessing methodology, for example, highlight extraction, picture combination, grouping and division need acclimatized clever strategies that can handle with the mass and decent variety of the data and frequently have the capacity to incorporate and process information from nonimaging sources.

7. Conclusion

This chapter mainly focused on signals and latest techniques in medical image processing which will create more interest in biomedical research fields. With the latest trends in data acquisition, a wide course of action of innovative works in clinical techniques applied in restorative applications. In biomedical imaging the data acquisition systems like computed tomography (CT), magnetic resonance imaging (MRI), ultrasound single photon emission computed tomography (SPECT), positron emission tomography (PET), optical microscopy etc., captures images of the patients. These systems grow exponentially and generate huge data which had more useful information. The high performance computing (HPC) methods analyze the images and visualize images in 3D view as well as pixel wise analysis with very less processing time. The major challenges in the brain tumor detection are to explore the exact location, shape and different tumor tissues and nontumor tissues. The artificial intelligence (AI) and machine learning (ML) address these challenges which supports radiologist and also for patients.

Author details

Mathiyalagan Palaniappan[1]* and Manikandan Annamalai[2]

1 Sri Ramakrishna Engineering College, Coimbatore, Tamilnadu, India

2 Vivekananda College of Technology for Women, Namakkal, Tamilnadu, India

*Address all correspondence to: mathiyalagan.p@srec.ac.in

IntechOpen

References

[1] Jin J, Allison BZ, Wang X, Neuper C. A combined brain-computer interface based on P300 potentials and motion-onset visual evoked potentials. Journal of Neuroscience Methods. 2012;**205**:265-276. DOI: 10.1016/j.jneumeth.2012.01.004

[2] Katzenbeisser S, Petitcolas FAP. Information Hiding: Techniques for Steganography and Digital Watermarking. Norwood, MA: Artech House; 2000

[3] Kohl P, Noble D. Systems biology and the virtual physiological human. Molecular Systems Biology 2009;**292**: 1-6. DOI: 10.1038/msb.2009.51

[4] Amini S, Veilleux D, Villemure I. Tissue and cellular morphological changes in growth plate explants under compression. Journal of Biomechanics. 2010;**43**(13):2582-2588

[5] Saini S, Vijay R. Back propagation artificial neural network. In: Proceedings of the 5th International Conference on Communication Systems and Network Technologies; Gwalior, India. April 2015. pp. 1177-1180

[6] Behr J, Choi SM, Grosskop S, Hong H, Nam SA, Peng Y, et al. Modeling, visualization, and interaction techniques for diagnosis and treatment planning in cardiology. Computers & Graphics. 2000;**24**(5):741-753

[7] McInerney T, Terzopoulos D. Deformable models in medical image analysis: A survey. Medical Image Analysis. 1996;**1**(2):91-108

[8] Lustig M, Donoho DL, Santos JM, Pauly JM. Compressed sensing MRI. IEEE Signal Processing Magazine. Mar. 2008;**25**(2):72-82

[9] Wang LV. Multiscale photoacoustic microscopy and computed

tomography. Nature Photonics. Sep. 2009;**3**(9):503-509

[10] Beard P. Biomedical photo acoustic imaging. Interface Focus. 2011;**1**(4):602-631

[11] Ghesu FC et al. Marginal space deep learning: Efficient architecture for volumetric image parsing. IEEE Transactions on Medical Imaging. May 2016;**35**(5):1217-1228

[12] Wang G. A perspective on deep imaging. IEEE Access. 2016;**4**:8914-8924

[13] Esteva A et al. Dermatologist-level classification of skin cancer with deep neural networks. Nature. 2017;**542**(7639):115-118

[14] Okada M. A digital filter for the QRS complex detection. IEEE Transactions on Bio-Medical Engineering BME. 1979;**26**:700-703

[15] Ergun E, Batakçı L. Audio watermarking scheme based on embedding strategy in low frequency components with a binary image. Digital Signal Processing. March 2009;**19**(2):277-286

[16] Kadambe S, Murray R, Boudreaux-Bartels GF. Wavelet transform-based QRS complex detector. IEEE Transactions on Biomedical Engineering. 1999;**46**:838-848

[17] Awad ES. Data interchange across cores of multi-core optical fibers. Optical Fiber Technology Volume 26, Part B. December 2015;**26**:157-162

[18] Hamilton PS, Tompkins WJ. Quantitative investigation of QRS detection rules using the MIT/BIH arrhythmia database. IEEE Transactions on Biomedical Engineering BME. 1986;**33**:1157-1165

[19] Kahn JM, Ho K-P. Spectral efficiency limits and modulation/detection techniques for DWDM Systems IEEE. Journal of Selected Topics in Quantum Electronics. 2004;**10**(2):259-272

[20] Chen SW, Chen HC, Chan HL. A real-time QRS detection method based on moving averaging incorporating with wavelet denoising. Computer Methods and Programs in Biomedicine. 2006;**82**:187-195

[21] He B, Li G, Lian J. A spline Laplacian ECG estimator in realistic geometry volume conductor. IEEE Transactions on Biomedical Engineering. 2002;**49**(2):110-117

[22] Perrin F, Pernier J, Bertrand O, Giard MH, Echallier JF. Mapping of scalp potentials by surface spline interpolation. Electroencephalography and Clinical Neurophysiology. 1987;**66**:75-81

[23] Kawakatsu H. Methods for evaluating pictures and extracting music by 2D DFA and 2D FFT. 19th international conference on knowledge based and intelligent information and engineering systems. Procedia Computer Science. 2015;**60**:834-840

[24] Kawakatsu H. Fluctuation analysis for photographs of tourist spots and music extraction from photographs. In: Lecture Notes in Engineering and Computer Science: Proceedings of the World Congress on Engineering 2014; WCE 2014: 2-4 July, 2014, London, UK. Vol. 1. 2014. pp. 558-561

[25] Manandhar P, Ward A, Allen P, Cotter DJ, Mcwhirter JG, Shepherd TJ. An automated algorithm for measurement of surgical tip excursion in ultrasonic vibration using the spatial 2-dimensional Fourier transform in an optical image. 44th annual symposium of the ultrasonic

industry association. Physics Procedia. 2016;**87**:139-146

[26] Bhateja V, Patel H, Krishn A, Sahu A, Lay-Ekualille A. Multimodal medical image sensor fusion framework using cascade of wavelet and contourlet transform domains. IEEE Sensors Journal. 2015;**15**(12):6783-6790

[27] Mjahad A, Rosado-Muñoz A, Bataller Mompeán M, Francés-Víllora JV, Ventricular Fibrillation G-MJF. Tachycardia detection from surface ECG using time-frequency representation images as input dataset for cyber-physical systems. Computer Methods and Programs in Biomedicine. 2017;**141**:119-127

[28] Arenja N, Riffel JH, Djioko CJ, Andre F, Fritz T, Halder M, et al. Right ventricular long axis strain-validation of a novel parameter in non-ischemic dilated cardiomyopathy using standard cardiac magnetic resonance imaging. European Journal of Radiology. 2016;**85**:1322-1328

[29] Mavratzakis A, Herbert C, Walla P. Emotional facial expressions evoke faster orienting responses, but weaker emotional responses at neural and behavioural levels compared to scenes: A simultaneous EEG and facial EMG study. NeuroImage. 2016;**124**:931-946

[30] Vuilleumier P, Pourtois G. Distributed and interactive brain mechanisms during emotion face perception: Evidence from functional neuroimaging. Neuropsychologia. 2007;**45**(1):174-194

[31] Wieser MJ, Brosch T. Faces in context: A review and systematization of contextual influences on affective face processing. Frontiers in Psychology. 2012;**3**:471

[32] Olofsson JK, Nordin S, Sequeira H, Polich J. Affective picture processing:

An integrative review of ERP
findings. Biological Psychology.
2008;77(3):247-265

[33] Rajeswari J, Jagannath M. Advances
in biomedical signal and image
processing—A systematic review.
Informatics in Medicine Unlocked. DOI:
10.1016/j.imu.2017.04.002

Chapter 9

Phase-Stretch Adaptive Gradient-Field Extractor (PAGE)

Madhuri Suthar and Bahram Jalali

Abstract

Emulated by an algorithm, certain physical phenomena have useful properties for image transformation. For example, image denoising can be achieved by propagating the image through the heat diffusion equation. Different stages of the temporal evolution represent a multiscale embedding of the image. Stimulated by the photonic time stretch, a realtime data acquisition technology, the Phase Stretch Transform (PST) emulates 2D propagation through a medium with group velocity dispersion, followed by coherent (phase) detection. The algorithm performs exceptionally well as an edge and texture extractor, in particular in visually impaired images. Here, we introduce a decomposition method that draws inspiration from the birefringent diffractive propagation. This decomposition method, which we term as **P**hase-stretch **A**daptive **G**radient-field **E**xtractor (**PAGE**) embeds the original image into a set of feature maps that selects semantic information at different scale, orientation, and spatial frequency. We demonstrate applications of this algorithm in edge detection and extraction of semantic information from medical images, electron microscopy images of semiconductor circuits, optical characters and finger print images. The code for this algorithm is available here (https://github.com/JalaliLabUCLA).

Keywords: computational imaging, physics-inspired algorithms, phase stretch transform, feature engineering, Gabor filter, digital image processing

1. Introduction

Physical phenomena described by partial differential equations (PDE) have inspired a new field in computational imaging and computer vision [1]. Such physics-inspired algorithms based on PDEs have been successful for image smoothening and restoration. Image restoration can be viewed as obtaining the solution to evolution equations by minimizing an energy function. The most popular PDE technique for image smoothening treats the original image as the initial state of a diffusion process and extracts filtered versions from its evolution at different times. This embeds the original image into a family of simpler images at a hierarchical scale. Such a scale-space representation is useful for extracting semantically important information [2]. Physics based algorithms not only outperform their conventional counterparts, but also have enabled new applications. Usage of these algorithms range from feature detection in digital images [3–5], to 3D modeling of objects from 2D images [6, 7], to optical character recognition [8] as well as for restoring audio quality [9].

Phase Stretch Transform (PST) is a physics inspired algorithm that emulates 2D propagation through a medium with group velocity dispersion, followed by coherent (phase) detection [10, 11]. The algorithm performs exceptionally well as edge and texture extractor, in particular in visually impaired images [12]. This transform has an inherent equalization ability that supports wide dynamic range of operation for feature detection [12–14]. It also exhibits superior properties over conventional derivative operators, particularly in terms of feature enhancement in noisy low contrast images. These properties have been exploited to develop image processing tools for clinical needs such as a decision support system for radiologists to diagnose pneumothorax [15, 16], for resolution enhancement in brain MRI images [17], single molecule imaging [18], and image segmentation [19].

PST emulates the physics of photonic time stretch [20], a real time measurement technology that has enabled observation as well as detection of ultrafast, non-repetitive events like optical rogue waves [21], optical fiber soliton explosions [22] and birth of mode locking in laser [23]. Further, by combining photonic time stretch technology with machine learning algorithms, a world record accuracy has been achieved for classification of cancer cells in blood stream [24, 25].

The photonic time stretch employs group-velocity dispersion (GVD) in an optical fiber to slow down an analog signal in time by propagating a modulated optical pulse through the time stretch system which is governed by the following equation:

$$E_o(z,t) = \frac{1}{2\pi} \int_{-\infty}^{+\infty} \tilde{E}_i(0,\omega) \cdot \left[e^{\frac{-j\beta_2 z \omega^2}{2}} \right] \cdot e^{j\omega t} d\omega \tag{1}$$

where, β_2 = GVD parameter, z is propagation distance, $E_o(z,t)$ is the reshaped output pulse at distance z and time t. The response of dispersive element in the time-stretch system can be approximated a phase propagator $\tilde{K}[\omega] = e^{\frac{-j\beta_2 z \omega^2}{2}}$ which leads to the definition of PST for a discrete 2D signal as following:

$$\mathbb{PST}\{E_i[x,y]\} \triangleq \measuredangle \left\{ IFFT^2 \left\{ FFT^2 \{E_i[x,y]\} \cdot \tilde{K}[u,v] \right\} \right\} \tag{2}$$

In the above equations, $E_i[x,y]$ is the input image, FFT^2 is 2D Fast Fourier Transform, $IFFT^2$ is 2D Inverse Fast Fourier Transform, x and y are the spatial variables and, u and v are spatial frequency variables. The function $\tilde{K}[u,v]$ is called the warped phase kernel implemented in frequency domain for image processing.

PST utilizes the GVD dispersion to convert a real image to a complex quantity such that the spatial phase after the $IFFT^2$ operation is a function of frequency. Upon thresholding, the high frequency edges survive. The phase kernel for the PST is designed by converting the 2D Cartesian frequencies u and v to polar coordinates which results in a symmetric Cartesian phase kernel. However, as digital images are fundamentally two-dimensional, there is an inherent loss of information in the features detected by PST. This motivates us to develop a more comprehensive approach that captures angular as well as spatial frequency information in a semantic fashion.

In this chapter, we introduce Phase-stretch Adaptive Gradient-field Extractor (PAGE), a new physics inspired feature engineering algorithm that computes a feature set comprising of edges at different spatial frequencies, at different orientations, and at different scales. These filters metaphorically emulate the physics of birefringent (orientation-dependent) diffractive propagation through a physical medium with a specific diffractive property. In such a medium, the dielectric constant of the medium and hence, its refractive index is a function of spatial frequency and the polarization in the transverse plane. To understand this metaphoric analogy,

we consider an optical pulse with two linearly orthogonal polarizations, $\tilde{E}_x$ and $\tilde{E}_y$, propagating through a dispersive diffractive medium such that

$$\tilde{E}_i(z,t) = \tilde{E}_x + \tilde{E}_y \tag{3}$$

As the propagation constant $\beta = \frac{n \cdot 2\pi}{\lambda}$ is a function of refractive index (spatially varying), the two orthogonal polarizations $\tilde{E}_x$ and $\tilde{E}_y$ will have different propagation constants and hence, a phase difference at the output given by the following equation:

$$\Delta\phi = \phi_x - \phi_y = \Delta\beta \cdot l = \frac{\omega_m}{c} |n_x - n_y| \cdot L \tag{4}$$

By controlling the value of n_x and n_y, as well the dependence of refractive index on frequency $n_x(\omega)$ and $n_y(\omega)$, we are able to detect a semantic hyper-dimensional feature set from a 2D image. We demonstrate with several visual examples in the later part of this chapter that the above filter banks can be applied for image processing and computer vision applications such as for detection of fabrication artifacts in semiconductor chips, development of clinical decision support systems, recognition of optical characters or finger prints. In particular, we show that PAGE features outperform the conventional derivative operators as well as directional Gabor filter banks.

Further, we address the dual problem of spatial resolution and dynamic range limitations in an imaging system. In an ideal imaging system, the numerical aperture and the wavelength of an optical set up are the only factors that determine the spatial resolution offered by the modality. But under non-ideal conditions, the number of photons collected from a specimen control its dynamic range (the ratio between the largest and the smallest value of a variable quantity) which in turn also limits the spatial resolution. This leads to the fundamental dual-problem of spatial resolution and dynamic range limitations in an imaging modality [26].

Certain approaches to improve the resolution of the imaging system include use of wide-field fluorescence microscopy [27, 28] which offers better resolution than confocal fluorescence microscopy [29], multiple fluorophores [30, 31]. Also, various image processing techniques such as multi-scale analysis using wavelets [32, 33] have been proposed for improving the resolution while retaining important visual information post the image acquisition. We show later in the chapter that we are able to alleviate this dual-problem by incorporating, in our algorithm, a local adaptive contrast enhancement operator, also known as Tone Mapping Operator (TMO) which leads to excellent dynamic range.

Other steps of the proposed decomposition method are discussed at length in the next section. The organization of the chapter is as follows. In Section 2, we describe the details of the proposed decomposition method. Experimental results and conclusions are presented in Sections 3 and 4, respectively.

2. Mathematical framework

Different steps of our proposed decomposition method Phase-stretch Gradient-field Extractor (PAGE) for feature engineering are shown in **Figure 1**. The first step is to apply an adaptive tone mapping operator (TMO) to enhance the local contrast. Next, we reduce the noise by applying a smoothening kernel in frequency domain (this operation can also be done in spatial domain). We then apply a spectral phase kernel that emulates the birefringence and frequency channelized diffractive

Figure 1.
Different steps of the phase-stretch gradient-field extractor (PAGE) algorithm. The pipeline starts with application of tone mapping in the spatial domain. This is followed by a smoothening and a spectral phase operation in the frequency domain. The spectral phase operation is the main component of the PAGE algorithm. The generated hyper-dimensional feature vector is thresholded and post-processed by morphological operations. PAGE embeds the original image into a set of feature maps that select semantic information at different scale, orientation, and spatial frequency.
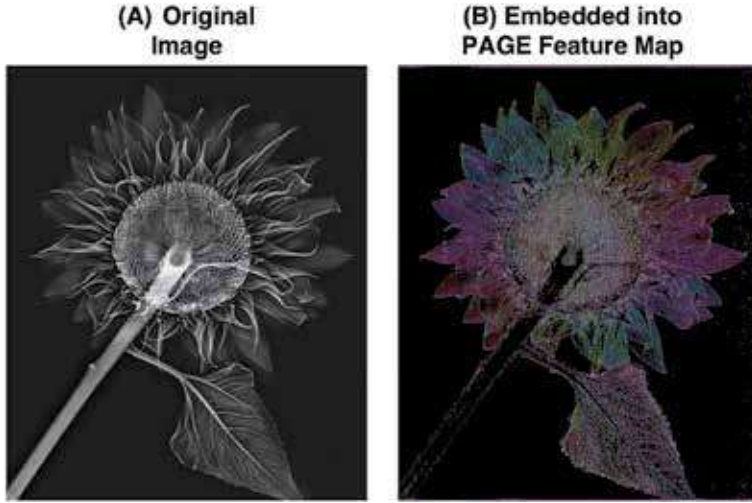

Figure 2.
The phase-stretch gradient-field extractor (PAGE) feature map of an X-ray image. The original image is shown on the left (A). PAGE embeds the original image into a feature map that selects semantic information at different orientations as shown in (B). The orientation of the edges is encoded into various color values here.

propagation. The final step of PAGE is to apply thresholding and morphological operations on the generated feature vectors in spatial domain to produce the final output. The PAGE output embeds the original image into a set of feature maps that select semantic information at different scale, orientation, and spatial frequency. We show in **Figure 2** how PAGE embeds semantic information at different orientations for an X-ray image of a flower.

The sequence of steps of our physics-inspired feature extraction method, PAGE, can be represented by the following equations. We first define the birefringent stretch operator $\mathbb{S}\{\}$ as follows:

$$E_o[x,y] = \mathbb{S}\{E_i[x,y]\} = IFFT^2\{\tilde{K}[u,v,\theta] \cdot \tilde{L}[u,v] \cdot FFT^2\{TMO\{E_i[x,y]\}\}\} \quad (5)$$

where $E_o[x,y]$ is a complex quantity defined as,

$$E_o[x,y] = |E_o[x,y]|e^{j\theta[x,y]} \quad (6)$$

In the above equations, $E_i[x,y]$ is the input image, x and y are the spatial variables, FFT^2 is the two-dimensional Fast Fourier Transform, $IFFT^2$ is the

two-dimensional Inverse Fast Fourier Transform, *TMO* is a spatially adaptive Tone Mapping Operator and u and v are frequency variables. The function $\tilde{K}[u, v, \theta]$ is called the PAGE kernel and the function $\tilde{L}[u, v]$ is a smoothening kernel, both implemented in frequency domain. For all our simulations here, we consider $\tilde{L}[u, v]$ to be low pass Gaussian filter whose cut off frequency is determined by the sigma of the Gaussian filter (σ_{LPF}).

The PAGE operator $\mathbb{P}\{\}$ can then be defined as the phase of the output of the stretch operation $\mathbb{S}\{\}$ applied on the input image $E_i[x, y]$:

$$\mathbb{P}\{E_i[x, y]\} = \measuredangle\{\mathbb{S}\{E_i[x, y]\}\} \tag{7}$$

where $\measuredangle\langle\cdot\rangle$ is the angle operator.

In the next subsections, we discuss each of the above mentioned kernels in detail and demonstrate the operation of each step using simulation results.

2.1 Tone mapping operator (TMO)

A tone mapping operator (*TMO*) is applied to enhance the local contrast in the input image $E_i[x, y]$. This technique is a standard method in the field of image processing to solve the problem of limited contrast in an imaging system while still preserving important details and thereby, helps in improving the dynamic range of an imaging system via post processing. By applying a tone mapping operator to the input image, an enhanced contrast can be achieved. While various TMO operators have been developed for adaptive contrast enhancement, here, we implement the TMO step by applying a Contrast Limited Adaptive Histogram Equalization (CLAHE) operator to the input image.

We operate on the input image using a *TMO* first, followed by smoothening operator (low pass filter) and not vice versa. The reason to follow this sequence of operation is as follows. Noise present in an image is mostly represented by the high frequency components in the spectrum. These high frequency components can be present at both low-light-level or at high-light-level in the spatial domain. Because of the use of a tone mapping operator, the low-light-level features get over emphasized [34, 35]. This also leads to amplification of the image noise particularly in low-light scenarios. By applying a smoothening filter after the TMO operation, we aim to remove these noise artifacts from the contrast enhancement step. Alternatively, where any noise is left after the application of a smoothening kernel on the input image, it could be amplified by the TMO operation in the next step. Therefore, one may need to alternate between the smoothening step and TMO before obtaining a final satisfactory result [36].

2.2 Phase-stretch adaptive gradient-field extractor (PAGE) kernel

Phase-stretch adaptive gradient-field extractor (PAGE) filter banks are defined by the PAGE kernel $\tilde{K}[u, v, \theta]$ and are designed to compute semantic information from an image at different orientations and frequencies. The PAGE kernel $\tilde{K}[u, v, \theta]$, consists of a phase filter which is a function of frequency variable u and v, and a steerable angle variable θ which controls the directionality of the response. We first define the translated frequency variable u' and v'

$$u' = u \cdot cos\,(\theta) + v \cdot sin\,(\theta) \tag{8}$$

$$v' = u \cdot sin\theta) + v \cdot cos\,(\theta) \tag{9}$$

such that the frequency vector rotates along the origin with θ

$$u' + jv' \Leftarrow u + jv \tag{10}$$

We then define the PAGE kernel $\tilde{K}[u, v, \theta]$ as a function of frequency variable u and v and steerable angle θ as follows:

$$\tilde{K}[u, v, \theta] = \tilde{K}[u', v'] = \exp\{j \cdot \phi_1(u') \cdot \phi_2(v')\} \tag{11}$$

where

$$\phi_1(u') = S_{u'} \cdot \frac{1}{\sigma_{u'}\sqrt{2\pi}} \cdot exp^{-(|u'| - \mu_{u'})^2 / 2\sigma_{u'}^2} \tag{12}$$

$$\phi_2(v') = S_{v'} \cdot \frac{1}{|v'|\sigma_{v'}\sqrt{2\pi}} \cdot exp^{-(ln(|v'|) - \mu_{v'})^2 / 2\sigma_{v'}^2} \tag{13}$$

There are two important things that should be noted here. First, we consider the modulus of our translated frequency variable u' and v' so that our kernel is symmetric for proper phase operation as discussed in [12]. Second, for all our simulation examples here, when we consider a bank of PAGE filters, we first normalize $\phi_1(u')$ and $\phi_2(v')$ in the range (0,1) for all values of θ and then, multiply the filter banks with $S_{u'}$ and $S_{v'}$, respectively, in order to make sure that the amplitude of each filter in the bank is same.

These filter banks can detect features at a particular frequency and/or in a particular direction. Therefore, by selecting a desired direction and/or frequency, a hyper-dimensional feature map can be constructed. We list all parameters in **Table 1** that control different functionalities of our proposed decomposition method PAGE.

Notation	Variable
u and v	Spatial frequency
θ	Steerable angle
u' and v'	Translated spatial frequency
$\phi_1(\cdot)$	Normal filter
$\phi_2(\cdot)$	Log normal filter
$S_{u'}$	Strength of ϕ_1 filter
$S_{v'}$	Strength of ϕ_2 filter
$\mu_{u'}$	Mean of normal distribution for ϕ_1 filter
$\mu_{v'}$	Mean of log-normal distribution for ϕ_2 filter
$\sigma_{u'}$	Sigma of normal distribution for ϕ_1 filter
$\sigma_{v'}$	Sigma of log-normal distribution for ϕ_2 filter
σ_{LPF}	Sigma of Gaussian distribution for $\tilde{L}[u, v]$ smoothening kernel
$Threshold(Min, Max)$	Bi-level feature thresholding for morphological operations

*The values of these parameters for **Figure 2** simulation result are: $S_{u'} = 3.4$, $S_{v'} = 1.2$, $\mu_{u'} = 0$, $\mu_{v'} = 0.4$, $\sigma_{u'} = 0.05$, $\sigma_{v'} = 0.7$, $\sigma_{LPF} = 0.1$ and $Threshold(Min, Max) = (-) 1,0.0019$. The number of filters considered for a 1° resolution is equals to 180.*

Table 1.
Different parameters of our physics-inspired feature decomposition method PAGE.

Figure 3A–P show the generated phase profiles for $\phi_1(u') \cdot \phi_2(v')$ that select semantic information at different orientation and frequency as described in Eqs. (10)–(13) using PAGE kernels. These phase kernels are applied to the input image spectrum. Using the steerable angle, the directionality of edge response can be controlled in the output phase of the transformed image. The detected output response for each directional filter is thresholded using a bi-level method. This is done to preserve negative high amplitude values as well as positive high amplitude values.

2.2.1 Directionality

In order to detect features in a particular direction spread over the all the frequency components in the spectrum, we construct the PAGE filter banks by using Eqs. (9)–(13) for $\tilde{K}[u, v, \theta]$, $\phi_1(u')$ and $\phi_1(v')$ respectively. By controlling the value of sigma $\sigma_{u'}$ of normal distribution for $\phi_1(u')$ filter, we avoid any overlapping of directional filters as seen in **Figure 4**.

We first evaluate the performance of these kernel by qualitatively comparing the feature detection of PAGE with PST. The image under analysis is a gray-scale image
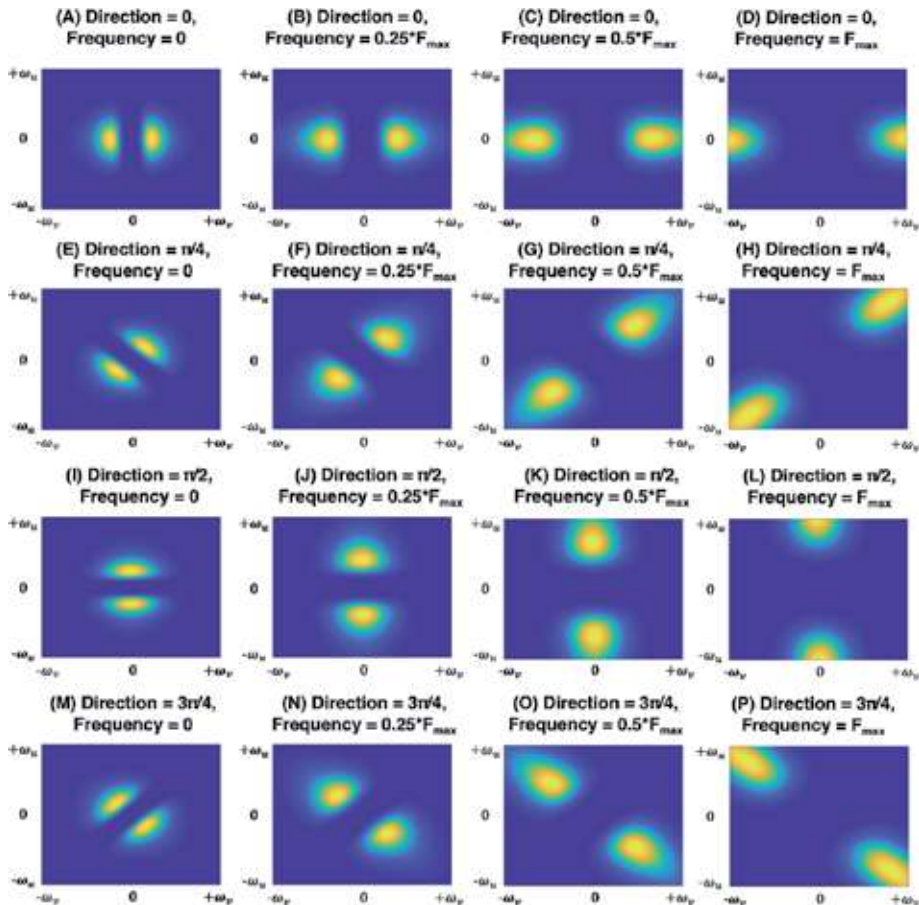

Figure 3.
Phase-stretch gradient-field extractor (PAGE) filter banks (A)–(P) phase filter banks as defined in Eqs. (8)–(13) for various frequencies and directions. The frequency variables u and v are normalized from $-\omega_u$ to $+\omega_u$ and $-\omega_v$ to $+\omega_v$, respectively. The center $\mu_{v'}$ of the phase kernel $S_{v'}$ is gradually increased for control over the frequency distribution. The values for steerable angle θ considered here are 0, $\pi/4, \pi/2, 3\pi/4$.
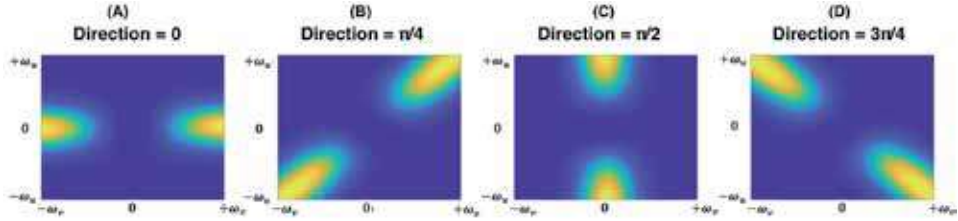
Figure 4.
Phase-stretch gradient field extractor (PAGE) directional filter banks (A)–(D) the directional filter banks of PAGE computed using the definition in Eqs. (9)–(13) for steerable angle θ = 0, π/4, π/2 and 3π/4, respectively. By monitoring the value of sigma $\sigma_{u'}$ of the normal filter $\phi_1(u')$, the angular spread of kernel $\tilde{K}[u, v, \theta]$ can be controlled to avoid any overlapping of directional filters.

of a rose. For a better visual understanding of our method, we first compute orthogonal directional responses as shown in **Figure 5**. We then show results of edge detection using PST and PAGE in **Figure 6**. The values for the parameters strength $S_{u'} = 2.8$, $S_{v'} = 0.5$, $\mu_{u'} = 0$, $\mu_{v'} = 0.4$, $\sigma_{u'} = 0.05$, $\sigma_{v'} = 0.7$, $\sigma_{LPF} = 0.1$ and $Threshold(Min, Max) = (-1, 0.0019)$. The number of filters considered for a 1° resolution is equals to 180. Morphological operations used for the result shown in **Figure 6C** include edge thinning and isolated pixel removing for each directional response. As evident in **Figure 6**, edges are accurately extracted with our technique. Different colors in the computed edge response indicate the edge directionality.

2.2.2 Frequency selectivity

The PAGE filter banks can also be designed to detect edges at a particular frequency by controlling the spread of log normal distribution. To demonstrate this
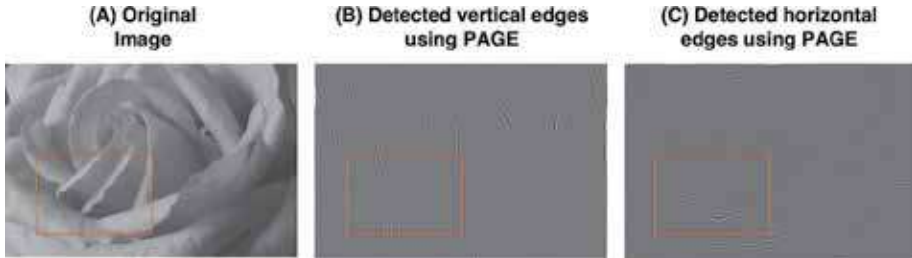

Figure 5.
Phase-stretch gradient-field extractor (PAGE) directional filter banks response the original image is shown in (A). We design two directional PAGE filters here to detect vertical ($\theta = \pi/2$) and horizontal ($\theta = 0$) edges as shown in (B) and (C) respectively.
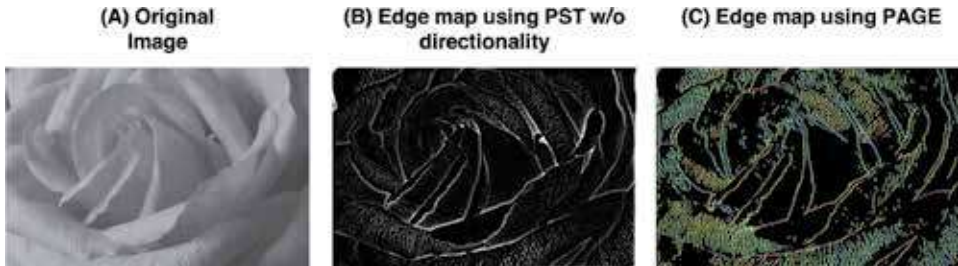

Figure 6.
Comparison of feature detection using phase stretch transform (PST) and phase-stretch gradient-field extractor (PAGE) the original image is shown in (A). The output edge image obtained using PST without the support of directional response is shown in (B). The edge map obtained using PAGE filter banks that support edge detection at all frequencies is shown in (C). Different color values are used to show the orientation of the edges.
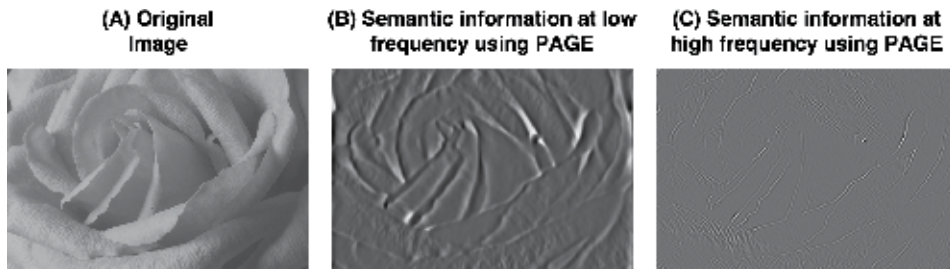
(A) Original Image   **(B) Semantic information at low frequency using PAGE**   **(C) Semantic information at high frequency using PAGE**

Figure 7.
Feature detection using phase-stretch gradient field extractor (PAGE) at low and high frequency: Features detected at low frequency are much smoother whereas for high frequency, the features are sharper. This demonstrates the frequency selectivity for feature detection using PAGE.

functionality, we show the features detected at low and high frequency using the rose image as an example in the **Figure 7**. As seen in the figure, the features detected at low frequency are smoother and at high frequency are sharper.

3. Discussion

3.1 Comparison to Gabor feature extractors

We demonstrate the effectiveness of our decomposition method by comparing the directional edge response obtained by applying Gabor filter banks to an optical character image. We design 24 Gabor directional filters and augment the response from each of the filters to generate the image in **Figure 8B**. As seen in **Figure 8C**, with PAGE we have a better spatial localization of the edge response. By spatial localization, we mean that inherently PAGE has a sharper edge response, as seen in the figure. This is because, unlike the Gabor filters whose bandwidth is determined by the sigma parameter of the filter, in PAGE, the bandwidth of the response is determined by the input image dimension. Therefore, there is better localization of edge with PAGE. The parameters values are strength $S_{u'} = 2.8$, $S_{v'} = 0.5$, $\mu_{u'} = 0$, $\mu_{v'} = 0.4$, $\sigma_{u'} = 0.05$, $\sigma_{v'} = 0.7$, $\sigma_{LPF} = 0.1$ and $Threshold(Min, Max) = (-1, 0.0019)$. The number of filters considered for a 1° resolution is equals to 180.
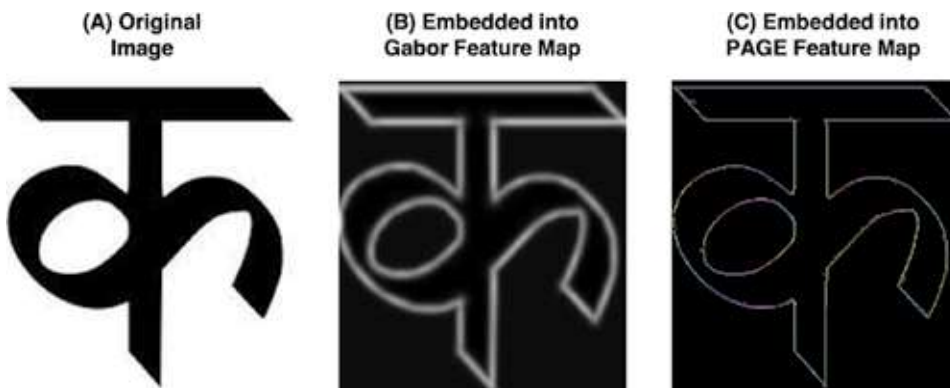
(A) Original Image   **(B) Embedded into Gabor Feature Map**   **(C) Embedded into PAGE Feature Map**

Figure 8.
Comparison to Gabor feature extractors: Features detected using Gabor do not have inherent spatial feature localization. With PAGE, the features are more sharper as the bandwidth of the response is determined by the input image dimension.

3.2 Comparison to derivative feature extractors

To demonstrate the superiority of our decomposition method, we compare the edge response obtained by applying derivative based operators to a test image shown in **Figure 9A**. The response to a derivative based operator is computed by using the edge function of Matlab software (canny) and is shown in **Figure 9B**. As seen in **Figure 9C**, PAGE outperforms derivative based operators by producing the orientation information and low contrast details. The parameters values are strength $S_{u'} = 2.7$, $S_{v'} = 0.5$, $\mu_{u'} = 0$, $\mu_{v'} = 0.4$, $\sigma_{u'} = 0.05$, $\sigma_{v'} = 0.7$, $\sigma_{LPF} = 0.1$ and $Threshold(Min, Max) = (-1, 0.0019)$. The number of filters considered for a 1° resolution is equals to 180.

3.3 Simulation results

We apply our decomposition method to different types of images to show that the directional edge response obtained by PAGE can be used for various computer vision applications. For example, in **Figure 10**, we show application of PAGE to a Single Electron Microscope (SEM) image of an integrated circuit chip. As seen, the
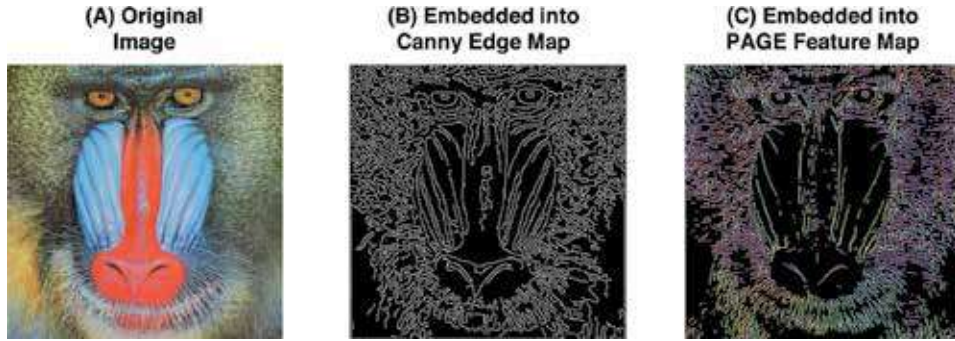

Figure 9.
Comparison to derivative feature extractors: Features detected with derivative based edge operators calculate the directionality based on the horizontal and vertical gradients and do not provide information about the spatial frequency of the edges. PAGE provides both the orientation as well as the spatial frequency selectivity in the output response.
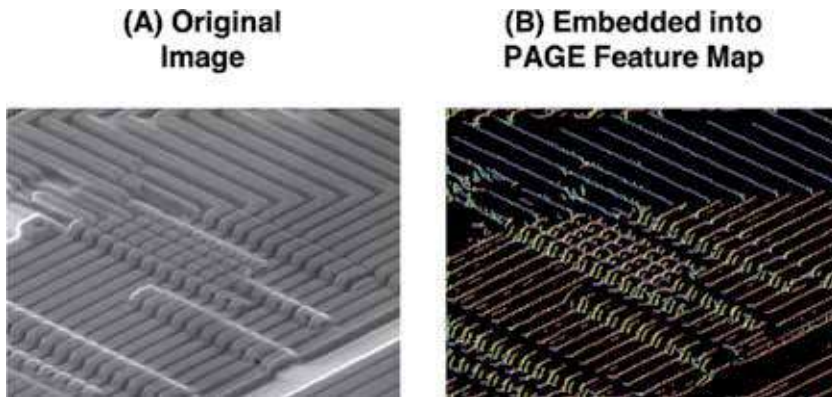

Figure 10.
Fabrication artifact detection using phase-stretch gradient-field extractor (PAGE) on a single Electron microscope (SEM) image of integrated circuit chip. The original image is shown in (A). The output edge image obtained using PAGE filter banks that support edge detection at all frequencies is shown in (B). Different color values are used to show the orientation of the edges that correspond to the chip layout and can be used to detect fabrication artifacts.

PAGE feature response is able to capture the edges corresponding to the chip layout (even the low contrast details). Based on the viewing angle (camera position), the layout edges should appropriately be rendered in the image as well as in the edge map. This can be used to identify any chip artifacts during the fabrication process. The parameters values for generating the feature map shown in **Figure 10** are strength $S_{u'} = 3.1$, $S_{v'} = 0.9$, $\mu_{u'} = 0$, $\mu_{v'} = 0.4$, $\sigma_{u'} = 0.05$, $\sigma_{v'} = 0.7$, $\sigma_{LPF} = 0.1$ and $Threshold(Min, Max) = (-1, 0.0042)$. The number of filters considered for a 1° resolution is equals to 180.

We also apply PAGE to detect directional edge response to an image of a finger print as shown in **Figure 11**. Not only does PAGE detects a directional edge response, but also has an inherent equalization property to detect low contrast edges. The parameters values are strength $S_{u'} = 1.5$, $S_{v'} = 0.4$, $\mu_{u'} = 0$, $\mu_{v'} = 0.4$, $\sigma_{u'} = 0.05$, $\sigma_{v'} = 0.7$, $\sigma_{LPF} = 0.08$ and $Threshold(Min, Max) = (-1, 0.0019)$. The number of filters considered for a 1° resolution is equals to 180.

Next, we show application of our decomposition method PAGE to extract edges of vessels from a retinal image in **Figure 12**. The distribution of vessels based on the orientation of the edges can be used as an important feature to detect any abnormalities in the eye structure. As seen, the PAGE feature response is able to capture both the low contrast details as well as information about the directionality of the
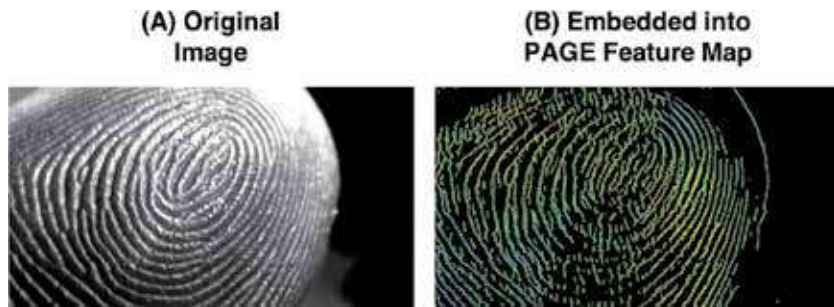

Figure 11.
Fingerprint feature map using phase-stretch gradient-field extractor (PAGE). The original image is shown in (A). The output edge image obtained using PAGE filter banks that support edge detection at all frequencies is shown in (B). As the edges of the fingerprint rotate, the response value changes (shown here with different color value).
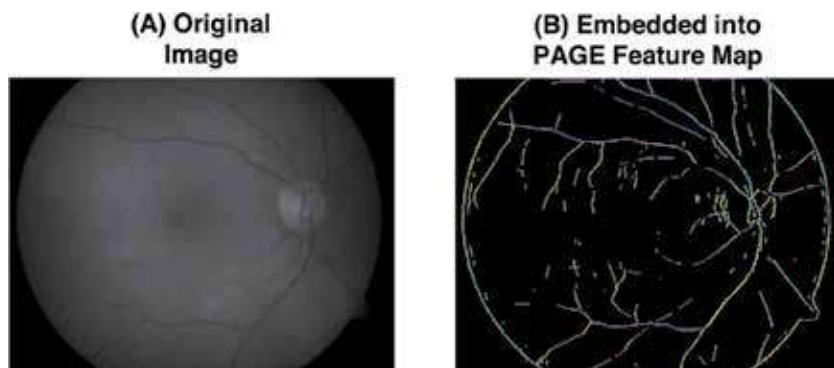
Figure 12.
Vessel detection using phase-stretch gradient-field extractor (PAGE) on an image of a retina. The original image is shown in (A). The output edge image obtained using PAGE filter banks that support edge detection at all frequencies is shown in (B). Different color values are used to show the orientation of the edges. The low contrast vessels are not only detected using PAGE but also information on how the direction of the blood flow changes across the eye based on the vessel distribution is extracted.

vessel edges which is coded in form of the color value in RGB space. The parameters values are strength $S_{u'} = 2.2$, $S_{v'} = 1.1$, $\mu_{u'} = 0$, $\mu_{v'} = 0.4$, $\sigma_{u'} = 0.05$, $\sigma_{v'} = 0.7$, $\sigma_{LPF} = 0.1$ and $Threshold(Min, Max) = (-1, 0.0019)$. The number of filters considered for a 1° resolution is equals to 180.

4. Conclusions

In this chapter, a presentation is made on a new feature engineering method that takes inspiration from the physical phenomenon of birefringence in an optical system. The introduced method called Phase-stretch Adaptive Gradient-field Extractor (PAGE) controls the diffractive properties of the simulated medium as a function of spatial location and channelized frequency. This method when applied to 2D digital images extracts semantic information from the input image at different orientation, scale and frequency and embeds this information into a hyper-dimensional feature map. The computed response is compared to other directional filters such as Gabor to demonstrate superior performance of PAGE. Applications of the algorithm for edge detection and extraction of semantic information from medical images, electron microscopy images of semiconductor circuits, optical character and finger print images is also shown.

Acknowledgements

Conflict of interest

The authors declare no conflict of interest.

Author details

Madhuri Suthar[1]* and Bahram Jalali[1,2,3,4]

1 Department of Electrical and Computer Engineering, University of California - Los Angeles, Los Angeles, California, USA

2 California NanoSystems Institute, Los Angeles, California, USA

3 Department of Bioengineering, University of California - Los Angeles, Los Angeles, California, USA

4 Department of Surgery, David Geffen School of Medicine, University of California - Los Angeles, Los Angeles, California, USA

*Address all correspondence to: madhurisuthar@ucla.edu

IntechOpen

References

[1] Perona P, Malik J. Scale-space and edge detection using anisotropic diffusion. IEEE Transactions on Pattern Analysis and Machine Intelligence. 1990;**12**(7):629-639

[2] Weickert J. Anisotropic Diffusion in Image Processing. Stuttgart: Teubner; 1998

[3] Catt F, Lions PL, Morel JM, Coll T. Image selective smoothing and edge detection by nonlinear diffusion. SIAM Journal on Numerical Analysis. 1992;**29**(1):182-193

[4] Alvarez L, Lions PL, Morel JM. Image selective smoothing and edge detection by nonlinear diffusion. II. SIAM Journal on Numerical Analysis. 1992;**29**(3): 845-866

[5] Nordstrom KN. Biased anisotropic diffusion: A unified regularization and diffusion approach to edge detection. Image and Vision Computing. 1990; **8**(4):318-327

[6] Zhao H, Lu M, Yao A, Guo Y, Chen Y, Zhang L. Physics inspired optimization on semantic transfer features: An alternative method for room layout estimation. In: Proceedings of the IEEE Conference on Computer Vision and Pattern Recognition; 2017. pp. 10-18

[7] Yang S, Pan Z, Amert T, Wang K, Yu L, Berg T, et al. Physics-inspired garment recovery from a single-view image. ACM Transactions on Graphics (TOG). 2018;**37**(5):170

[8] Phan TQ, Shivakumara P, Tan CL. Detecting text in the real world. In: Proceedings of the 20th ACM International Conference on Multimedia. ACM; 2012. pp. 765-768

[9] Fadeyev V, Haber C. A novel application of high energy physics technology to the problem of audio preservation. Nuclear Instruments and Methods in Physics Research Section A: Accelerators, Spectrometers, Detectors and Associated Equipment. 2004;**518** (1–2):456-462

[10] Asghari MH, Jalali B. Edge detection in digital images using dispersive phase stretch transform. International Journal of Biomedical Imaging. 2015;**2015**: 687819

[11] JalaliLabUCLA/Image-feature-detection-using-Phase-Stretch-Transform. Available from: https://github.com/JalaliLabUCLA/Image-feature-detection-using-Phase-Stretch-Transform/

[12] Suthar M, Asghari H, Jalali B. Feature enhancement in visually impaired images. IEEE Access. 2017;**6**: 1407-1415

[13] Jalali B, Suthar M, Asghari M, Mahjoubfar A. Physics-based feature engineering. In: Optics, Photonics and Laser Technology. Cham: Springer; 2017. pp. 255-275

[14] Jalali B, Suthar M, Asghari M, Mahjoubfar A. Optics-inspired computing. In: Proceedings of the 5th International Conference on Photonics, Optics and Laser Technology, Vol. 1; 2017. pp. 340-345

[15] Suthar M, Mahjoubfar A, Seals K, Lee EW, Jalaii B. Diagnostic tool for pneumothorax. In: 2016 IEEE Photonics Society Summer Topical Meeting Series (SUM). IEEE; 2016. pp. 218-219

[16] Suthar M. Decision support systems for radiologists based on phase stretch transform [Doctoral dissertation]. USA: UCLA; 2016. Available from: https://escholarship.org/uc/item/39p0h9jp

[17] He S, Jalali B. Medical image super-resolution using phase stretch anchored

regression (Conference presentation). In: Optical Data Science II, Vol. 10937. International Society for Optics and Photonics; 2019. p. 109370E

[18] Ilovitsh T, Jalali B, Asghari MH, Zalevsky Z. Phase stretch transform for super-resolution localization microscopy. Biomedical Optics Express. 2016;**7**(10):4198-4209

[19] Ang RB, Nisar H, Khan MB, Tsai CY. Image segmentation of activated sludge phase contrast images using phase stretch transform. Microscopy. 2018;**68**(2):144-158

[20] Mahjoubfar A, Churkin DV, Barland S, Broderick N, Turitsyn SK, Jalali B. Time stretch and its applications. Nature Photonics. 2017; **11**(6):341

[21] Solli DR, Ropers C, Koonath P, Jalali B. Optical rogue waves. Nature. 2007;**450**(7172):1054

[22] Herink G, Kurtz F, Jalali B, Solli DR, Ropers C. Real-time spectral interferometry probes the internal dynamics of femtosecond soliton molecules. Science. 2017;**356**(6333): 50-54

[23] Herink G, Jalali B, Ropers C, Solli DR. Resolving the build-up of femtosecond mode-locking with single-shot spectroscopy at 90 MHz frame rate. Nature Photonics. 2016;**10**(5):321

[24] Chen CL, Mahjoubfar A, Tai LC, Blaby IK, Huang A, Niazi KR, et al. Deep learning in label-free cell classification. Scientific Reports. 2016;**6**:21471

[25] Mahjoubfar A, Chen CL, Jalali B. Artificial Intelligence in Label-Free Microscopy. Springer; 2017. Available from: https://scholar.google.com/scholar?hl=en&as_sdt=2005&cites=2319859981831178467&scipsc=&q=Artificial+Intelligence+in+Label-free+Microscopy&btnG=#d=gs_cit&u=%2Fscholar%3Fq%3Dinfo%3A4wixwVzMMSAJ%3Ascholar.google.com%2F%26output%3Dcite%26scirp%3D0%26hl%3Den

[26] Yasuma F, Mitsunaga T, Iso D, Nayar SK. Generalized assorted pixel camera: Postcapture control of resolution, dynamic range, and spectrum. IEEE Transactions on Image Processing. 2010;**19**(9):2241-2253

[27] Gustafsson MG. Nonlinear structured-illumination microscopy: Wide-field fluorescence imaging with theoretically unlimited resolution. Proceedings of the National Academy of Sciences. 2005;**102**(37):13081-13086

[28] Gustafsson MG, Shao L, Carlton PM, Wang CR, Golubovskaya IN, Cande WZ, et al. Three-dimensional resolution doubling in wide-field fluorescence microscopy by structured illumination. Biophysical Journal. 2008;**94**(12):4957-4970

[29] Hell S, Stelzer EH. Fundamental improvement of resolution with a 4Pi-confocal fluorescence microscope using two-photon excitation. Optics Communications. 1992;**93**(5–6):277-282

[30] Hess ST, Girirajan TP, Mason MD. Ultra-high resolution imaging by fluorescence photoactivation localization microscopy. Biophysical Journal. 2006;**91**(11):4258-4272

[31] Bates M, Huang B, Zhuang X. Super-resolution microscopy by nanoscale localization of photo-switchable fluorescent probes. Current Opinion in Chemical Biology. 2008; **12**(5):505-514

[32] Temizel A, Vlachos T. Wavelet domain image resolution enhancement using cycle-spinning. Electronics Letters. 2005;**41**(3):119-121

[33] Piao Y, Park H. Image resolution enhancement using inter-subband

correlation in wavelet domain. In: 2007 IEEE International Conference on Image Processing, Vol. 1. IEEE; 2007. p. I-445

[34] Granados M, Aydn TO, Tena JR, Lalonde JF, Theobalt C. HDR image noise estimation for denoising tone mapped images. In: Proceedings of the 12th European Conference on Visual Media Production. ACM; 2015. p. 7

[35] Perry S. Image and video noise: An industry perspective. In: Denoising of Photographic Images and Video. Cham: Springer; 2018. pp. 207-234

[36] Milanfar P. A tour of modern image filtering: New insights and methods, both practical and theoretical. IEEE Signal Processing Magazine. 2012;**30**(1): 106-128

Section 3

Image Compression

Chapter 10

Many-Core Algorithm of the Embedded Zerotree Wavelet Encoder

Jesús Antonio Alvarez-Cedillo, Teodoro Alvarez-Sanchez, Mario Aguilar-Fernandez and Jacobo Sandoval-Gutierrez

Abstract

In the literature, the image compression was implemented using a variety of algorithms; such as vector quantization and subband coding and transform-based schemes. The current problem is that the selection of an image compression algorithm depends on criteria of compression ratio, but the quality of reconstructed images depends on the technology used. Some papers about of the wavelet transform-based coding show this field as an emerging option for image compression with high coding efficiency. It is well known that the new wavelet-based image compression scheme JPEG-2000 has been standardized. This chapter shows the developed novel algorithm executed in parallel using the embedded Zerotree wavelet coding scheme, in which the programs integrate parallelism techniques to be implemented and executed in the many-core system Epiphany III.

Keywords: image compression, vector quantization, subband coding, embedded systems, Zerotree wavelet

1. Introduction

Wavelet transform consists in uses a compact multi-resolution representation of an image, allows uses the energy compaction to exploit redundancy and to achieve compression [1].

The discrete wavelet transform (DWT) usually was used in the literature using a two-channel wavelet filter bank in a recursive process [2].

A two-dimensional image of the DWT type is usually calculated using a separable approach, this consists of scanning the input image in a horizontal direction, and passing it through the decomposition filters passes low and passes high [3]. All the selected data are subsampled vertically in order to classify the low frequency and high-frequency data in the horizontal direction. The result produces output data which is scanned vertically; the filters are repeated to generate characteristic frequency subbands [4]. After the subsampling stage, the transformation generates four LL, LH, HL and HH subbands, where each image represents 25% of the original image size [5–8].

In this particular case, the energy was concentrated in the low-frequency LL subband, so it represents a low-resolution version of the original image. The most frequent subbands contain very detailed information in three directions (horizontal, vertical and diagonal).
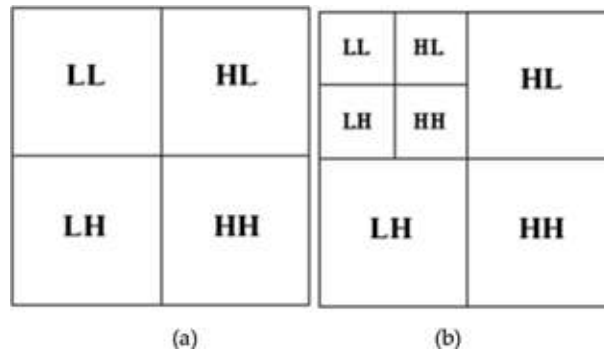
Figure 1.
(a) Wavelet decomposition in subbands and (b) higher and lower level coefficients for an original image.

At the end of the process, the image was decomposed by applying the 2-D DWT algorithm to the LL subband [9]. With this iterative process, multiple levels of transformation will be generated where the energy is fully compacted and represented with few low-frequency coefficients [10]. The above can be seen in **Figure 1(a)** and **(b)**. **Figure 1** shows an example of decomposition of three levels of an image using the wavelet transformation, and both images defined the parent/child relationship between levels.

2. Many-core technology

Epiphany III is a low-cost embedded system formed with the main memory and 16 cores distributed in a mesh, as shown in **Figure 2**. The system is characterized by having low energy consumption and a high level of parallelism, concurrency and high computing power. All these features and in combination, allow data to be processed at different levels of software and hardware, thereby performing operations at each core [11, 12].

A multi-core system needs a shared memory space that consists of 232 bytes for this system. The memory addresses for access are accessed as unsigned numbers, from 0 to 232, together, they represent 230 of 32-bit words in which any core has access concurrently through a 2D mesh type topology [13]. The use of this interconnection topology avoids overloading or blocking access to shared memory that is reported in the literature as a factor that affects the high-performance system [14–17].
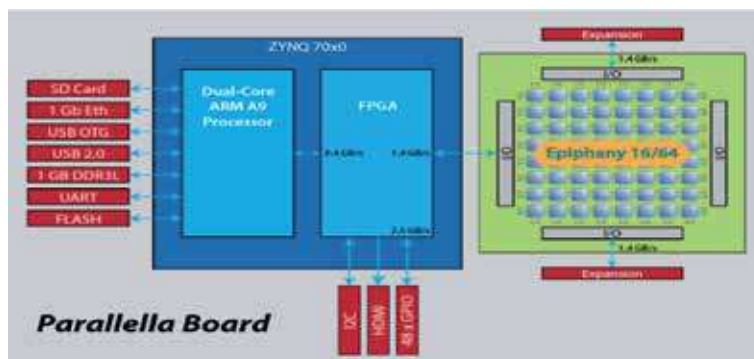

Figure 2.
Components of the Epiphany III architecture [11].

This system has an energy consumption of 1 W per 50 Gigaflops in simple precision calculations; these cores measure 65 nm. This technology is RISC and can be run at a speed of 1 GHz, and the 16 cores have the same architecture [11, 14].

With this memory capacity in the Epiphany III system, it is possible to process an image of (128 × 128 pixels) that is equivalent to 16 kB of memory.

3. Embedded Zerotree coding

A wavelet represents a waveform of limited duration that has an average value close to zero. A wavelet transform modifies a signal from the time domain to the whole time scale domain. Wavelet coefficients are two-dimensional, given this, an image can be represented using trees due to the subsampling that is performed in the transformation.

Fourier analysis allows dividing a signal into sine waves of various frequencies, due to this the wavelet analysis is the breaking of a signal in displaced and scaled versions of the original or mother wavelet.

In zerotree coding, each wavelet coefficient of an arbitrary scale can be related to a set of coefficients in the next more excellent scale.

Zerotree root (ZTR) represents a low-scale zero value coefficient for which all larger scale coefficients have that same value. By specifying a ZTR, the encoder can track and reset all related coefficients on a larger scale.

The EZW encoder is a particular type of encoder used to encode image or sound signals of any dimension; it offers the advantages found in denoising algorithms.

When using the wavelet transform on an input image, the embedded zerotree encoding (EZW) will allow the encoder to quantify the coefficients using a binary encoding to create a representation of the image [18]. EZW uses the direct relationship between the upper and lower level coefficients (parents and children) to obtain maximum coding efficiency [19, 20].

In order to perform the EZW encoding, it is necessary to perform the following steps:

STEP 1: Determine the initial threshold using bit plane coding, where the subsequent iterations, the threshold (Ti) is reduced by half, and the coefficients <2Ti are only encoded in each flow.

EZW involves two passes, as a recursive process:

- Dominant pass.

- Subordinate pass.

STEP 2: Two individual lists are defined:

a. Dominant pass: Contains the coordinates of those non-significant coefficients.

b. Subordinate pass: Contains the magnitudes of the significant coefficients for each threshold, involves the use of two passes:

1. Key stage.

2. Low pass.

In the dominant step, the magnitude of the wavelet coefficients is compared to an arbitrary threshold value; the essential data is determined, and the coefficients

are defined with an absolute value. The scanning was done with spatial frequencies; two bits are used to define the sign and the position of the significant coefficients. The positive significant coefficient and the non-significant coefficients are above an arbitrary threshold, usually starting with the two highest powers, two below the maximum wavelet value, where the wavelet coefficient is insignificant and has a significant descendant.

STEP 3: Dominant pass (significant pass):

Let wavelet coefficients in the dominant list are compared with Ti to determine the importance and, if significant, its sign. The resulting significance map is coded and sent by a zero tree. The inclusion of the ZTR symbol increases the coding efficiency because the encoder maximizes the correlation between image scales.

STEP 4: Four symbols are used to form a code:

1. Zerotree root.

2. Zero isolated.

3. Significant positive.

4. Significant negative

The EZW technique can be significantly improved using entropy coding as a preoccupation to achieve better compression [22].

STEP 5: Define the entropy code.

The low pass filter follows, where significant coefficients are detected and refined under the successive approach quantification (SAQ) approach [21].

STEP 6: Define refinement pass.

STEP 7: The entropy code sequence of 1 and 0 is defined, and adaptive AC is used, and send STOP.

4. Proposed algorithm

The development of proposed EZW (embedded zerotree wavelet) image coding has attracted considerable attention among researchers [23–25]. It is the most popular wavelet-based compression algorithm and is widely used in several image-based applications. In this paper is used the recursive transformation method for multi-level decomposition, where the result data is then preprocessed before of the zerotree compression, the block diagram of a wavelet-based image coding algorithm is shown in **Figure 3**.

Our objective of this paper is to show our proposed algorithm to enhance the compression of an image eviting to minimal loss during reconstruction.

Our algorithm was applied as a preprocessing stage; this allows to eliminate unused data in the transformed image that is not important and significant in the reconstruction of the image.

However, it is necessary to mention that more bits are required during compression and the processing time increases so that a parallel proposal can help.

When compensation is used to a greater extent between the compression ratio and reconstruction in image quality, it is possible to eliminate irrelevant data in the image where higher compression is achieved with a slight reduction in quality [21].

In an image transformed by wavelet, the coefficients represent a low-resolution image in the LL subband. The high-frequency subbands contain subbands of specific data in each direction.
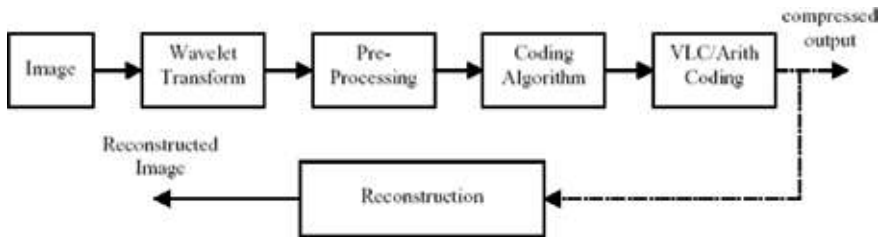
Figure 3.
Block diagram of a wavelet-based image coding algorithm.

The use of the three subbands contributes to a smaller scale within the image reconstruction process because the coefficients are mostly zero, and few large values correspond to border information and textures in the image [22].

In this article, an algorithm was proposed to reduce less essential data in order to achieve higher compression, and thus preserve high-value coefficients, thereby eliminating the lowest values of the minimum value subband.

Our proposed algorithm uses the weight calculation method to have the minimum value subband for each level. The weight of each subband is calculated by adding the absolute value in all subband coefficients. Only three subbands (LHi, HLi and HHi) with a minimum weight are seen in detail.

Eq. (1) shows it.

$$Ws = \sum abs(coefficients\ in\ subbands)\big(\ \min(subbandi)$$
$$= Subband\ with\ minimum\ weight, at\ the\ level\ I \qquad (1)$$

After finding the required subbands in each level, the algorithm reduces the depreciable data in these subbands depending on the importance of the data for preserver the reconstruction. In this age, the majority of the values are close to zero, and the coefficients have the smallest data in each subband, where it is used as a threshold to eliminate low-valued data in that subband.

The coefficients whose value is higher than a set threshold value are retained, and the value is near to zero are deleted. In our experiments, it was used different two threshold values to show the effect of compressed output and reconstructed image.

In the zerotree coding, the reduction of low valued significant coefficients in minimum weight subbands, result in higher compression ratio with a slight loss in decoded PSNR. Our results show that this algorithm shows better efficiency with a cost of negligible loss in picture quality.

5. Parallel implementation

In the Epiphany, III System is used a memory model and also a programming model, in a flow system that includes single instruction multiple data (SIMD), single program multiple data (SPMD), master–slave programming, multiple instruction multiple data (MIMD).

Can also be programmed, to data flow, static, dynamic, systolic array, multi-threads, message passing and sequential communication processes (SCP) [26].

First, the operating system performs a review of the hardware of the Epiphany system and then begins to configure the cores that are in the mesh-type topology and then the distributed information of the matrices A, B. This is due to the structural nature of the epiphany system, and finally the distribution of tasks in small blocks that is appropriate (**Figure 4**).
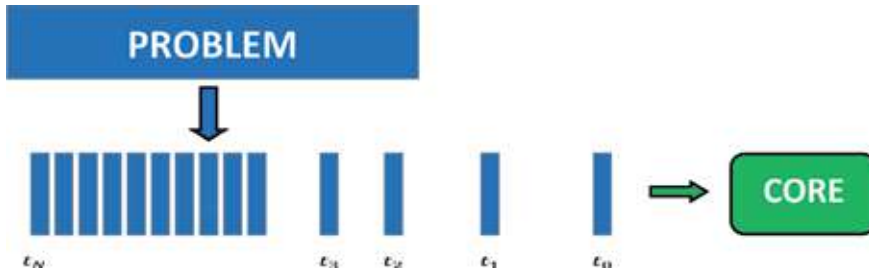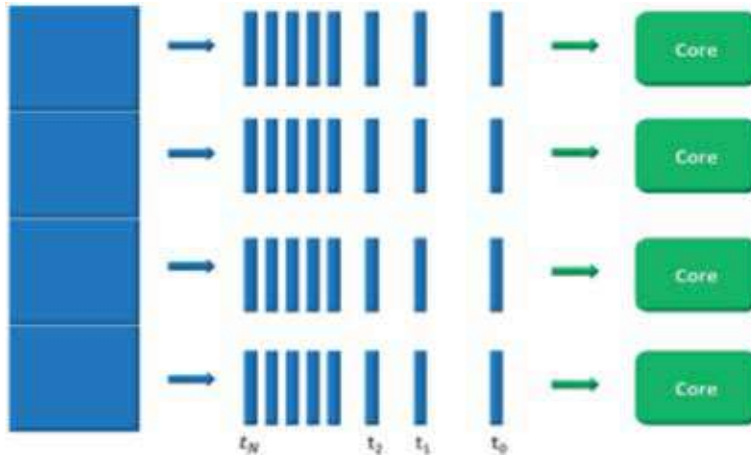
Figure 4.
Sequential execution.

Figure 5.
Execution SPMD.

For this distribution, the programming model single program multiple data (SPMD) is used [27], which is responsible for distributing the execution for each of the cores, as shown in **Figure 5**.

6. Distributions of data and tasks

Depending on the problem. It can choose between two approaches to decompositions: data decomposition or task decomposition.

Establish strategies to choose decompositions: decomposition of instructions or decomposition of tasks.

Decomposition of instructions: this refers to the distribution of instructions for the cores, which will handle the processing. Then, it describes the process of distributing the instructions that can execute in parallel on different cores.

In which the results of each one of the executions of each nucleus, of this type of executions in parallel accelerates n times faster if a single nucleus were executed. Except for the minimum delay involved in the initial distribution of workload or instructions, and the final collection of data results, resulting in linear acceleration with the number of cores.

Decomposition of tasks: this refers to the distribution of tasks for each of the cores, which will be responsible for processing tasks. That is to say that the whole program is devoted to tasks. A task is a sequence of the program that can be executed in parallel, concurrent with other tasks. This approach is beneficial when tasks maintain high levels of independence.

If each task and algorithm are different, then both can be implemented, the functional decomposition, in which the particular characteristics of each type of task or algorithms will be used to execute them in the nucleus for that purpose.

Recalling that the new technologies of embedded systems have integrated circuits with several cores, in which the cores perform threads that are the tasks that are executed in parallel, so the applications will be made in less time. This allows increasing the parallelism and the concurrence in hardware and software. It is also important to make the distribution between cores, the tasks, as well as the synchronization between the cores.

Matrices are mathematical operations that scientists use. In which, the algorithm used for matrix multiplications that run in parallel is described by IBM [28]. The importance of data communication between neighboring cores according to the Cannon algorithm [29] is also mentioned. The memory in each core represents a challenge in the implementation because it is limited, which makes it necessary to use the available memory space for communication between the cores. These are some important factors for the system dedicated to parallel processing.

Figure 6 shows the multiplications of matrices for each core. It also shows the sending of data for the execution of the tasks, between each core, so the Epiphany III system incorporates the mechanism, message passing, to synchronize the sending of the threads avoiding conflicts between the cores or accesses to the shared global memory.

Figure 6 shows the data flow for matrix multiplication that runs in specific numbers of steps, this is determined by the quadratic root of $\sqrt{P}$. Then P is the number of cores, in which the matrix multiplication is the data set of size $\sqrt{P} \times \sqrt{P}$.

At each repetition, element C of the product matrix obtained, then matrix A moves down and matrix B moves to the right. This example can be programmed using the standard high-level ANSI programming language "C." The Epiphany III system provides specific functions to simplify the programming of many cores, thanks to the open operating system, but its use is not mandatory for programmers.

The implementation of the algorithm, in the Epiphany III system with 16 cores, operating at 1 GHz, which solves matrix multiplication of 128 × 128 in 2 ms. The performance of the Epiphany III system grows linearly, using appropriate programming and data distribution models, and this is seen in the cost/performance of an optimized system [11, 30–33].

To exploit the parallelism, in the hardware platform epiphany, it is encouraged that the application is broken down into tasks (code portions). Thus, each of the cores could run a program part in parallel to other cores.
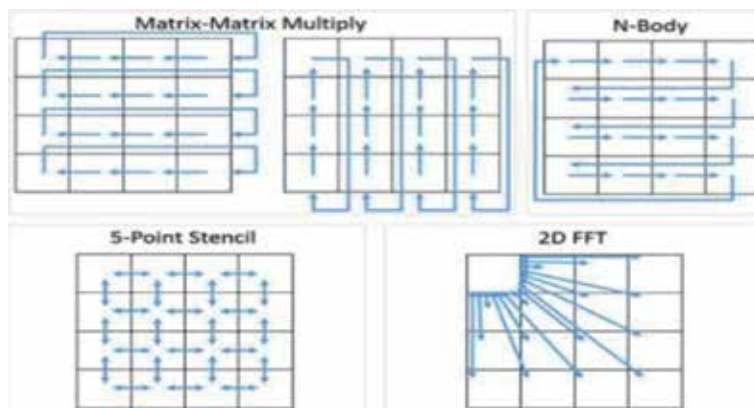

Figure 6.
Data flow in matrix multiplication.

The decomposition of tasks must be followed by a synchronization of the different parties involved to ensure data consistency.

In **Figure 6**, it represents the matrix mathematically. It also shows the simplification of matrix multiplication. This multiplication is represented by (2).

$$C_{ij} = \sum_{k=0}^{N-1} \left(A_{ij} \, B_{kj} \right) \qquad (2)$$

The input matrices are A and B, C is the resulting matrix of A_i and B_j, in which they have as coordinate (i, j), which is (row, column), these are elements of the matrix. The procedure to program matrix multiplication in a single core is shown below.

```
1  for (i=0;i<M; i++)
2  for (i=0;j<M ;j++)
3      for (i=0;k<K; k++)
4  C[i][j]+=A[i][k]* B[k][j]
5
6
```

The previous code used the standard language C, which compiles and executes in a single core.

If these matrices A, B, will proceed to run on each of the cores in the system and the result of each element of the matrix C. are placed in the local memory of each of the cores.

7. Experiment results

Different image outputs of the wavelet-based compression were shown in **Figure 7**.

Table 1 shows the values when was applied our proposed, **Table 2** shows the obtained values using adaptive arithmetic coding.

Image	Min weight subband			EZW method		Proposed method threshold = 2		Proposed method threshold = 5	
	L3	L2	L1	Bytes	PSNR	Bytes	PSNR	Bytes	PSNR
Lena	HH	HH	HH	63,456	22.98 dB	62,256	25.57 dB	61,465	24.96 dB

Table 1.
Obtained values.

Image	Min weight subband			EZW method		Proposed method threshold = 2		Proposed method threshold = 5	
	L3	L2	L1	Bytes	PSNR	Bytes	PSNR	Bytes	PSNR
Lena	HH	HH	HH	3024	22.98 dB	2952	25.57 dB	2830	24.96 dB

Table 2.
Obtained values using the adaptive arithmetic coding.
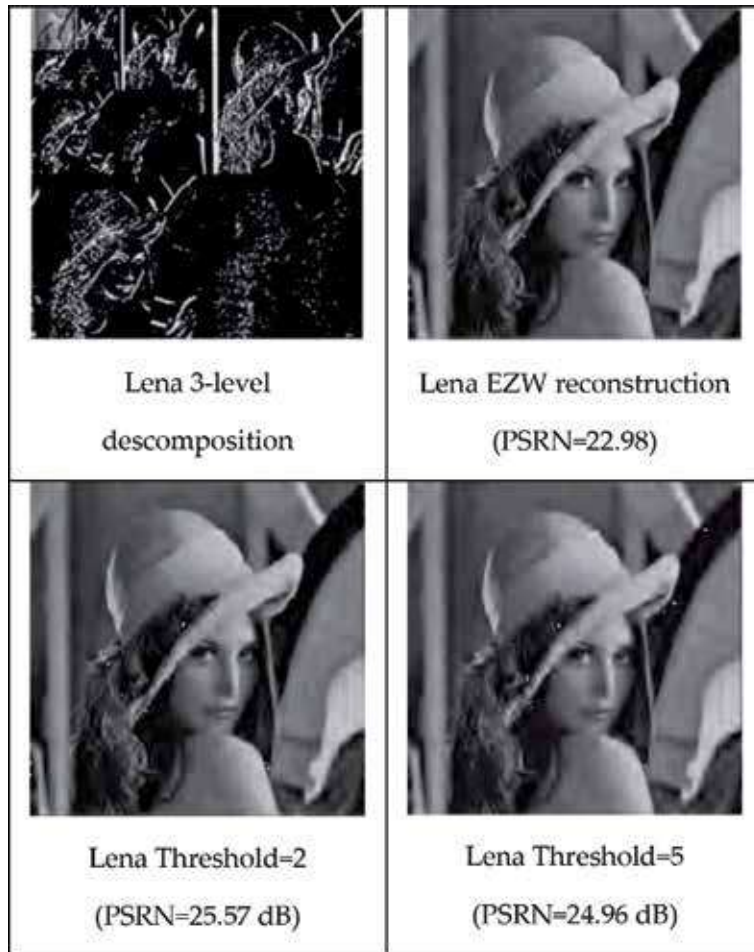
Figure 7.
Output images.

8. Conclusion

The above method exploits the property of tradeoff between compression ratio and output PSNR and reduces the least essential data in order to attain further compression. The better compression ratio is achieved compared to original EZW coder after applying threshold with a slight reduction in PSNR during reconstruction.

Acknowledgements

Author details

Jesús Antonio Alvarez-Cedillo[1*], Teodoro Alvarez-Sanchez[2],
Mario Aguilar-Fernandez[1] and Jacobo Sandoval-Gutierrez[3]

1 Instituto Politécnico Nacional, UPIICSA, Iztacalco, Granjas México, Mexico

2 Instituto Politécnico Nacional, CITEDI, Mesa de Otay, Mexico

3 Universidad Autónoma Metropolitana, Lerma de Villada, Mexico

*Address all correspondence to: jaalvarez@ipn.mx

IntechOpen

References

[1] Yamamoto A. Wavelet analysis: Theory and applications. Transform. 1994. DOI: 10.1051/jp1:1997114

[2] Shensa MJ. The discrete wavelet transform: Wedding the À Trous and Mallat algorithms. IEEE Transactions on Signal Processing. 1992. DOI: 10.1109/78.157290

[3] Tzanetakis G, Essl G, Cook P-R. Audio analysis using the discrete wavelet transform. In: Proceedings of the WSES International Conference Acoustics and Music: Theory and Applications (AMTA 2001). 2001

[4] Filters W, Transforms W. Preview of Wavelets, Wavelet Filters, and Wavelet Transforms. Space & Signals Technologies LLC; 2009

[5] Misiti M, Misiti Y, Oppenheim G, Poggi JM. Wavelets and Their Applications. 2010. DOI: 10.1002/9780470612491

[6] Letelier JC, Weber PP. Spike sorting based on discrete wavelet transform coefficients. Journal of Neuroscience Methods. 2000. DOI: 10.1016/S0165-0270(00)00250-8

[7] Nason GP, Silverman BW. The discrete wavelet transform in S. Journal of Computational and Graphical Statistics. 1994. DOI: 10.1080/10618600.1994.10474637

[8] Goodman RW. Discrete wavelet transforms. In: Discrete Fourier and Wavelet Transforms. 2016. DOI: 10.1142/9789814725781_0003

[9] Tzanetakis G, Essl G, Cook P-R. Audio analysis using the discrete wavelet transform. In: Proceedings of the WSES International Conference Acoustics and Music: Theory and Applications (AMTA 2001). 2001

[10] Mitra SK. Digital signal processing—Computer-based approach. Microelectronics Journal. 2001. Sanjit K. Mitra.pdf. DOI: 10.1016/S0026-2692(98)00072-X

[11] Alvarez-Sanchez T, Alvarez-Cedillo JA, Sandoval-Gutierrez J. Many-core parallel algorithm to correct the gaussian noise of an image. In: Communications in Computer and Information Science. Vol. 948. 2019. DOI: 10.1007/978-3-030-10448-1_7

[12] Vajda A. Programming Many-Core Chips. 2011. DOI: 10.1007/978-1-4419-9739-5

[13] Boyd-Wickizer S, Clements A, Mao Y, Pesterev A, Kaashoek M, Morris R, et al. An Analysis of Linux Scalability to Many Cores. MIT Web Domain; 2010

[14] Hibbs AE, Thompson KG, French D, Wrigley A, Spears I. Optimizing performance by improving core stability and core strength. Sports Medicine. 2008. DOI: 10.2165/00007256-200838120-00004

[15] Manferdelli JL, Govindaraju NK, Crall C. Challenges and opportunities in many-core computing. Proceedings of the IEEE. 2008. DOI: 10.1109/JPROC.2008.917730

[16] Bates D. Introduction to the Matrix Package. R Core Development Group; 2012. DOI: 10.1016/j.amjmed.2014.09.011

[17] Guz Z, Bolotin E, Keidar I, Kolodny A, Mendelson A, Weiser UC. Many-core vs. many-thread machines: Stay away from the valley. IEEE Computer Architecture Letters. 2009. DOI: 10.1109/L-CA.2009.4

[18] Shapiro JM. Embedded image coding using Zerotrees of wavelet

coefficients. IEEE Transactions on Signal Processing. 1993. DOI: 10.1109/78.258085

[19] Said A, Pearlman WA. A new, fast, and efficient image codec based on set partitioning in hierarchical trees. IEEE Transactions on Circuits and Systems for Video Technology. 1996. DOI: 10.1109/76.499834

[20] Hong ES, Ladner RE. Group testing for image compression. IEEE Transactions on Image Processing. 2002. DOI: 10.1109/TIP.2002.801124

[21] Amit Y, Geman D. Shape quantization and recognition with randomized trees. Neural Computation. 1997. DOI: 10.1162/neco.1997.9.7.1545

[22] Blanco-Velasco M, Cruz-Roldán F, Moreno-Martínez E, Godino-Llorente JI, Barner KE. Embedded filter bank-based algorithm for ECG compression. Signal Processing. 2008. DOI: 10.1016/j.sigpro.2007.12.006

[23] George R, Manimekalai MAP. A novel approach for image compression using zero tree coding. In: 2014 International Conference on Electronics and Communication Systems, ICECS 2014. 2014. DOI: 10.1109/ECS.2014.6892611

[24] Zhou J, Huang PS, Chiang F-P. Wavelet-based pavement distress image compression and noise reduction. Wavelets XI. 2005. DOI: 10.1117/12.612926

[25] Shen K, Delp EJ. Wavelet based rate scalable video compression. IEEE Transactions on Circuits and Systems for Video Technology. 1999. DOI: 10.1109/76.744279

[26] Duncan R. A survey of parallel computer architectures. Computer. 1990. DOI: 10.1109/2.44900

[27] Omiecinski E. Highly parallel computing. Information and Software Technology. 2003. DOI: 10.1016/0950-5849(90)90035-p

[28] Lord N, Golub GH, Van Loan CF. Matrix computations. The Mathematical Gazette. 2007. DOI: 10.2307/3621013

[29] Williams S, Oliker L, Vuduc R, Shalf J, Yelick K, Demmel J. Optimization of sparse matrix-vector multiplication on emerging multicore platforms. Parallel Computing. 2009. DOI: 10.1016/j.parco.2008.12.006

[30] Haibo SB, Rong C, Yandong C, Kaashoek F, Morris R, Pesterev A, et al. Corey: An Operating System for Many Cores. OSDI '08; 2008

[31] Guz Z, Bolotin E, Keidar I, Kolodny A, Mendelson A, Weiser UC. Many-core vs. many-thread machines: Stay away from the valley. IEEE Computer Architecture Letters. 2009. DOI: 10.1109/L-CA.2009.4

[32] Diaz J, Muñoz-Caro C, Niño A. A survey of parallel programming models and tools in the multi and many-core era. IEEE Transactions on Parallel and Distributed Systems. 2012. DOI: 10.1109/TPDS.2011.308

[33] Hill MD, Marty MR. Amdahl's law in the multicore era. Computer. 2008. DOI: 10.1109/MC.2008.209

On the Application of Dictionary Learning to Image Compression

Ali Akbari and Maria Trocan

Abstract

Signal models are a cornerstone of contemporary signal and image-processing methodology. In this chapter, a particular signal modelling method, called synthesis sparse representation, is studied which has been proven to be effective for many signals, such as natural images, and successfully used in a wide range of applications. In this kind of signal modelling, the signal is represented with respect to dictionary. The dictionary choice plays an important role on the success of the entire model. One main discipline of dictionary designing is based on a machine learning methodology which provides a simple and expressive structure for designing adaptable and efficient dictionaries. This chapter focuses on direct application of the sparse representation, i.e. image compression. Two image codec based on adaptive sparse representation over a trained dictionary are introduced. Experimental results show that the presented methods outperform the existing image coding standards, such as JPEG and JPEG2000.

Keywords: image compression, dictionary learning, sparse representation

1. Introduction

Signal models are fundamental tools for efficiently processing of the signals of interesting, including audio recordings, natural images, video clips, and medical scans, to name just a few. A signal model formulates a mathematical description of the family of signals of interesting in a way which faithfully captures their behaviour. Designing accurate signal models, which efficiently capture useful characteristics of the signals, has been a crucial aim in the signal processing area for so many years and a variety of mathematical forms has been proposed. Sparsity-based modelling has been used in many applications in which each signal is represented in terms of linear combinations of an underlying set, called *dictionary*, of elementary signals known as atoms, resulting in simple and compact models. The driving force behind this model is *sparsity*, i.e. the rapid decay of the representation coefficients over the dictionary. In this signal modelling, the dictionary plays an important role for the success of entire model in an efficient representation of the signal.

Finding appropriate dictionaries with good predictive power of various signal classes of interest and high compactness ability, especially natural images, has been an active field of research during past decades. The early attempts for designing dictionaries were based on building the model using harmonic analysis of the signal classes and extracting some mathematical functions, resulting in a fixed off-the-shelf dictionary called *analytic* or mathematical dictionary. The sparse

representation using these fixed mathematical dictionaries is called *analysis* sparse modelling. The long series of works on designing the analytic dictionaries lead to appearing various transforms such as Fourier and its discrete version, discrete cosine, wavelets, curvelets, contourlets, bandlets, and steerable wavelets.

A significantly different approach to the sparse modelling, originally introduced by Olshausen and Field [1], consists of learning a dictionary from some training data. The sparse representation using this trained dictionary is called, *synthesis* sparse modelling. The trained dictionaries, also called *synthetic* dictionary, could efficiently capture the underlying structures in the natural image patches and are well adapted to a large class of natural signals.

The analysis and synthesis sparse signal modelling has led to the design effective algorithms for many image-processing applications, such as compression [2–8] and solving inverse problems [9–22]. A straightforward application of the sparse signal modelling in the field of image processing has been image compression due to providing a compact representation of the signal. This chapter presents the theoretical and practical aspects of using the dictionary-based sparse signal modelling for image compression. We address one important question: How to efficiently represent an image over a trained dictionary in order to improve the performance of the image compression? Based on this concept, we present two novel image compression methods. Experimental results show that the introduced methods outperform the existing image coding standards, such as JPEG and JPEG2000.

The remainder of chapter is organized as follows: It starts with introducing the concept of sparsity in signal processing. The use of sparse representation modelling with respect to trained dictionaries is presented. Next, a brief description of a well-known and yet effective dictionary learning algorithm, introduced by Aharon et al. [23], is given. The end of chapter is devoted to introducing two generic image compression schemes. Finally, we conclude the chapter.

2. Sparsity-based signal models

One of the well-known methods in designing of the signal models is linear approximation. In this modelling technique, given a set of vectors $\left[\mathbf{d}_k \in \mathbb{R}^N\right]_{k=0}^{K-1}$, a signal $\mathbf{x} \in \mathbb{R}^N$ is represented as a linear combination of K basis,

$$\mathbf{x} \simeq \sum_{k=0}^{K-1} c_k \mathbf{d}_k, \tag{1}$$

where set $[c_k]_{k=0}^{K-1}$ consists of representation coefficients. The signal approximation Eq. (1) can be reformulated in a matrix form as

$$\mathbf{x} \simeq \mathbf{D}\mathbf{c}, \tag{2}$$

where $\mathbf{c} = [c_1, c_2, \cdots c_k]^T \in \mathbb{R}^K$ is the coefficients vector. The matrix $\mathbf{D} = [\mathbf{d}_1 \mathbf{d}_2 \cdots \mathbf{d}_K] \in \mathbb{R}^{N \times K}$ is called dictionary and its columns constitute the dictionary atoms.

With the right choice of dictionary, the coefficients vector $\mathbf{c}$ is expected to be sparse, in the sense that its sorted coefficients decay rapidly. Motivated by this idea, the design of efficient complete dictionaries, in which, i.e., $K = N$ was an active area of research during the last decades of twentieth century. The well-known Fourier transform [24], used in the JPEG compression standard [25], and wavelet transform [2], used in JPEG2000 compression standard [26], are the results of these

works which sparsify uniformly the smooth signals. However, this signal modelling loses its optimality in representation of the image signals due to existence of curve singularities (elongated edges) in these types of signals [27]. As an instance, the images encoded by the JPEG2000 standard suffer from the ringing (smoothing) artefacts near edges.

In an attempt to minimize this weakness of the dictionaries, the design of more general over-complete dictionaries, which have more atoms than the dimension of signal, i.e. $K>N$, has been investigated over the past decades, and is still intensely ongoing. These dictionaries have a more descriptive ability to represent a wide range of interesting signals, in comparison with the invertible complete dictionaries.

2.1 Sparse modelling using over-complete dictionaries

Compared to the complete case, representation with over-complete dictionaries must be more carefully defined. There are two distinct paths for representing a signal using the over-complete dictionaries: analysis path and synthesis path. The *analysis* sparse modelling relies on the classical basics of the signal modelling in which the representation of the signal is identified as a linear combination of atoms,

$$\mathbf{x} \simeq \mathbf{D}\mathbf{c}_a, \qquad (3)$$

where the coefficients vector $\mathbf{c}_a$ is obtained via the inner products of the signal and the dictionary $\mathbf{c}_a = \mathbf{\Omega}\mathbf{x} = \mathbf{D}^T\mathbf{x}$. This method has the advantage of providing a simple and efficient way to achieve sparse representation over the dictionary. In this case, every signal has an unique representation as a linear combination of the dictionary atoms.

Increasing sparsity, in order to obtain a well-defined representation, requires departure from this linear representation towards a more flexible and non-linear representation. Each signal is represented using a different set of atoms from a pool, called dictionary, in order to achieve the best sparsity. Thus, the approximation process becomes

$$\mathbf{x} \simeq \mathbf{D}\mathbf{c}_s, \qquad (4)$$

where the coefficients vector $\mathbf{c}_s$ is obtained via a non-linear approach, in contrast to the linear-based approach in the analysis path. This signal modelling approach, called *synthesis* sparse representation, needs further refinement to find the well-defined representation due to degrees of freedom identified by the null-space of $\mathbf{D}$ [27], which leads to a non-unique choice of $\mathbf{c}_s$ in Eq. (4), as opposed to the analysis sparse modelling which has a unique solution. In order to find the most informative representation, the coefficients vector $\mathbf{c}_s$ is obtained with respect to some cost function $\mathbf{F}(\cdot)$, which minimizes the sparsity of the coefficients vector $\mathbf{c}_s$ under a reconstruction constraint:

$$\mathbf{c}_s = \arg\min_{\mathbf{c}\in\mathbb{R}^K} \mathbf{F}(\mathbf{c}) \ subject\ to\ \ \|\mathbf{x} - \mathbf{D}\mathbf{c}\|_2^2 \le \epsilon, \qquad (5)$$

where ϵ is the prior knowledge about the noise level. The penalty function $\mathbf{F}(\cdot)$ is defined in a way that is tolerant to the large coefficients and aggressively penalizes the small coefficients [27]. The normal choice for this function is ℓ_p norm with $0 \le p \le 1$. Of specific interest is the ℓ_0 case, i.e., $\mathbf{F}(\mathbf{c}) = \|\mathbf{c}\|_0$, which counts the number of non-zeros in the representation. For this case, the problem Eq. (5) becomes

$$\mathbf{c}_s = \arg\min_{\mathbf{c} \in \mathbb{R}^K} \|\mathbf{c}\|_0 \quad \textit{subject to} \quad \|\mathbf{x} - \mathbf{Dc}\|_2^2 \leq \epsilon. \tag{6}$$

This problem, known to be NP-hard in general, can be efficiently approximated based on the idea of iterative greedy pursuit. The earliest and yet effective one includes the orthogonal matching pursuit (OMP) [28].

This formulation Eq. (6) has gained a large success beyond the statistics and signal processing communities and has been extensively employed in different signal processing algorithms. In the image-processing applications, since the size of natural images is too large, it is chosen to partition the image into blocks and the sparse modelling is done on the set of image blocks $\mathbf{X} = [\mathbf{x}_1 \ \mathbf{x}_2 \cdots x_L]$, each of size $\sqrt{N} \times \sqrt{N}$ pixels, where $\sqrt{N}$ is an integer value and $\mathbf{x}_i \in \mathbb{R}^N$ is lexicographically stacked representation of the i-th image patches.

2.2 Dictionary choice

In the discussion so far, it is assumed that the dictionaries of the analysis and synthesis models are known. Choosing the dictionary carefully is an important and involving task, in which substantial research has been invested. Based on analysis and synthesis models, the scientific community has developed two main routes for designing the dictionaries [27].

The first one is *analytic* dictionaries derived from a set of mathematical assumptions made on the family of the signals. The dictionaries of this type are generated by finding the appropriate mathematical functions through harmonic analysis of the interesting signals for which an efficient representation is obtained. For instance, Fourier basis is designed for optimal representation of smooth signals, while the wavelet dictionary is more suitable for piecewise-smooth signals with point singularities.

Designing analytic over-complete dictionaries are formulated as $\mathbf{DD}^T\mathbf{x} = \mathbf{x}$ for all $\mathbf{x}$. Then, the approach tries to establish an appropriate dictionary by analysing the behaviour of $\mathbf{D}^T\mathbf{x}$ and establishing a decay rate. The curvelet [29], contourlet [30], and bandlet [31] transforms are some of the analytic dictionaries which provide comprehensive frameworks in order to handle the multi-dimensional signals.

Finding the more compact sparse representation has been a major driving force for the continued development of more efficient dictionaries. The synthesis formulation of the sparse representation paved the way to the design of an efficient dictionary, called *synthetic* dictionaries, from signal realizations via machine-learning techniques. The basic assumption behind this approach is that the structure of the complex natural signals can be more accurately extracted directly from the data than by using a general mathematical model [27]. In fact, this approach replaces prior assumptions on the signal behaviour with a training process which constructs the dictionary based on the observed signal properties. Compared to the analytic dictionaries, the synthetic dictionaries deliver an increased flexibility and the ability to adapt to specific signals and are superior in terms of representation efficiency at the cost of a non-structured and substantially more complex dictionary.

In this approach, a dictionary is trained for the sparse representation of small patches collected from a number of training signals. The desire to efficiently train a dictionary for the sparse representation led to developing some algorithms so far [1, 23, 32–34]. The earlier works on the dictionary learning mostly focused on statistical methods. Given the training image patches $\mathbf{X} = [\mathbf{x}_1 \ \mathbf{x}_2 \cdots \mathbf{x}_L]$, where L is

the number of training patches, this method finds a dictionary which either maximizes the likelihood of the training data $P(\mathbf{X}|\mathbf{D})$ [35] or the posterior probability of the dictionary $P(\mathbf{D}|\mathbf{X})$ [36]. These formulations lead to some optimization problems that are solved in an expectation-maximization fashion, alternating estimation of the sparse representation and the dictionary using gradient descent or similar methods.

In neuroscience area, Olshausen and Field [1] proposed a significantly different approach for designing the dictionary using the training data, benefiting from modelling the receptive fields of simple cells in the mammalian primary visual cortex. In another attempt, the K-SVD algorithm introduced by Aharon et al. [23] is one of the well-known methods of dictionary learning. Given a set of examples $\mathbf{X} = [\mathbf{x}_1 \ \mathbf{x}_2 \cdots \mathbf{x}_L]$, the goal of the K-SVD algorithm is to search the best possible dictionary $\mathbf{D} \in \mathbb{R}^{N \times K}$ for the sparse representation of the training set $\mathbf{X}$ through the optimization problem of Eq. (7):

$$\arg \min_{\mathbf{C}, \mathbf{D}} \sum_{i=1}^{L} \|\mathbf{c}_i\|_0 \quad subject\ to \quad \|\mathbf{X} - \mathbf{DC}\|_2^2 \leq \epsilon, \tag{7}$$

where ϵ is a fixed small value and $\mathbf{C} = [\mathbf{c}_1 \ \mathbf{c}_2 \cdots \mathbf{c}_L]$ is a matrix of size $K \times L$, consisting of the representation coefficients vectors $[\mathbf{c}_i]_{i=1}^{L}$ of the training samples. The expression in Eq. (7) is performed iteratively. First, by considering an initial dictionary, the algorithm tries to find the best coefficients matrix $\mathbf{C}$ that can be found. Once $\mathbf{D}$ is known, the penalty, posed in Eq. (6), reduces to a set of L sparse representation operations, like the ones seen in (Section 2.1). The OMP algorithm [28] is used for the near-optimal calculation of the coefficients matrix $\mathbf{C}$.

At the next stage, the columns of dictionary are sequentially updated and relevant coefficients in the matrix $\mathbf{C}$ are simultaneously changed. At a time, one column is updated and the process of updating one column is based on the singular value decomposition (SVD) on the residual data matrices, computed only on the training samples that use this atom. The K-SVD algorithm includes a mechanism to control and rescale the ℓ_2-norm of the dictionary elements. Indeed, without such a mechanism, the norm of $\mathbf{D}$ would arbitrarily go to infinity. For more details, refer to [23].

In the image-processing applications, since the size of natural images is too large for learning a full matrix $\mathbf{D}$, it is chosen to learn the dictionary on a set of natural image patches $\mathbf{X} = [\mathbf{x}_1 \ \mathbf{x}_2 \cdots \mathbf{x}_L]$, each of size $\sqrt{N} \times \sqrt{N}$ pixels, where $\sqrt{N}$ is an integer value and $\mathbf{x}_i \in \mathbb{R}^N$ is lexicographically stacked representations of the i-th image patches.

2.3 Analysis versus synthesis

As mentioned before and also outlined in [27], some of the most important elements of effective dictionary design include localization, multi resolution, and adaptivity. Modern dictionaries typically provide localization in both the analysis and synthesis routes. However, multi-resolution property is usually better supported by the analytic structures, whereas adaptivity is mostly found in the synthetic methods.

The most important advantage of the analytic dictionaries is the easy and fast implementation. On the other hands, the main advantage of the trained dictionaries is their ability to provide a much higher degree of specificity to the particular signal properties, allowing them to produce better results in many practical applications such as image compression, feature extraction, content-based image retrieval and others. However, some drawbacks might arise after the compactness introduced by

synthesis scheme. In this case, only if a few atoms for presenting a signal, the importance of all atoms largely varies. Consequently, any wrong choice of one atom could potentially lead to additional erroneous atoms that are selected as compensation, deviating further from the desired reconstruction. This weakness is usually appeared in the ℓ_0-norm-based non-convex optimization problem of Eq. (6). The convex relaxation approaches from ℓ_0 to ℓ_1 are more stable for the sparse representation at the expense of computational complexity. In the analysis formulation, however, all atoms take an equal part in describing the signal, thus minimizing the dependence on each individual one, and stabilizing the recovery process.

3. Image compression

Reducing the cost for storage or transmission of image signals with negligible degradation in the quality is the main goal of an lossy image compression algorithm. It tries to remove the redundancies among the image data by adopting different ways, such as transferring the image into a transform domain with compressible coefficients. In the transform domain, a few significant coefficients capture a large part of the image information. A typical lossy image compression algorithm usually encodes these significant transform coefficients to reduce the requirements for image storage or transmission. The analysis and synthesis sparse modellings are two powerful tools for transforming the image into a compressible domain. The JPEG [25] and JPEG2000 standards [26] are the results of using the analysis sparse representation of the image by designing analytic dictionaries, e.g. discrete cosine transform (DCT) and discrete wavelet transform (DWT), respectively. Since analytic dictionaries-based image sparse representation is typically over-simplistic, it fails to represent the high-textured images efficiently [27]. Due to this weakness of analysis sparse modelling in the efficient expressiveness, an extensive body of literature has recently focused on various applications of the synthesis sparse signal modelling via a trained dictionary. In this way, the performance can be significantly improved for the image compression application, benefiting the sparse representation of the image over a dictionary specifically adapted to it.

In order to improve the limitations of the traditional sparse representation approaches over a trained dictionary, several studies have been proposed in the literature [37–39]. In [37], the authors train a set of dictionaries. In order to improve the compression performance, the sparse representation is achieved by choosing an optimal dictionary among the trained dictionaries. In [38], a set of dictionaries in a tree structure is trained. At each level of tree, a dictionary is learned via generating the image residual. The residual is obtained by difference between the original and recovered images using the trained dictionary at the previous level of tree. Sparse representation is done by selection of one atom from each dictionary at each tree level. The total number of atoms is determined according to the sparsity level. Authors in [39] introduce the concept of multi-sample sparse representation (MSR) and incorporate it into the dictionary learning process. Each image patch is encoded with a certain sparsity level. To do this purpose, multiple neighbouring image patches are considered during the sparse representation to explore different sparsity levels. Based on this concept, an MSR-based image coding approach is proposed in [39].

Using a trained dictionary, each image is represented over the dictionary. The coefficients vector can be obtained via different algorithms such as the basis pursuit algorithms, matching pursuit techniques and other schemes [40]. These conventional approaches usually consider constant sparsity level, i.e. a fixed number of dictionary atoms is considered for representing all the image patches with different characteristics. This approach leads to a weak image compression performance.

In this section, an adaptive sparse representation approach is presented. It is based on this fact that the visual significance, called visual saliency, of each image patch varies with its location within the image [41]. In other words, the human visual system (HVS) usually focuses on some parts of the image (salient regions), while other parts of the image have a lower level of visual interest. Therefore, designing an adaptive sparse representation scheme by considering the HVS characteristics plays an important role in designing an efficient image compression algorithm.

3.1 Dictionary learning-based image codec

Figure 1 presents the block diagram of the dictionary learning-based image coding (DLC) framework [7]. The DLC mainly has four main parts, pre-processing, dictionary learning, adaptive sparse representation and entropy coding. First, at the pre-processing step, the input image is divided into L non-overlapping image patches $\mathbf{X} = [\mathbf{x}_i]_{i=1}^{L}$. $\mathbf{x}_i \in {}^{N}$ represents a $B \times B$ image patch vectorized into a vector of size N. As other coding algorithms, the mean values of image patches (DC components) $\mathbf{M} = [m_i]_{i=1}^{L}$ and AC components $\mathbf{Y} = [\mathbf{y}_i]_{i=1}^{L}$ are separately encoded. The AC components are represented with respect to a trained dictionary $\mathbf{D}$ of size $N \times K$ learned by the K-SVD dictionary learning algorithm [23]. As other dictionary-based image compression methods, the trained dictionary should be shared between encoder and decoder. The OMP algorithm is used for sparse representation step in an adaptive manner using the visual saliency information. Incorporating this adaptive sparse representation step into the image coding framework aims to further reduce the reconstructed errors. Finally, the DC elements $\mathbf{M} = [m_i]_{i=1}^{L}$ and representation coefficients $\mathbf{C} = [\mathbf{c}_i]_{i=1}^{L}$ are entropy coded, where $\mathbf{c}_i \in {}^{K}$ denotes the coefficients vector of the i-th image patch. In the following sections, the adaptive sparse representation and entropy coding steps are detailed. We ignore the details of decoder. However, it should be noted that the decoder can retrieve the image by a minor application of the above steps.

3.1.1 Adaptive synthesis sparse representation

The sparse representation step has a strong impact on effectively encoding of image patches and thus the rate-distortion performance. Graph-based visual saliency (GBVS) model, proposed in [42], has an capability to extract the saliency map of an image, i.e. locations within an image where have a high visual interest to a human observer. By incorporating this model into the sparse representation step, we build up an image coding scheme which compresses the image more efficiently than the traditional coders. Please refer to [42] for the details of the GVBS model. This saliency map of the image is exploited to determine the visual significance of the image patches in order to allocate different sparsity levels to each patch according to its visual significance to the HVS.
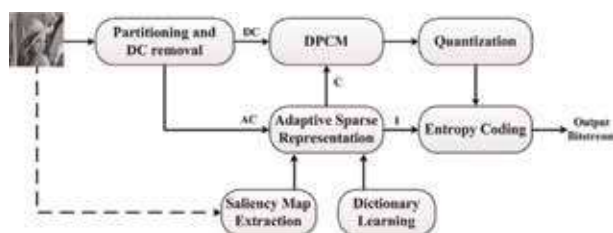

Figure 1.
Block diagram of the dictionary-based image coding (DLC) framework.

It should be noted that we normalize the saliency map values to the range $[0, 1]$. Therefore, the intensity of each pixel of this normalized saliency map stands for the probability belonging that pixel to a salient region. Some examples of saliency maps are shown in **Figure 2**. In the second row, brighter regions represent the salient locations which a human observer pays more attention to, while the darker areas represent the less-saliency regions.

To obtain the saliency value of each image patch, first, the saliency map is partitioned into non-overlapping blocks of size $B \times B$ pixels. Then, the average of the saliency values of pixels belonging to each block is considered as the saliency value of the corresponding patch. Let H_i denotes the saliency value of i-th image patch. Since saliency value of each image patch varies with its position within the image; therefore, by assigning different sparsity level to each block according to its saliency value leads to an improvement in the rate-distortion performance.

Consider the sparsity level of i-th image patch as:

$$S_i = \alpha_i S. \tag{8}$$

Given the target sparsity level S, we aim to allocate a different sparsity level S_i to the i-th image patch. It should be noted that the average of sparsity levels of all image patches must be equal (or slightly inferior) to the target sparsity level S. The factor α_i can be easily obtained via:

$$\alpha_i = \frac{L \times H_i}{\sum_{i=1}^{L} H_i}. \tag{9}$$

where $[H_i]_{i=1}^{L}$ denotes the set of saliency values. As a result, a set of sparsity levels $[S_i]_{i=1}^{L}$ is obtained via Eq. (8). Based on these new obtained sparsity levels, the sparse representation of each patch x_i over the dictionary $\mathbf{D}$ is achieved by:

$$\underset{\mathbf{c}_i}{\mathrm{argmin}} \, \|\mathbf{x}_i - \mathbf{Dc}_i\|_2 \text{ Subject To } \|\mathbf{c}_i\|_0 \leq S_i. \tag{10}$$

The OMP method in [43] is used to solve this problem. By assigning different sparsity level S_i to each block, a more effective sparse representation of the image is obtained.

3.1.2 Quantization step and entropy coding

Differential pulse-coded modulation (DPCM) scheme is used to quantize the DC elements. Let $e_i = m_i - m_{i-1}$ denotes the residual between DC values of two
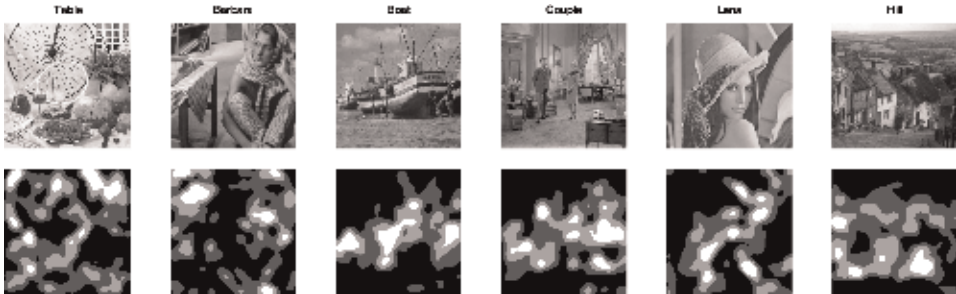

Figure 2.
The original images and their saliency maps.

neighbouring patches i and $i-1$ (here we set m_0 as 0). Instead of encoding $\mathbf{M} = [m_i]_{i=1}^L$ directly, the residuals between subsequent DC elements, i.e. $\mathbf{E} = [e_i]_{i=1}^L$ are quantized and encoded. The quantization is achieved via $round(e_i/b)$ where b is a constant value. A dead-zone quantizer is used for quantization of the residuals [43].

In order to further remove the redundancy, the Huffman coder is used to entropy-code the quantized DC values. During the entropy coding step, pre-defined code-word tables are used built offline. The same procedure is employed for quantizing and encoding the nonzero coefficients of $\mathbf{C} = [\mathbf{c}_i]_{i=1}^L$.

A big part of the bit-stream generated by the above scheme is occupied by encoding the indices of the representation coefficients, $\mathbf{I}$. The reason behind this fact is that the non-zero coefficients in $\mathbf{C} = [\mathbf{c}_i]_{i=1}^L$ have a random structure. To efficiently encode this random pattern, a quad-tree splitting algorithm is employed. First, each vector $\mathbf{c}_i$ is divided into two equal parts. At the next step, a binary evaluation is achieved on each part: if each part consists of one nonzero coefficient, the encoder outputs 1; otherwise, the encoder sends 0. Each part including one nonzero coefficient at least, is then divided into two separate parts and the binary evaluation is again performed. This process continues until the maximum depth of partitioning is reached. In comparison with other methods like fixed length coding [39], this quad-tree splitting algorithm encodes the indices of nonzero coefficients more efficient.

3.2 Down-sampling-based codec

In a basic image compression approach, a down-sampling strategy is employed at the encoder side, as another lossy operation. Then, at the decoder side, an up-scaling algorithm is employed to reconstruct the high resolution (HR) image. In this technique, the high-frequency details within the image are removed by employing the down-sampling operator before the quantization lossy operator. Thus low frequency information within an image, where contain most of the energy image, is encoded by higher bit-rate. This bit allocation scheme leads to the better rate-distortion performance at the low bit-rates. Although the down-sampling operator improves the rate-distortion performance at low bit-rates, it eliminates the high frequency (HF) details. These information should be reproduced in order to recover a high quality image at the higher bit-rates.

In the DLC encoder, presented in previous section, the quantization and sparse representation are the main compression tools. In this section, the down-sampling operator is incorporated into the DLC codec as another lossy operator to further remove redundancies existing within an image. Instead of encoding the whole image, its low-resolution (LR) version is encoded. At the decoder side, an up-scaling algorithm is carefully designed to recover the high-frequency details. As discussed before, this strategy enhances the coding efficiency at the low bit-rates. However, designing an efficient up-scaling algorithm is an important step at the decoder side by which the high frequency information can be correctly recovered. A failure in designing a good up-scaling algorithm leads to a weak rate-distortion performance at the high bit-rates. The presented up-scaling scheme in this section recovers the HR image by encoding and sending the residual image, i.e. difference between the original image and the up-scaled one, as side information. The encoder generates the residual image and encodes it by the sparse representation of the residual image over a trained dictionary. Decoder recovers the final image by combination of the LR decoded image and the reconstructed residual. Both dictionaries used for the sparse representation of LR residual images are trained by a bilevel dictionary learning algorithm. Further, an image analyser is designed and

incorporated into the encoder. The goal of this image analyser is for designing an adaptive sparse representation in order to assign higher bit-rate to the salient parts of the image. Experimental results illustrate that this down-sampling-based image compression scheme based on sparse representation (DCSR) achieves better rate-distortion performance when compared with the conventional codecs, such as JPEG and JPEG2000, and the DLC codec, described in Section 3.1.

The block diagram of the DCSR encoder is shown in **Figure 3**. This framework mainly consists of five parts, including down-sampling, up-scaling, sparse representation, quantization and entropy coding [8]. An image analyser is also introduced to the core of codec. At the pre-processing step, the down-sampling operator uses a blurring convolution kernel and a simple decimator by three to produce the LR image with only 1/9 of total pixels of the original image. At the up-scaling step, the down-sampled image is restored back to its original resolution. The goal of the up-scaling step is designing an accurate algorithm to improve the rate-distortion performance at the higher bit-rates. A joint sparse representation method is employed to solve this ill-posed, complex inverse problem. This method guarantees to restore the high frequency details which are enough and sufficient for reconstruction of the HR image.

Assume the LR image, X^L, is obtained via $\mathbf{X}^L = \mathbf{H}\mathbf{X}^H$, where $\mathbf{H}$ is the down-sampling operator and $\mathbf{X}^H$ denotes the HR image. After the image recovery via the up-scaling algorithm, the relationship between the HR and the reconstructed images is described as $\mathbf{X}^H = \tilde{\mathbf{X}}^H + \mathbf{E}$, where $\mathbf{E}$ is the residual image. The LR image $\mathbf{X}^L$ and the residual image $\mathbf{E}$ are separately partitioned into non-overlapping image patches of size $B \times B$. Let us assume $[\mathbf{x}_i]_{i=1}^{T_L}$ and $[\mathbf{e}_i]_{i=1}^{T_E}$ denote the vectorized image blocks in the $\mathbf{X}^L$ and $\mathbf{E}$, respectively, where T_L and T_E are the number of patches in the $\mathbf{X}^L$ and $\mathbf{E}$, respectively. Moreover, note that $T_L = 1/9 T_E$.

At the sparse representation step, the LR image patches $[\mathbf{x}_i]_{i=1}^{T_L}$ are sparsely represented over an over-complete dictionary $\mathbf{D}^L$ of size $N \times K$ using the OMP algorithm. An image analyser is carefully designed to use the visual saliency information at the sparse representation step. The goal of the analyser is to further reduce the reconstructed errors in the areas within the image where have higher visual interest to the HVS. The same procedure is also applied for the sparse representation of the image patches of the residual image $[\mathbf{e}_i]_{i=1}^{T_E}$. A different over-complete dictionary $\mathbf{D}^E$ of size $N \times K$ is used for the sparse representation of the residual patches. The two dictionaries $\mathbf{D}^L$ and $\mathbf{D}^E$ are trained offline using a bi-level dictionary learning algorithm. It is assumed that these dictionaries are shared between the encoder and decoder. Finally, the obtained sparse coefficients of LR patches and residual patches, i.e. $\mathbf{C}^L = \left[\mathbf{c}_i^L\right]_{i=1}^{T_L}$ and $\mathbf{C}^E = \left[\mathbf{c}_i^E\right]_{i=1}^{T_E}$ respectively, are quantized and entropy coded in order to obtain the bit-stream. $\mathbf{c}_i^L \in \mathbb{R}^K$ and $\mathbf{e}_i^L \in \mathbb{R}^K$
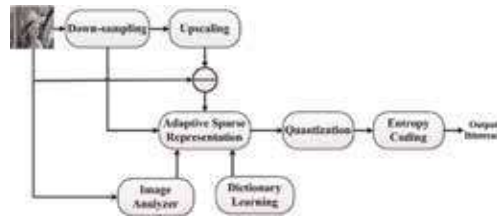

Figure 3.
Block diagram of the DCSR codec.

denote the coefficients vector of the i-block in the LR image $\mathbf{X}^L$ and the residual image $\mathbf{E}$, respectively.

At the decoder side, the image is reconstructed by a minor application of the above steps. First, the reconstructed LR image $\hat{\mathbf{X}}^L$ is up-scaled by the up-scaling operator to restore the image $\hat{\mathbf{X}}^H$ of size of the original image. Then, the final restored image is obtained via $\mathbf{X}^D = \hat{\mathbf{X}}^H + \hat{\mathbf{E}}$, where $\hat{\mathbf{E}}$ denotes the decoded residual image.

3.2.1 Image analyser for adaptive sparse representation

The main goal of image analyser is to enhance the performance of the DCSR encoder. It reduces the reconstructed error in some parts of the image which have higher visual interest to a human observer. Therefore, the image analyser extracts the salient regions within the image according to its visual significance to the HVS. Then, it allocates higher rates to the salient regions by assigning different sparsity levels to the image patches, located within the salient parts, in both LR and residual images. As mentioned before, the GBVS model [42] is used to obtain the salient regions within an image. Some examples of saliency maps are shown in **Figure 2**.

For finding the sparsity levels of the image patches in the LR image, the obtained saliency map is re-sized to the same size of the LR image. Then, it is divided into $B \times B$ blocks to obtain the corresponding saliency value H_i of the i-th block by taking the average of the saliency values of pixels within that block. The goal is assign a different sparsity level S_i to each block. Note that the average of the sparsity levels assigned to all blocks within the image should be equal (or slightly inferior) to the target sparsity level S. Given the target sparsity level S and the set of saliency values $[\mathbf{H}_i]_{i=1}^{T_L}$, the sparsity level of the i-th block is obtained by:

$$S_i^L = \frac{T_L \times H_i}{\sum_{i=1}^{T_L} H_i} S, \tag{11}$$

where T_L is the number of blocks in the LR image. Based on this strategy, different sparsity levels are allocated for the sparse representation of the image patches in the LR image. Given the obtained sparsity levels $\left[S_i^L\right]_{i=1}^{T_L}$, the sparse representation of the LR patch $\mathbf{x}_i$ in the LR image over the dictionary $\mathbf{D}^L$ is achieved by [44]:

$$\underset{\mathbf{c}_i^L}{\mathrm{argmin}} \|\mathbf{x}_i - \mathbf{D}^L \mathbf{c}_i^L\|_2, \text{ s.t. } \|\mathbf{c}_i^L\|_0 \leq S_i^L. \tag{12}$$

The same procedure is applied to obtain the sparsity levels $\left[S_i^E\right]_{i=1}^{T_E}$ for the image patches in the residual image. The set of saliency values $[\mathrm{H}_i]_{i=1}^{T_E}$ is obtained using the saliency map of the original image, as described before. The sparse representation of each patch e_i in residual image with respect to the dictionary $\mathbf{D}^E$ is achieved by:

$$\underset{\mathbf{e}_i^E}{\mathrm{argmin}} \|\mathbf{e}_i - \mathbf{D}^E \mathbf{c}_i^E\|_2, \text{ s.t. } \|\mathbf{c}_i^E\|_0 \leq S_i^E. \tag{13}$$

The OMP method is used to solve these problems. At the low bit-rates, DCSR encodes only the LR image. At the higher bit-rates, DCSR encodes the residual image and send it as side information in order to improve the coding efficiency. In

this case, the patches within the residual and LR images are represented over the corresponding dictionaries with the same target sparsity level S.

3.2.2 Joint dictionary-mapping learning for up-scaling

The goal of up-scaling algorithm is to recover the high frequency information eliminated during the down-sampling operation. One well-known up-scaling approach is to learn a function which maps the LR and HR image patches. This mapping function can be obtained using two training databases of the LR and HR image patches. Instead of finding the direct mapping function between the LR and HR patches, authors in [44] show that the mapping function can be efficiently learned in the transform domain. In this approach, first, the LR and HR patches are transferred into the representation space over the trained dictionaries and then the relationship between representation coefficients is learned.

Let two sets $\mathbf{X}$ and $\mathbf{Y}$ consist of N training LR and corresponding HR image patches, respectively. Suppose $\mathbf{D}_x \in \mathbb{R}^{M \times K}$ and $\mathbf{D} \in \mathbb{R}^{M_y \times K}$ denote the trained dictionaries for the sparse representation of the LR and HR patches. These two dictionaries are trained jointly such that the sparse representation of all training LR and HR patches are mapped to each other via a linear function $\mathbf{M} \in \mathbb{R}^{K \times K}$. The dictionaries and mapping matrix are obtained by solving the following minimization problem:

$$\underset{\mathbf{D}_x,\, \mathbf{D}_y,\, \mathbf{\Lambda}_x,\, \mathbf{\Lambda}_y,\, \mathbf{M}}{\arg\min} \ \left\| \mathbf{X} - \mathbf{D}_x \mathbf{\Lambda}_x \right\|_2^2 + \left\| \mathbf{Y} - \mathbf{D}_y \mathbf{\Lambda}_y \right\|_2^2 + \gamma \left\| \mathbf{\Lambda}_x - \mathbf{M} \mathbf{\Lambda}_y \right\|_2^2$$
$$+ \lambda \left\| \mathbf{\Lambda}_x \right\|_1 + \lambda \left\| \mathbf{\Lambda}_y \right\|_1 + \lambda_m \left\| \mathbf{M} \right\|_2^2, \tag{14}$$

where $\mathbf{\Lambda}_x \in \mathbb{R}^{K \times N}$ and $\mathbf{\Lambda}_y \in \mathbb{R}^{K \times N}$ represent the corresponding sparse representation matrices. The terms γ, λ and λ_m denote regularization parameters. As proposed in [45], the minimization problem Eq. (14) is solved in an iterative approach with respect to a variable while all the other variables are considered as fixed parameters.

After training process, the up-scaling is achieved by the dictionary pair (i.e. $\mathbf{D}_x$ and $\mathbf{D}_y$) and the mapping matrix $\mathbf{M}$. First, the LR image is divided into overlapping blocks of size $B_s \times B_s$. Then, the sparse representation vector $\boldsymbol{\alpha}_y$ of an LR patch $\mathbf{y}$ is obtained with respect to the trained dictionary $\mathbf{D}_y$. In the minimization problem Eq. (14), we use ℓ_1-norm to train the dictionaries. Given these trained dictionaries, the up-scaled algorithm uses ℓ_0-norm, instead of ℓ_1 norm, in order to improve the rate-distortion performance. Thus, the sparse representation of LR patch $\boldsymbol{\alpha}_y$ is obtained by solving the following minimization problem:

$$\boldsymbol{\alpha}_y = \arg \underset{\boldsymbol{\alpha}}{\min} \left\| \mathbf{y} - \mathbf{D}_y \boldsymbol{\alpha} \right\|_2^2 + \delta \left\| \boldsymbol{\alpha} \right\|_0, \tag{15}$$

where δ denotes the regularization parameter. At the next step, we derive $\hat{\boldsymbol{\alpha}}_x = \mathbf{M} \boldsymbol{\alpha}_y$ and restore the HR patch via $\hat{\mathbf{x}} = \mathbf{D}_x \hat{\boldsymbol{\alpha}}_x$. At the last step, the restored up-scaled image $\hat{\mathbf{X}}^H$ is obtained by replacing the recovered image patches into the whole image grid and taking the average over the overlapped pixels. For more details about solving the above optimization problems, please refer to [44].

3.2.3 Bi-level dictionary learning algorithm for image compression

The up-scaling algorithm, described in previous section, leads to a bi-level dictionary learning algorithm which used for image compression at the DCSR encoder.

Note that the trained dictionary D^L and the up-scaling operator are used to estimate a large part of signal energy. The remained energy of residual is captured by representing the residual over another trained dictionary. This residual is encoded as side information to improve the quality of the restored image at the higher bit-rates. The bi-level dictionary learning algorithm is achieved by the following steps: first, the training images are down-sampled by a factor 3. Second, these LR images are employed to train a dictionary D^L by the K-SVD algorithm [23]. Third, the LR training images are represented with respect to the trained dictionary D^L. Forth, the reconstructed LR images are then up-scaled by the algorithm described in previous section. Fifth, these up-scaled images are used to create the training residual images which are subsequently used to train the second dictionary D^R by the K-SVD algorithm.

3.2.4 Quantization and entropy coding

Differential pulse-coded modulation (DPCM) is used to quantize the non-zero elements in the sparse representation vectors C^L and C^E. A dead-zone quantizer is used for quantization. Further, the classical Huffman coding is employed to entropy-code the quantized sparse coefficients. Predefined code-word tables, needed for Huffman encoder, are constructed offline and stored at both encoder and decoder sides.

The location of non-zero coefficients in C^L and C^E follow a random pattern. Therefore, encoding the indices of these coefficients occupies a big part output bit-stream. For efficiently encoding these indices I, the quad-tree splitting algorithm, explained in Section 3.1.2, is employed.

3.3 Experimental results

In this section, the rate-distortion performance of the DCSR codec is examined by performing a suite of experiments on a set of 8-bit grey-scale standard images. All evaluated images are re-sized to size of 528×528 pixels in order to produce the LR image with only 1/9 of total pixels of the original image. The well-known peak signal-to-noise ratio (PSNR) and structural similarity (SSIM) index are chosen as a measure in the experiments. Further, the rate distortion performance is compared with the JPEG and JPEG2000 standards, as well as the DLC codec, presented in Section 3.1.

Block size is set as 8×8 for encoding the LR and residual images. Further, two dictionaries D^L and D^E of size 64×440 are trained using the bi-level dictionary learning algorithm presented in Section 3.2.3. We use the images from the CVG-Granada dataset[1] for training. All these training images are partitioned into 8×8 image patches and 12,000 ones are randomly selected for training. One hundred epochs, each processing 12,000 training vectors, are considered during training process. For up-scaling, the dictionary pair of size 25×256 and the mapping matrix of size 256×256 are trained using the algorithm introduced in Section 3.2.2. The regularization parameters γ, λ, and λ_m are empirically set as 0.1, 0.1, and 0.01, respectively.

Next, we present the rate-distortion graph for the test images in **Figures 4** and **5**. Note that we also provide the results for different baseline algorithms, i.e. JPEG,[2]
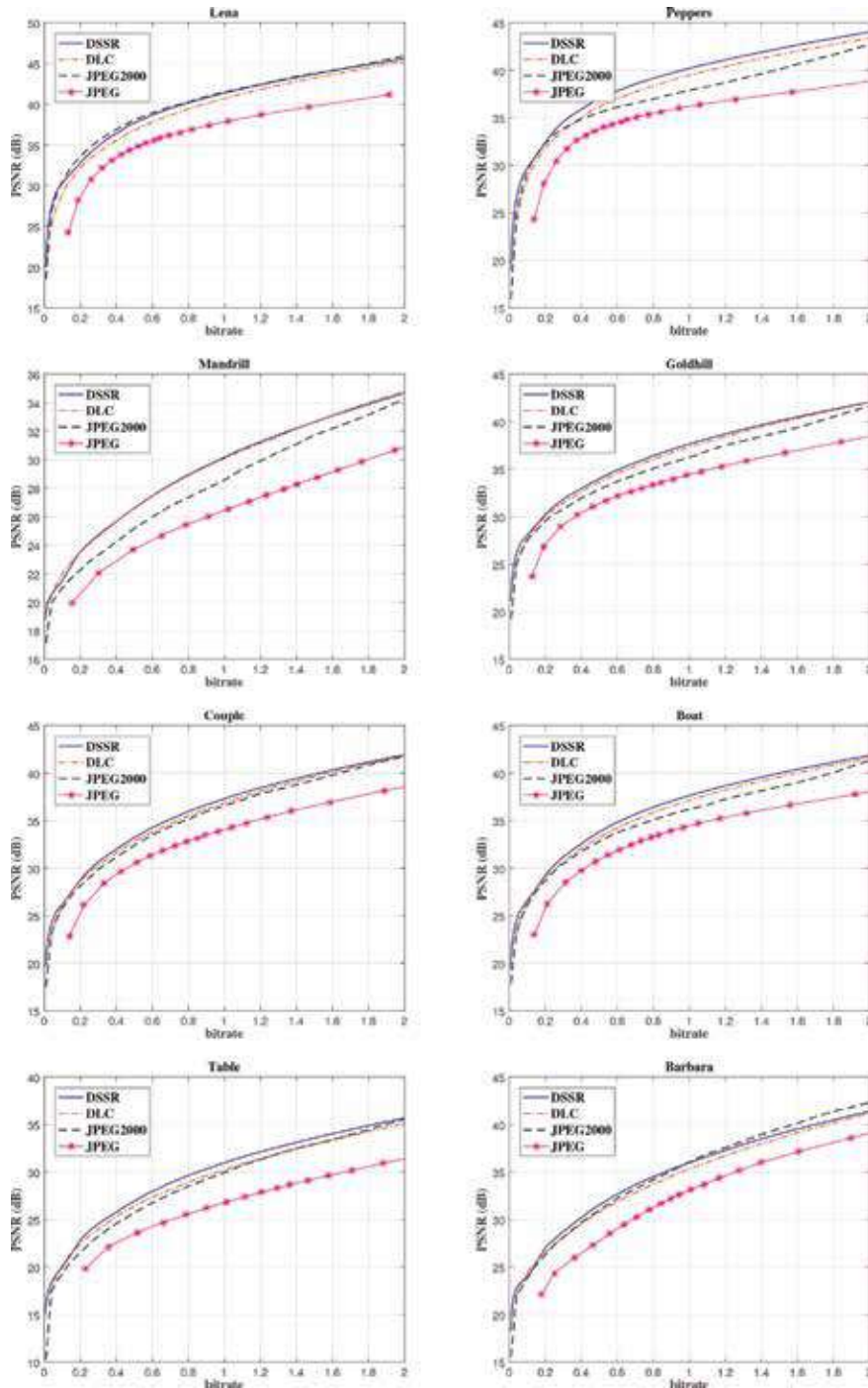
---

[1] 1http://decsai.ugr.es/cvg/dbimagenes
[2] http://www.ijg.org

Figure 4.
Rate-distortion performance of the DCSR codec compared to JPEG, JPEG2000 and DLC codecs in terms of PSNR for several test images (size 528 × 528, grey-level).

JPEG2000,[3] and DLC algorithm [12]. As these figures shows DLC and DCSR codecs provide a better performance (in terms of PSNR and SSIM) than the available image coding standards JPEG and JPEG2000. Interestingly, as the **Figure 4** demonstrates,
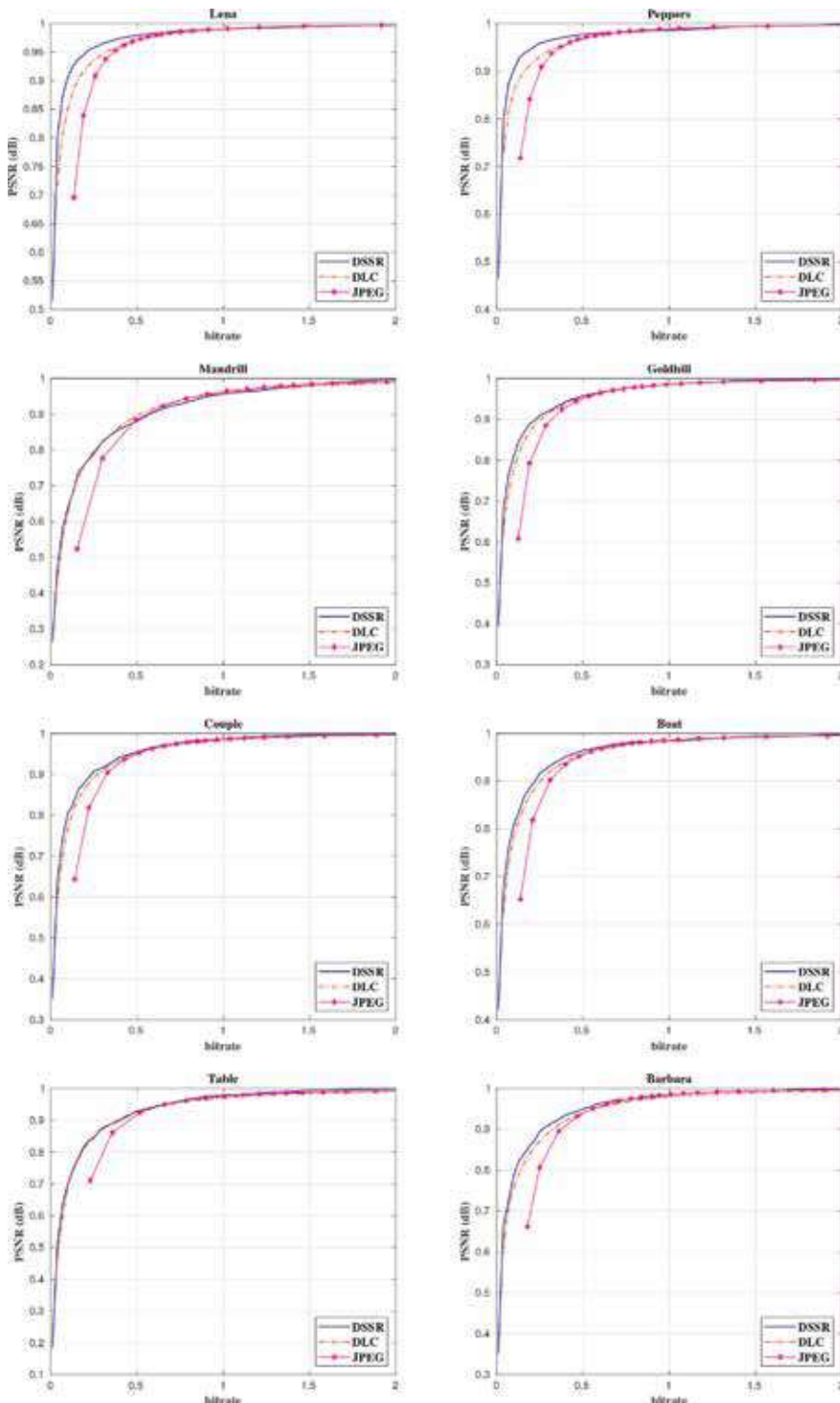
_____

[3] http://www.openjpeg.org

Figure 5.
Rate-distortion performance of the DCSR codec compared to JPEG and DLC codecs in terms of MSSIM for several test images (size 528 × 528, grey-level).

the DCSR algorithm enhances the quality of the image over the JPEG2000 codec. The enhancement depends on the statistics of the image, so different enhancement is observed in different images. Please note that SSIM shows the perceived quality
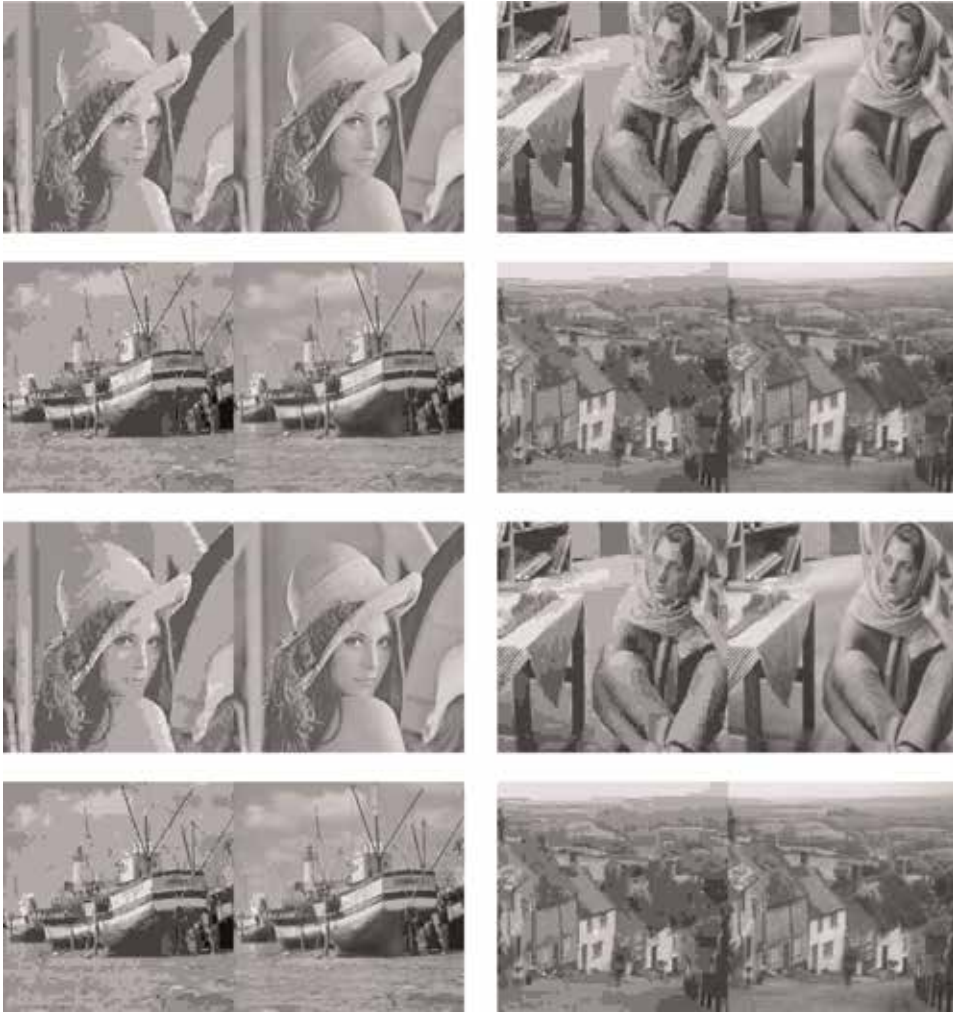
Figure 6.
Compressed images at bit-rate (0.15) using JPEG (left) and DCSR (right) scheme.

of the compressed image, therefore, SSIM curves for DCSR and JPEG2000 are very close to each other. For a better visualization, we removed the rate-distortion performance for JPEG2000 in **Figure 5**. As the trained dictionary performs a better capture and presents the contours more accurate, DCSR codec presents a higher performance compared to the analytic dictionaries such as the wavelet transform basis. Moreover, a 0.2 dBs improvement is observed using the DLC algorithm, marginally better for simpler images, like *Mandrill*.

Several compressed images are shown in **Figure 6** for visual comparisons. All images are coded with the same bit-rate (0.15) using JPEG and DCSR algorithm. As it can be seen, the JPEG standard fails to reconstruct images compressed at very low bit rates. In comparison, DCSR algorithm can preserve more image details. It is more effective in reconstruction of both the smooth area and the complex regions, including texture and edges, leading to visually much more pleasant recovery.

As a consequence, the down-sampling-based coding results in the high-frequency details in the image before performing the quantization lossy, hence larger number of bits are assigned low frequency information occupying more energy in the image. The presented bit assigning strategy brings a higher

performance for images coded at low bit-rate. In higher bit-rates, the efficiency of coding is enhanced after the residual image is encoded as side information.

4. Conclusions

A brief summary of the signal modelling methodology has been given at the first part of chapter. We continued with the explicit and straightforward formulation of the sparse representation being more suitable for the compression tasks. We have just focused on the synthesis-based signal modelling because of being mature of the image compression using the analysis-based sparse signal modelling. An adaptive sparse representation over a trained over-complete dictionary was presented to compress the images. More specifically, given the saliency map of the image to be encoded, an image patch could be well represented with the linear combination of atoms selected from an over-complete and trained dictionary based on the sparsity level. Finally, at the end part of this chapter, a down-sampling operation is incorporated into the codes in order to improve the compression performance. The experimental results demonstrated that the presented image compression frameworks outperform image coding standards, such as JPEG and JPEG2000, which use an analytic dictionary.

Author details

Ali Akbari[1,2]* and Maria Trocan[2]

1 University of Surrey, Guildford, UK

2 Institut supérieur d'électronique de Paris, Paris, France

*Address all correspondence to: ali.akbari@isep.fr

IntechOpen

References

[1] Olshausen A, Field DJ. Sparse coding with an overcomplete basis set: A strategy employed by v1? Vision Research. 1997;**16**(4):3311-3325

[2] Mallat S. A Wavelet Tour of Signal Processing. 3rd ed. Academic Press; 2008

[3] Pennec EL, Mallat S. Bandelet image approximation and compression. SIAM Multiscale Modeling & Simulation. 2005;**4**(3):992-1039

[4] Villegas OOV, Elias RP, Villela PR, Sanchez VGC, Salazar AM. Edging out the competition: Lossy image coding with wavelets and contourlets. IEEE Potentials. 2008;**27**(2):39-44

[5] Wang S, Shu Z, Zhang L, Liu G, Gan L. Iterative image coding with overcomplete curvelet transform. In: Proceedings of IEEE Congress on Image and Signal Processing (CISP), vol. 1; May 2008; Hainan, China. pp. 666-670

[6] Beferull-Lozano B, Ortega A. Coding techniques for oversampled steerable transforms. In: Proceedings of Asilomar Conference on Signals, Systems, and Computers, vol. 2; October 1999; Pacific Grove, CA. pp. 1198-1202

[7] Akbari A, Mandache D, Trocan M, Granado B. Adaptive saliency-based compressive sensing image reconstruction. In: Proceedings of IEEE International Conference on Multimedia Expo Workshops (ICMEW); July 2016; Seattle, WA. pp. 1-6

[8] Akbari A, Trocan M. Downsampling based image coding using dual dictionary learning and sparse representations. In: Proceedings of IEEE International Workshop on Multimedia Signal Processing (MMSP); August 2018. pp. 1-5

[9] Akbari A, Trocan M. Sparse recovery-based error concealment for multiview images. In: Proceedings of IEEE International Workshop on Computational Intelligence for Multimedia Understanding (IWCIM); October 2015; Prague, Czech Republic. pp. 1-5

[10] Akbari A, Trocan M, Granado B. Synthesis sparse modeling: Application to image compression and image error concealment. In: Proceedings of Signal Processing with Adaptive Sparse Structured Representations Workshop (SPARS); June 2017; Lisbon, Portugal

[11] Mandache D, Akbari A, Trocan M, Granado B. Image compressed sensing recovery using intra-block prediction. In: Proceedings of IEEE International Conference on Telecommunications Forum (TELFOR); November 2015; Belgrade, Serbia. pp. 748-751

[12] Akbari A, Trocan M, Granado B. Image compression using adaptive sparse representations over trained dictionaries. In: Proceedings of IEEE International Workshop on Multimedia Signal Processing (MMSP); September 2016; Montreal, Canada. pp. 1-6

[13] Akbari A, Trocan M, Granado B. Image error concealment using sparse representations over a trained dictionary. In: Proceedings of IEEE Picture Coding Symposium (PCS); December 2016; Nuremberg, Germany. pp. 1-5

[14] Akbari A, Trocan M, Granado B. Residual based compressed sensing recovery using sparse representations over a trained dictionary. In: Proceedings of International ITG Conference on Systems, Communications and Coding (SCC); February 2017; Hamburg, Germany. pp. 1-6

[15] Akbari A, Trocan M, Granado B. Sparse recovery-based error

concealment. IEEE Transactions on Multimedia. 2017;**19**(6):1339-1350

[16] Akbari A, Trocan M, Granado B. Joint-domain dictionary learning-based error concealment using common space mapping. In: Proceedings of IEEE International Conference on Digital Signal Processing (DSP); August 2017. pp. 1-5

[17] Akbari A, Trocan M, Granado B. Image error concealment based on joint sparse representation and non-local similarity. In: Proceedings of IEEE Global Conference on Signal and Information Processing (GlobalSIP); November 2017

[18] Akbari A, Trocan M, Sanei S, Granado B. Joint sparse learning with nonlocal and local image priors for image error concealment. IEEE Transactions on Circuits and Systems for Video Technology. 2019

[19] Akbari A, Trocan M, Granado B. Image compressed sensed recovery using saliency-based adaptive sensing and residual reconstruction. In: Compressed Sensing: Methods, Theory and Applications. New York: Nova Science Publishers; 2018

[20] Akbari A, Trevisi M, Trocan M, Carmona-Galán R. Compressive imaging using rip-compliant cmos imager architecture and landweber reconstruction. IEEE Transactions on Circuits and Systems for Video Technology. 2019:1-1

[21] Akbari A, Trocan M. Robust image reconstruction for block-based compressed sensing using a binary measurement matrix. In: 2018 25th IEEE International Conference on Image Processing (ICIP); October 2018. pp. 1832-1836

[22] Akbari A, Trevisi M, Trocan M. Adaptive compressed sensing image reconstruction using binary

measurement matrices. In: 2018 25th IEEE International Conference on Electronics, Circuits and Systems (ICECS); December 2018. pp. 659-660

[23] Aharon M, Elad M, Bruckstein A. K-SVD: An algorithm for designing overcomplete dictionaries for sparse representation. IEEE Transactions on Signal Processing. 2006;**54**(11): 4311-4322

[24] Ahmed N, Natarajan T, Rao KR. Discrete cosine transform. IEEE Transactions on Computers. 1974;**C-23** (1):90-93

[25] G. K. Wallace, "The jpeg still picture compression standard," IEEE Transactions on Consumer Electronics, vol. 38, no. 1, pp. xviii-xxxiv, 1992

[26] Skodras A, Christopoulos C, Ebrahimi T. The jpeg 2000 still image compression standard. IEEE Signal Processing Magazine. 2001;**18**(5):36-58

[27] Rubinstein R, Bruckstein AM, Elad M. Dictionaries for sparse representation modeling. Proceedings of the IEEE. 2010;**98**(6):1045-1057

[28] Pati YC, Rezaiifar R, Krishnaprasad PS. Orthogonal matching pursuit: Recursive function approximation with applications to wavelet decomposition. In: Proceedings of Asilomar Conference on Signals, Systems and Computers; November 1993; Pacific Grove, CA. pp. 40-44

[29] Candés E, Demanet L, Donoho D, Ying L. Fast discrete curvelet transforms. SIAM Multiscale Modeling & Simulation. 2006;**5**(3):861-899

[30] Do MN, Vetterli M. Contourlets: A new directional multiresolution image representation. In: Proceedings of Asilomar Conference on Signals, Systems and Computers, vol. 1; November 2002; Pacific Grove, CA. pp. 497-501

[31] Pennec EL, Mallat S. Sparse geometric image representations with bandelets. IEEE Transactions on Image Processing. 2005;**14**(4):423-438

[32] Engan K, Skretting K, Husoy JH. Family of iterative LS-based dictionary learning algorithms, ILS-DLA, for sparse signal representation. Digital Signal Processing. 2007;**17**(1):32-49

[33] Vidal R, Ma Y, Sastry S. Generalized principal component analysis (GPCA). IEEE Transactions on Pattern Analysis and Machine Intelligence. 2005;**27**(12): 1945-1959

[34] Sulam J, Ophir B, Zibulevsky M, Elad M. Trainlets: Dictionary learning in high dimensions. IEEE Transactions on Signal Processing. 2016;**64**(12): 3180-3193

[35] Lewicki MS, Sejnowski TJ. Learning overcomplete representations. Neural Computation. 2000;**12**(2):337-365

[36] Kreutz-Delgado K, Murray JF, Rao BD, Engan K, Lee TW, Sejnowski TJ. Dictionary learning algorithms for sparse representation. Neural Computation. 2003;**15**(2): 349-396

[37] Gurumoorthy KS, Rajwade A, Banerjee A, Rangarajan A. A method for compact image representation using sparse matrix and tensor projections onto exemplar orthonormal bases. IEEE Transactions on Image Processing. 2010;**19**(2):322-334

[38] Mazaheri JA, Guillemot C, Labit C. Learning a tree-structured dictionary for efficient image representation with adaptive sparse coding. In: Proceedings of IEEE International Conference on Acoustics, Speech and Signal Processing (ICASSP); May 2013; Vancouver, Canada. pp. 1320-1324

[39] Sun Y, Tao X, Li Y, Lu J. Dictionary learning for image coding based on multisample sparse representation. IEEE Transactions on Circuits and Systems for Video Technology. 2014;**24**(11): 2004-2010

[40] Peyre G. A review of adaptive image representations. IEEE Journal of Selected Topics in Signal Processing. 2011;**5**(5):896-911

[41] Borji A, Cheng MM, Jiang H, Li J. Salient object detection: A benchmark. IEEE Transactions on Image Processing. 2015;**24**(12):5706-5722

[42] Harel J, Koch C, Perona P. Graph-based visual saliency. In: Proceedings of Neural Information Processing Systems (NIPS); 2006. pp. 545-552

[43] Skretting K, Engan K. Image compression using learned dictionaries by rls-dla and compared with K-SVD. In: Proceedings of IEEE International Conference on Acoustics, Speech and Signal Processing (ICASSP); May 2011; Prague, Czech Republic. pp. 1517-1520

[44] Wang S, Zhang L, Liang Y, Pan Q. Semi-coupled dictionary learning with applications to image super-resolution and photo-sketch synthesis. In: Proceedings of IEEE Conference on Computer Vision and Pattern Recognition (CVPR); June 2012; Providence, RI. pp. 2216-2223

[45] Huang DA, Wang YCF. Coupled dictionary and feature space learning with applications to cross-domain image synthesis and recognition. In: Proceedings of IEEE Conference on Computer Vision (ICCV); December 2013; Sydney, Australia. pp. 2496-2503

The DICOM Image Compression and Patient Data Integration using Run Length and Huffman Encoder

Trupti N. Baraskar and Vijay R. Mankar

Abstract

Maintaining human healthcare is one of the biggest challenges that most of the increasing population in Asian countries are facing today. There is an unrelenting need in our medical community to develop applications that are low on cost, with high compression, as huge number of patient's data and images need to be transmitted over the network to be reviewed by the physicians for diagnostic purpose. This implemented work represents discrete wavelet-based threshold approach. Using this approach by applying N-level decomposition on 2D wavelet types like Biorthogonal, Haar, Daubechies, Coiflets, Symlets, Reverse Biorthogonal, and Discrete Meyer, various levels of wavelet coefficients are obtained. The lossless hybrid encoding algorithm, which combines run-length encoder and Huffman encoder, has been used for compression and decompression purpose. This work is proposed to examine the efficiency of different wavelet types and to determine the best. The objective of this research work is to improve compression ratio and compression gain.

Keywords: DICOM, discrete wavelet, N-level decomposition, threshold approach, data hiding algorithms

1. Introduction

Digital technology has, in the last few decades, entered in almost every aspect of medicine. There has been a huge development in noninvasive medical imaging equipment. Since there are multiple medical equipment manufacturers, there is a strong need to develop a standard for storage and exchange of medical images. DICOM (Digital Imaging and Communications in Medicine) makes medical image exchange easier and independent of the imaging equipment manufacturer. The DICOM standard has been developed by ACR-NEMA to meet the needs of manufacturers and users of medical imaging equipment for interconnection of devices on standard networks. The DICOM technology is suitable when sending images between different departments within hospitals and/or other hospitals and the consultant. DICOM file contains both a header, which include text information such as patient's name, modality, image size, etc., and image data in the same file. Hence DICOM standards are widely used in the integration of digital imaging systems in medicine. **Figure 1** shows the structure of DICOM image file. It has two main

Figure 1.
The structure of a DICOM image file.

components. The first is header; it consists of 128 bytes of file preamble which is followed by string by 4-byte prefix, and it contains four-character string. The second is data set; it consists of multiple set of data elements. Each data element has four fields; these are tag, value representation, value length, and value field. The third is image pixel intensity data; it contains necessary medical image data display like number of frames, lines, columns, etc.

1.1 File format used by DICOM images

There are four major file formats in medical imaging, and they are Neuroimaging Informatics Technology Initiative (NIfTI), Analyze, DICOM, and MINC. The task of the image file format is to provide a standardized way to store the unique data in a much organized and systematic manner and showcase how the pixel data understood the correct loading, visualization, and analysis was derived by the software. The major file format currently useful in medical imaging is DICOM format. The DICOM format includes some information that can be useful for image registration, such as position and orientation of the image with respect to the data acquisition device and patient information with respect to voxel size. DICOM file format design consideration is based on the following concept such as pixel depth, photometric interpretation, metadata, and pixel data. The DICOM file format is created by addition of header size and pixel data. Mathematical equations are as follows:

$$\textbf{\textit{DICOM File Format}} = \textbf{\textit{Header Size}} + \textbf{\textit{Pixel Data Size}} \qquad (1)$$

$$\textbf{\textit{Pixel Data Size}} = \textbf{\textit{Rows}} \times \textbf{\textit{Columns}} \times \textbf{\textit{Pixel Depth}} \times \textbf{\textit{Number of Frames}} \quad (2)$$

The more popular formats used in daily practice are the JPEG, JPEG 2000, TIFF, GIF, PNG, and BMP formats. The images saved in these formats can be accessed on any personal computer without the need of specific viewers. File format are designed with the help of image conversion technique and coding schemes.

The rest of the chapter is organized as follows. Section 2 provides an overview of image file format and image standard used for medical image compression, and data hiding methods are described in the Section 3. Section 4 provides proposed work brief explanation. Section 5 discusses regarding results that are obtained after implementation of application. Finally, Section 6 concludes the chapter.

2. Related work

The related work is a comprehensive summery of previous research on image file format, standard image compression using transform coding, and patient information integration into image for DICOM images. The more popular formats used in daily practice are the JPEG, JPEG 2000, TIFF, GIF, PNG, and BMP formats. The images saved in these formats can be accessed on any personal computer without the need of specific viewers. File formats are designed with the help of image conversion technique and coding schemes [1–3]. **Figure 2** shows the basic digital image file formats and its classification. The vector images are not commonly used in medical data processing.

Table 1 gives the summary of various parameters of raster image file format [4, 5, 7–11]. **Table 2** gives a characteristic overview of the major file formats currently used in medical imaging, i.e., NIfTI, Analyze, DICOM, and MINC [6, 12, 13].

Two types of compression methods are classified. The lossless image has huge application in archival of medical and digital radiography document, where loss of information in original image could consider improper diagnosis. The medical imaging application required lossless image compression. Thus, medical image compression application development is a challenging problem. The survey paper [14] conveys that compression ratio 4:1 is possible using lossless compression. An increasing volume of data generated by new imaging modality, CT scan and MRI lossy compression technique are used to decrease the cost of storage and increase the efficiency of transmission over networks for teleradiology application [12]. There are two main categories of compression lossless (reversible) and lossy (irreversible). DICOM support lossless compression schemes like run-length encoding, Huffman coding, LZW coding, area coding, and arithmetic coding. The RLE is used
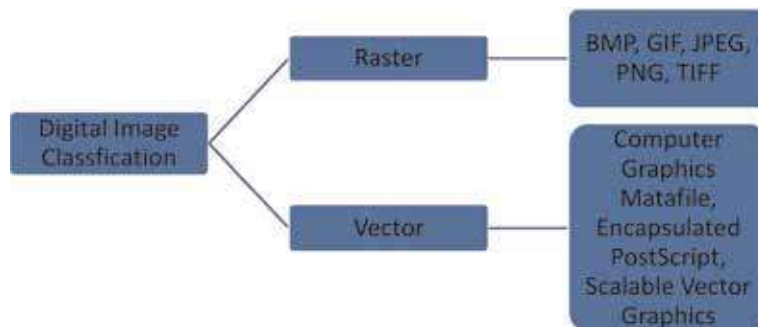

Figure 2.
Basic digital classification image file format.

Sr. no.	File format	Extension	Bit depth		Compression type	Compression performance	Name of supported free image viewer
			Gray	**Color**			
1	BMP	bmp	1,4,8	1,4,8,24	Lossless	Very low	IrfanView, XnView, Osiris, ImageJ
2	DICOM	dcm	8, 16	8, 24, 48	Lossless	Low	IrfanView, XnView, Osiris, ImageJ
3	GIF	gif	1, 4, 8	1, 4, 8	Lossless	Medium	IrfanView, XnView, Osiris, ImageJ
4	JPEG	jpg	8	24	Lossy	Average	IrfanView, XnView, Osiris, ImageJ
5	JPEG 2000	Jp2	8, 16	24, 48	Lossless	High	IrfanView, XnView
6	PNG	png	1, 4, 8, 16	1, 4, 8, 24, 48	Lossless	High	IrfanView, XnView
7	TIFF	tiff	8, 16	8, 24, 48	Lossless or lossy	Very high	IrfanView, XnView

Table 1.
Summary of raster (bitmap) image file format.

Sr. no.	File format	Extension	Data type			Header	Compression scheme supported
			Integer	**Float**	**Complex**		
1	DICOM	.dcm	Signed and unsigned (8 bit, 16 bit, 32 bit)	Not supported	Not supported	Variable length binary format	JPEG, RLE, JPEG-LS, MPEG2/MPEG4, JPEG XR
2	NIfTI	.nii	Signed and unsigned (8 bit to 64 bit)	Signed and unsigned (32 bit to 128 bit)	Signed and unsigned (64 bit to 256 bit)	Fixed length (532 byte binary format)	gzip (it is a software application used to store compressed and decompressed file)
3	MINC	.mnc	Signed and unsigned (8 bit to 32 bit)	Signed and unsigned (32 bit to 64 bit)	Signed and unsigned (32 bit to 64 bit)	Extended binary format	gzip (it is a software application used to store compressed and decompressed file)
4	Analyze	.hdr and .img	Signed (8 bit to 32 bit) and unsigned (8 bit)	Signed (32 bit to 64 bit)	Signed (64 bit)	Fixed length (348 byte binary format)	High dynamic range (HDR) imaging uses sub-band coding technique which is an example of lossy technique

Table 2.
Characteristics of medical image file format.

for medical image compression in hybrid approach, where gray scale value gives certain interesting fact about the distribution in image. The background pixels of all the medical image are low values, and they differ by +3 or −3. The RLE is based on dynamic array implementation, no need to process whole image [8]. The paper served that the number of repeated zero count which is represented as "RUN" and

appends the nonzero coefficients represented as "LEVEL" [15, 16]. The Huffman coding is a lossless compression technique, which is used for medical image compression. This works on variable length encoding principal, which includes calculation of length of unique codes. It generates a binary tree, which is also known as Huffman tree. Huffman algorithm gives higher compression ratio in the case of medical image compression. During the whole process of compression, there should not be any loss of information that will affect proper diagnosis [17, 18]. The Huffman code is designed to integrate the lowest probable symbols, and this integration is repeated until only two probabilities of two symbols are left. In this survey paper, certain improvements are discussed on the existing Huffman technique which will help to preserve any loss of information during compression that will affect proper diagnosis [19]. In lossy compression method, data are rejected during compression and cannot be recovered completely. This method reaches much greater compression performance than lossless compression. Wavelet and higher-level JPEG are the example of lossy compression technique where JPEG 2000 is a progressive lossless-to-lossy compression algorithm [20–22]. This article uses the concept of data hiding into image for data encryption. In order to enable large capacity of data hiding and maintaining good image quality, the data integration is applied on detail coefficients of high-frequency sub-bands. It works on transform domain of multilevel two-dimensional discrete wavelet transform. The objective of this implementation is to perform image compression as much as possible. It will help to reduce the redundancy of the image and to store or transmit data in an efficient form. As in telemedicine, the medical images are transmitted through advanced hyperlinks; medical image compression without any loss of useful information is of immense importance for the fast transfer of the medical data [23].

3. Proposed work

This proposed compression approach deals with .dcm file of DICOM format. It splits .dcm file into patient data with bmp.txt extension and gray scale image with .bmp extension. Then N-level DWT using various wavelet types is applied to a gray image. Firstly, this splits the image into n number of high-frequency sub-bands (HLn, LHn, HHn) where n = 1, 2, 3 ... ..N and one low-frequency sub-band (LLn) where n = maximum level (N). The high-frequency sub-bands at levels 1, 2, 3, and 4 are threshold and quantized and find detail coefficients are encoded directly through run-length encoding. Secondly, the one low-frequency sub-band is also threshold and quantized and find high-level approximate coefficient. Lastly, both the coefficients (detail coefficients, high-level approximate coefficient) are encoded by Huffman coding.

In a gray scale image, each pixel is represented by 8-bit unsigned integer value. The minimum and maximum value of unsigned integer is 0 to 255. The 0 represented black and 255 represent white. In text file every text file is represented by ASCII value. The ASCII value is run between 0 and 128. The extended ASCII value is 8 bit, and it matched with 8-bit pixel intensity. So, both the entities are treated as normal integer. In this proposed system, we have practiced bitwise XOR approach for text integration into image. The proposed work deals ASCII conversion of patient data and multilevel two-dimensional discrete wavelet transform. Advantages of this work are high data integrity even with large patient data. Accepted levels of imperceptibility, excellent PSNR values, and high CR and good payload capacity are obtained. **Figures 3** and **4** represented the block diagram of compression and decompression with data integration scheme. The decompression process is the inverse process of DICOM image compression as shown in block
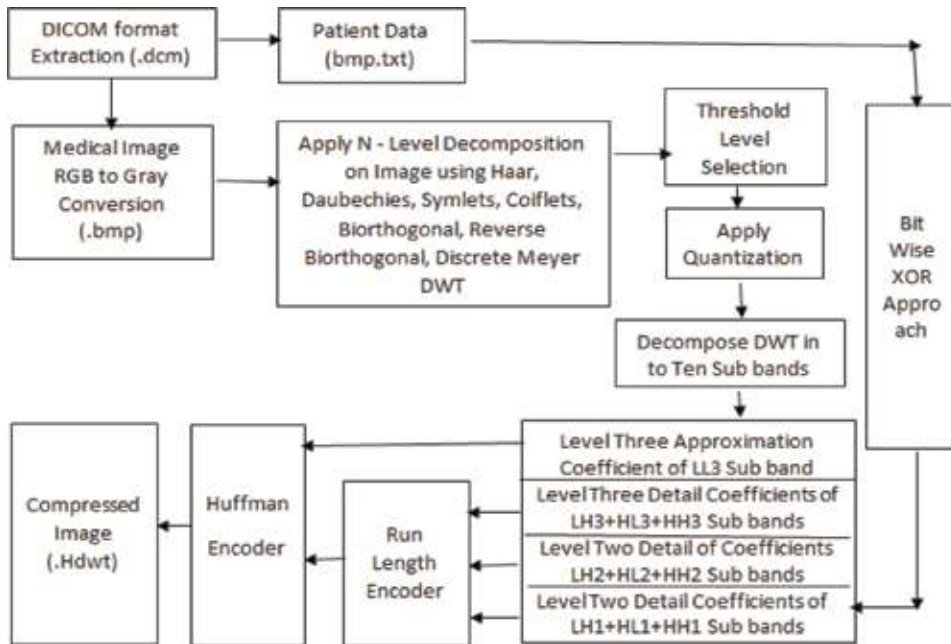
Figure 3.
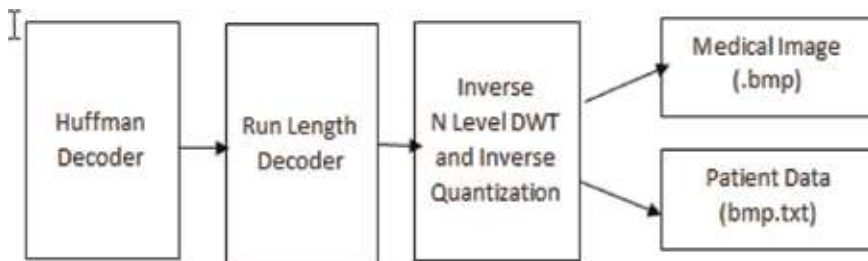*Block diagram of DICOM image compression and data integration method.*

Figure 4.
Block diagram of DICOM image decompression and data and image extraction.

diagram in **Figure 4**. The DICOM compressed image is recreated with acceptable quality through the abovementioned process.

3.1 Algorithm for integration of patient information (text) into image file

1. Select a proper Greyscale BMP image.

2. Select patient text file with .txt extension

3. Execute while loop (Number of Character Count in text file < = Number of pixels in the image)

4. Convert Character vector and pixel value into an unsigned 16-bit integer using function str2num and unit 16.

5. Integration of text in to Image Pixel = (Converted 16-bit unsigned pixel value) XORing_Bitwise (Converted 16-bit unsigned character value)

6. Increment Pixel value until last value.

7. Increment Character value until last value

8. Check the Character Count in text file = Character Count +1

9. End Loop

10. Rest of Integration of text in Image Pixel = original pixels of image

3.2 Extraction of patient information (text) from the image file

1. Open the original image and Integration of text in to Image Pixel

2. Execute while loop (Number of Pixel Count in image file ≤ Number of pixels in the image)

3. Convert pixel value into 16-bit integer value

4. Integration of text in to Image Pixel = convert to 16-bit integer (Integration of text in to Image Pixel)

5. A = (Original value of Pixel) XORing_Bitwise (Integration of text in to Image Pixel)

6. if A = 0 then break, else extracted text file which is equal to A

7. Extract original Pixel = Next original Pixel in image

8. Integration of text in to Image Pixel = Next Integration of text in to Image Pixel

9. End Loop

3.3 Multilevel 2D DWT decomposition on wavelet types

We implement an N-level 2D DWT decomposition. At each level of decomposition, the LL sub-band from the previous level is obtained, and each previous level is replaced with four new sub-bands. Each new sub-band is half the width and half the height of the LL sub-band from its parent sub-bands. The formula to calculate the total number of sub-bands depends on the number of level n. The number of sub-bands is therefore 3n + 1, where HHn represent high-frequency band, LLn is low-frequency band, and LHn and HLn are middle-frequency bands. The coefficients in LL are dominant. If any of the coefficients in LLn frequency band are changed, observer can observe that the corresponding spatial domain image has been modified.

Figure 5 shows the process of character integration in LHn sub-band, and it generates wavelet coefficients. It shows the scale and orientation selectivity of the DWT. Greatest energy is contained in the LLn sub-band, and the least energy is in the HHn sub-band. The HLn sub-band contains the vertical edges, and the LHn sub-band contains the horizontal edges. In this proposed work, we focus on data integration in LHn sub-bands because this band has high energy distribution as compared to other bands like HLn and HHn. The finest wavelet type and the appropriate coefficient selection method using threshold and quantization.
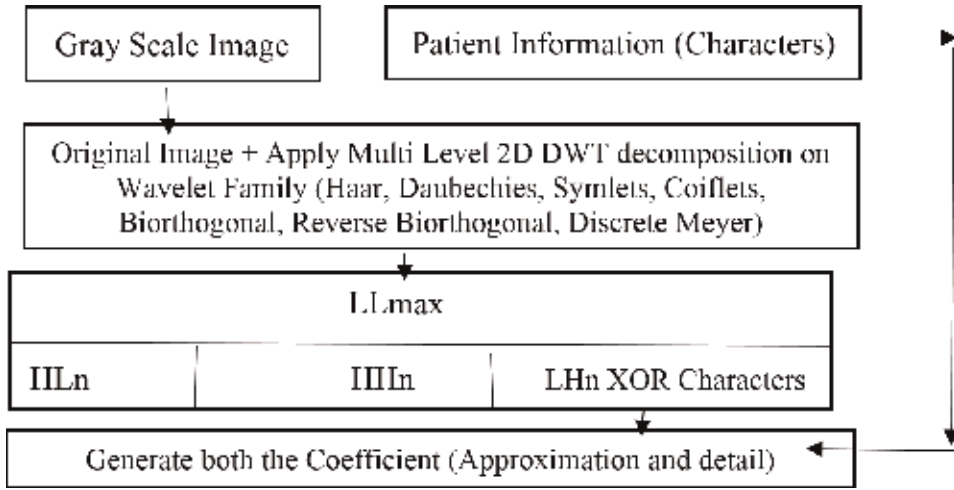
Figure 5.
The process of character integration in LHn sub-bands and generation of wavelet coefficients.

3.4 Apply thresholding and quantization technique on generated coefficients

3.4.1 Thresholding

Let n × n be matrix of an original image; noise observation can be written as $s = x + n$, where s = noise observation, x = original image, and n = noise. Let s (i), x(i), and n(i) denote ith sample of pixels. By applying discrete wavelet transform, the observed noised image obtained wavelet coefficients y = θ + z, where y = Ws, θ = Wx, and z = Wn, respectively. To recover θ and y, y is transformed into wavelet domain that decomposes y into many sub-bands [19, 20]. Then the coefficients with small value in the sub-bands are dominated by noise, thus replacing noise coefficients by zero. It is denoted by

$$y(i) = \theta(i) + z(i) \tag{3}$$

If

$$\widehat{y(i)} = abs[y(i)] < \lambda \tag{4}$$

$$y\,(i) = 0 \tag{5}$$

where y (i) is the input and noise wavelet coefficients, λ is the Threshold Valu, $\widehat{y(i)}$ is the *Threshold output.*

We define the PCDZ parameter; this parameter is required to calculate the percentage of nonzero DWT coefficients.

$$PCDZ = 100 * \frac{NBz}{Ly} \tag{6}$$

where NBz = number of zeros in DWT coefficients.
Ly = Number of Coefficients in DWT.

The proposed method used in the global threshold value that is derived by Donoho [19, 20] is given by the equation below. It is known to have a universal threshold.

$$\lambda = \sigma\sqrt{2\mathrm{log}Ly} \tag{7}$$

where Ly is the number of pixels in the medical image and σ is the noise variance.

3.4.2 DWT coefficient quantization

The quantization of each level permits to collect the set of nearest values. The uniform quantization on thresholded DWT coefficients in sub-bands will be transformed and to be contained in the interval width for quantization is between $0\ to\ 2^Q$. The quantized matrix will be computed as follows: to choose the quantization value Q (Q represents the interval width for quantization of the DWT coefficients in sub-bands), further determine the max(y(i)) and min(y(i)) values of the DWT coefficients which will represent as DWTmax and DWTmin. The uniform quantization on the resulting DWT coefficient sub-bands is formulated by the following equation:

$$DWTmin = \min(y(i)) \tag{8}$$

$$DWTmax = max(y(i)) \tag{9}$$

$$DWTCQ = round\left(\left(-1 + 2^Q\right) * \frac{\widehat{y(i)} - DWTmin}{DWTmax - DWTmin}\right) \tag{10}$$

$$\%ofIDWTCQ = round((DWTmax - DWTmin))/round\left(\left(-1 + 2^Q\right) * DWTCQ + DWTmin\right) \tag{11}$$

3.5 Encoding of wavelet coefficients using run-length encoder and Huffman encoder

In this implementation, hierarchical relationship of wavelet structure is explored to arrange wavelet coefficients into odd rows and even rows. The wavelet coefficients odd rows contain an ordering of wavelet coefficient that acts as approximate (smooth) value, and even rows contain different sign data that act as detail values. After evaluated many zeros in different orders of wavelets, by applying hard thresholding condition Eqs. (4), (5) on wavelet coefficients. In this whole process, separated approximate coefficients contain best information, while detail coefficients contain information like shapes and edges of image. The threshold condition chooses fixed threshold value to obtain desired quality of reconstructed image. After classifying threshold coefficients, need to transmit those coefficients using lossless method which will further be used for decompression purpose. Now encoded detail coefficients with run-length encoding excluding the highest approximate coefficient LL3 sub-bands, because LL3 sub-band does not have much long run of zeros.
To convert repetitive data into bit stream, Huffman encoder has been used in this implementation. Huffman code is an example of optimum prefix code; these codes are generated using variable code length where a number of bits are essential. This will be helpful in average code length calculations, and thus the data compression is taking place where sometimes compressed image is smaller than original image.

4. Results and discussion

The performances of implemented method are based on few essential criteria: the obtained compression ratio (CR), compression gain, and the quality of the

reconstructed image using PSNR, MSE (mean squared error), and SNR. Data compression equations are given below.

Data compression ratio = Uncompressed size/Compressed size

$$CR = \frac{X}{Y} \tag{12}$$

Space saving (%) determines performance of transformation efficiency over storage of data bits for original bit size to unprocessed bit size. It is like compression ratio; however it reflects percentage of how much data space is saved following compression [21]. It is given by the following equation:

Percentage of Compression Gain = 1 – Compressed size/Uncompressed Size

$$Compression\ Gain = \left(1 - \frac{Y}{X}\right) * 100 \tag{13}$$

The calculated peak signal to noise ratio between maximum values is power of signal and power of distorting noise which affects the quality of its representation. The PSNR is generally expressed in terms of logarithmic decibel scale [22].

$$PSNR = 20\log_{10}\left(\frac{MAX_f}{\sqrt{MSE}}\right) \tag{14}$$

MAX_f is the maximum signal value which exists in the original image, which is known to be good value of image?

where the MSE

$$MSE = \frac{1}{mn}\sum_{0}^{m-1}\sum_{0}^{n-1}\|f(i,j) - g(i,j)\|^2 \tag{15}$$

where f is the matrix data of our original image. g is the matrix data of our degraded image. m is the numbers of rows of pixels of the images. i is the index of that row. n is the number of columns of pixels of the image. j is the index of that column.

where SNR is given as the ratio of the mean value of the signal and the standard deviation of the noise.

$$SNR = 20 * \log\left(\frac{Intensity\ Signal}{Intensity\ Noise}\right) \tag{16}$$

To analyze the performance of our proposed method, we take **Table 3** as an input MR image for evaluation of various parameters, and their information are as follows:

Image name	Input size (in KB)	Level of decomposition (N)	Noise variance (σ^2)	The size of the DWT coefficient arrays (Ly)	Threshold value (λ)
1.2.840.113619.2.5.1762583153. 215519.978957063.122.dcm	522	3,4	$\sigma = 1$	266,539	3.29416477

Table 3.
Input MR image for evaluation of various parameters.

Figure 6 shows that pop-up message is generated after compression of DICOM input image, and it displayed warning dialog that image is compressed successfully, and then after pressing the ok button, compressed image is stored in image folder with. Hdwt extension (**Figure 7**).
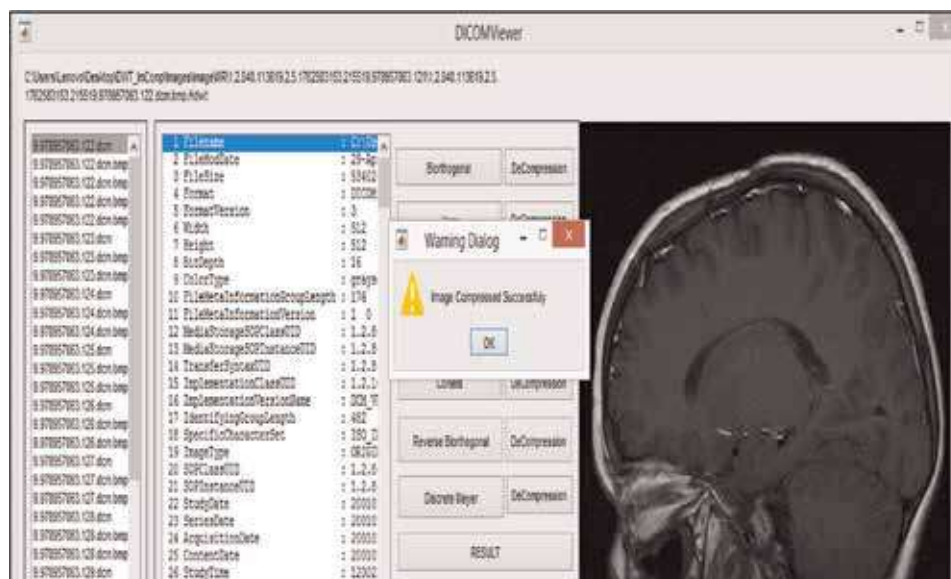

Figure 6.
Graphical user interface of DICOM image 1.2.840.113619.2.5.1762583153.215519.978957063.122.dcm of 522 KB for N = 3 and after pressing pop-up button of image compression successfully with size.
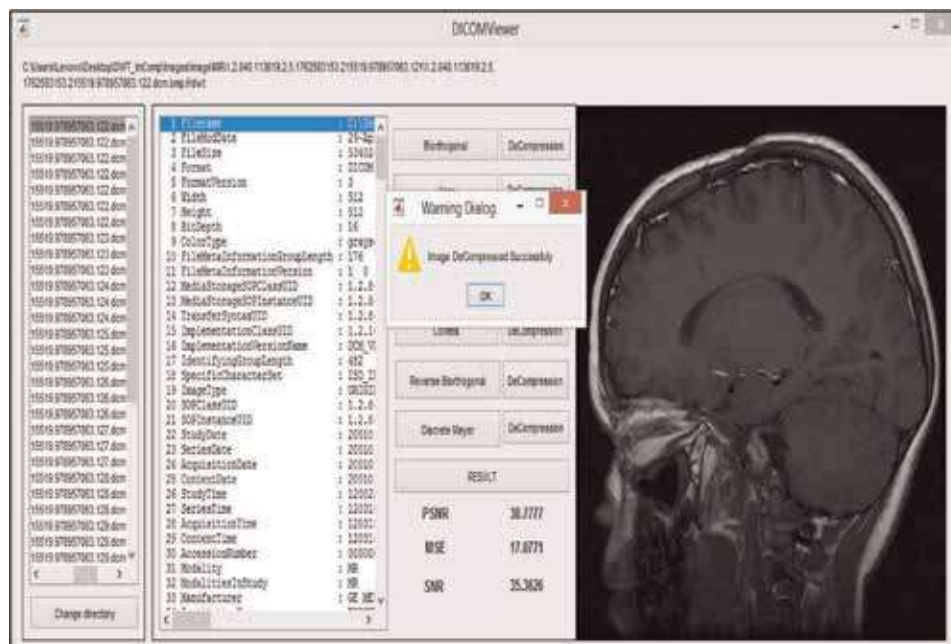

Figure 7.
Graphical user interface of DICOM image 1.2.840.113619.2.5.1762583153.215519.978957063.122.dcm of 522 KB for N = 4 has displayed PSNR, MSE, and SNR parameters after pressing pop-up button of decompression.
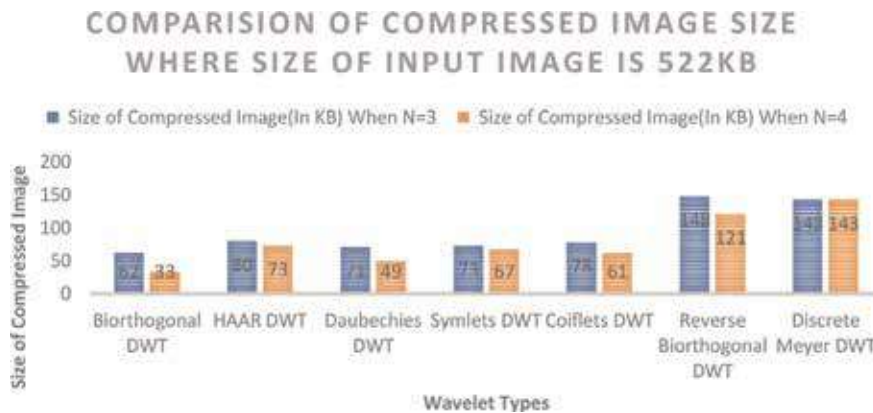
Figure 8.
The plot for size of compressed image in KB vs wavelet types for N = 3 and 4.

Figure 8 shows that if input image size is 522 KB, then Biorthogonal DWT give highest compressed size, and Reverse Biorthogonal DWT gives lowest compressed size. The decomposition level = 4 gives better result than N = 3.

Figure 9 plot shows comparison of compression ratio when decomposition level is 3 or 4 for various wavelet types where size of input MRI is 522 KB. Biorthogonal
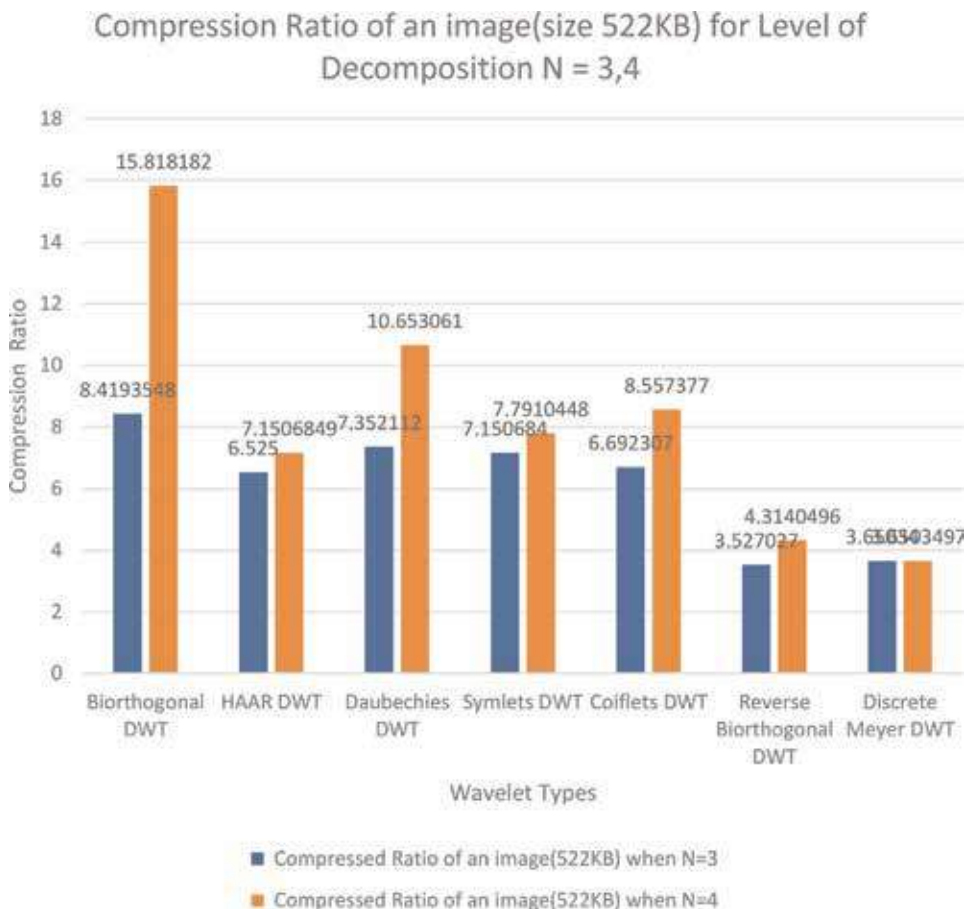

Figure 9.
The plot for compression ratio vs wavelet types For image size of input (MRI) image size 522 KB, when N = 3 and 4 compare.

DWT gives higher compression ratio, and Discrete Meyer DWT and Reverse Biorthogonal DWT give lower compression size. N = 4 gives better compression ratio (15:1 for Biorthogonal DWT and 10:1 Daubechies DWT) than N = 3.

In **Figure 10**, figure graph shows comparison of compression gain when decomposition level is 3 or 4 for various wavelet types where size of input MRI is 522 KB. Biorthogonal DWT gives higher compression gain, and Discrete Meyer DWT and Reverse Biorthogonal DWT give lower compression gain. N = 4 gives better compression gain (93.6781% for Biorthogonal DWT and 90.6130% for Daubechies DWT) than N = 3 (**Figure 11**).

Table 4 shows comparison of image quality parameters when application run at decomposition levels 3 and 4 for various wavelet types where size of input MRI is 522 KB. Daubechies DWT gives higher PSNR (42.0998db) where MSE is (35.2626db) and SNR is (28.3993 db). So, picture quality is good for N = 3. When we consider N = 4 decomposition level, we can choose Daubechies DWT for
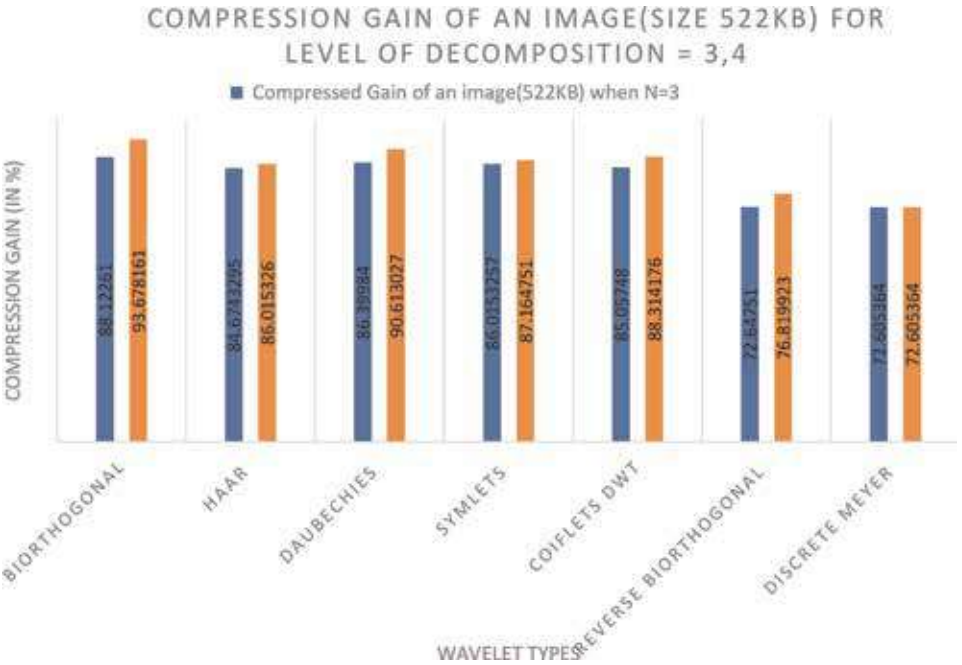

Figure 10.
The plot for compression gain vs wavelet types where image size of input (MRI) image size 522 KB for N = 3 and 4.

Figure 11.
The 36 KB of input .dcm file, compressed HDWT file, text file, and patient data integrated into the image file for Biorthogonal DWT.

205

Initial size of image: 522 KB (image name: 1.2.840.113619.2.5.1762583153.215519. 978957063.122.dcm)	Image quality parameter for N = 3 (in decibels)			Image quality parameter for N = 4 (in decibels)		
Wavelet types	**PSNR**	**MSE**	**SNR**	**PSNR**	**MSE**	**SNR**
Biorthogonal DWT	35.3358	35.2626	21.6352	30.7777	35.3626	17.0771
Haar DWT						
Daubechies DWT	42.0998	35.2626	28.3993	39.6729	35.3626	25.9723
Symlets DWT	39.0696	35.3626	25.3691	36.6956	35.3626	22.995
Coiflets DWT	40.4769	35.3626	26.7763	36.1026	35.3626	22.402
Reverse Biorthogonal DWT	32.0256	35.3626	18.325	26.3603	35.3626	12.6597
Discrete Meyer DWT	40.6572	35.3626	26.9566	32.5428	35.3626	18.8423

Table 4.
Input MRI .dcm file input having 522 KB size for evaluation of various image quality parameters.

compression to achieve higher quality of medical image. This tool does not work on Haar DWT; there is no output for Haar wavelet type.

Table 5 indicates that Daubechies, Symlets, and Coiflets DWT give higher compressed image size (9 KB) and highest compression ratio (4) and gain (75%). Decompression is working in this input size (36 KB). So, when the small-size input .dcm file, image reconstruction is required, this implementation work will be applicable. This application gives good PSNR (45.1486) and better MSE (29.88) and SNR (30.0124) for Daubechies DWT.

Table 6 indicates that Biorthogonal DWT gives higher compressed image size (2 KB) and highest compression ratio (18:1) for threshold value = 50. But image quality is degraded due to PSNR value = 32.7496.

Table 7 shows that CT0081 gives good compression result for implemented method, but other input CT images give less compression ratio than .jpg file format. The obtained result shows that.

Sr. no.	Wavelet type	Size of compressed image (in KB)	CR	% of CG	PSNR (in db)	MSE (in db)	SNR (in db)
1	Biorthogonal DWT	15	2.4	58.33333	35.2407	19.9722	39.0124
2	Haar DWT	11	3.272727	69.44444	44.8457	29.5771	30.0124
3	Daubechies DWT	9	4	75	45.1486	29.88	30.0124
4	Symlets DWT	9	4	75	44.9406	29.6721	39.0124
5	Coiflets DWT	9	4	75	38.9493	23.6808	39.0124
6	Reverse Biorthogonal DWT	18	2	50	35.7811	20.5126	39.0124
7	Discrete Meyer DWT	15	2.4	58.33333	44.6503	29.3818	39.0124

Table 5.
Compression and image quality performance of input (CT scan) image size 36 KB for different wavelet types.

Parameters	$\lambda = 3$	$\lambda = 10$	$\lambda = 20$	$\lambda = 30$	$\lambda = 50$
Compressed image in KB	9	5	4	3	2
Compression ratio	4	7.2	9	12	18
PSNR	35.1707	34.5081	33.673	33.1783	32.7496
MSE	19.9022	19.2396	18.4	17.9098	17.9098
SNR	39.0124	39.0124	39.0124	39.0124	39.0124

Table 6.
Compression and image quality performance of input (CT scan) image size 36 KB (gray scale) for different threshold values on Biorthogonal DWT using proposed method.

Sr. no.	Image ID	Dimension	Depth in bit	Input file size in KB	DICOM size in KB	.jpg file size in KB	Implemented method .hdwt size in KB
1	CT0014	512×512	24	1030	769	25	29
2	CT0051	512×200	24	204	301	17	22
3	CT0052	250×512	24	254	376	17	26
4	CT0059	350×512	24	353	526	23	46
5	CT0074	512×512	24	5130	769	61	67
6	CT0081	888×733	24	2547	1908	167	165
7	CT0090	512×512	24	3591	769	93	152
8	CT0101	512×512	24	516	769	92	71
9	CT102	512×605	24	609	909	153	162
10	CT110	512×512	24	4616	769	61	68

Table 7.
Comparison of implemented method and .JPG format for 10 CT scan DICOM images.

5. Conclusions

Compression and decompression are necessary tasks in medical imaging applications. This implementation provides patient data integration within the medical image. It is very important to maintain the patient data security. This implementation work is very helpful to hide and recover patient information within the medical image and follow compression/decompression without any data loss. In this implanted work, 2D DWT and N-level decomposition are applied on medical image, and then the extracted detail coefficients are firstly encoded by RLE. Secondly, the extracted approximate coefficient and encoded detailed coefficients are encoded by Huffman encoder. The generated result shown that Biorthogonal DWT gives better compression size, compression ratio, and compression gain for higher decomposition level (N = 4), but image quality parameters like PSNR and MSE are degraded. After comparison with JPEG file format and implemented work, this work gives less compression size. We conclude that for medical image compression, we can select N = 3, decomposition level with $\lambda = 3$, threshold value, and Biorthogonal DWT for good image quality.

Acknowledgements

Conflict of interest

The authors declare that there is no conflict of interests, financial, potential, or otherwise associated with this manuscript.

Author details

Trupti N. Baraskar[1]* and Vijay R. Mankar[2]

1 Department of Electronic Engineering, Sant Gadge Baba Amravati University, Amravati, India

2 Department of Electronic and Telecommunication Engineering, Government Polytechnic, Washim, India

*Address all correspondence to: trupti.baraskar@mitwpu.edu.in

IntechOpen

References

[1] NEMA Publications. DICOM Standard. Digital Imaging and Communications in Medicine (DICOM). 2008. Available from: ftp://medical.nema.org/medical/dicom/2008/

[2] Cho K, Kim J, Jung SY, Kim K. Development of Medical Imaging Viewer Role in DICOM Standard. Hyun-Kook Kuhng Daegu University, School of Computer and Communication Engineering **ETRI, Broadcasting Media Research Group 0-7803-8940-91051 IEEE; 2005

[3] Mousa WA, Shwehdi MH, Abdul-Malek MA. Conversion of DICOM System Images to Common Standard Image Format Using Matlab. Asia SENSE. SENSOR; 2003. pp. 251–255

[4] Suapang P, Dejhan K, Yimmun S. Medical Image Compression and DICOM-Format Image Archive. Bangkok, Thailand: Department of Telecommunication Engineering, King Mongkut's Institute of Technology Ladkrabang, ICCAS-SICE; 2009

[5] Larobina M, Murino L. Medical image file format. Journal of Digital Imaging. 2014;**27**(2):200-206. DOI: 10.1007/s10278-013-9657-9

[6] Verma DR. Managing DICOM image: Tips and tricks for radiologist. Indian Journal of Radiology and Imaging. 2012;**22**(1):004-013. DOI: 10.4103/0971-3026.95396

[7] Graham RNJ, Perriss RW, Scarsbrook AF. DICOM demystified: A review of digital file formats and their use in radiological practice. Clinical Radiology. 2005;**60**(11):1133-1140. DOI: 10.1016/j.crad.2005.07.003

[8] Baraskar T, Pawar A. Conversion of DICOM image to common standard image formats. International Journal of Emerging Technology and Advanced Engineering. 2013;**3**:1-5

[9] Ujgare NS, Baviskar SP. Conversion of DICOM image in to JPEG, BMP and PNG image format. International Journal of Computer Applications. 2013;**62**(11):22-26

[10] Kaur S, Jindal G. Survey of databases used in image processing and their applications. International Journal of Scientific and Engineering Research. 2011;**2**(10):1-9

[11] Chen P. Study on medical image processing technologies based on DICOM. Journal of Computers. 2012;**7**(10):1-8. DOI: 10.4304/jcp.7.10.2354-2361

[12] Vinayak B, Gaikwad AN, Kanaskar M. DICOM medical data compression for telemedicine IN rural areas. Advances in Engineering Science. 2008;**2**:001-006

[13] Zhifeng L, Changhong F, Xu F, Zhicong Q, Shunxiang W. An easy image compression method and its realization base on MATLAB, Information Engineering and Computer science International Conference; 2009

[14] Dimitrovski I, Guguljanov P, Loskovska S. Implementation of web-based medical image retrieval system in Oracle. In: IEEE 2nd Intl. Conference on Adaptive Science & Technology. 2009

[15] Xiaolei SHI, Wang M. Transformation of DICOM digital medical image format into BMP general image format. Microcomputer Informatics. 2010;**26**:195-197

[16] Aliming H. The conversion between DICOM medical image format and common graphic format [master degree dissertation]. Chengdu, Sichuan: Chinqi Sichuan University; 2006

[17] Cyriac M, Chellamuthu C. Medical image compression using visual quantization and modified run length encoding. Biomedical Imaging and Intervention Journal. 2013;**7**(2):1-8. DOI: 10.2349/biij9.2.e5

[18] Hussain AJ, Al-Fayadh A, Radi N. Image compression technique: A survey in lossless and lossy algorithms. Neurocomputing. 2018;**300**:44-69

[19] Akhtar MB, Qureshi AM, Qamar ul Islam. Optimum Run Length Coding for JPEG Image Compression used in Space Research Program of IST. IEEE; 2011

[20] Janet J, Mohandass D, Meenalosini S. Lossless Compression Techniques for Medical Images in Telemedicine-Advances in Telemedicine Technologies, Enabling Factors, Scenarios. Austria: INTECH; 2011. pp. 111-130. ISBN 978-953307-159-6

[21] Salomon D. Data Compression-the Complete Reference. 2nd ed. Heidelberg: Springer; 2001

[22] Shajun Nisha S, Kothar Mohideen S. Wavelet coefficients Thresholding techniques for Denoising MRI images. Indian Journal of Science and Technology. 2016;**9**(28):1-8. DOI: 10.17485/ijst/2016/v9i28/93872

[23] Ray A. Performance evaluation of various image compression techniques using SVD, DCT and DWT. International Journal of Research in Engineering and Technology. 2017;**6**(6): 1-6

*Edited by Sudhakar Radhakrishnan
and Muhammad Sarfraz*

This book is intended to attract the attention of practitioners and researchers in academia and industry interested in challenging paradigms of coding theory and computer vision. The chapters in this comprehensive reference explore the latest developments, methods, approaches, and applications of coding theory in a wide variety of fields and endeavours. This book is compiled with a view to provide researchers, academicians, and readers with an in-depth discussion of the latest advances in this field. It consists of twelve chapters from academicians, practitioners, and researchers from different disciplines of life. All the chapters are authored by various researchers around the world covering the field of coding theory and image and video processing. This book mainly focusses on researchers who can do quality research in the area of coding theory and image and video processing and related fields. Each chapter is an independent research study, which will motivate young researchers to think about. These twelve chapters are presented in three sections and will be an eye-opener for all systematic researchers in these fields.

IntechOpen